

**The impact of tropical convection on the dynamics  
and predictability of midlatitude Rossby waves:  
a climatological study**

Zur Erlangung des akademischen Grades eines  
DOKTORS DER NATURWISSENSCHAFTEN  
der Fakultät für Physik des Karlsruher Instituts für Technologie (KIT)  
Karlsruhe

genehmigte

DISSERTATION

von

Dipl.-Met. Julian Francesco Daniel Quinting  
aus Menden (Sauerland)

Tag der mündlichen Prüfung:	16. Januar 2015
Referent:	Prof. Dr. Sarah C. Jones
Korreferent:	Prof. Dr. Peter Braesicke



# Kurzfassung

Organisierte tropische Konvektion beeinflusst nicht nur das Wetter, die Witterung und das Klima in ihrer unmittelbaren Umgebung, sondern auch in weit entfernten Regionen der mittleren Breiten. Der Einfluss macht sich in den mittleren Breiten zum Beispiel durch ungewöhnlich frühe Kaltlufteinbrüche, Starkniederschläge, Sturmtiefs sowie lang anhaltende Kälte- und Hitzeperioden bemerkbar. Die korrekte Wiedergabe der komplexen tropisch-außertropischen Wechselwirkungen, welche zu den genannten außergewöhnlichen Wettererscheinungen führen, stellt eine große Herausforderung für globale numerische Wettervorhersage Modelle dar. Eine verbesserte Wiedergabe dieser Wechselwirkungen in den numerischen Modellen würde helfen, die Vorhersagbarkeit der teilweise extremen Wettererscheinungen auf der mittelfristigen bis saisonalen Skala zu verbessern. Bevor jedoch diese Verbesserungen vorgenommen werden können, bedarf es einem exakten physikalischen Verständnis der entscheidenden Prozesse und der Identifizierung von systematischen Modellfehlern, welche die Vorhersagbarkeit begrenzen. Mit dem Fokus auf diesen beiden Aspekten, werden in der vorliegenden Arbeit die Wechselwirkungen zwischen zwei tropischen Wettersystemen – tropischen Wirbelstürmen und der Madden-Julian Oszillation (MJO) – und den mittleren Breiten klimatologisch betrachtet.

Bisherige Studien untersuchten den Einfluss von tropischen Wirbelstürmen auf die Strömung der mittleren Breiten anhand einzelner Fälle oder anhand idealisierter numerischer Experimente. Diese Arbeiten zeigten, dass die Interaktion eines tropischen Wirbelsturms während seiner außertropischen Umwandlung mit der Strömung der mittleren Breiten zur Auslösung von synoptisch-skaligen horizontalen Wellen, so genannten Rossbywellen, führen kann. In der vorliegenden Arbeit wird auf der Grundlage von Reanalysedaten die Auslösung von Rossbywellen durch tropische Wirbelstürme erstmals systematisch über einen Zeitraum von 30 Jahren untersucht. Dazu wurden synoptisch-skalige Rossbywellen Pakete (RWP) mit Hilfe einer räumlichen Filterung des meridionalen Windfeldes in der oberen Troposphäre identifiziert und ihre Häufigkeit sowie ihre Amplitude vor und nach der außertropischen Umwandlung von tropischen Wirbelstürmen über dem Westpazifik, dem Südindischen Ozean und dem Nordatlantik bestimmt. Die Ergebnisse zeigen, dass RWP in den mittleren Breiten nach der außertropischen Umwandlung von tropischen Wirbelstürmen über dem Westpazifik und dem Südindischen Ozean häufiger vorkommen als klimatologisch üblich. Ihre Amplitude ist zudem statistisch signifikant größer als die von RWP, welche im Zusammenhang mit außertropischen Tiefdruckgebieten stehen. Die Unterscheidung zwischen außertropischen Umwandlungen, die der Auslösung einer Rossbywelle vorhergehen, und solchen, die nicht mit der Amplifizierung einer Rossbywelle verbunden sind, ermöglicht die Identifizierung von Prozessen und Orten, die für die Verstärkung der Rossbywelle

entscheidend sind. Eine Kompositanalyse zeigt, dass sich Rossbywellen bevorzugt stromab der außertropischen Umwandlung von tropischen Wirbelstürmen verstärken, wenn bereits vor der außertropischen Umwandlung eine Rossbywelle stromauf des Sturms existiert hat. Die Analyse von Energiebudgets und von Feldern potentieller Wirbelstärke in einer Vielzahl von Fällen zeigt, dass die Prozesse zwischen einem Trog stromauf der außertropischen Umwandlung und dem tropischen Wirbelsturm selbst von Bedeutung sind für die weitere Amplifizierung der Welle. Aus energetischer Sicht wird während der außertropischen Umwandlung potentielle in kinetische Energie umgewandelt. Die Produktion von kinetischer Energie ist deutlich höher in Fällen mit Wellenanregung als in Fällen ohne Wellenanregung. Die Akkumulation der kinetischen Energie zwischen dem Trog stromauf und dem Sturm selbst trägt dann entscheidend zur Wellenamplifizierung bei. Dementsprechend legen die Ergebnisse nahe, dass eine falsche Repräsentation der Akkumulation von Energie zwischen Trog und Wirbelsturm in numerischen Modellen die Vorhersagbarkeit in Regionen stromab dramatisch verringert.

Im zweiten Teil der vorliegenden Arbeit wird der Einfluss der Madden-Julian Oszillation auf die Eigenschaften von RWP in den mittleren Breiten untersucht. Diese wurden aus Reanalysedaten für die Monate Dezember bis Februar 1980–2009 durch räumliche Filterung des Meridionalwindes identifiziert. Die Häufigkeit und die Ausbreitungseigenschaften von RWP zeigen eine signifikante Abhängigkeit vom Zustand der MJO. Wenn sich die Konvektion der MJO über dem maritimen Kontinent befindet, ist global, insbesondere über dem Ostpazifik und dem Nordatlantik, eine erhöhte Häufigkeit von RWP zu beobachten. Dem gegenüber erreicht die Häufigkeit der RWP am Ende eines Lebenszyklus der MJO ihr Minimum. Die Ergebnisse deuten darauf hin, dass die Ausbreitungseigenschaften der RWP von planetaren Zirkulationsmustern (z. B. Nordatlantische Oszillation), die im Zusammenhang mit der MJO stehen, beeinflusst werden. Wenn sich die Konvektion der MJO über dem maritimen Kontinent befindet, ermöglicht eine relativ schwache westliche Strömung in den mittleren Breiten die Verlagerung von RWP in die Subtropen. Ebenso führt eine relativ schwache westliche Strömung am Ende eines MJO-Lebenszyklus zur Verlagerung von RWP in den subtropischen Ostatlantik. Ein Vergleich der Reanalysedaten mit einem Vorhersagedatensatz zeigt, dass die Vorhersagen diese Verlagerungen der RWP nicht korrekt wiedergeben. Außerdem überschätzen sie systematisch die Häufigkeit von RWP.

Die Ergebnisse dieser Arbeit zeigen, dass zwei tropische Wettersysteme – tropische Wirbelstürme und die Madden-Julian Oszillation – maßgeblich zur Variabilität von synoptisch-skaligen Rossbywellen Paketen in den mittleren Breiten beitragen. Sowohl dieses Ergebnis als auch die Tatsache, dass stark amplifizierte Rossbywellen im Zusammenhang mit extremen Wetterereignissen stehen, legen nahe, dass die korrekte Wiedergabe der Wechselwirkungen zwischen den zwei genannten tropischen Wettersystemen und den mittleren Breiten entscheidend ist für die korrekte Prognose von Wetter, Klima und insbesondere ihrer Extreme.

# Abstract

Organized tropical convection does not only impact the weather conditions and climate in its adjacencies. It impacts weather from medium-range to seasonal to decadal timescales in remote regions. The impact on the midlatitudes, for example, is characterized by early cold-air-outbreaks, heavy precipitation, extratropical storms as well as long-lasting heat and cold spells. The accurate representation of complex tropical-extratropical interactions which lead to these unusual weather events poses a challenge to state of the art global numerical weather prediction models. An improved representation of the tropical-extratropical interactions would help to better predict the partly extreme weather events on a medium-range to seasonal timescale. However, this requires first to understand the physical mechanisms of the main processes and second to identify systematic model errors that limit the predictability. Focusing on these two aspects, this study investigates the interactions between two tropical weather systems – tropical cyclones and the Madden-Julian Oscillation – and the midlatitudes in reanalyses and reforecasts from a climatological perspective.

Previous studies that investigated the impact of tropical cyclones (TCs) on the midlatitude flow focused on single cases and performed idealized numerical experiments. These studies revealed that TCs which undergo extratropical transition (ET) and interact with the midlatitude flow may excite horizontal waves in the upper troposphere, so-called Rossby waves. For the first time, this study investigates systematically the excitation of midlatitude Rossby waves by western North Pacific, South Indian Ocean and North Atlantic TCs over a 30 year period. We applied a spatial filter to the upper-level meridional wind in reanalysis data to identify synoptic-scale Rossby wave packets (RWPs) and determined their amplitude and occurrence frequency prior and after the ET of TCs. The results reveal an anomalously high RWP occurrence frequency downstream of western North Pacific and South Indian Ocean TCs. The amplitude of the RWPs differs statistically significant from the general midlatitude variability which indicates that RWPs which are associated with TCs are more extreme than those which are associated with extratropical cyclones. The distinction between ET events that were followed by a downstream Rossby wave development and events that were not followed by a downstream Rossby wave development provided insights into processes that are essential for the amplification of a Rossby wave. A composite analysis suggests that a precursor Rossby wave upstream of a TC favors the conditions for the development of a Rossby wave downstream of the TC. The analysis of potential vorticity and energy budgets in a number of cases reveals that the phasing between an upstream trough and the TC are crucial for the further amplification of the wave. From an energetics perspective, potential energy is converted into kinetic energy in the vicinity of the TC. The conversion is much stronger in cases with wave amplification

than in cases without wave amplification. The accumulation of kinetic energy between the upstream trough and the TC contributes essentially to the wave amplification. Thus, the results suggest that an inaccurate representation of the accumulation of kinetic energy between the trough and the TC in numerical models reduces dramatically the predictability in downstream regions.

The second part of this study deals with the impact of the Madden-Julian Oscillation (MJO) on the characteristics of midlatitude RWPs. We identified the RWPs in reanalysis data for the period December to February 1980–2009. The propagation characteristics and the occurrence frequency of RWPs exhibit a significant variation with the life-cycle of the MJO. The RWP occurrence frequency increases globally, in particular over the eastern North Pacific and the North Atlantic, when the MJO related convection is located over the Maritime Continent. The midlatitude RWP occurrence frequency is lowest at the end of the MJO life-cycle, i.e. when the MJO related convection decays east of the date line. The results indicate that planetary-scale circulation patterns (e.g. the North Atlantic Oscillation) which are modified through the MJO impact significantly the propagation characteristics of RWPs. When the MJO related convection is located over the Maritime Continent, a weaker jet over the Pacific allows RWPs to propagate into the subtropics. At the end of an MJO life-cycle, a weaker jet over the North Atlantic allows RWPs to propagate into the subtropical east Atlantic. A systematic comparison between RWPs in a reanalysis dataset and RWPs in a reforecast dataset reveals that forecasts do not adequately represent the propagation characteristics of RWPs. In addition, the forecasts systematically overestimate the RWP occurrence frequency.

The results of this study show that two tropical weather systems – TCs and the MJO – significantly modify the variability of synoptic-scale RWPs. Since previous studies have shown that strongly amplified RWPs are associated with extreme weather events, the results of this study suggest that the correct representation of interactions between the MJO or TCs and the midlatitude flow is crucial for the correct prediction of weather, climate and in particular its extremes.

# Contents

<b>1</b>	<b>Introduction</b>	<b>1</b>
<b>2</b>	<b>Background and theoretical basis</b>	<b>5</b>
2.1	The Madden-Julian oscillation . . . . .	6
2.2	Tropical cyclones . . . . .	11
2.3	Rossby waves . . . . .	13
2.4	Tropical-extratropical interactions . . . . .	16
2.4.1	Tropical-extratropical interactions through the MJO . . . . .	17
2.4.2	Extratropical transition of tropical cyclones . . . . .	24
<b>3</b>	<b>Data and methods</b>	<b>33</b>
3.1	ERA-Interim reanalyses and reforecasts . . . . .	33
3.2	Tropical Cyclone dataset . . . . .	34
3.3	Identification of Rossby wave packets . . . . .	36
3.4	Eddy kinetic energy budget analysis . . . . .	41
3.4.1	Derivation of eddy kinetic energy tendency equation . . . . .	41
3.4.2	Downstream baroclinic development from an eddy kinetic energy perspective . . . . .	45
3.5	Quasi-geostrophic forcing diagnostics . . . . .	47
<b>4</b>	<b>The impact of tropical cyclones on midlatitude Rossby wave packets</b>	<b>49</b>
4.1	Rossby wave packets downstream of ET events . . . . .	49
4.1.1	Two contrasting cases: Typhoons Sinlaku (2008) and Choi-Wan (2009) . . . . .	49
4.1.2	Climatology of Rossby wave packets . . . . .	51
4.1.3	Western North Pacific tropical cyclones . . . . .	53
4.1.4	South Indian Ocean tropical cyclones . . . . .	54
4.1.5	North Atlantic tropical cyclones . . . . .	55
4.1.6	Sensitivity of the results . . . . .	56
4.2	Composite analysis of cases with and without Rossby wave development . . . . .	60
4.2.1	Identification of cases . . . . .	60
4.2.2	Rossby wave amplification from a potential vorticity perspective . . . . .	64
4.2.3	The role of warm conveyor belts in the amplification of Rossby waves during extratropical transition . . . . .	78
4.2.4	Rossby wave amplification from an eddy kinetic energy perspective . . . . .	84
<b>5</b>	<b>The interaction between the MJO and midlatitude Rossby waves</b>	<b>95</b>
5.1	The interaction between the MJO and RWPs in analyses . . . . .	95

---

5.2	The representation of the MJO in ERA-Interim reforecasts . . . . .	106
5.3	The interaction between the MJO and RWP in a reforecast data set . . .	110
<b>6</b>	<b>Conclusions and Outlook</b>	<b>119</b>
	<b>List of abbreviations</b>	<b>129</b>
	<b>Bibliography</b>	<b>131</b>

# 1 Introduction

“Hurricane Gonzalo to hit UK on Monday night after battering Bermuda” – This headline from “THE INDEPENDENT” on 20 October 2014 emphasizes that tropical weather systems impact the midlatitude weather directly. However, the events during which a former tropical system impacts the midlatitude weather directly are relatively rare. Less obvious, but omnipresent, is the indirect impact of tropical systems on midlatitude dynamics and forecasts. Two prominent examples of tropical weather systems which have been recognized as important modifiers of the midlatitude weather are tropical cyclones (TCs) and the Madden-Julian Oscillation (MJO). Although very different in their spatial, temporal and physical characteristics one common feature is that the MJO as well as TCs may perturb the midlatitude westerly flow. These perturbations are well-known as upper-level troughs and ridges that propagate eastward along the midlatitude flow. A sequence of troughs and ridges is referred to as a Rossby wave.

Tropical cyclones that recurve and move into midlatitudes may transition from a symmetric TC into an asymmetric extratropical low-pressure system. This process is referred to as extratropical transition (ET) (Jones et al., 2003). During the ET, the transitioning TCs interact with the upper-level jet stream and deflect the jet stream pole- and equatorward. These deflections of the jet stream – well-known as troughs and ridges – can propagate along the jet stream into remote regions which is referred to as an upper-level Rossby wave. It has been shown that Rossby waves which are associated with the ET of TCs have the ability to cause surface cyclogenesis (Agustí-Panareda et al., 2004; Cordeira and Bosart, 2010) or high-impact weather events such as cold-air outbreaks (Archambault et al., 2007), heat waves (Parker et al., 2013) and severe precipitation (Martius et al., 2008; Grams et al., 2011). Furthermore, ET events may lead to considerable forecast challenges in downstream regions as uncertainties associated with the ET events tend to grow and spread into downstream regions in connection with the development of midlatitude Rossby wave trains (Harr et al., 2008; Anwender et al., 2010).

Planetary-scale Rossby waves that are excited by the MJO convection can influence flood events, heat waves and droughts, forest fires, tornado activity and climate modes in the extratropics (Zhang, 2013). Several recent flood events in midlatitude and tropical regions have been linked to the MJO (e.g. Zhu et al., 2003; Barlow et al., 2005; Aldrian, 2008). Statistical investigations showed that the occurrence of flood events over North America depends strongly on the location of the MJO related convection (e.g. Jones, 2000; Bond and Vecchi, 2003; Becker et al., 2011). Large flood events over the northwest United States occur preferentially when the MJO convective center is located over the western

Pacific. Less likely are flood events over the northwest United States when the main MJO convection is located east of the dateline (Zhang, 2013). Temperature extremes occurring worldwide can be linked to the MJO. Three very recent examples are the anomalously cold winter 2009–2010 in East Asia (Park et al., 2010), the North American Heat wave in March 2012 (Dole et al., 2014) and the unusually cold European March 2013 (Slingo, 2013). Two thirds of east Asian extreme cold surges occur when the MJO convection is located over the Indian Ocean (Jeong et al., 2005). At the same time, positive temperature anomalies of +2 to +5  $K$  occur in central/northern Alaska and central/eastern Canada. The eastward propagation of the MJO convection causes a northward shift of warm anomalies in Canada and a change from above normal to below normal temperatures over Alaska. Several studies suggested that these midlatitude temperature anomalies are related to teleconnections (e.g. Pacific North American pattern, North Atlantic Oscillation) between the MJO and the midlatitudes (Cassou, 2008; Lin et al., 2009). A planetary Rossby wave that emanates from enhanced convection of the MJO creates above (below) normal temperatures through steady warm (cold) advection (e.g. Vecchi and Bond, 2004; Lin et al., 2009).

The examples above illustrate that the TCs and the MJO may have an economic and societal impact in remote regions through the excitation of Rossby waves. Hence, it is necessary to better understand the dynamics and to improve the forecasts of the Rossby wave excitation process as this is essential for the correct prediction of weather and in particular its extremes. To achieve this goal we address the following research questions in this thesis from a climatological perspective. Do TCs impact the occurrence frequency and amplitude of synoptic-scale RWPs? How does this impact vary between various ocean basins? How do ET related RWPs differ from the general variability of midlatitude RWPs? Under which synoptic conditions are TCs preferentially associated with the excitation of a Rossby wave? Which physical processes are most relevant during the excitation of a Rossby wave? How does the synoptic-scale RWP occurrence frequency vary with the location of the MJO convectively active region? How does the synoptic-scale wave activity relate to planetary wave patterns that are associated with the MJO? How well is the MJO represented in a state of the art reforecast data set? And does an inaccurate representation of the MJO project back onto forecasts of midlatitude synoptic-scale Rossby waves?

Whereas many recent studies focused on a limited number of cases, this study documents the midlatitude Rossby wave response to tropical convection and the Rossby wave excitation process associated with TCs in a composite view. The availability of atmospheric reanalysis data allows us to analyze the atmospheric dynamics of the wave excitation process for a large number of cases with different diagnostic tools. Thus, this study provides a climatological analysis of the connection between the MJO or TCs and midlatitude Rossby waves. In addition, reforecast data, i.e. forecasts that were initialized from reanalysis data and computed with a uniform configuration of a numerical weather prediction system, allow us to identify systematic forecast errors concerning the midlatitude Rossby wave response to tropical convection.

The remainder of this thesis is organized as follows. Chapter 2 provides background information on the MJO, TCs, Rossby waves and tropical-extratropical interactions. The

data and methods used are described in Chapter 3. The results of this thesis are presented in two parts. A climatological investigation of the impact of TCs on midlatitude Rossby waves (Chapter 4) is followed by a climatological investigation of the impact of the MJO on midlatitude Rossby waves (Chapter 5). The thesis completes with conclusions and a discussion of future research opportunities in Chapter 6.



## 2 Background and theoretical basis

The large-scale circulations of the Earth's atmosphere are driven by spatial variations of incoming solar radiation. The main reason for these spatial variations is the spherical shape of the Earth which causes a strong latitudinal dependence of incoming solar radiation. The latitudinal variation of net radiation ( $-100 \text{ W m}^{-2}$  at the poles;  $+75 \text{ W m}^{-2}$  at the equator) and the resulting radiative imbalance lead to substantial temperature differences between the poles and the tropics. These imbalances are reduced via heat-transporting horizontal and vertical motions within the atmosphere and the ocean.

In the atmosphere, a large amount of heat is transported by an axisymmetric mean meridional circulation – the Hadley circulation (Hadley, 1735). The circulation is characterized by rising motion in the tropics and descent in subtropical regions between  $25\text{--}30^\circ\text{N/S}$ . Satellite imagery and satellite derived precipitation data show a band of convective activity associated with the ascending branch of the Hadley cell that is centered on average around the equator. This band of mainly deep convection forms at a convergent zone of the northern and southern hemispheric trade winds – the intertropical convergence zone (ITCZ). The air that rises in the ITCZ quickly reaches saturation so that latent heat is released. This latent heat release leads to a concentration of the ascending motion of the Hadley cell into the rather narrow ITCZ. So far, we only considered zonal means which gives the impression of a zonal symmetric circulation in the tropics. However, in particular the Hadley cell is far from being zonally symmetric due to longitudinally asymmetric forcing by orography, sea surface temperature anomalies and land-sea heating contrasts. These longitudinally dependent components are separated into steady circulations (Walker circulation), semi-annual circulations (e.g. Monsoon circulations) and intraseasonal circulations. The dominant component of the intraseasonal (30–90 days) variability in the tropical atmosphere is the Madden-Julian Oscillation (MJO) (Madden and Julian, 1971; Madden and Julian, 1972). In addition to the stationary, semi-annual and intraseasonal circulations the tropical climate comprises a variety of weather systems on a shorter timescale, e.g. African Easterly waves, upper-tropospheric troughs, monsoon depressions and TCs.

The study focuses on the interaction of the MJO and TCs with midlatitude synoptic-scale Rossby waves. Therefore, we provide first a brief introduction into the characteristics of the MJO, TCs and Rossby waves and give a review on tropical-extratropical interactions in the last part of this chapter.

## 2.1 The Madden-Julian oscillation

Signatures of a coherent oscillation over periods ranging from 30 to 60 days were initially found in analyses and observations of surface pressure and zonal wind components at many tropical locations (Madden and Julian, 1971; Madden and Julian, 1972). Subsequent studies tied these variations to the organization of tropical convection centered on the equator at planetary scales with disturbances propagating eastward from the Indian Ocean to the western/central Pacific ocean at an average speed of  $3 - 5 \text{ m s}^{-1}$  (Hendon and Salby, 1994; Zhang, 2005) – the MJO. The MJO related convection is confined to and usually best developed in these regions as convective instability is sustained over this “warm pool”.

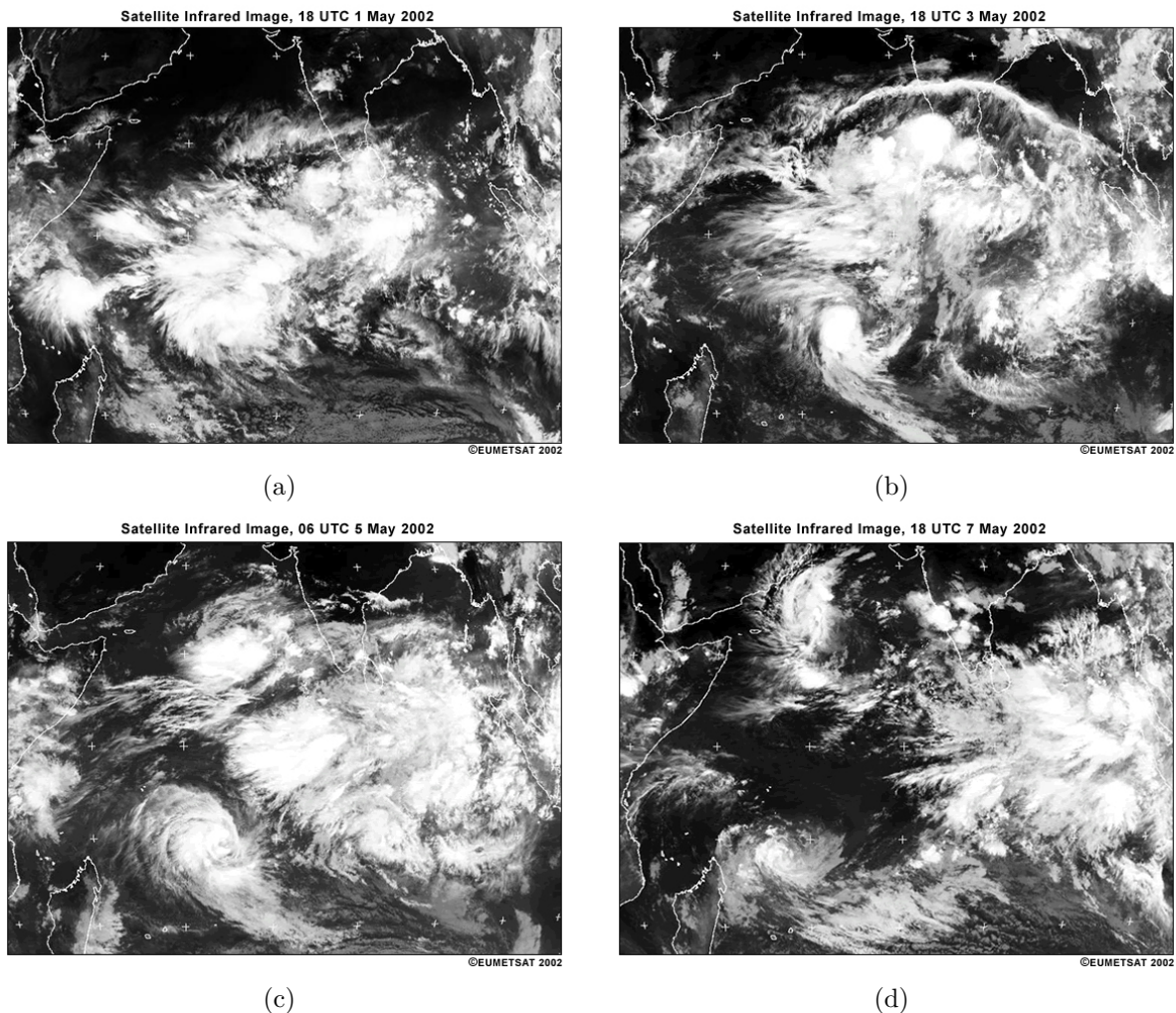


**Figure 2.1:** Sequence of infrared satellite imagery for the initiation of an MJO event in May 2002 over the Indian Ocean. Image courtesy of EUMETSAT and the University Corporation for Atmospheric Research (UCAR) available at [http://www.meted.ucar.edu/tropical/synoptic/MJO\\_EqWaves/print.htm](http://www.meted.ucar.edu/tropical/synoptic/MJO_EqWaves/print.htm), retrieved on 15 December 2014.

The onset of an MJO event occurs over the tropical western Indian Ocean (Fig. 2.1a, Fig. 2.2a) and the decay of a full MJO life-cycle occurs over the tropical western hemisphere (Fig. 2.2h). Typically, an MJO event is characterized by an eastward propagating center of deep convection centered on the equator and is flanked by regions of weak convective activity to the west and east. After the initialization of deep convection over the Indian Ocean, this convection starts to intensify and to propagate eastward (Fig. 2.1a-d). The well-developed deep convection is associated with a negative anomaly in sea level pressure which was identified in the original work of Madden and Julian (1971). A positive pressure anomaly at upper-levels indicates that the MJO related tropical convection lifts the tropopause and causes an anticyclonic flow anomaly at upper-levels. In response to the diabatic heating in the MJO convectively active region equatorially trapped Kelvin waves propagate eastward at a much higher speed than the MJO. Typically the Kelvin waves reach a phase speed of  $12 - 25 \text{ m s}^{-1}$ . To the west of the MJO convectively active region westward propagating equatorial Rossby waves develop. Equatorial Rossby waves typically reach a phase speed of  $5 - 7 \text{ m s}^{-1}$ . They are characterized by cyclonic disturbances on either side of the equator. These cyclonic disturbances may serve as a nucleus for tropical cyclogenesis (see section 2.2) so that TCs may develop simultaneously on both sides of the equator (Schreck III and Molinari, 2009) in response to the diabatic heating associated with the MJO (Fig. 2.1c-d). The theoretical aspects of the dynamic response to a MJO-like heating centered on the equator are discussed in section 2.4.1.

The negative sea level pressure anomaly becomes strongest and extends furthest east of the convective center when the MJO is situated above the Maritime Continent (Fig. 2.1d; Fig. 2.2c) and the western Pacific (Fig. 2.2d). The convective component of the MJO spreads over zonal wave numbers 1–3. Thus, the convective component exhibits a much less zonal scale than the anomalies of the dynamical fields associated with the MJO which reach scales of 12,000 to 20,000 km (Rui and Wang, 1990), i.e. a zonal wave number 1. The MJO related low-level dynamical fields are characterized by anomalously westerly/easterly winds to the west/east of the deep convection. A divergent flow characterizes the dynamical field at upper-levels in the region of the deep convection with reversed zonal wind anomalies. The relative phase between the large-scale zonal wind anomalies and the convection varies during the life-cycle of an MJO event. At early stages of an MJO life-cycle the convection is centered at the low-level convergence of the zonal wind anomalies. When the MJO is located over the western Pacific, low-level westerlies prevail through the convective center so that low-level convergence is displaced to the east of the convective center (Knutson and Weickmann, 1987; Hendon and Salby, 1994).

The convective signals of the MJO usually start to weaken over the eastern Pacific (Fig. 2.2f). However, the signals in the dynamical fields such as surface pressure and wind persist. They propagate farther east at a much higher phase speed of about  $30\text{--}35 \text{ m s}^{-1}$  (Milliff and Madden, 1996; Matthews, 2000). In particular the dynamical fields at upper-levels can complete a circumferential propagation along the equator (Knutson and Weickmann, 1987). The descending, i.e. the convectively passive branches of the MJO are accompanied by positive sea level pressure anomalies and negative pressure anomalies

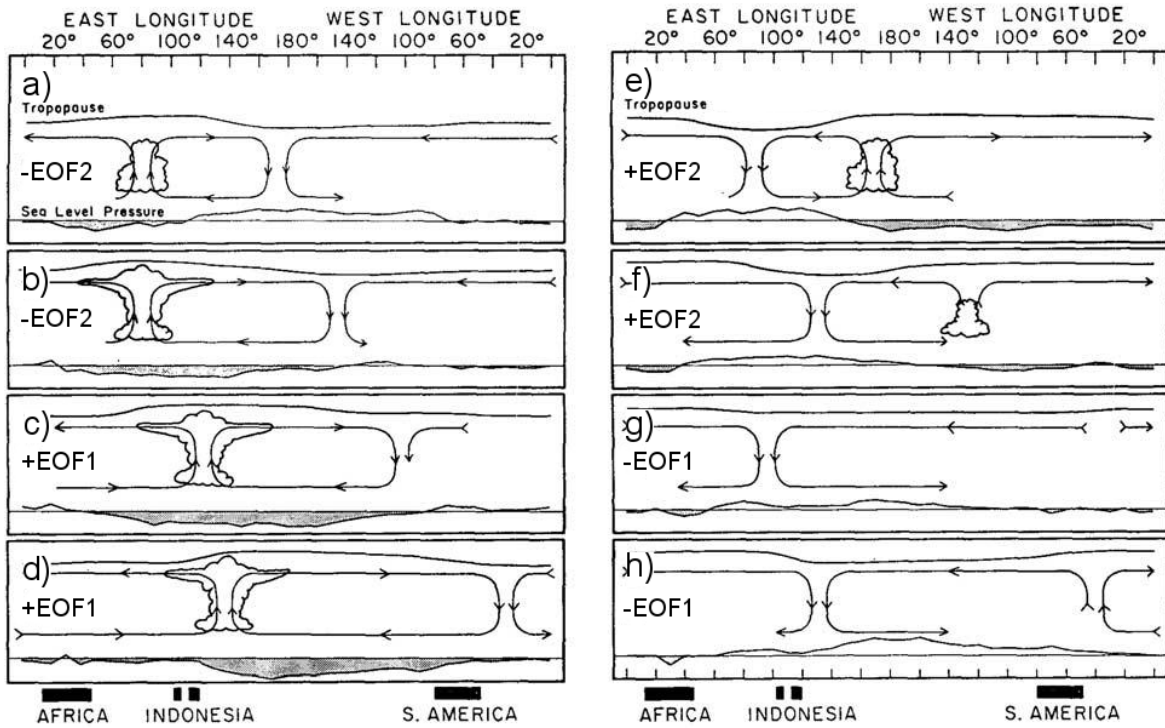


**Figure 2.2:** Longitude-height schematic diagram along the equator illustrating the fundamental large-scale features of the Madden-Julian oscillation through its life-cycle (from top left to bottom right). Cloud symbols represent the convective center, arrows indicate the zonal circulation, and curves above and below the circulation represent perturbations in the upper tropospheric and sea level pressure. Adapted from Madden and Julian (1972).

on the tropopause during the decay of the MJO related convection (Fig. 2.2 e) - h)). This indicates the existence of cyclonic flow anomalies at upper-levels.

Several approaches have been made to describe objectively an MJO life-cycle. A widely used diagnostic is the all-season real-time multivariate MJO Index (RMM-Index) as defined by Wheeler and Hendon (2004). This index is based on a multivariate statistical technique, the Empirical Orthogonal Function (EOF) analysis. This method enables us to identify spatial patterns of variability and how they change with time by partitioning a field into mathematically orthogonal modes. The RMM-Index is based on the two leading EOFs of the combined fields of 850 and 200 hPa zonal wind anomalies and outgoing longwave radiation (OLR) anomalies. The zonal wind data are obtained from global reanalyses data and the OLR is obtained from the National Oceanic and Atmospheric Administration (NOAA) satellite measurements<sup>1</sup>.

In a first step, the anomalies are calculated by removing the long-term mean and the climatological seasonal cycle (first three harmonics determined via Fourier transform) from each field at each grid point. Additionally, a 120-day mean of the most recent 120

<sup>1</sup>[http://www.esrl.noaa.gov/psd/data/gridded/data.uninterp\\_OLR.html](http://www.esrl.noaa.gov/psd/data/gridded/data.uninterp_OLR.html)

days is subtracted at each grid point to remove low-frequency variability. In this study, the variability associated with El Niño was not removed since it has only a minor impact on the results (Lin et al., 2008). Second, the EOF analysis is performed on daily, equatorially-

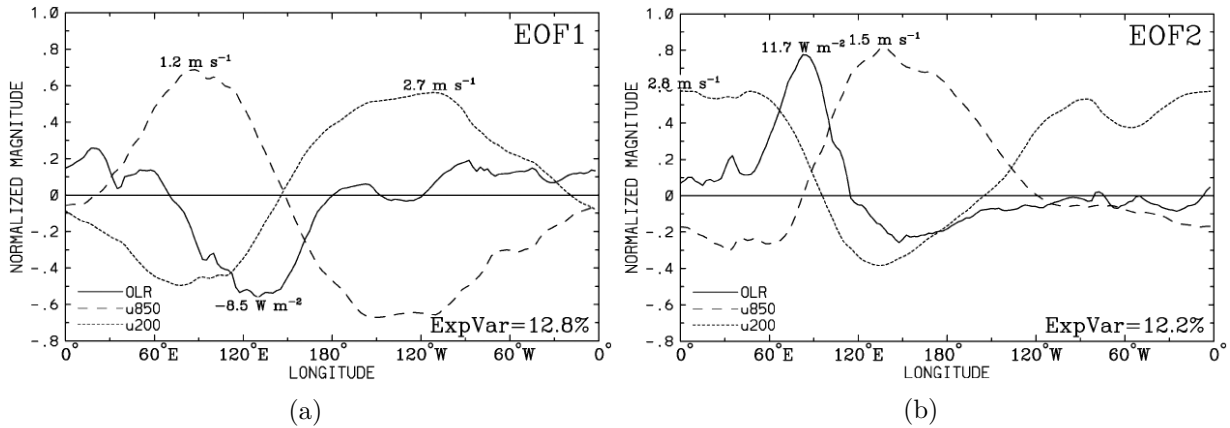


**Figure 2.3:** Spatial structures of EOFs 1 and 2 of the combined analysis of anomalies of OLR and zonal winds at 850 and 200 hPa. Multiplying each normalized magnitude by its global variance gives the field anomaly that occurs for a one standard deviation perturbation of the principal component, as given for the absolute maxima of each field. The variance explained by the respective EOFs is 12.8% and 12.2%. Fig. 1 from Wheeler and Hendon (2004).

averaged (15°S to 15°N) anomalies for the period 1979 to 2001. The leading EOF explains 12.8% of the total variance of the three combined fields and exhibits several features that are characteristic of the MJO (Fig. 2.3a). A region of negative OLR anomalies between 80°E and 180° indicates enhanced deep convection. The 850 hPa zonal winds show a convergence approximately collocated with this region. The upper-level zonal winds are of opposite sign and thus indicate a divergence above the deep convection. This circulation pattern as expressed by the first EOF resembles strongly the circulation anomalies in the schematic diagram in Fig. 2.2c, d. The second EOF explains around 12.2% of the total variability (Fig. 2.3b). Positive OLR anomalies west of about 120°E indicate suppressed convection whereas convection is maintained in the remainder of the tropics. Low-level divergence and upper-level convergence are now juxtaposed with the region of suppressed convection. EOF2 resembles strongly the circulation characteristics in Fig. 2.2e, f. The spatial structures of the two leading EOFs thus represent the spatially propagating signal of the MJO. Finally, daily anomalies of an analysis or of a forecast are projected on the observed EOFs to obtain the two projection coefficients. The deviation of the projection coefficients by their observed standard deviations yields the normalized principal components, i.e.  $RMM_1$  and  $RMM_2$ .  $RMM_1$  and  $RMM_2$  define a two-dimensional phase space that is useful to diagnose the location of the MJO convection and the strength of a particular MJO event (Fig. 2.4). A typical MJO life-cycle starts in phase 1 and traces an anticlockwise circle around the origin which signifies the eastward propagation of the MJO. Phase 1 corresponds to a negative  $RMM_2$  and is thus closely related to the structure described by the negative second EOF. Hence, phase 1 is characterized by enhanced convection over Africa and the western Indian

ocean and reduced convection elsewhere. Contrary to that, MJO phase 5 corresponds to a positive  $RMM_2$ . Thus, MJO phase 5 is best described by the positive second EOF which is characterized by reduced convection between 60 to 120°E and enhanced convection elsewhere. Phases 4 (8) of the MJO correspond to positive (negative)  $RMM_1$  and are thus best represented by the structures associated with the positive (negative) leading EOF. Events where  $\sqrt{RMM_1^2 + RMM_2^2} < 1$  are defined as weak or inactive MJO.

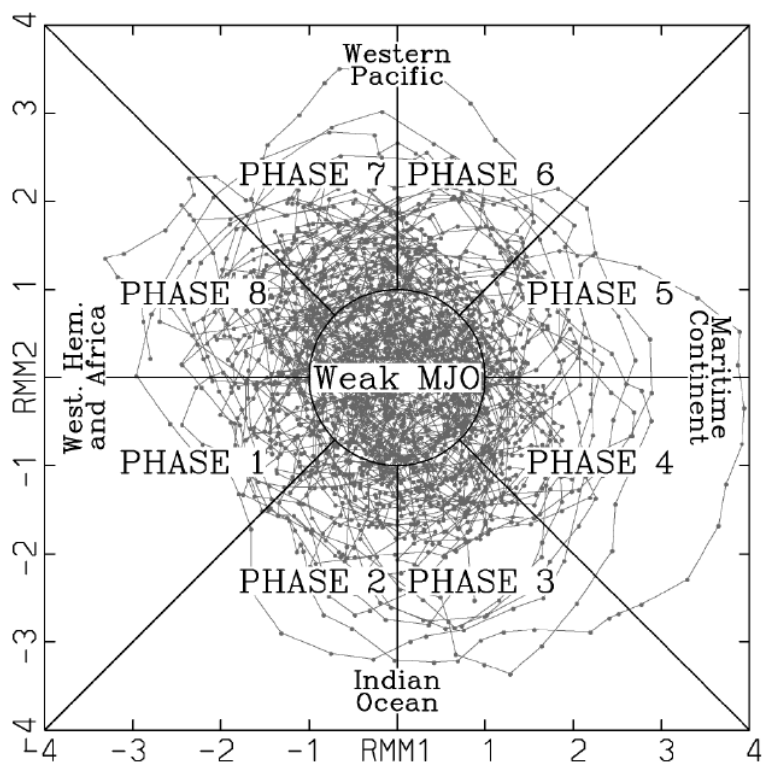


**Figure 2.4:**  $RMM_1 - RMM_2$  phase space points for all available days in DJF season from 1974 to 2003. Eight defined regions of the phase space are labeled, as is the region considered to signify weak MJO activity. Also labeled are the approximate locations of the enhanced convective signal of the MJO for that location of the phase space, e.g. the Indian Ocean for phases 2 and 3. Fig. 7 from Wheeler and Hendon (2004).

The MJO is not only the main component of tropical intraseasonal variability, it also affects other tropical phenomena such as the El Niño Southern Oscillation or TCs (Zhang, 2013). Tropical cyclone activity increases by twofold over the southern Indian Ocean when the active MJO is located over the Indian Ocean (Liebmann et al., 1994). The location of heavy TC genesis locations shifts eastward with the MJO convection center across the Indian Ocean (Ho et al., 2006). A minimum in TC activity occurs over the Southern Indian Ocean when the MJO is in its inactive phase. Similar results were found for the Northern Indian Ocean and TC activity near the northwestern coast of Australia (Hall et al., 2001). Tropical cyclone activity over the western Pacific increases when the MJO related convection is located over the Maritime Continent and over the western tropical Pacific. Less TCs occur over the western Pacific when the MJO convection center is situated over the Indian Ocean. Possible features that explain the influences of the MJO on TC

activity are reduced vertical wind shear, enhanced low-level convergence, cyclonic relative vorticity, deep convection, midlevel moisture and synoptic disturbances (e.g. equatorial Rossby wave) that serve as a nucleus of TC genesis (e.g. Liebmann et al., 1994; Mo, 2000; Maloney and Hartmann, 2001).

## 2.2 Tropical cyclones

Tropical cyclones are the most intense weather systems in the tropics and they occur in nearly all ocean basins of the world (Fig. 2.5). Worldwide about 80 TCs develop each year

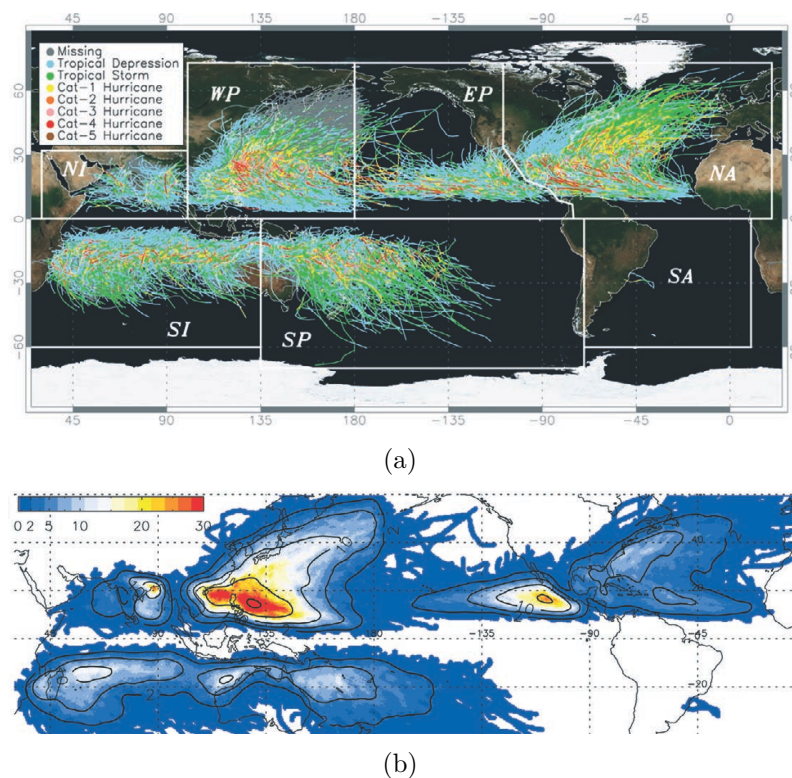


**Figure 2.5:** (a) All International Best Track Archive for Climate Stewardship (IBTrACS) storm tracks (1979–2007) colored by their Saffir-Simpson Hurricane Scale category (where “missing” indicates maximum sustained wind was not reported) and (b) frequency of storms within 55 km of any point for 1945–2007 from IBTrACS contoured at 2, 5, 10, 20 and 30 storms per decade. From Knapp et al. (2010).

(Emanuel, 2003). Intense winds of more than  $350 \text{ km h}^{-1}$  (e.g. Typhoon Haiyan, 2013), storm surges and heavy rainfalls cause severe damage at sea and on land. The present annual global damage from TCs is US\$26 billion or 0.04% of the gross world product (Mendelsohn et al., 2012). Nine of the ten costliest Atlantic hurricanes occurred between 2004 and today. With about 1800 deaths and a damage of US\$125 billion Hurricane Katrina (2005) was the most severe Atlantic Hurricane (Knabb et al., 2005). Very recently Typhoon

Fitow (2013) made landfall in China and with damages of US\$10.4 billion was the costliest typhoon in the West Pacific.

By definition, TCs are cyclones that originate over tropical oceans and are driven by heat transfer from the ocean (Emanuel, 2003). Tropical cyclones that do not exceed maximum winds of  $17 \text{ m s}^{-1}$  at an altitude of 10 m, averaged over 10 minutes, are called tropical depressions. Cyclones that exhibit maximum winds in the range of 18 to  $32 \text{ m s}^{-1}$  are defined as tropical storms. Tropical cyclones with winds of  $33 \text{ m s}^{-1}$  or more are called “Hurricanes” in the North Atlantic and East Pacific, “Typhoons” in the western North Pacific, and simply “Cyclones” in all other ocean basins. Tropical cyclone activity peaks in September in the North Atlantic region, during July and August in the eastern North Pacific, and in late summer in the tropical western North Pacific belt. The South Indian Ocean and south Pacific TC activity peaks during the warmer months in the Southern Hemisphere. The reasons for the peak TC activity during the warmer months in both hemispheres can be found in the parameters that favor a TC development.

Favored conditions for a TC genesis are sea surface temperatures that exceed 299 K in an ocean layer of 50 m, a preexisting atmospheric disturbance (e.g. African Easterly Wave, Monsoon trough, Equatorial Rossby wave) poleward of  $5^\circ$  latitude, mid-tropospheric high humidity and low vertical shear of the horizontal wind (Riehl, 1950). After the convection associated with the preexisting disturbance has organized to a TC, it steers west-northwestward (west-southwestward in the southern hemisphere) along the southern/western side of the subtropical anticyclone with a typical translation speed of 2 to  $10 \text{ m s}^{-1}$ . This propagation is mainly determined by the steering flow (i.e. the background wind at mid-tropospheric levels) in which the cyclone is embedded. However, strong TCs can deflect the steering flow through the advection of planetary vorticity and thus modify their own track.

Mature TCs can be regarded at nearly all heights as axisymmetric vortices with a strong cyclonic primary circulation (Fig. 2.6) which is approximately in gradient wind balance. The radius of maximum winds occurs 10–100 km from the center. In outer regions, i.e. between 100 to 1000 km, the primary cyclonic circulation becomes indistinguishable from the environmental flow.

As noted earlier, the energy for TCs is latent heat transfer from warm ocean waters. Frictional effects in the planetary boundary layer or inflow layer of the TC force the air to spiral from outer regions toward the cyclone center. It should be noted that the radial velocity toward the cyclone center is much weaker than the tangential winds of the primary circulation. On its path toward the cyclone center the air assimilates energy due to strong latent heat fluxes (Fig. 2.6). The radial winds converge in the eyewall region (ring(s) of deep convection surrounding the TC center) where the air is forced to ascend along moist isentropes. Water vapour condenses and energy that was assimilated in the inflow region is released by latent heating. The latent heating in the eyewall region forces even stronger ascent to the tropopause. There, continuity of mass results in a shallow-layer of divergent outflow which is deflected anticyclonically by Coriolis force. The outflow layer

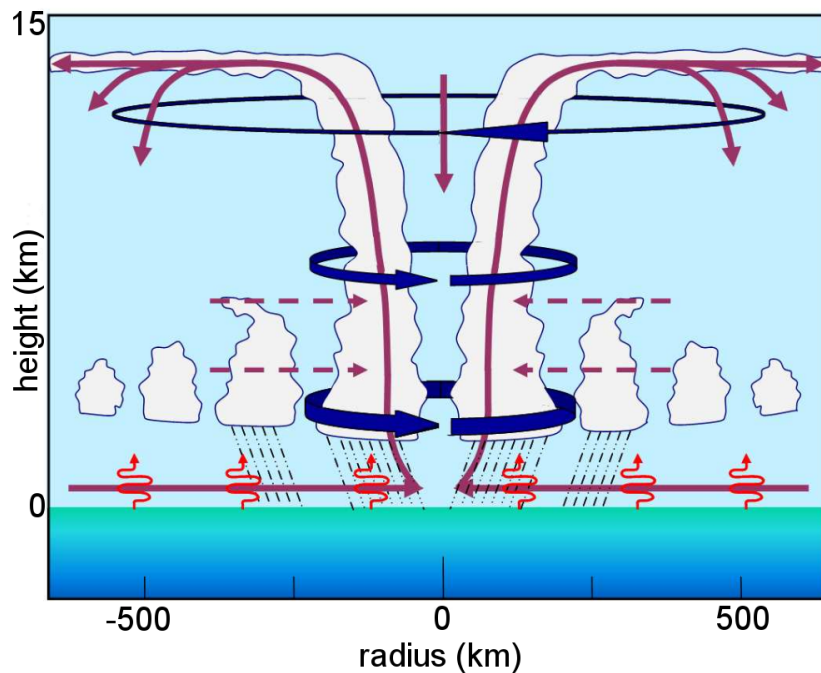


**Figure 2.6:** Idealized vertical cross section of a mature TC. Blue arrows indicate the primary cyclonic (anticyclonic) circulation at lower (upper) levels. Purple arrows show the secondary circulation. Red meandering arrows represent sensible and latent heat fluxes from the sea surface into the troposphere. Figure 2.1 of Riemer (2007) adapted from Jones (2002).

often spreads over much larger regions than the primary cyclonic circulation of the TC. The low-level inflow, the ascent in the eyewall region and the upper-level outflow form the secondary circulation of the TC. The associated energy cycle is very similar to that of an ideal Carnot engine (Emanuel, 1986).

On their poleward track, TCs propagate along the western side of the subtropical anticyclone and undergo recurvature, i.e. their heading changes from west-northwesterly to northeasterly directions in the northern hemisphere. Following recurvature TCs usually reach regions with lower sea surface temperatures and dissipate. Under certain conditions, TCs keep their intensity and interact with the midlatitude flow. This interaction of a TC with the midlatitude flow modifies the structure of the TC itself, but it frequently modifies the structure of the midlatitude flow also. Chapter 2.4.2 provides a detailed description of this interaction that is referred to as extratropical transition (Jones et al., 2003).

## 2.3 Rossby waves

The MJO as well as TCs may have a considerable impact on the dynamics of planetary- to synoptic-scale waves which are well-known as Rossby waves (Rossby et al., 1939; Rossby,

1940). Before we examine the interaction between the MJO or TCs and midlatitude Rossby waves we briefly recapitulate the theory of Rossby waves. The dynamics of these waves are based on the conservation of absolute vorticity ( $d\eta/dt = d(\zeta + f)/dt = 0$ ) where  $\zeta = \partial v/\partial x - \partial u/\partial y$  is the relative vorticity,  $f$  is the planetary vorticity and  $u$  and  $v$  are the horizontal wind components. Considering an air parcel which exhibits planetary vorticity, but no relative vorticity, a perturbation will lead to a change of latitude so that the relative vorticity must change in order to conserve the absolute vorticity. For example, a northward perturbation leads to an increase of planetary vorticity so that the relative vorticity of the air parcel becomes negative, i.e. anticyclonic. The opposite mechanism holds true for a southward perturbation. As noted earlier, Rossby waves occur in a non-divergent atmosphere. Therefore, their occurrence is limited to altitudes above the planetary boundary layer which comprises the lowest kilometre of the atmosphere.

Assuming simple harmonic waves on a beta plane in an inviscid, isothermal, non-divergent and incompressible atmosphere, the Rossby wave phase speed  $c$  is derived from the barotropic vorticity equation

$$\frac{\partial \zeta}{\partial t} = -(\zeta + f)\left(\frac{\partial u}{\partial x} + \frac{\partial v}{\partial y}\right) - v\beta \quad (2.1)$$

and given by

$$c = U - \beta L^2/4\pi^2 \quad (2.2)$$

$U$  denotes the background zonal wind,  $\beta$  the meridional gradient of the planetary vorticity, and  $L$  the wavelength. Equation 2.2 shows that Rossby waves propagate westward relative to the background flow. It reveals further that waves with a large wavelength propagate slower than Rossby waves with a small wavelength. The group velocity of the waves is given by

$$c_g = U + \beta L^2/4\pi^2 \quad (2.3)$$

which shows that in a westerly flow the group velocity  $c_g$  exceeds the phase velocity  $c$ . This suggests that a sudden perturbation gives rise to an increasing number of new waves downstream of the initial disturbance. The waves increase their kinetic energy as a result of the transport of vorticity. They disperse the energy eastward at a speed that exceeds  $U$  even though individual waves propagate more slowly than  $U$  (Rossby, 1945). This behaviour of Rossby waves is well-known as Rossby wave dispersion. The phase and group velocity derived from this simple barotropic approach show fundamental characteristics of Rossby waves which agree with observations.

Rossby (1945) noted that the barotropic assumption does not coincide with observations which show an rapid increase of the wind speed with height. Assuming geostrophically balanced motion in the presence of a strong midlatitude temperature gradient, the strength of a westerly thermal wind depends on the strength of the temperature gradient. At some point this westerly thermal wind becomes baroclinically unstable and baroclinic waves develop. These waves (together with planetary waves and ocean currents) transport momentum and heat poleward and contribute in this way to a minimization of the temperature gradient between subtropics and polar regions. They intensify as long

as their heat transport is not sufficient to balance the radiation deficit in polar regions (e.g. Holton, 2004). Furthermore, the baroclinic waves convert potential energy into kinetic energy and maintain in this way the kinetic energy of the atmosphere against frictional dissipation. The growth of eddies in a baroclinic environment was first investigated by Charney (1947) and Eady (1949). Charney (1947) setup a model that corresponded closely with the mean atmosphere. Key findings were that baroclinic instability increases with shear, lapse rate and latitude, and decreases with wave length. The computed unstable waves showed features that were analyzed in previous observational studies. The waves propagated in easterly directions, the phase speed was approximately equal to the surface zonal current, waves exhibited a thermal asymmetry and a westward tilt with height. As will be discussed in section 4.2.4, baroclinic instabilities mainly grow by the conversion of potential energy associated with the mean horizontal temperature gradient into kinetic energy. The maximum growth rate occurs for waves of lengths from 2500 to 3000 km.

The Rossby wave dispersion mentioned previously can be identified in Hovmöller diagrams of the meridional wind component. A prominent example of Rossby wave dispersion is shown in Fig. 2.7. The Rossby wave was excited by cyclogenesis east of Japan on 1 August 2002. The subjectively defined group velocity reaches values of about  $16 \text{ m s}^{-1}$  whereas the phase velocities of synoptic-scale troughs and ridges are much lower with about  $2 \text{ m s}^{-1}$ . This illustrates nicely the eastward dispersion of kinetic energy, also known as downstream development (Chang, 1993). The rapid downstream development of

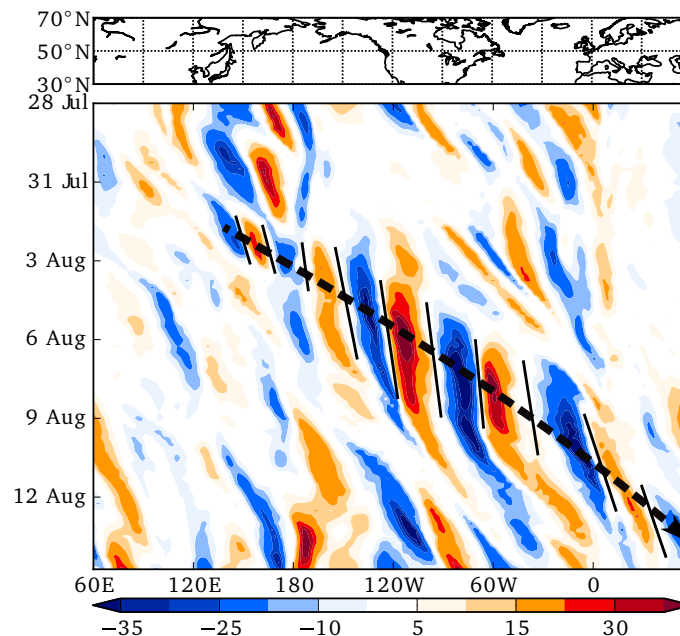


**Figure 2.7:** Hovmöller (time-longitude) diagram of the 250 hPa meridional wind component (shaded,  $\text{m s}^{-1}$ ) for the period 28 July - 14 August 2002 and the latitudinal belt 40–60°N. Thick dashed line denotes the subjectively defined group velocity, thin continuous lines denote the subjectively defined phase velocity. Adapted from Shapiro and Thorpe (2004).

high-amplitude Rossby waves led to severe flooding in Europe on 11 August 2002 (Shapiro and Thorpe, 2004).

Regions of high amplitude meridional flow (as seen in Fig. 2.7) in the upper troposphere associated with Rossby wave dispersion characteristics, i.e. downstream development are defined as Rossby wave packets (RWPs) (Lee and Held, 1993; Hakim, 2003). A systematic investigation of the RWP structure and evolution has been of major interest in recent studies. Rossby wave packets are tightly linked to the storm track regions in the North Pacific and North Atlantic (Souders et al., 2014). Preferred regions of RWP generation are the western North Pacific and the western North Atlantic. Regions of RWP generation are confined to these storm track regions since the development of a RWP begins with an initial meridional (usually baroclinic) perturbation (Blackmon et al., 1984; Chang and Yu, 1999). Rossby wave packet decay occurs preferentially over central North America and western/central Europe (Glatt and Wirth, 2013). Extreme RWPs (amplitude  $> 30 \text{ m s}^{-1}$ ) occur in November and January in the Northern Hemisphere (Souders et al., 2014).

The northern hemispheric peak in November is most likely related to a peak in RWP activity over the North Pacific at this time. Rossby wave packets that develop over the western North Pacific are preceded by disturbances (e.g. shortwave troughs) that reach the western North Pacific on the poleward side of the Himalayan Plateau (Hakim, 2003). Once the initial disturbances reach the Asian coastline they amplify, propagate eastward and reach North America approximately 72 h later. Mechanisms that contribute to a rapid intensification of the initial disturbance are e.g. low-level cyclogenesis or TCs that interact favorably with the midlatitude flow (section 2.4.2).

In order to propagate into downstream regions and to avoid meridional dispersion, RWPs require a waveguide, i.e. a sharp meridional gradient in potential vorticity (PV) at tropopause levels (Martius et al., 2010). These waveguides are stronger in winter so that RWPs are stronger and more prevalent during winter than in other seasons (Chang, 1999). Rossby wave packets that reach North America are quite often a precursor for a RWP development over the western North Atlantic. Atlantic RWPs refract equatorward onto the subtropical jet and pass south of the source region for Pacific RWPs. Therefore, Atlantic wave packets seem to have less effect on the Pacific storm track than Pacific wave packets have on the Atlantic storm track (Hakim, 2003). Hakim (2003) related this to the fact that Atlantic RWPs must travel a longer distance to reach the Pacific storm track so that they suffer a greater subtropical attenuation.

## 2.4 Tropical-extratropical interactions

So far, we considered the dynamics of the tropics and extratropics as disconnected features. However, in the real-atmosphere the dynamics of these two regions are far from being disconnected. The focus of sections 2.4.1 and 2.4.2 are tropical-extratropical interactions

associated with the MJO and the ET of TCs, respectively. Particular attention is paid to the excitation of Rossby waves.

### 2.4.1 Tropical-extratropical interactions through the MJO

As noted at the beginning of this chapter, the MJO is the dominant component of the intraseasonal variability in the tropical atmosphere. Figure 2.2 illustrates several tropical synoptic features related to the MJO. An important characteristic of the MJO is the eastward propagation of a convectively active region from the Indian Ocean toward the central North Pacific.

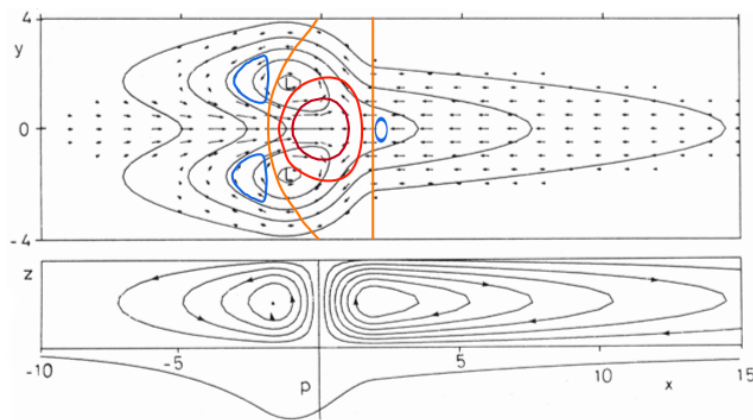


**Figure 2.8:** Solution of a simple analytic model (Gill, 1980) for the case of heating symmetric about the equator. Upper plot shows vertical velocity (colored contours) superimposed on the velocity field for the lower layer. The field is dominated by the upward motion (reddish colors) in the heating region where it has approximately the same shape as the heating function. Elsewhere there is subsidence (bluish colors) with the same pattern as the pressure field. Perturbation pressure (black contours) which is everywhere negative. There is a trough at the equator in the easterly regime to the east of the forcing region. On the other hand, the pressure in the westerlies to the west of the forcing region is high relative to its value off the equator. Two cyclones are found on the north-west and south-west flanks of the forcing region. Lower plot shows the meridionally integrated stream function (contours) and perturbation pressure. Note the rising motion in the heating region and subsidence elsewhere. Adapted from Fig. 1 in Gill (1980).

The convectively active region is accompanied by large-scale diabatic heating anomalies which are approximately balanced by adiabatic cooling. Matsuno (1966) investigated the response of the tropical atmosphere to anomalous equatorial mass sources and sinks using a two-layer equatorial shallow-water model. These mass sources (sinks) can be considered as equivalents to cooling (diabatic heating) through sustained anomalous (suppressed) tropical convection. The response in the shallow-water model is characterized by a convergence of westerlies (from the west) and easterlies (from the east) into the

convectively active region. The westerlies can be interpreted as a “monsoon-like” westerly inflow to a region of heating. The easterlies can be interpreted as the trade winds representing the lower branch of the Walker circulation. Equivalent results were found with a simple analytic model of the response of a resting tropical atmosphere to heat sources and sinks symmetric about the equator (Gill, 1980). However, Gill (1980) found a “somewhat surprising” response of the meridional flow which was directed poleward in the lower (convergent) layer (Fig. 2.8) and equatorward in the upper (divergent) layer of the heating region. The explanation of the meridional flow response to the heating follows from the linearized vorticity equation for a steady motion which is

$$\beta v = f \partial w / \partial z \quad (2.4)$$

with the meridional wind  $v$ , the Coriolis parameter  $f$  and the vertical gradient of the vertical velocity  $\partial w / \partial z$ . The heating region is associated with vertical motion which causes the stretching of vortex lines in the lower layer. The stretching results in an increase of positive absolute vorticity. Assuming a steady motion of small amplitude, this can happen only if air parcels move in a direction in which the planetary vorticity  $f$  increases, i.e. in poleward direction. The meridional velocity at which the air parcels move poleward is given by equation 2.4. Under the assumption that the vertical velocity vanishes at the surface and at the upper boundary, equation 2.4 indicates that the meridional flow response increases with the vertical velocity and hence with the heating rate.

Gill (1980) interpreted the response to the west of the heating region as an equatorially trapped westward propagating Rossby wave. This Rossby wave is characterized by low-level cyclonic anomalies and upper-level anticyclonic anomalies to the northwest of the heating region. Hsu et al. (1990) and Jin and Hoskins (1995) found a similar atmospheric response to tropical heating in a baroclinic atmosphere. Observation based

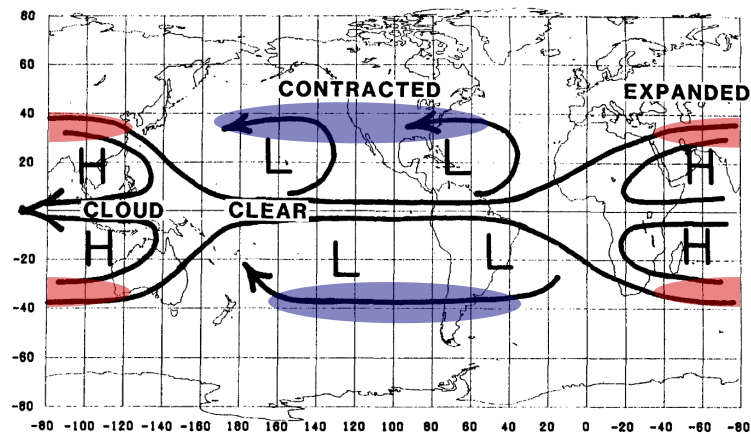


**Figure 2.9:** Schematic of relationship between OLR and 250 hPa circulation anomalies. Red (blue) shadings indicate regions of westerly (easterly) zonal wind anomalies. Fig. 7 from Weickmann et al. (1985).

*intraseasonal* relationships between tropical and extratropical circulation patterns during northern hemisphere winters were first investigated by Weickmann (1983), Weickmann

et al. (1985) and Knutson and Weickmann (1987). They found upper-level flow features that were similar to the solutions which were obtained by Gill (1980). Regions of active convection (labeled as “cloud” in Fig. 2.9) are flanked by upper-level westerlies to the east and upper-level easterlies to the west. Upper-level anticyclones to the northwest and southwest of the convection indicate the development of an equatorially trapped Rossby wave in response to the convection. Westerly wind anomalies at the northern flank of the upper-level anticyclone lead to an anomalously strong subtropical jet (labeled as “expanded” in Fig. 2.9). Regions of suppressed tropical convective activity (labeled as “clear” in Fig. 2.9) are associated with an upper-level cyclonic circulation in subtropical regions. Easterly wind anomalies at the northern flank of the cyclonic circulation lead to an anomalously weak westerly subtropical jet (labeled as “contracted” in Fig. 2.9). Thus, the results reveal that during northern hemisphere winters, tropical eastward-moving convective anomalies associated with the MJO lead to the development of anomalous circulations in subtropical regions which may modify the midlatitude westerly flow. The modification of the jet has considerable implications for synoptic-scale Rossby wave propagation, as will be discussed later in this section.

Composite maps of MJO filtered anomalies (see section 2.1 for filtering process) for December, January, February for the period 1980–2010 document the MJO related midlatitude response (Fig. 2.10). They reveal clearly that the extratropical response is much stronger in the northern hemisphere during boreal winter than in the southern hemisphere. At early stages of the MJO life-cycle (RMM-phases 1 and 2) the convectively active region of the MJO is located over Africa and the western Indian Ocean (Fig. 2.10 a, b). Positive OLR anomalies over the Maritime Continent and the western Pacific indicate suppressed convective activity. Identical to the results of Weickmann et al. (1985), a cyclonic circulation anomaly exists to the north of the suppressed convection. The MJO related eastward propagating convection intensifies remarkably during MJO phases 3 and 4 over the Indian Ocean (Fig. 2.10 c, d). The intensification of the convection is accompanied by the development and amplification of upper-level subtropical anticyclones to the northwest of the convectively active region. The subtropical cyclonic anomalies to the north of the suppressed convection weaken gradually and propagate eastward at a speed that is similar to that of the MJO related convection. A nice example of a midlatitude response develops to the north of the subtropical cyclonic anomaly during phase 3 and 4 of the MJO. A dominant feature is an anticyclonic anomaly over the North Pacific centered at  $45^{\circ}\text{N}$  and  $180^{\circ}$  (Fig. 2.10c). Together with a cyclonic anomaly over Alaska and an anticyclonic anomaly over Canada, the circulation anomalies form a planetary-scale Rossby wavetrain. The wavetrain anomalies follow approximately great circle routes which have been documented in previous studies, e.g. Jin and Hoskins (1995) and Matthews et al. (2004). During MJO phase 4, the wave pattern shows downstream dispersion as a strong cyclonic anomaly develops over the Greenland region (Fig. 2.10d). Cassou (2008) and Lin et al. (2009) could show that this cyclonic anomaly projects onto the positive phase of the North Atlantic Oscillation (NAO).

With strong convection over the Maritime Continent (RMM-phase 5), subtropical anticyclonic anomalies exist over the Asian continent and subtropical cyclonic circulations

over the eastern Pacific (Fig. 2.10 e). These upper-level circulation anomalies reach their peak intensity at this stage of the MJO life-cycle. The MJO related convective anomaly weakens during the subsequent MJO phases. However, the subtropical anticyclonic response to the north of the convection is maintained. A quadrupole of cyclonic and anticyclonic anomalies over the North Pacific, for example, characterizes the MJO related midlatitude circulation anomalies during phase 6 of the MJO (Fig. 2.10 f). During the last two phases of the MJO, the convective activity is suppressed over the Indian Ocean and the Maritime Continent and enhanced along the South Pacific convergence zone (Fig. 2.10g, h). The extratropical northern hemispheric circulation anomalies still indicate the existence of a planetary-scale Rossby wave train that is formed by cyclonic anomalies over the eastern North Pacific and the subtropical North Atlantic, and anticyclonic anomalies over the central Pacific, Alaska and the Greenland region (Fig. 2.10h). Anomalously easterly winds at the southern flank of the anticyclone over the Greenland region project back onto the negative phase of the NAO (Cassou, 2008; Lin et al., 2009).

The impact of the MJO on the extratropical flow pattern is not limited to the excitation of poleward propagating, planetary-scale Rossby waves on the climatological mean flow. Barotropic Rossby wave theory suggests that the East-Asian jet acts as a waveguide for synoptic-scale Rossby waves (high-frequency transients) (Matthews and Kiladis, 1999b). Therefore, structural changes of the waveguide through tropical convection may also have a significant impact on the propagation characteristics of synoptic-scale Rossby waves. Under mean DJF conditions, the East-Asian jet extends east of the date line and traps Rossby waves. The formation of anticyclonic circulation anomalies to the northwest of the MJO convection has considerable implications for the midlatitude jet structure.

When the MJO related convective center occurs over the equatorial Indian Ocean and the Maritime Continent, the Asian Pacific jet is strengthened and shifted northward over the Asian continent, and retracted westward over the western to central North Pacific (Knutson and Weickmann (1987) and Fig. 2.10 b, c, d). The jet amplification over the Asian continent can be attributed to the anomalous westerly winds at the northern flank of the upper-level subtropical anticyclone. In contrast, the northern branch of the subtropical cyclonic anomaly and the southern branch of an anticyclonic anomaly over the North Pacific lead to easterly midlatitude wind anomalies. These anomalies indicate an extraction of kinetic energy from the mean flow by the MJO related circulation anomalies. The jet configuration allows synoptic-scale Rossby waves to leak out of the relatively weak waveguide over the North Pacific (see easterly wind anomalies in Fig. 2.10 b, c, d) and to propagate/break back into the tropics (Matthews and Kiladis, 1999b; Moore et al., 2010). An increase of eddy kinetic energy ( $K_e$ ) over the central North Pacific confirms this behaviour and indicates an increase in wave activity (Matthews and Kiladis, 1999b; Deng and Jiang, 2011). The  $K_e$  of high-frequency transients increases on the flanks of the jet rather than in the jet core. This indicates the split of an existing wave train into two parts. One wavetrain continues over North America, whereas the other is refracted southward into the equatorial westerlies over the eastern Pacific. The equatorward refraction of midlatitude

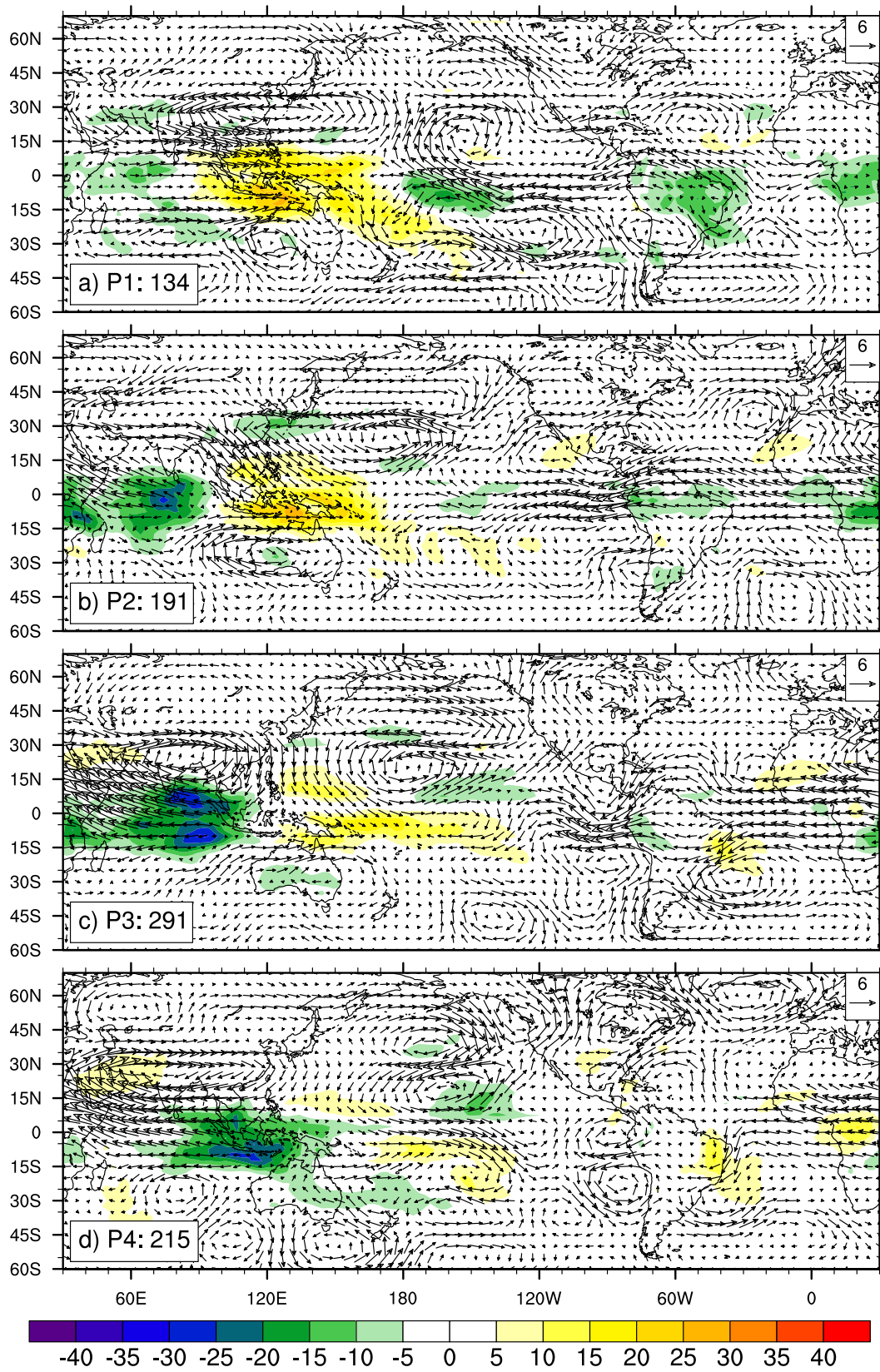
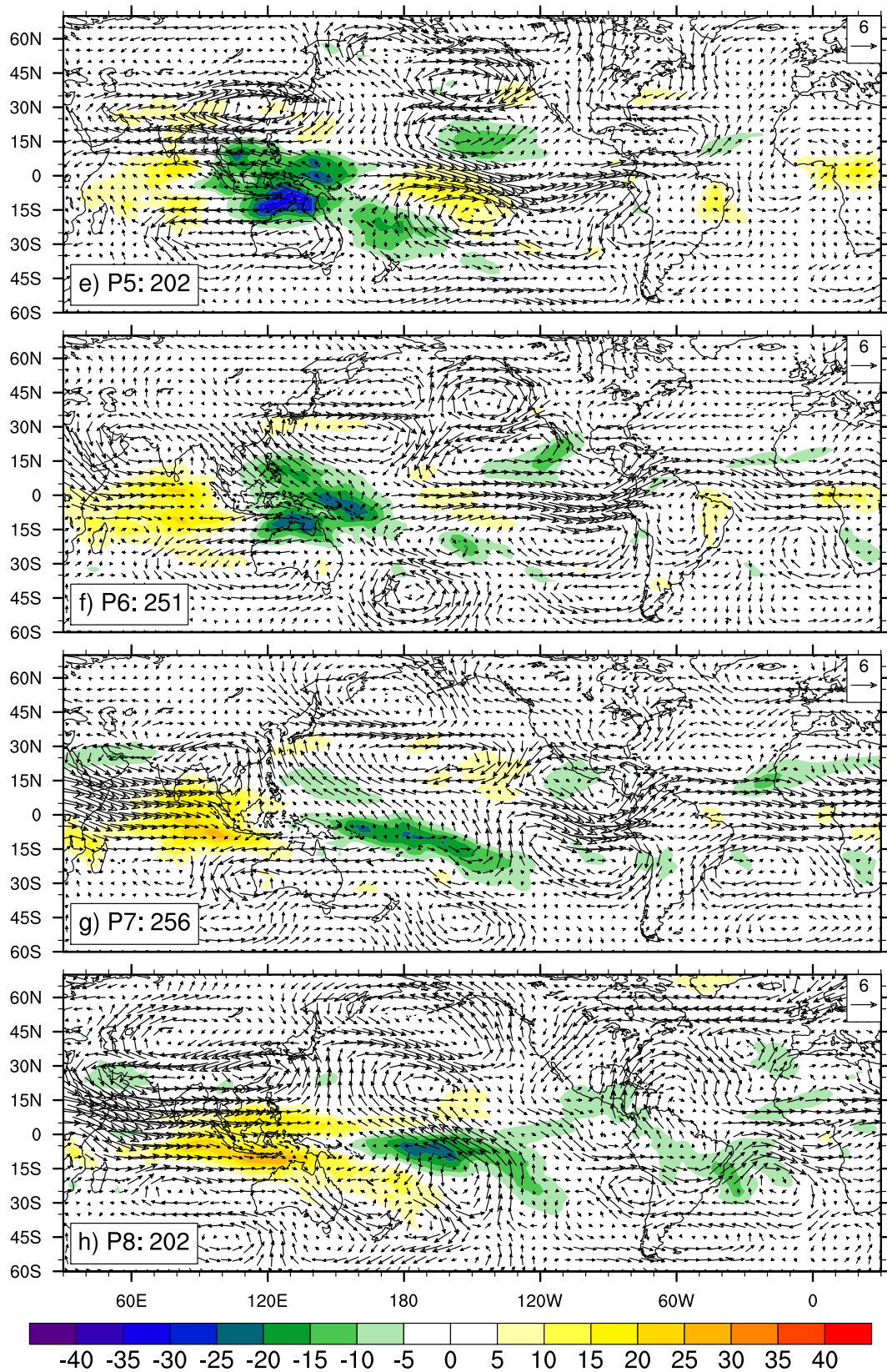


**Figure 2.10:** 30 year composites of MJO-filtered OLR anomalies (shaded,  $W m^{-2}$ ) (NOAA satellite measurements) and anomalous 200 hPa winds (ERA-Interim) for RMM-phases 1 to 8. ... (continued on next panel)



... (continued). The subcaptions in the lower left of each panel give the phase and the number of cases considered in each composite, i.e. a) shows the composite for MJO phase 1 which has been computed from 134 cases. Reference vector for wind speed is given at top right in  $m s^{-1}$ .

Rossby waves is due to a change of the background flow that affects the stationary wave number ( $K_s$ ) (Hoskins and Ambrizzi, 1993) defined as

$$K_s = \left( \frac{\beta - \bar{U}_{yy}}{\bar{U}} \right)^{1/2} . \quad (2.5)$$

$\beta$  is the meridional gradient of planetary vorticity,  $\bar{U}$  is the time-mean zonal wind and  $-\bar{U}_{yy}$  is the time-mean meridional gradient of the relative vorticity  $\zeta$ . Propagation of Rossby waves is only possible if  $K_s$  is real and greater than the zonal wave number  $k$  of a Rossby wave. Thus, Rossby waves are refracted toward (away from) regions of high (low)  $K_s$ . In regions where  $K_s$  is imaginary and  $k > K_s$  Rossby waves are evanescent. Hence, shorter waves (i.e. waves with a large  $k$ ) are likely to be evanescent, except for regions with very small but positive  $U$ . During the phase 5 of the MJO life-cycle, the region of mean easterlies over the warm pool retracts westward. Therefore,  $K_s$  becomes real over the central Pacific which allows Rossby waves to propagate into the deep tropics near the date line (Matthews and Kiladis, 1999b). The propagation/breaking of Rossby waves back into the tropics reduces static stability and provides upper-level forcing for vertical motion which induces convection along  $150^\circ\text{W}$  (Fig. 2.10 d, e). This convection may project back onto the MJO diabatic heating field and thereby aid the MJO to propagate eastward (Matthews and Kiladis, 1999a).

The eastward propagation of the MJO convective center leads to an eastward extension and a northward shift of the jet over the western North Pacific (Fig. 2.10 e, f) which is accompanied by an increased frequency of cyclonic Rossby wave breaking events (Moore et al., 2010). Changes in the local environment due to the direct response of the atmosphere to the MJO convection lead to enhanced baroclinic instability. Thus, these conditions are favorable for wave breaking and surface cyclogenesis on the northern flank of the locally strong jet (Moore et al., 2010). The extratropical response during these phases of the MJO is further characterized by enhanced frequency of poleward-propagating Rossby waves (Yoo et al., 2012). Yoo et al. (2012) documented, that the increase of Rossby wave activity was associated with increased eddy heat fluxes that contributed to Arctic warming.

At later stages of an MJO life-cycle, i.e. when the MJO crosses the dateline and the convection starts to decay, the jet over central and eastern Asia is shifted to the south (Fig. 2.10 g, h). Simultaneously, the jet exhibits its most eastward extension over the North Pacific. This synoptic setup is favorable for baroclinic life-cycles along this well developed waveguide spanning the central North Pacific (Moore et al., 2010). Waves are trapped along the strong waveguide and do not propagate equatorward as during early stages of the life-cycle. The region of positive zonal winds in the (sub)tropics extends further east, so that  $K_s$  becomes real over the central Pacific. Hence, less Rossby waves propagate into the deep tropics at this stage of the MJO. Surface cyclone frequency and cyclonic wavebreaking frequency are enhanced in the jet exit region in the eastern North Pacific. Baroclinic processes associated with these events might help to maintain blocking events that occur preferentially over central North America during these phases of the MJO (Deng and Jiang, 2011; Hamill and Kiladis, 2014).

The results of previous research suggest that large-scale circulation anomalies associated with the MJO have a significant impact on the midlatitude jet structure. The modifications of the midlatitude jet may have considerable implications for the occurrence frequency and the propagation characteristics of midlatitude synoptic-scale Rossby waves. The change in RWP occurrence frequency and the propagation characteristics of RWPs as a function of the MJO phases is documented in chapter 5.1.

## 2.4.2 Extratropical transition of tropical cyclones

Tropical cyclones that reach the midlatitudes often weaken under the influence of strong vertical shear and colder sea surface temperatures. Other cases exist in which the TC evolves into a fast-moving and occasionally rapidly developing extratropical cyclone. This process of complex interactions and transformations is well-known as ET (Jones et al., 2003). The ET may be associated with severe rainfall, large waves and strong winds in the vicinity of the remnant TC (e.g. Bosart and Dean, 1991; McTaggart-Cowan et al., 2001). Even remote regions that are not directly affected by TCs may be affected by extratropical systems that developed out of a TC (e.g. Lili in 1996 (Browning et al., 1998)). An introduction into the ET process at the beginning of this section is followed by a discussion of mechanisms through which a TC may impact the downstream midlatitude upper-level flow.

Surface analyses were used to define three ET classifications in early case studies. Matano and Sekioka (1971) classified the interaction of the TC with a midlatitude low pressure system as *compound* and the interaction of the TC with a surface baroclinic zone as *complex*. A third classification included the dissipation of TC remnants while moving into the midlatitude environment (Brand and Guard, 1979). These three classifications of ET are still used operationally by the Japan Meteorological Agency (Kitabatake, 2002).

Another subjective, but widely used two-stage classification of ET is based on an examination of 30 ET events by Klein et al. (2000). The interaction of the TC with a pre-existing, midlatitude baroclinic zone and the transformation into a baroclinic system characterize the *transformation stage*. A conceptual model describes the *transformation stage* in three steps (Fig. 2.11). In step 1, the TC translates poleward over regions with lower sea surface temperatures. Its outer circulation impinges on the midlatitude baroclinic zone which separates warm, moist tropical air from cool, dry midlatitude air. The cyclonic wind field advects midlatitude air masses to the west of the TC equatorward (labeled as 1 in Fig. 2.11) and tropical air masses to the east of the TC poleward (labeled as 3 in Fig. 2.11). The advection of the dry environmental equatorward flow becomes visible in satellite imagery as a dry slot to the southwest of the TC, decreased deep convection in that region and open-cell cumulus over the relatively warm ocean (labeled as 2 in Fig. 2.11). The poleward flow of warm moist air masses to the east of the TC maintains the deep convection. The interaction of this poleward flow with the midlatitude baroclinic zone produces ascent over tilted isentropic surfaces (labeled as 4 in Fig. 2.11). This isentropic,

slantwise ascent is comparable to warm conveyor belts (WCBs) which occur in extratropical cyclones (Carlson, 1980).

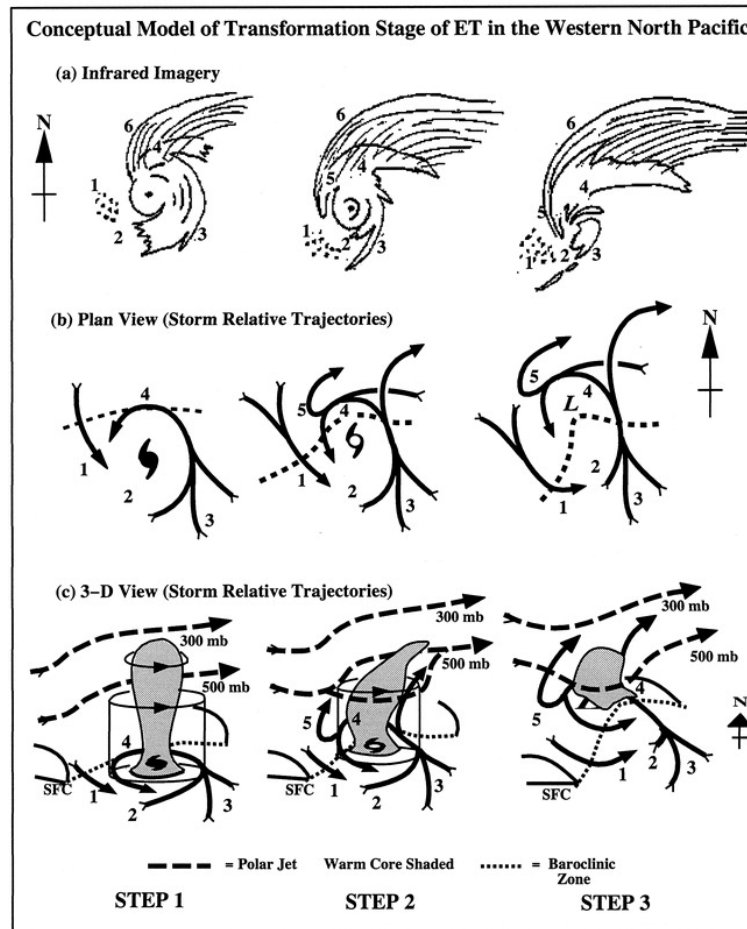


**Figure 2.11:** Figure 5 from Klein et al. (2000): Conceptual model of transformation stage of ET in the western North Pacific, with labeled areas as follows: 1) environmental equatorward flow of cooler, drier air (with corresponding open cell cumulus); 2) decreased TC convection in the western quadrant (with corresponding dry slot) in step 1, which extends throughout the southern quadrant in steps 2 and 3; 3) environmental poleward flow of warm, moist air is ingested into TC circulation, which maintains convection in the eastern quadrant and results in an asymmetric distribution of clouds and precipitation in steps 1 and 2; steps 2 and 3 also feature a southerly jet that ascends tilted isentropic surfaces; 4) ascent of warm, moist inflow over tilted isentropic surfaces associated with baroclinic zone (dashed line) in middle and lower panels; 5) ascent (undercut by dry-adiabatic descent) that produces cloudbands wrapping westward and equatorward around the storm centre; dry-adiabatic descent occurs close enough to the circulation centre to produce erosion of eyewall convection in step 3; 6) cirrus shield with a sharp cloud edge if confluent with polar jet.

In step 2 of the transformation stage, the juxtaposition of the cyclonic TC circulation and the baroclinic zone produces a dipole of lower-tropospheric cold (warm)

temperature advection to the west (east). Hence, the baroclinic zone is rotated cyclonically which results in the development of a frontal wave. The slantwise ascending air masses to the east of the TC split into two branches (labeled as 5 in Fig. 2.11). Some of the ascending air parcels turn cyclonically and descend dry adiabatically to the west of the TC center. Simultaneously, other air parcels continue their ascent to the upper-troposphere and turn anticyclonically due to the Coriolis force and upper-level westerlies. The confluence of these air masses and the polar jet forms a cirrus shield with a sharp cloud edge to the north of the TC (labeled as 6 in Fig. 2.11). The upper-tropospheric warm core of the TC is sheared away by strong westerly winds. A weak lower-tropospheric warm core remains over the surface center in step 3 of the transformation stage. The surface center is now embedded in the baroclinic zone. Cold (warm) advection produced by the environmental flow west (east) of the storm maintain isentropic descent (ascent) to the west (north). Finally, the dipole of cold/warm advection and the interaction of the outer circulation with the baroclinic zone results in the formation of a frontal system. The warm front is located on the poleward side of the storm and characterized by a large swath of multilayer clouds. The cold front is less pronounced and characterized by a cloud band to the southeast of the storm center.

The frontogenetical processes continue during step 3 of the ET. The interaction between the decaying TC and the low-level baroclinicity modifies the gradient of lower-tropospheric equivalent potential temperature. However, a direct thermal circulation to the west of the cyclone often suppresses the development of a well-defined cold front (Harr and Elsberry, 2000). Depending on the environmental changes and the interaction with the midlatitude circulation pattern, the TC may decay and not complete transformation or it completes ET, enters the *extratropical stage* (Jones et al., 2003) and may intensify under certain conditions.

A strong zonal flow between a primary midlatitude cyclone to the northeast of the TC and the subtropical anticyclone characterizes the *Northeast* pattern (Harr et al., 2000). The TC propagates rapidly eastward without significant intensification or even decays. In the *Northwest* pattern the TC propagates northward ahead of an upstream trough which represents the primary midlatitude circulation pattern. This type-B (Petterssen and Smebye, 1971) like pattern provides favorable conditions for an extratropical reintensification. An upper-level PV maximum, represented as a cold anomaly of potential temperature on the dynamic tropopause, characterizes the upstream trough. In the case of a trough with sufficiently large amplitude and small static stability, the associated cyclonic circulation will extend to the lower troposphere. The interaction of the southerly flow at the surface associated with the upper PV anomaly and the midlatitude baroclinic zone creates a surface warm potential temperature anomaly by advection. A phasing of the southerly winds of the upper-level PV anomaly and the low-level, remnant warm core of the TC can amplify this surface warm anomaly. On the other hand, the surface warm anomaly, i.e. in this case the remnant cyclonic TC circulation which is associated with a PV anomaly can extend vertically to the tropopause. There, it produces a cold (warm) potential temperature anomaly to the west (east) of the circulation center through advective processes. A phasing of the upper-level trough and the region of upper-level maximum cold air advection through

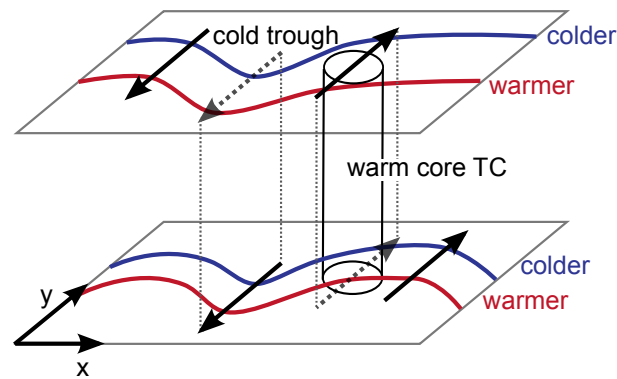


**Figure 2.12:** Idealized schematic illustrating the *Northwest* pattern from a PV perspective. At upper and lower levels, two isentropes are drawn (blue and red contours). The black arrows represent the circulations associated with the PV anomalies of the upper-level trough and the warm core TC. Adapted from Lackmann (2011).

the TC amplifies the upper-level cyclonic circulation. Under favorable conditions the lower- and upper-level circulation can amplify mutually (Hoskins, 1990).

The phasing between an upper-level trough and the remnant TC is crucial for the further development and propagation of the transitioning TC. Tropical cyclones re-intensify strongly when they are initially close (within  $15^\circ$  latitude) to the upper-level trough and dissipate when they are  $25^\circ$  south of the trough (Ritchie and Elsberry, 2007).

Beyond the direct impact of a transitioning TC on its adjacencies, the ET of TCs may impact remote regions by the modification of the extratropical flow pattern. This modification of the wave guide can be associated with the excitation of a Rossby wave (Riemer et al., 2008; Harr and Dea, 2009; Grams et al., 2011). The dispersion of these Rossby waves into downstream regions (section 2.3) has the ability to cause surface cyclogenesis (Agustí-Panareda et al., 2004; Cordeira and Bosart, 2010) or high-impact weather events such as cold-air outbreaks (Archambault et al., 2007) and severe precipitation (Martius et al., 2008; Grams et al., 2011). Furthermore, ET may lead to considerable forecast challenges in downstream regions as uncertainties associated with the ET event tend to grow and spread into downstream regions in connection with the development of midlatitude Rossby wave trains (Harr et al., 2008; Anwender et al., 2010). The excitation of these Rossby wave trains through the interaction of a TC with the midlatitude flow is elucidated in the following.

As noted earlier, a positive low-level temperature anomaly, i.e. in this case the remnant cyclonic TC circulation with its corresponding PV anomaly acts to create positive and negative potential temperature anomalies on the dynamic tropopause through advective processes. The interaction of a TC with a straight jet nicely illustrates the development of these anomalies (Riemer et al., 2008). The positive PV anomaly of the TC core leads to the formation of dipoles of northward (southward) advection of potential temperature on the dynamic tropopause to the east (west) of the TC (Fig. 2.13a). A similar dipole pattern

with reversed signs is associated with the anticyclonic outflow anomaly (Fig. 2.13b). The advection of potential temperature through the outflow anomaly is stronger and extends further to the east and west. Therefore, the outflow anomaly dominates the impact of the TC on the dynamic tropopause. However, the sum of the advection through the TC related PV anomaly and the outflow anomaly is out of phase with the developing ridge (Fig. 2.13c). This suggests that these advective processes do not contribute to an amplification of the midlatitude wave disturbance. Crucial for the initial amplification of the wave disturbance is the northward advection of high potential temperature air into the crest of the ridge through the divergent wind of the TC outflow (Fig. 2.13d) (Riemer et al., 2008; Torn, 2010).

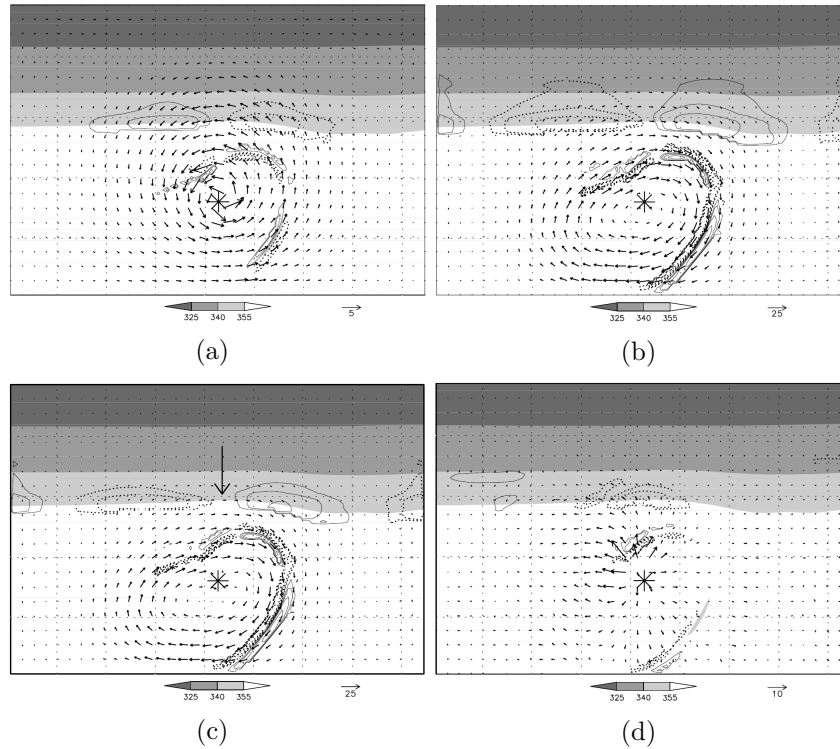


**Figure 2.13:** Potential temperature  $\theta$  (shading), balanced wind (arrows) and meridional advection of  $\theta$  (contours) on the dynamic tropopause ( $2 PVU$ ) for PV anomalies of (a) the cyclonic PV tower of the TC, (b) the outflow, (c) the transforming TC, and for (d) the divergent component of the flow after 72 hours of simulation. Contour lines at 2, 4, 8 and  $16 \times 10^{-5} K s^{-1}$  for  $\theta < 360 K$ . Dashed contours denote northward advection of high- $\theta$  air, solid lines southward advection of low- $\theta$  air. The asterisk marks the position of the TC. Dotted grid lines are drawn every 1000 km. Note the different scaling of the wind arrows. The arrow in (c) denotes the axis of the ridge. Fig. 6 from Riemer et al. (2008).

The patterns of potential temperature advection change in the subsequent evolution. The anticyclonic outflow anomaly propagates eastward with the developing upper-level wave pattern. However, the TC center exhibits a slower eastward propagation so that it is shifted westward relative to the anticyclonic outflow anomaly and the ridge. The

TC related cyclonic circulation is approximately in phase with the ridge and advects high potential temperature air into the crest of the ridge (Fig. 2.14a). Furthermore, the southward advection of low potential temperature air through the outflow anomaly into the base of the downstream trough leads to an amplification (Fig. 2.14b). Thus, the TC related circulation anomalies now contribute to an amplification of the wave disturbance (Fig. 2.14c) and lead to the formation of a ridge-trough couplet. The advection through the circulation anomalies of the upper-level wave itself (Fig. 2.14d) and through the divergent wind of the TC outflow are out of phase with the ridge. Hence, they hinder the eastward propagation of the wave and therefore allow a phase locking of the TC and the upper-level wave.

At later stages of the interaction, the advection patterns show a similar structure. Interestingly, the adiabatic processes, i.e. the advection of potential temperature by the circulation anomalies, are the primary contributors to the ridge amplification. Diabatic reduction of upper-level PV by a differential heating profile are rather small (Riemer et al., 2008). However, this does not mean that diabatic processes within the ET system do not modify the upper-level PV. In particular, mid-tropospheric condensational heating in the slantwise ascending WCB-like air masses reduces the static stability aloft. The reduction of the static stability leads to the generation of low-PV air which is transported to the upper-troposphere. There, it steepens the tropopause (Atallah and Bosart, 2003) and may have a significant impact on the upper-level ridge building (Torn, 2010; Grams et al., 2011; Grams et al., 2013b).

Near the completion of ET a midlatitude baroclinic wave has developed. The anticyclonic outflow anomaly of the TC contributes further to the intensification of the downstream trough. Downstream of the ET event typical characteristics of a midlatitude Rossby wave can be observed. High potential temperature air is advected into the crest of the second downstream ridge through the circulation anomalies of the wave itself. Thus, the downstream propagation of the Rossby wave can be explained by the advection of the circulation anomalies themselves (Hoskins et al., 1985). One aspect that has not been discussed yet is the modification of the dynamic tropopause through the ET system. The cyclonic circulation of the remnant PV tower wraps low potential temperature air around the circulation center. It has been shown in several previous studies that the wrap-up of the dynamic tropopause might be crucial for the redevelopment of the TC as an extratropical cyclone (Agustí-Panareda et al., 2005; Riemer et al., 2008).

A similar downstream development was observed in several case studies when the TC interacted with a developing baroclinic wave (Riemer and Jones, 2010). As the TC recurves ahead of a trough, a ridge-trough couplet and a jet streak form downstream of the transitioning TC (Agustí-Panareda et al., 2004; Grams et al., 2013a). The advection of high potential temperature air through divergent winds of the TC outflow amplifies the downstream ridge at early stages of the interaction. At later stages, the TC related cyclonic circulation becomes crucial for the ridge amplification. The anticyclonic outflow anomaly of the TC becomes the dominant contributor to the trough intensification further downstream. Riemer and Jones (2010) showed that the amplification of the leading edge

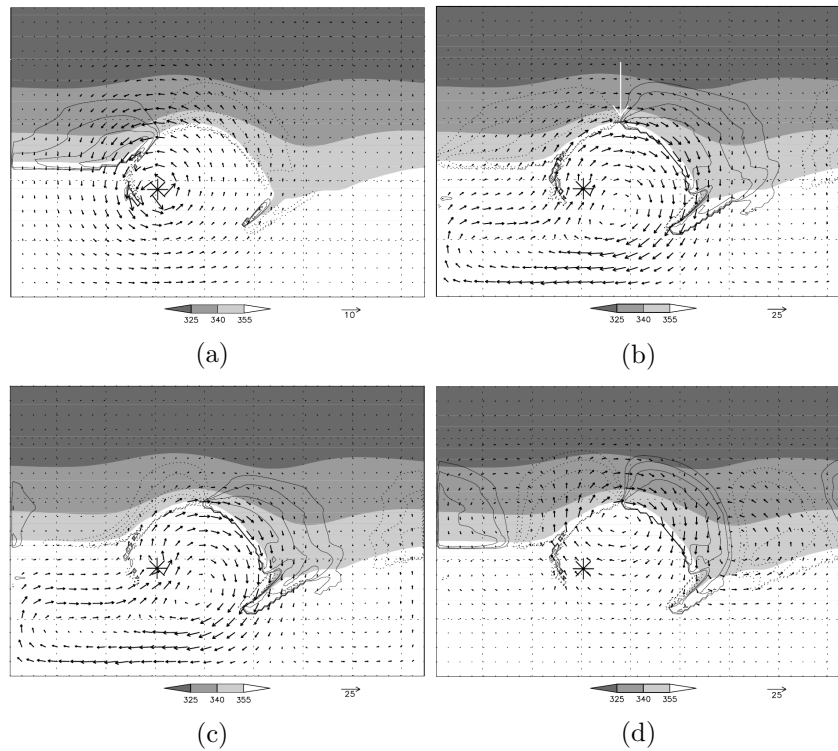


**Figure 2.14:** As Fig. 2.13, but for the balanced flow induced by PV anomalies of (a) the cyclonic PV tower of the TC, (b) the outflow, (c) the transforming TC, and (d) upper-level wave pattern after 132 hours of simulation. Note the different scaling of the wind arrows. The arrow in (b) denotes the axis of the ridge. Fig. 7 from Riemer et al. (2008).

of the downstream development was exceptionally strong when a transitioning TC was involved. Thus, Riemer and Jones (2010) suppose that the leading edge of the developing baroclinic wave represents an optimal location where the interaction with a transitioning TC can lead to the most significant impact on the downstream flow.

The previously mentioned slantwise ascent of warm air masses in WCB-like structures to the east of the transitioning TC describes the conversion from available potential energy into kinetic energy (Palmén, 1958; Kornegay and Vincent, 1976; Keller et al., 2014). On the one hand, this generation of kinetic energy prevents the transitioning TC from dissipation. On the other hand, large amounts of the kinetic energy are dispersed into the midlatitude flow as a result of ageostrophic cross-contour flow. Thus, TCs that undergo ET serve as an additional source of kinetic energy to the midlatitude flow and may initiate a downstream development (Orlanski and Sheldon, 1995). The generation of kinetic energy during the ET strongly depends on the large-scale midlatitude circulation pattern (Harr et al., 2000). The coupling of the TC and a midlatitude trough in the *northwest* pattern leads to exceptionally strong generation rates of kinetic energy. The cross-isobaric TC outflow from higher toward lower pressure heights associated with the upstream trough contributes strongest to the kinetic energy production. Partly, this kinetic

energy is exported at upper-levels into the midlatitudes and contributes to an acceleration of the midlatitude flow.

Harr and Dea (2009) investigated four ET events and their impact on the downstream flow in a kinetic energy framework. They could show that all four ET events were followed by a progression of maxima in kinetic energy from the western North Pacific to the eastern North Pacific. A common feature of the four cases was the dispersion of baroclinically generated kinetic energy into the midlatitude flow. However, there was a large variability associated with the role of the TCs in influencing the downstream development (Harr and Dea, 2009). A detailed description of the kinetic energy perspective on downstream development follows in section 3.4. An investigation of the ET of TCs in a composite PV framework and in a composite kinetic energy framework follows in sections 4.2.2 and 4.2.4, respectively.



## 3 Data and methods

The impact of TCs and of the MJO on midlatitude RPWs and the processes these tropical-extratropical interactions are diagnosed on the base of reanalysis data. We briefly introduce the reanalysis data at the beginning of this chapter and provide some general information on the TC dataset. The description of the primary datasets is followed by an introduction of methods that were applied to the reanalysis data. Substantial methods are the identification of RWP, the eddy kinetic energy budget analysis and the related concept of downstream development, and the quasi-geostrophic forcing diagnostic.

### 3.1 ERA-Interim reanalyses and reforecasts

The primary data source of this thesis are ERA-Interim reanalyses and ERA-Interim reforecasts provided by the European Centre for Medium-Range Weather Forecasts (ECMWF). These data cover the period from 1 January 1979 onwards and are computed using model cycle 31r2 of ECMWF's Integrated Forecast System (IFS) which was used operationally at ECMWF from 12 December 2006 to 5 June 2007 (Berrisford et al., 2009). The reanalyses are produced in a 12-hourly analysis cycle (Fig. 3.1) in which available observation-based information on the atmospheric state are combined with prior information from a short-range model forecast (Dee et al., 2011). This forecast was initialized with a previous analysis. Since the forecast model integrates the full model equations, information from locally observed parameters can be extrapolated in a physically meaningful way to unobserved parameters. A key component of the ERA-Interim data (and a major step forward from ERA-40 (Uppala et al., 2005)) is the four-dimensional variational analysis of the upper-air atmospheric state which uses the equations of the forecast model to confine the analysis within each analysis window. Thus, the forecast model is used as a strong constrain so that the analysis of observations has to satisfy the model equations. The analyses produced at 0000 UTC contain observations between 1500 UTC on the previous day and 0300 UTC on the present day; the analyses produced at 0600 UTC involve observations between 2100 UTC on the previous day and 0900 UTC on the present day etc.

The analysis data include 6-hourly atmospheric variables at 60 vertical levels covering the troposphere and stratosphere (Dee et al., 2011). The basic dynamical fields exhibit a T255 spherical-harmonic representation which corresponds to a horizontal resolution of  $0.75^\circ$ . The ERA-Interim data used in this study were interpolated from  $0.75^\circ$  to  $1^\circ$  horizontal resolution. Although ERA-Interim data have difficulties in representing the

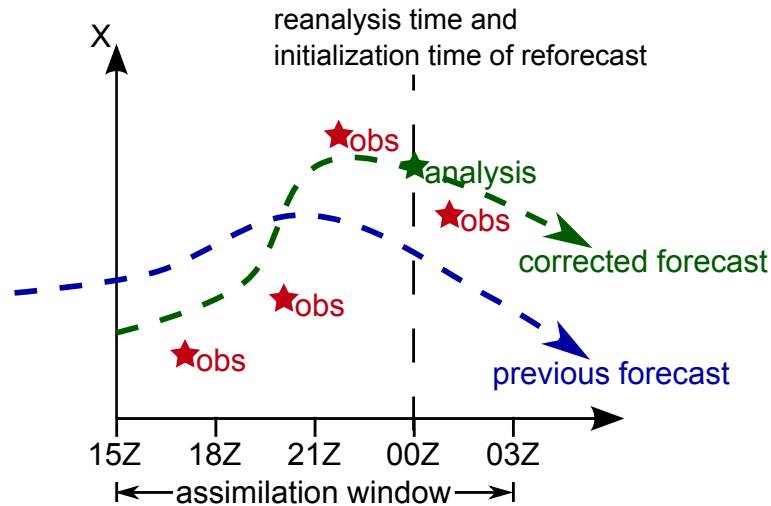


**Figure 3.1:** Schematic of four-dimensional variational 12-hourly analysis cycle of variable  $X$  valid at 0000 UTC.

intensity of TCs due to their rather coarse resolution (Schenkel and Hart, 2012; Murakami, 2014), we expect that the analyses adequately represent the synoptic-scale midlatitude flow structure downstream of TCs.

The reforecast data are available at the same vertical and horizontal resolution. The ten-day forecasts were initialized twice daily at 0000 and 1200 UTC from reanalysis data (Fig. 3.1). A major issue of the ERA-Interim reforecast dataset is that it was computed with a model configuration which had difficulties in sustaining the amplitude of the MJO throughout the integration period (e.g. section 5.2). More recent modifications to the ECMWF IFS led to significant advances in the simulation of the atmospheric variability on intraseasonal time-scales (Bechtold et al., 2008; Hirons et al., 2013). Therefore, we assume that the midlatitude response to the MJO convection might be better resolved in more recent model cycles of the ECMWF IFS.

## 3.2 Tropical Cyclone dataset

The climatological investigation of ET events focuses on western North Pacific, North Atlantic and South Indian Ocean TCs that recurved and that were designated as extratropical by the responsible WMO Regional Specialized Meteorological Centers (RSMCs) in the period June to November 1980–2010 and December to April 1980–2010, respectively. The time at which a TC was designated as extratropical (ET-time) is the reference time for the following investigations. We chose this time as reference time as the extratropical designation indicates a considerable interaction of the TC with the midlatitude flow since the (ex)-TC exhibits characteristics of an extratropical cyclone. Six hourly TC positions were retrieved from the International Best Track Archive for Climate Stewardship-WMO (IBTrACS-WMO) database (Knapp et al., 2010) which contains combined data from the

RSMCs. It should be noted here, that the RSMCs possibly use different criteria for the definition of ET for different regions. Therefore, the ET-time might differ between the RSMCs and from objective definitions of ET-time such as introduced by Hart (2003) and Evans and Hart (2003). Nevertheless, we expect that the definitions of ET are consistent within a RSMC and that the definitions by the RSMCs are convenient for a large number of cases.

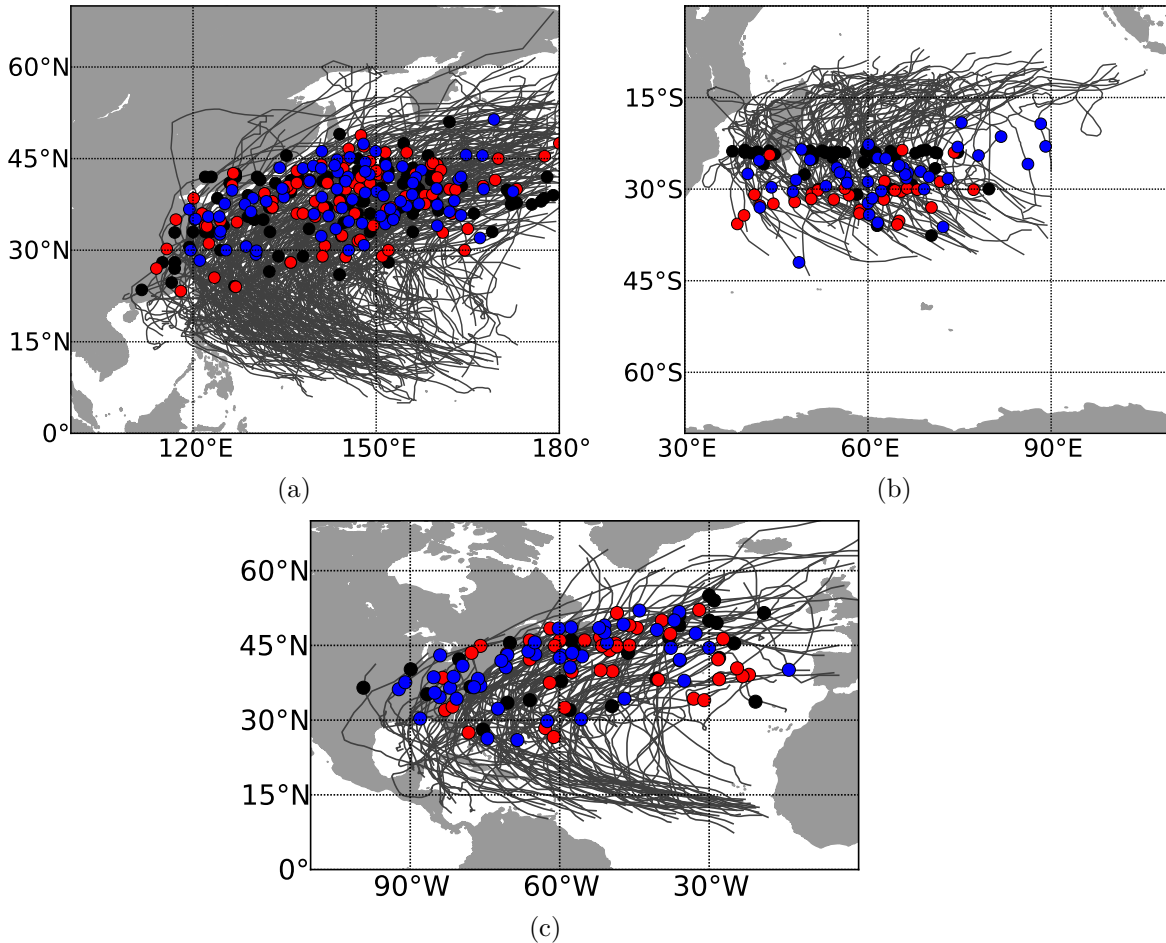


**Figure 3.2:** Best tracks of western North Pacific (a), South Indian Ocean (b) and North Atlantic TCs (c) that recurved and were designated as extratropical by one of the RSMCs from June to November and December to April, respectively, in the period 1980 to 2010 (Source: IBTrACS). Circles denote the position of each TC at ET-time. Circles are colored by decade: 1980–1989 is black, 1990–1999 red and 2000–2010 blue.

In total, 280 out of 656 TCs (42.7%) fulfilled these criteria in the selected time period in the western North Pacific (Fig. 3.2a), 114 out of 413 TCs (27.6%) in the South Indian Ocean (Fig. 3.2b) and 124 out of 428 TCs (29.0%) in the North Atlantic (Fig. 3.2c). Most of the western North Pacific TCs underwent ET between 30° to 45°N and North Atlantic TCs between 30° to 50°N. The ET of TCs in the South Indian Ocean occurred closer to the equator between 20° and 35°S. It should be noted here that for nearly all

South Indian Ocean ET events during the period 1980–1989 the latitude of ET in the best track data was 24°S. This is most probably an artefact of the rather subjective definition of ET-time by the WMO RSMC. Griffin and Bosart (2014) identified several inconsistencies in the best track data for the South Indian Ocean TCs prior to the late 1980s. Therefore, the locations and times of ET for South Indian Ocean TCs should be handled with care. We considered the uncertainty of the ET-time of South Indian Ocean TCs by redoing our investigations with the recurvature time as reference time. The development of a new best track dataset for the South Indian Ocean is under consideration (Caroff 2014, personal communication).

### 3.3 Identification of Rossby wave packets

The desire to identify and to characterize Rossby wave packets in observed atmospheric data is almost as old as the first appearance of Rossby waves in literature (Rossby et al., 1939). The Hovmöller diagram (also known as trough-ridge diagram) was used to detect the propagation characteristics of synoptic-scale Rossby waves (Hovmöller, 1949). In this type of diagram, a selected atmospheric variable or the deviation of this variable from a temporal mean is averaged over a latitude band and plotted as a time-longitude diagram. Propagating wave packets are characterized by a series of alternating positive and negative regions of meridional wind or geopotential height anomalies. This allows us to infer subjectively quantities like phase and group velocities of the Rossby wave packets. The southern and northern boundaries of the latitudinal band have to be defined in advance. Therefore, an automatic application to long time series might be difficult since the Rossby wave packets may leave the latitudinal band through meridional propagation or due to a shift of the waveguide as a function of season. In addition, the usage of a Hovmöller diagram can lead to misleading results when Rossby wave packets coexist at different latitudes with a phase shift of 180°. In this case positive and negative anomalies would cancel out so that the Hovmöller diagram would not show any signal of a Rossby wave packet.

In order to consider the effect of the meridional propagation, Martius et al. (2006) proposed a Hovmöller diagram in which the atmospheric variable considered is averaged over a latitude band along the Rossby wave guide. For this application, the Rossby wave guide is defined as a contour line of constant PV that is characteristic of the dynamical tropopause at a certain isentropic level. The atmospheric variable of interest (e.g. geopotential height or meridional wind) is averaged over a latitudinal band that is centered on the selected PV contour line. In a comparison of various types of Hovmöller diagrams, Glatt et al. (2011) showed that Rossby wave packets that are identified along the wave guide exhibit larger amplitudes than those in a conventional Hovmöller diagram.

As noted previously, a Hovmöller diagram can lead to obscure results when Rossby wave packets co-exist in close proximity at different latitudes. This caveat is avoided by utilizing the method of complex demodulation (Lee and Held, 1993; Chang and Yu, 1999;

Chang, 2000). Complex demodulation is based on the assumption that Rossby wave packets exist in the form

$$v'(x, t) = \text{Re}[A(x, t)e^{ikx}] \quad . \quad (3.1)$$

$A(x, t)$  describes the envelope of the Rossby wave packets and  $k$  gives the wave number of a typical midlatitude baroclinic wave (carrier wave number). With a given  $v'(x, t)$  the envelope function  $A(x, t)$  can be retrieved. Chang and Yu (1999) showed that the result is insensitive to the choice of the carrier wave number as long as it is chosen from a plausible wave number range (e.g.  $6 \leq k \leq 8$  in midlatitudes). However, the complex demodulation leads to an incorrect computation of the Rossby wave packet envelope when wave packets of distinct carrier wave numbers coexist at the same latitude (Zimin et al., 2003).

An alternative approach that does not require the specification of a carrier wave number was proposed by Zimin et al. (2003). This method is a fundamental part of this thesis so that the procedure is recapitulated in the following. The approach is based on a Hilbert transform filtering technique that is well-known in digital signal processing. In a first step, a Fourier transform of the meridional wind  $v(x)$  along a latitude circle is computed (Fig. 3.3).  $v(x)$  is considered on an equidistant grid whose grid points are located at  $x = 2\pi l/N$ , with  $0 < x \leq 2\pi$  and  $l = 1, 2, \dots, N$ . The finite Fourier transform of  $v(x)$  is computed by

$$v_{fft} = \frac{1}{N} \sum_{l=1}^N v \left( \frac{2\pi l}{N} \right) e^{-2\pi i k l / N}, \quad \left( k = -\frac{N}{2} + 1, \dots, \frac{N}{2} \right) \quad . \quad (3.2)$$

In a second step, we apply an inverse Fourier transform to a selected band ( $0 < k_{min} \leq k \leq k_{max}$ ) of the positive wave number half of the Fourier spectrum (Fig. 3.3). This enables us to restrict the zonal wave number range to the synoptic range ( $k_{min} = 5, k_{max} = 15$ ). The inverse Fourier transform is then

$$v_{ifft} \left( \frac{2\pi l}{N} \right) = 2 \sum_{k=k_{min}}^{k_{max}} v_{fft} e^{2\pi i k l / N} \quad . \quad (3.3)$$

Third, the RWP envelope  $E_m$  along a full latitude circle is computed (Fig. 3.3) by the modulus of  $v_{ifft}$

$$E_m(2\pi l/N) = |v_{ifft}(2\pi l/N)| \quad . \quad (3.4)$$

We repeat the above steps for each latitude circle from the equator to the pole in  $1^\circ$  steps. By concatenating the one-dimensional envelope  $E_m$  for each latitude circle we obtain finally the RWP envelope  $E$  over an entire hemisphere (Fig. 3.4).

In order to identify the RWPs as single objects we clip the envelope  $E$  at a threshold value  $\tau$  so that all values smaller than  $\tau$  are set to zero (thick black contour in Fig. 3.4b). As proposed by Glatt and Wirth (2013) we define  $\tau$  by

$$\tau = \tau^* \cdot \bar{E} \quad (3.5)$$

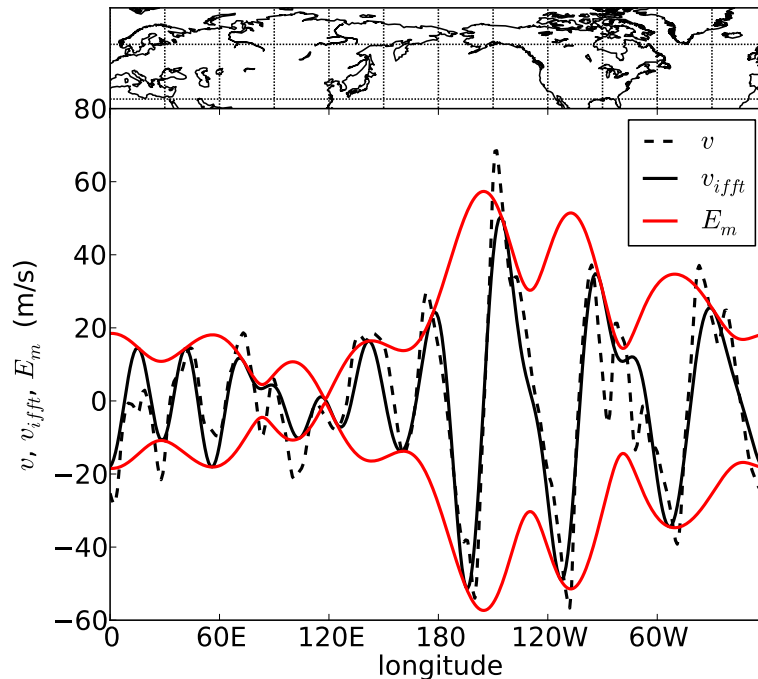


**Figure 3.3:** Meridional wind  $v$ , filtered meridional wind  $v_{ift}$  and envelope  $E_m$  of filtered meridional wind along  $45^\circ\text{N}$  on 22 September 2009 0000 UTC.

where  $\tau^*$  is a dimensionless number and  $\bar{E}$  denotes the spatial average of  $E$  over the entire northern/southern hemisphere. In this study, we decided to apply  $\tau^* = 3.2$  which is in the range that was suggested by Glatt and Wirth (2013). The usage of a relative threshold allows us to account for the seasonal variation of the meridional wind. A sensitivity analysis of the results concerning the choice of the zonal wave number band and the clipping parameter can be found in Glatt and Wirth (2013) and later in this thesis.

The application of a Fourier transform along latitude circles is based on the assumption that the background flow guiding the propagation of a wave packet is zonal. In situations where the background flow is strongly non-zonal this assumption can lead to an artificial split of the packet envelope so that the technique indicates multiple wave packets at nearby latitudes (Zimin et al., 2006). In particular, when the spatial structure of Rossby wave packets is of interest the impact of the background flow on the Rossby wave propagation and its shape needs to be considered.

In a modified version of the Zimin et al. (2003) method, Zimin et al. (2006) assumed that Rossby wave packets propagate along the background flow which is defined by a 20-day running mean of the wind field. A filter algorithm similar to Zimin et al. (2003) is applied to the meridional wind  $v(s)$  defined along a streamline of the basic flow instead of along a latitude circle. Under the assumption that the background wind components  $u_m(x, y)$ ,  $v_m(x, y)$  and the meridional wind  $v(x, y)$  are specified on a rectangular grid a piecewise-linear approximation of the streamline defined by  $(u_m, v_m)$  at  $(x_0, y_0)$  can be

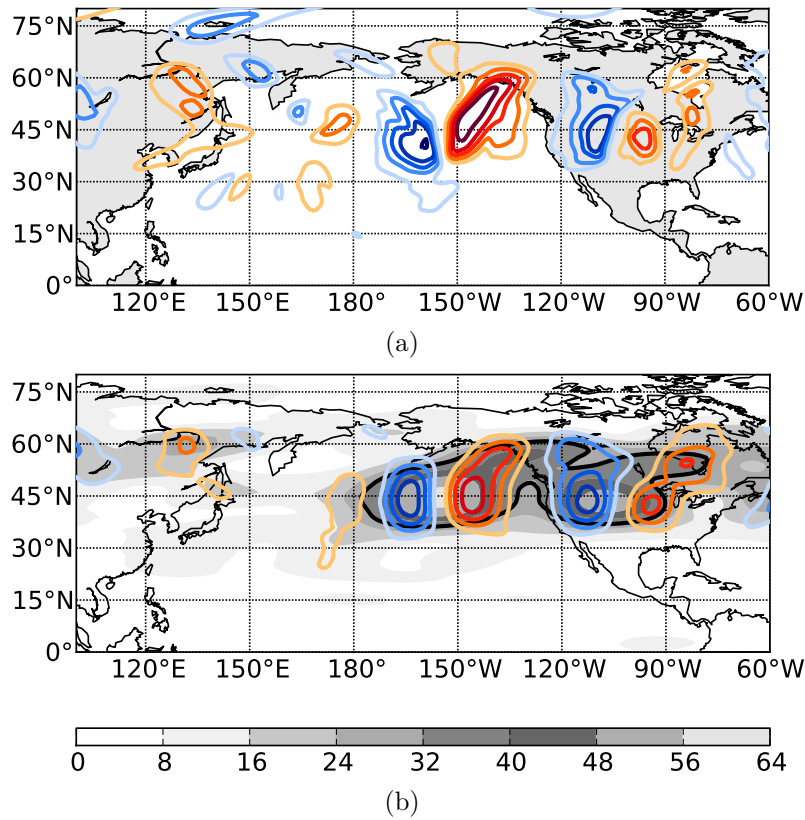


**Figure 3.4:** a) meridional wind and b) filtered meridional wind (colored contours,  $\pm 15, 25, 35, 45, 60 m s^{-1}$ ) at 250 hPa on 22 September 2009 0000 UTC. Envelope of the filtered meridional wind (shaded,  $m s^{-1}$ ) according to Zimin et al. (2003), thick black contour gives the value of the clipping parameter  $\tau$ .

computed. The point  $(x_1, y_1)$  that lies in a distance  $\delta$  in the direction of the streamline starting in  $(x_0, y_0)$  is

$$x_1 = x_0 + \frac{\delta}{\cos y_0} \frac{u_m(x_0, y_0)}{\sqrt{v_m(x_0, y_0)^2 + u_m(x_0, y_0)^2}} \quad \text{and} \quad (3.6)$$

$$y_1 = y_0 + \delta \frac{v_m(x_0, y_0)}{\sqrt{v_m(x_0, y_0)^2 + u_m(x_0, y_0)^2}} \quad (3.7)$$

The coordinates  $x_N, y_N$  and  $\delta$  are measured in units of longitude and latitude.  $N\delta$  is roughly the length of a latitude circle. The coordinates  $(x_2, y_2), \dots, (x_N, y_N)$  of the streamline are computed iteratively according to 3.6 and 3.7. Since the envelope of the meridional wind

at  $(x_0, y_0)$  is of interest we need to compute  $(x_{-1}, y_{-2}), \dots, (x_{-N}, y_{-N})$ , i.e. the coordinates of a backward streamline as well. These are defined as

$$x_{-j-1} = x_j - \frac{\delta}{\cos y_{-j}} \frac{u_m(x_j, y_j)}{\sqrt{v_m(x_j, y_j)^2 + u_m(x_j, y_j)^2}} \quad \text{and} \quad (3.8)$$

$$y_{-j-1} = y_j - \delta \frac{v_m(x_j, y_j)}{\sqrt{v_m(x_j, y_j)^2 + u_m(x_j, y_j)^2}} \quad (3.9)$$

This computation results in a streamline with coordinates  $(x_j, y_j)$ ,  $j = -N, \dots, N$ . After a 3rd-order spline interpolation of the meridional wind onto the streamline,  $v(s)$  is localized using a Gaussian filter function centered at  $j = 0$ .

$$\bar{v}(x_j, y_j) = v(x_j, y_j) e^{-\alpha^2 \frac{j^2}{N^2}} \quad (3.10)$$

$1/\alpha$  is roughly the length of the analyzed wave packet as a fraction of the length of the

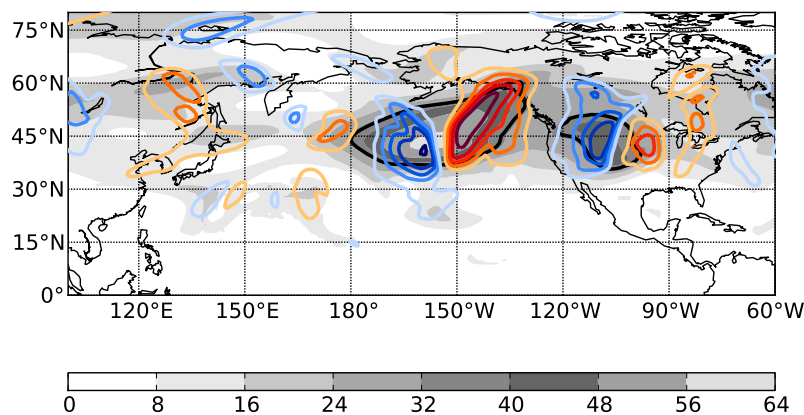


**Figure 3.5:** Meridional wind at 250 hPa on 22 September 2009 0000 UTC (colored contours,  $\pm 15, 25, 35, 45, 60 \text{ m s}^{-1}$ ). Envelope of the filtered meridional wind (shaded,  $\text{m s}^{-1}$ ) along a streamline according to Zimin et al. (2006), thick black contour gives the value of the clipping parameter  $\tau$ .

latitude circle. The focus of the investigation are synoptic-scale waves so that we set  $\alpha = 6$ . Since  $\alpha$  is needed only for the Gaussian filter function,  $\alpha$  does not have a strong impact on the results as long as it is in a reasonable range. Finally, the Hilbert transform of  $v(s)$  given by  $\bar{v}(x_j, y_j)$  gives the amplitude  $A(x_j, y_j)$  at the center point  $(x_j, y_j)$ . The described procedure is repeated for every grid point so that we finally obtain the envelope of the meridional wind (Fig. 3.5). A comparison between Fig. 3.4b and Fig. 3.5 shows small differences between the two methods. The RWPs computed with the Zimin et al. (2006) method are slightly weaker than those computed with the Zimin et al. (2003) method. This leads to a split of the RWP over western North America. The structure of the RWP in Fig. 3.4b indicates a possible latitudinal split of the packets along  $50^\circ\text{N}$ . This artifact vanishes with the method of Zimin et al. (2006).

To conclude, the Zimin et al. (2006) method is computationally more expensive than the method of Zimin et al. (2003). As long as the focus of a study is not the two-dimensional structure of Rossby wave packets, the method of Zimin et al. (2003) is a quite

robust and reliable method. However, as soon as the 2-dimensional structure and especially the meridional propagation of Rossby wave packets is of interest the identification method proposed by Zimin et al. (2006) is necessary. As the Zimin et al. (2006) method yields weaker RWPs, the results of the two methods are not comparable quantitatively. Since we investigate the impact of TCs on midlatitude RWPs on the base of meridional averages of the RWP envelope we adhere to the Zimin et al. (2003) method in chapter 4. However, in chapter 5 the propagation characteristics of the midlatitude RWPs are of major concern. Therefore, we investigate the impact of the MJO on midlatitude RWPs by applying the Zimin et al. (2006) method.

Midlatitude troughs tend to be smaller (stronger) in size (amplitude) than midlatitude ridges. This asymmetry results from a deviation from pure QG dynamics (Hakim et al., 2002) and has implications for the detection of RWPs. The application of the Hilbert transform has the tendency to split a single RWP into several fragments. This undesirable effect can be avoided by applying a semi-geostrophic coordinate transformation prior to the computation of the Hilbert transform (Wolf and Wirth, 2014). The semi-geostrophic transformation narrows (widens) midlatitude ridges (troughs) and reduces semi-geostrophic dynamics to QG dynamics. Wolf and Wirth (2014) showed for several cases of RWPs that this technique yields a better representation of the RWPs than applying the Hilbert transform on the regular latitude-longitude grid. A sensitivity analysis of the results concerning the semi-geostrophic transformation will be presented in section 4.1.6.

## 3.4 Eddy kinetic energy budget analysis

Rossby wave propagation is characterized by the dispersion of kinetic energy into downstream regions. This behaviour, the so called downstream development, can be described in a PV framework (e.g. Hoskins et al., 1985; Davis and Emanuel, 1991) or from an  $K_e$  perspective (Orlanski and Katzfey, 1991; Orlanski and Sheldon, 1995). Here we describe the  $K_e$  perspective.

### 3.4.1 Derivation of eddy kinetic energy tendency equation

The eddy kinetic energy is defined as  $K_e = \frac{1}{2}(u^2 + v^2)$  with  $u$  and  $v$  being the eddy parts of the zonal and meridional wind respectively. The eddies are defined as a deviation from a time (e.g. monthly) mean. The local change of  $K_e$  can be described via a budget equation that is derived from the momentum equation in pressure coordinates

$$\frac{d\mathbf{V}}{dt} + \omega \frac{\partial \mathbf{V}}{\partial p} + f\mathbf{k} \times \mathbf{V} = -\nabla\Phi + \mathbf{F} \quad . \quad (3.11)$$

$\mathbf{V}$  is the two-dimensional horizontal wind velocity,  $d/dt$  is defined as  $\partial/\partial t + \mathbf{V} \cdot \nabla_p$ ,  $\omega$  is the vertical velocity,  $f$  is the Coriolis parameter,  $\Phi$  is the geopotential height and  $\mathbf{F}$  represents

frictional forces. In order to describe energy transfers between the mean flow and transient eddies (and vice versa) the scalar and vector quantities are decomposed into a time mean part (subscript  $m$ ) and deviations from this time mean (lower case), i.e. in detail

$$\mathbf{V} = \mathbf{V}_m + \mathbf{v} \quad (3.12)$$

$$\Phi = \Phi_m + \phi \quad (3.13)$$

In this study the time mean is defined as a 30-day running mean. The time mean flow is assumed to be non-divergent so that  $\omega$  is attributable to the eddies. Hence, the deviation from the time mean  $\omega$  is the instantaneous vertical velocity. The insertion of the decomposed variables into equation 3.11 yields

$$\frac{d(\mathbf{V}_m + \mathbf{v})}{dt} + \omega \frac{\partial \mathbf{V}_m}{\partial p} + \omega \frac{\partial \mathbf{v}}{\partial p} + f\mathbf{k} \times \mathbf{V}_m + f\mathbf{k} \times \mathbf{v} = -\nabla \Phi_m - \nabla \phi + \mathbf{F}_m + \mathbf{f} \quad (3.14)$$

The temporal average of equation 3.14 leads us to the time mean momentum equation

$$\mathbf{V}_m \cdot \nabla \mathbf{V}_m + \overline{\mathbf{v} \cdot \nabla \mathbf{v}} + \omega \frac{\partial \mathbf{v}}{\partial p} + f\mathbf{k} \times \mathbf{V}_m = -\nabla \Phi_m + \mathbf{F}_m + \mathbf{F}_o \quad (3.15)$$

A basic assumption of the averaging process is that the 30-day mean flow is steady such that the local temporal derivative of  $\mathbf{V}_m$  vanishes. However, an average circulation calculated for a period as short as one month certainly cannot be considered steady (Orlanski and Katzfey, 1991). In order to compensate for this assumption a forcing term  $\mathbf{F}_o$  is introduced.  $\mathbf{F}_o$  can be interpreted as the temporal average of the local momentum tendency. The time mean of the combined parameters

$$\overline{\mathbf{v} \cdot \nabla \mathbf{v}} + \omega \frac{\partial \mathbf{v}}{\partial p}$$

represents the time mean eddy forcing term. Finally, the difference between the total momentum equation 3.14 and the time mean momentum equation 3.15 gives the momentum equation for the time deviation

$$\begin{aligned} \frac{\partial \mathbf{v}}{\partial t} + \mathbf{V}_m \cdot \nabla \mathbf{v} + \mathbf{v} \cdot \nabla \mathbf{V}_m + \omega \frac{\partial \mathbf{V}_m}{\partial p} + \mathbf{v} \cdot \nabla \mathbf{v} - \overline{\mathbf{v} \cdot \nabla \mathbf{v}} + f\mathbf{k} \times \mathbf{v} \\ = -\nabla \phi - \omega \frac{\partial \mathbf{v}}{\partial p} + \omega \frac{\partial \mathbf{v}}{\partial p} + \mathbf{F}_e - \mathbf{F}_o \end{aligned} \quad (3.16)$$

where  $\mathbf{F}_e$  indicates the difference between the total and the time mean frictional forces. The  $K_e$  tendency equation is obtained by scalar multiplication of equation 3.16 by  $\mathbf{v}$  and the combination of the horizontal and vertical advection terms into the three dimensional perturbation velocity  $\mathbf{v}_3$  and the three dimensional nabla operator  $\nabla_3$  (see underlined terms). The tendency equation for  $K_e$  is given as

$$\begin{aligned} \frac{\partial K_e}{\partial t} + \mathbf{V}_m \cdot \nabla K_e + \mathbf{v} \cdot \nabla_3 K_e \\ = -(\mathbf{v} \cdot \nabla \phi) - \mathbf{v} \cdot (\mathbf{v}_3 \cdot \nabla_3 \mathbf{V}_m) + \mathbf{v} \cdot (\mathbf{v}_3 \cdot \nabla_3 \mathbf{v}) - \mathbf{v} \cdot \mathbf{F}_e - \mathbf{v} \cdot \mathbf{F}_o \end{aligned} \quad (3.17)$$

The terms on the left hand side (lhs) of equation 3.17 describe the local tendency of  $K_e$ , the advection of  $K_e$  by the mean flow and advection of  $K_e$  by the eddies. Equation 3.17 can be further simplified by combining the second and third term of the lhs

$$\begin{aligned} & \mathbf{V}_m \cdot \nabla K_e + \mathbf{v} \cdot \nabla_3 K_e \\ &= \nabla \cdot (\mathbf{V}_m K_e) - K_e (\nabla \cdot \mathbf{V}_m) + \nabla_3 \cdot (\mathbf{v} K_e) - K_e (\nabla_3 \cdot \mathbf{v}) \end{aligned} \quad (3.18)$$

$$= \nabla \cdot (\mathbf{V} K_e) + K_e \frac{\partial \omega}{\partial p} \quad (3.19)$$

under the assumption that  $\nabla \cdot \mathbf{V}_m = 0$  and by considering the continuity equation in pressure coordinates ( $\nabla \cdot \mathbf{v} + \partial \omega / \partial p = 0$ ).

The first term on the right hand side (rhs) of equation 3.17 represents the pressure work term associated with the eddies. This term describes the conversion from eddy available potential energy into  $K_e$  which is done by accelerations through the eddy wind from regions with high geopotential height toward regions with low geopotential height. A partition of  $\mathbf{v}$  into a geostrophic component  $\mathbf{v}_g$  and an ageostrophic component  $\mathbf{v}_{ag}$  shows that the acceleration is only done by the ageostrophic component of the eddy wind since  $\mathbf{v}_g \perp \nabla \phi$ . As the geostrophic flow is non-divergent, it follows from the continuity equation that the ageostrophic flow is directly linked to vertical motions. Thus, the pressure work term can be written as

$$-\mathbf{v} \cdot \nabla \phi = -\nabla \cdot (\mathbf{v}_{ag} \phi) + \phi \nabla \cdot \mathbf{v}_{ag} \quad (3.20)$$

$$= -\nabla \cdot (\mathbf{v}_{ag} \phi) - \phi \frac{\partial \omega}{\partial p} \quad (3.21)$$

$$= -\nabla \cdot (\mathbf{v}_{ag} \phi) - \omega \alpha - \frac{\partial(\omega \phi)}{\partial p} \quad (3.22)$$

From equation 3.21 to equation 3.22 the hydrostatic approximation in pressure coordinates  $\partial \phi / \partial p = -\alpha$  was used.

The third term on the rhs of equation 3.17 is similar to the second term and represents the net conversion of  $K_e$  to the kinetic energy of the first-order correlation which is defined as  $K_l = \mathbf{V}_m \cdot \mathbf{v}$ . Averaged over time, the third term equals zero (Orlanski and Katzfey, 1991). Frictional forces are described by the fourth term on the rhs. Orlanski and Katzfey (1991) argued that a time-mean average of the fifth term on the rhs ( $\mathbf{v} \cdot \mathbf{F}_o$ ) equals zero for long time-mean averages, but becomes also small for shorter time scales.  $\mathbf{F}_o$  was introduced in equation 3.15 to compensate for the assumption that the temporal derivative of  $\mathbf{V}_m$  vanishes. The following dimension analysis shows that  $\mathbf{F}_o$  becomes small for temporal averages over a period of 30-days as applied in this study even when the temporal change is in the same magnitude as the magnitude of the velocity field.

$$\mathbf{F}_o = \frac{\Delta \mathbf{v}}{\Delta t} \approx \frac{\mathbf{v}}{\Delta t} \approx \frac{20 \text{ m s}^{-1}}{2592000 \text{ s}} \approx 8 \times 10^{-6} \text{ m s}^{-2} \quad (3.23)$$

Inserting these simplifications into equation 3.17 leads us to the final form of the kinetic energy equation

$$\begin{aligned} \frac{\partial K_e}{\partial t} = & -\nabla \cdot (\mathbf{v}_{ag}\phi) - \omega\alpha - \frac{\partial(\omega\phi)}{\partial p} - \nabla \cdot (\mathbf{V}K_e) \\ & - K_e \frac{\partial\omega}{\partial p} - (\mathbf{v} \cdot (\mathbf{v}_3 \cdot \nabla_3 \mathbf{V}_m)) + residue \end{aligned} \quad (3.24)$$

In order to evaluate the evolution of the  $K_e$  in the whole troposphere, the terms in equation 3.24 are integrated vertically from 1000 to 100 hPa. The integration leads to a further simplification as the vertical divergence of the eddy ageostrophic geopotential flux and the vertical divergence of the  $K_e$  fluxes, i.e. the third and fifth term in equation 3.24, become very small. A normalization of the integrated terms by the gravitational constant  $g = 9.81 \text{ m s}^{-2}$  leads to the units of  $J \text{ m}^{-2}$  for the  $K_e$  and  $W \text{ m}^{-2}$  for the budget terms. In this study, we analyze the  $K_e$  budgets terms in the integrated form of equation 3.24 which is

$$\begin{aligned} \frac{1}{g} \int_{1000}^{100} \frac{\partial K_e}{\partial t} dp = & \frac{1}{g} \int_{1000}^{100} -(\mathbf{v}_{ag} \cdot \nabla \phi) - \underbrace{\nabla \cdot (\mathbf{V}K_e)}_{\textcircled{3}} - \underbrace{(\mathbf{v} \cdot (\mathbf{v}_3 \cdot \nabla_3 \mathbf{V}_m))}_{\textcircled{4}} + residue dp \\ \text{with } \frac{1}{g} \int_{1000}^{100} -(\mathbf{v}_{ag} \cdot \nabla \phi) dp = & -\frac{1}{g} \int_{1000}^{100} \underbrace{\nabla \cdot (\mathbf{v}_{ag}\phi)}_{\textcircled{1}} dp - \frac{1}{g} \int_{1000}^{100} \underbrace{\omega\alpha}_{\textcircled{2}} dp \end{aligned} \quad (3.25)$$

According to term  $\textcircled{1}$  in equation 3.25, horizontal convergence (divergence) of the eddy ageostrophic geopotential fluxes results in a generation (destruction) of  $K_e$ . It should be noted here that the ageostrophic geopotential fluxes always point into downstream regions. This characteristic results from the subgeostrophic (supergeostrophic) flows in midlatitude upper-level troughs (ridges) as inferred from gradient wind balance. Under the assumption of a zonal mean circulation, troughs appear as negative geopotential anomalies ( $\phi < 0$ ) and ridges as positive geopotential anomalies ( $\phi > 0$ ). Thus, the ageostrophic geopotential flux ( $\mathbf{v}_{ag}\phi$ ) is always positive and directed downstream at all points of the wave. Term  $\textcircled{1}$  will be referred to as ageostrophic geopotential flux convergence/divergence.

Term  $\textcircled{2}$  represents the conversion from eddy available potential energy into  $K_e$  and vice versa. The ascent (descent) of warm (cold) air masses generates  $K_e$  whereas the ascent (descent) of cold (warm) air masses destructs  $K_e$ . Term  $\textcircled{2}$  will be referred to as baroclinic conversion.

Term  $\textcircled{3}$  describes the redistribution of  $K_e$  through the divergence of  $K_e$  fluxes. The divergence (convergence) is strongest at the rear (front) of energy centers which are typically located at the flanks of the midlatitude troughs and ridges. It should be noted here that the fluxes of  $K_e$  do not contribute to the transport of  $K_e$  between centers of  $K_e$ . The strong zonal component of the  $K_e$  fluxes contributes rather to an eastward propagation of energy centers with phase velocity  $C_{ph}$ . A meridional propagation of energy centers does not occur as most of the meridional energy flux  $\mathbf{V}K_e$  is compensated by ageostrophic

geopotential flux divergence. Thus, the advection of  $K_e$  centers through the base (crest) of a midlatitude trough (ridge) can not be observed. The energy centers rather “jump” from the eastern flank to the western flank of a trough with the group velocity  $C_g$ . Since  $C_g$  is larger than  $C_{ph}$ , these two velocities illustrate Rossby wave dispersion as described in section 2.3.

Term ④ describes the energy conversion by the Reynolds stresses which can be interpreted as a transfer of energy between the mean and eddy flow. This term will be referred to as barotropic conversion.

### 3.4.2 Downstream baroclinic development from an eddy kinetic energy perspective

A three-stage conceptual model that describes a downstream baroclinic development from an eddy kinetic energy perspective was introduced by Orlanski and Sheldon (1995). The basic ideas of this conceptual model are illustrated in Fig. 3.6 and elucidated in the following. In Fig. 3.6, the two solid lines represent upper-level geopotential height contours and the ellipses denote maxima in the vertically integrated  $K_e$ . The wide solid arrows represent the vertically integrated  $K_e$  fluxes and the open arrows represent the vertically integrated ageostrophic geopotential fluxes. The “+” and “-” symbols denote sources and sinks of  $K_e$  through baroclinic and barotropic conversion as well as dissipation by surface friction. The positioning of the “+” and “-” symbols within the ellipses is arbitrary, however the dominance of one symbol indicates net  $K_e$  generation or dissipation.

#### Stage 1: Upstream system decay, generation of energy center $\mathcal{W}$ west of new trough

The initial situation is characterized by an upstream, mature trough that is associated with a  $K_e$  center on the eastern flank of this trough (Fig. 3.6). The trough starts to decay as it disperses  $K_e$  via ageostrophic geopotential fluxes (open arrow) through a downstream ridge toward a new  $K_e$  center  $\mathcal{W}$  on the western flank of the incipient trough. The ageostrophic fluxes are maximized in the base (crest) of the troughs (ridges) and minimized on the flanks where the  $K_e$  centers are located. Therefore, flux divergence occurs at the exit region of the old, pre-existing energy center and flux convergence at the entrance region of the intensifying downstream energy center  $\mathcal{W}$ . This intensification of the  $K_e$  center is characterized by an increased geopotential height gradient and corresponds therefore to the formation of a jet streak.

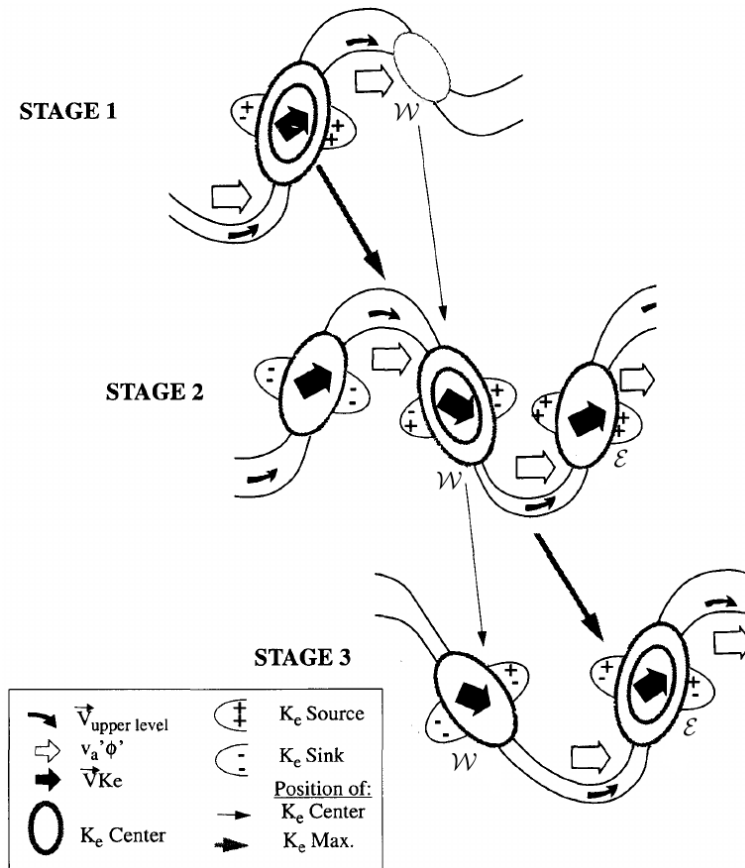


**Figure 3.6:** The three stages in the evolution of a baroclinic wave. Symbols are as given in the figure. Stage 1: Upstream system decay and generation of energy center  $\mathcal{W}$  west of new trough via geopotential fluxes. Stage 2: Energy fluxes emanate from a mature  $\mathcal{W}$  and foster growth of energy center  $\mathcal{E}$  east of trough. Stage 3: Dissipation of energy center  $\mathcal{W}$ , maturation of energy center  $\mathcal{E}$ . Fig. 3 from Orlanski and Sheldon (1995).

### Stage 2: Energy fluxes from mature $\mathcal{W}$ , growth of energy center $\mathcal{E}$ east of trough

The  $K_e$  center  $\mathcal{W}$  on the western flank of the incipient trough grows due to convergent energy fluxes. Upper-level convergence of the ageostrophic circulation to the west of the trough induces sinking motion in a region of a cold anomaly which implies additional generation of kinetic energy via baroclinic conversion. The acceleration of ageostrophic winds into the base of the trough constantly removes  $K_e$  at the exit region of  $\mathcal{W}$  (“-” symbols) and contributes to the initial development of the energy center  $\mathcal{E}$  on the eastern flank of the trough. Convergence of  $K_e$  fluxes amplifies the new energy center (“+” symbols) and the trough at upper-levels which leads to a divergent upper-level ageostrophic flow. This divergent flow induces warm ascending motion so that the  $K_e$  center on the eastern flank is strengthened further by baroclinic conversion. The described events are equivalent to a type-B cyclogenesis (Petterssen and Smebye, 1971). Latent heating and increased buoyancy intensify the ascending motion and the upper-level divergence. The resulting

fluxes are able to export energy further downstream and contribute this way to the initiation of another  $K_e$  center.

### Stage 3: Dissipation of energy center $\mathcal{W}$ , maturation of energy center $\mathcal{E}$

A decrease of geopotential fluxes from the upstream system accompanies the decay of energy center  $\mathcal{W}$  (dominance of “–” symbols) through the divergence of geopotential fluxes. In addition, barotropic decay as well as surface friction may also contribute to a weakening of  $\mathcal{W}$ . The divergent ageostrophic geopotential fluxes emanating from this energy center (open arrow) lead to an accumulation of  $K_e$  in the downstream center  $\mathcal{E}$ . Baroclinic conversion in the vicinity of  $\mathcal{W}$  provides a continuous, indirect energy source for the downstream center due to the fluxes exiting  $\mathcal{W}$ . Energy center  $\mathcal{E}$  intensifies further (“+” symbols) due to ascending warm air masses ahead which lead to a generation of  $K_e$  through baroclinic conversion. At some point, the energy center  $\mathcal{W}$  does no longer supply  $K_e$  to  $\mathcal{E}$  so that baroclinic conversion becomes the sole source of  $K_e$ . After reaching peak intensity,  $K_e$  center  $\mathcal{E}$  starts to decay through divergent ageostrophic fluxes, barotropic conversion and frictional effects. The further development of  $K_e$  in  $\mathcal{E}$  resembles the initial energy center in the Stage 1 picture.

The described three stage conceptual picture strongly resembles the concept of type B cyclogenesis (Petterssen and Smebye, 1971) since an upper-level disturbance exists prior to any baroclinic conversion. A baroclinic development without an initial upper-level disturbance is limited to regions of strong low-level baroclinicity such as the entrance region of the Pacific storm track.

A composite analysis of eddy kinetic energy budget terms during the ET of TCs and downstream of the ET of TCs is presented in section 4.2.4. This allows us to identify regions which are most relevant to the initial amplification of a Rossby wave. An qualitative investigation of eddy kinetic energy budget terms for two different MJO phases and its representation in the ERA-Interim reforecast dataset is examined in sections 5.1 and 5.3 respectively.

## 3.5 Quasi-geostrophic forcing diagnostics

In order to quantify the contribution of quasi-geostrophic (QG) forcings to the vertical velocity during the ET of TCs, we computed a height attributable solution of the QG omega equation (Clough et al., 1996). This diagnostic allows us to distinguish at a specific level between vertical motion induced through low-level flow features and upper-level large-scale waves, and to separate it from convective vertical motions associated with the TC as the QG diagnostic strongly underestimates vertical motion in regions with intense latent heating (Böttcher and Wernli, 2011). The QG approximation is based on the assumption that the synoptic midlatitude horizontal flow can be decomposed into a geostrophic ( $\mathbf{v}_g$ ) and

ageostrophic ( $\mathbf{v}_{ag}$ ) wind component where  $\mathbf{v}_g \gg \mathbf{v}_{ag}$ . The continuity equation under QG approximation reveals that vertical motion results from the vertically integrated divergence of the ageostrophic wind, driving a secondary circulation. The combination of the QG momentum equation and the continuity equation yields the barotropic vorticity equation. A second fundamental equation of the QG theory is the QG thermodynamic equation which results from the thermodynamic energy equation assuming adiabatic processes and that horizontal advection is accomplished by the geostrophic wind. The combination of the barotropic vorticity equation and the QG thermodynamic equation yields an equation for the QG vertical velocity, the omega equation defined as

$$N^2 \nabla^2 w + f^2 \frac{\partial^2 w}{\partial z^2} = f \frac{\partial}{\partial z} (\mathbf{v}_g \cdot \nabla \zeta_g) - \frac{g}{\theta_0} \nabla^2 (\mathbf{v}_g \cdot \nabla \theta) \quad . \quad (3.26)$$

$N$  is the Brunt-Väisälä-frequency,  $w$  the vertical velocity,  $f$  the Coriolis parameter,  $\mathbf{v}_g$  the geostrophic wind,  $\zeta_g$  the geostrophic relative vorticity and  $\theta$  is the potential temperature. This equation describes the vertical motion that results from differential temperature and differential vorticity advection. According to Hoskins et al. (1978), the omega equation can be written as

$$N^2 \nabla^2 w + f^2 (\partial^2 w / dz^2) = 2 \nabla \cdot \mathbf{Q} \quad , \quad (3.27)$$

where  $\mathbf{Q}$  is the Q-vector. The Q-vector

$$\mathbf{Q} = -g/\theta_0 ((\partial \mathbf{v}_g / \partial x) \cdot \nabla \theta, (\partial \mathbf{v}_g / \partial y) \cdot \nabla \theta) \quad (3.28)$$

gives the vector rate of change of the horizontal potential temperature gradient following the geostrophic flow. According to equation 3.27, ascent is forced by the convergence of  $\mathbf{Q}$  and descent is forced by divergence of  $\mathbf{Q}$ .

The method to solve the differential equation 3.27 was kindly provided by Sue Gray and was supported by Maxi Böttcher and Christian Grams. This method allows us to distinguish between forcings from upper-levels (650 to 100 hPa) and from low-levels (1000 to 750 hPa). Following Böttcher and Wernli (2011) and Grams et al. (2013a), we investigated the contribution from these two layers to the vertical velocity at 700 hPa.

# 4 The impact of tropical cyclones on midlatitude Rossby wave packets

Several recent idealized numerical studies (e.g. Riemer et al., 2008; Riemer and Jones, 2010; Scheck et al., 2011b) as well as case studies (e.g. Harr and Dea, 2009; Grams et al., 2011; Grams et al., 2013b) showed that TCs which move into the midlatitudes may excite Rossby wave trains. A climatological investigation by Archambault et al. (2013) highlighted that recurving western North Pacific TCs significantly amplify the meridional flow pattern in downstream regions which indicates an increase of Rossby wave activity. In this chapter, we present a climatological investigation of the impact of western North Pacific, South Indian Ocean and North Atlantic TCs on the amplitude and occurrence frequency of midlatitude RWPs. Physical processes that are essential for the amplification of RWPs are identified in a composite framework. The presented results in this chapter are closely related to a recent study by Quinting and Jones (2014).

## 4.1 Rossby wave packets downstream of ET events

The climatological investigation of RWPs downstream of ET events is based on the method of Zimin et al. (2003) (see section 3.3). After using the filtering technique and clipping the envelope, a meridional average is performed between  $20^{\circ}$  to  $80^{\circ}$  North and  $20^{\circ}$  to  $80^{\circ}$  South. This way a one-dimensional field for each time is obtained. This meridional average excludes the tropics and the poles from further consideration but ensures that the entire extratropics are included. Since zonal averages of the wave packet envelope are investigated we adhere to the technique described in Zimin et al. (2003) and do not use the refined method of Zimin et al. (2006). By concatenating the one-dimensional fields for several time steps a Hovmöller diagram is obtained which illustrates the evolution of the upper-tropospheric midlatitude Rossby waves.

### 4.1.1 Two contrasting cases: Typhoons Sinlaku (2008) and Choi-Wan (2009)

We describe first the midlatitude development downstream of the recurvature of the Typhoons Sinlaku (2008) and Choi-Wan (2009) before presenting the climatological investi-

gation. The life-cycles of Sinlaku and Choi-Wan as well as their impact on the downstream midlatitude flow differ markedly. Typhoon Sinlaku underwent ET to the east of Japan on 21 September 2008 according to the RSMC best track data and then dissipated in a region of strong zonal shear over the western North Pacific. The midlatitude flow configuration was characteristic of the *northwest* pattern. According to the RSCM best track data, Typhoon Choi-Wan underwent ET on 20 September 2009 ahead of a midlatitude trough (*northeast* pattern), merged with a midlatitude low pressure system and re-intensified as an extratropical low.

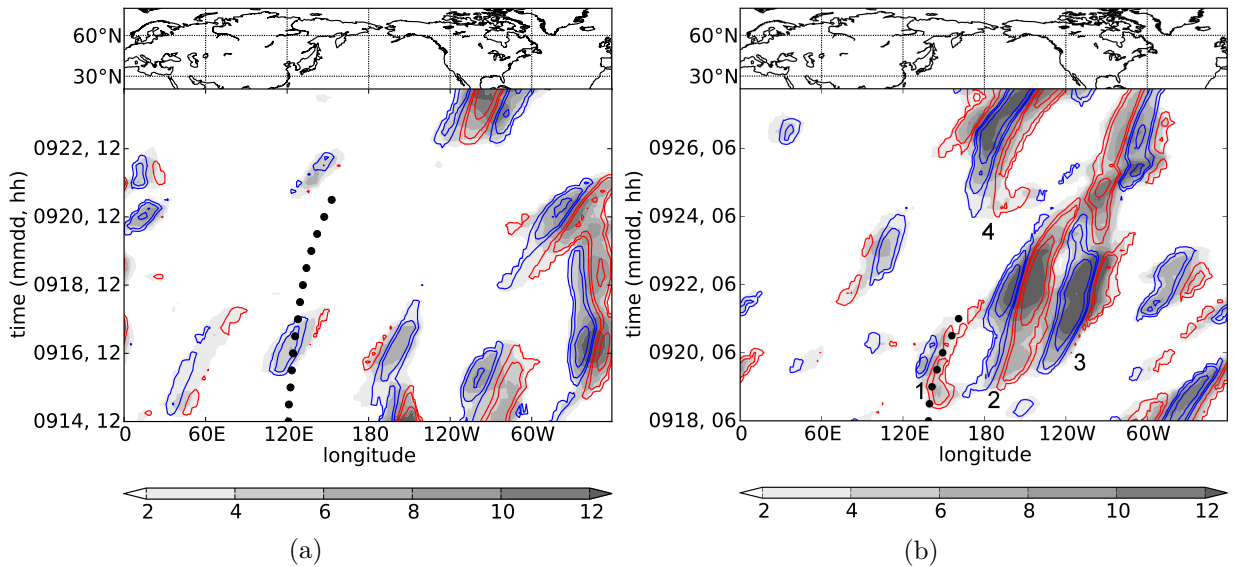


**Figure 4.1:** 20° to 80°N Hovmöller diagram of the envelope of the meridional wind (shading,  $m s^{-1}$ ) at 250 hPa after the recurvature of the Typhoons Sinlaku 2008 (a) and Choi-Wan 2009 (b). Meridional wind in the zonal wave number range 5–15 at 250 hPa (colored contours,  $\pm 2, 4, 8 m s^{-1}$ ). Contours are masked where the envelope falls below  $2 m s^{-1}$ . Rossby waves in (b) are labeled according to text. Black dots mark the best track longitudes of the typhoons from recurvature to dissipation.

A rather weak Rossby wave with an amplitude of  $6 m s^{-1}$  exists in the same longitudinal range as Sinlaku between 16 September 0000 UTC and 17 September 1200 UTC (Fig. 4.1a). During this time period Sinlaku was still located in the subtropics whilst the midlatitude Rossby wave was located north of 45°N. In addition, the phase velocity of the Rossby wave identified was considerably larger than the zonal propagation of Sinlaku. Hence, the eastward moving RWP and its associated trough passed north of Sinlaku so that Sinlaku and this midlatitude trough did not interact. The midlatitude trough weakened downstream of Sinlaku. Therefore, the Hovmöller diagram does not indicate any downstream development associated with Sinlaku's ET.

The Hovmöller diagram of the midlatitude flow evolution after the recurvature of Typhoon Choi-Wan (Fig. 4.1b) exhibits in total four major Rossby waves that might be associated with its ET. The first Rossby wave is collocated with Choi-Wan's track between 18 September 1800 UTC and 21 September 0600 UTC. In contrast to the ET of

Sinlaku, Choi-Wan is situated ahead of a midlatitude trough that dug into the subtropics. Furthermore, the trough had a phase speed which is similar to Choi-Wan's meridional displacement. These conditions enabled an interaction between the midlatitude trough and the TC which in turn favored the extratropical re-intensification of Choi-Wan. A second Rossby wave develops downstream of the ET between 180° and 150°W on 19 September. This wave propagates downstream with a phase speed of about 7° per day and decays on 24 September over the eastern North Pacific. A third Rossby wave which is part of the same RWP developed immediately downstream of the second wave. The onset of this wave was on 20 September over the eastern North Pacific. In the following days it propagated downstream to central North America until 23 September where it led to a remarkable cold-air outbreak. On 24 September, i.e. three days after the dissipation of Choi-Wan, a fourth Rossby wave formed over the central North Pacific.

### 4.1.2 Climatology of Rossby wave packets

In order to assess the impact of ETs on the amplitude and occurrence frequency of Rossby waves we performed a climatological analysis. We applied the Hilbert transform filtering technique in six-hourly time intervals from seven days prior to ten days after all ET events in the period 1980 to 2010 (Fig. 3.2) and created for each TC a Hovmöller diagram as illustrated in section 4.1.1. Finally, we made a Hovmöller composite centered on the ET-time of the TCs. We choose not to composite the data on a central longitude as we do not want to enhance the observed signal artificially. In the following, we investigate the mean RWP occurrence frequency  $F$  and the mean RWP amplitude  $\hat{E}$  defined as

$$F = \frac{1}{N_c} \sum_c M_{i,j}^c \quad \text{and} \quad \hat{E} = \frac{\sum_c E_{i,j}^c}{\sum_c M_{i,j}^c} . \quad (4.1)$$

$N_c$  denotes the number of cases,  $M_{i,j}^c$  is a mask at the grid point  $i, j$  in the Hovmöller diagram for case  $c$  that is set to 1 if the clipped envelope  $E_{i,j}^c > 0$ .

Following Scherrer et al. (2006), we investigate the statistical significance of the results via a Monte-Carlo approach. We create 1000 random Hovmöller composites of the RWP occurrence frequency and the RWP amplitude. Each of the composites consists of 280 cases that are centered on a randomly chosen date so that they contain data with and without TCs. Each date consists of a randomly chosen year out of the period 1980 to 2010 and a randomly chosen day and month from a 14 day period around each ET event that was incorporated in the ET relative composite. By choosing the day from a range of days around each ET event we account for the seasonal variability in the random composites. Finally, we determine the upper and lower 5% percentiles of the Monte-Carlo composites and define those values of the ET relative composite as statistically significant that either exceed or fall below these percentiles.

In order to compare the ET relative composites of RWP occurrence frequency and RWP amplitude with a climatological value we computed a climatology of both quantities.

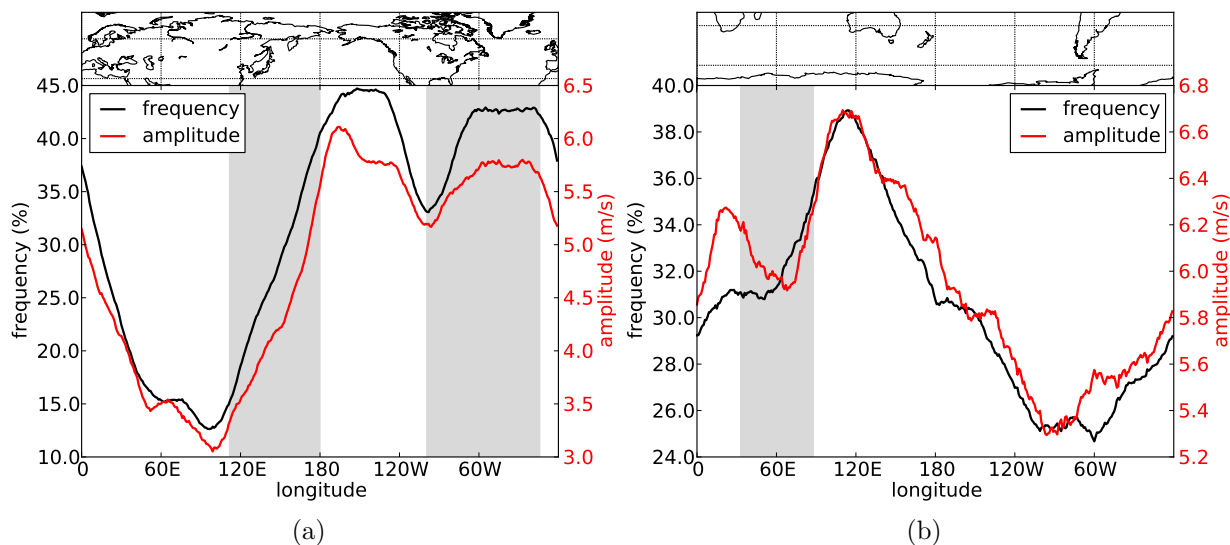


**Figure 4.2:** Mean RWP frequency (%) and mean RWP amplitude ( $m s^{-1}$ ) on the Northern Hemisphere (a) and on the Southern Hemisphere (b) from June to November and December to April, respectively. The gray shading indicates the range of longitudes where ET events investigated in this study occurred.

Thereby, we focus on the months June to November for the Northern Hemisphere and December to April for the Southern Hemisphere. In the Northern Hemisphere, the lowest values of RWP occurrence frequency and amplitude occur over the Asian continent between  $50^{\circ}$  and  $120^{\circ}$ E (Fig. 4.2a). The occurrence frequency exhibits minimum values of 13% with a minimum amplitude of about  $3 m s^{-1}$  in this region. Highest values of RWP occurrence frequency can be found in the storm track regions over the eastern North Pacific and the western North Atlantic with RWP occurrence frequencies between 40% to 45%.

The occurrence frequency in the southern hemisphere exhibits a dipole-like structure (Fig. 4.2b). The highest RWP occurrence frequency of more than 45% can be found over the eastern South Indian Ocean along  $120^{\circ}$ E. Lowest values of less than 15% occur over South America. Preferred regions of Rossby wave onset as illustrated by the increase of RWP occurrence frequency are the South Atlantic and the South Indian ocean. A decrease of RWP occurrence frequency over the South Pacific indicates a region of Rossby wave decay. The zonal variability in RWP occurrence frequency and amplitude is much lower than over the Northern Hemisphere. The amplitude varies between maximum values of  $6.6 m s^{-1}$  over the eastern South Indian Ocean and lowest values of  $3.5 m s^{-1}$  over South America. A climatological investigation for the period 1979 to 2010 by Souders et al. (2014) showed a similar spatial distribution of RWP occurrence frequency for both the northern and southern hemisphere.

### 4.1.3 Western North Pacific tropical cyclones

The RWP occurrence frequency exceeds the climatological value downstream of western North Pacific ET events from the western North Pacific to central North America (Fig. 4.3a). A statistically significant increase of RWP occurrence frequency of 15% occurs over the western North Pacific already one day prior to ET. This early increase of the RWP occurrence frequency is most probably associated with an amplification of the upstream (downstream) trough (ridge). The eastward extension of the statistically significant increase of RWP occurrence frequency with time indicates downstream Rossby wave dispersion in the ET-time relative composite. Maximum RWP occurrence frequency anomalies occur shortly after ET-time. The occurrence frequency exceeds the climatological value by more than 20% along 180°E. This maximum can be attributed to the development of a downstream ridge-trough couplet. The remarkable positive RWP occurrence frequency anomaly over the western North Pacific show that the ET events lead to an enhancement of Rossby wave activity. One day after ET, a minimum in the anomalous RWP occurrence frequency

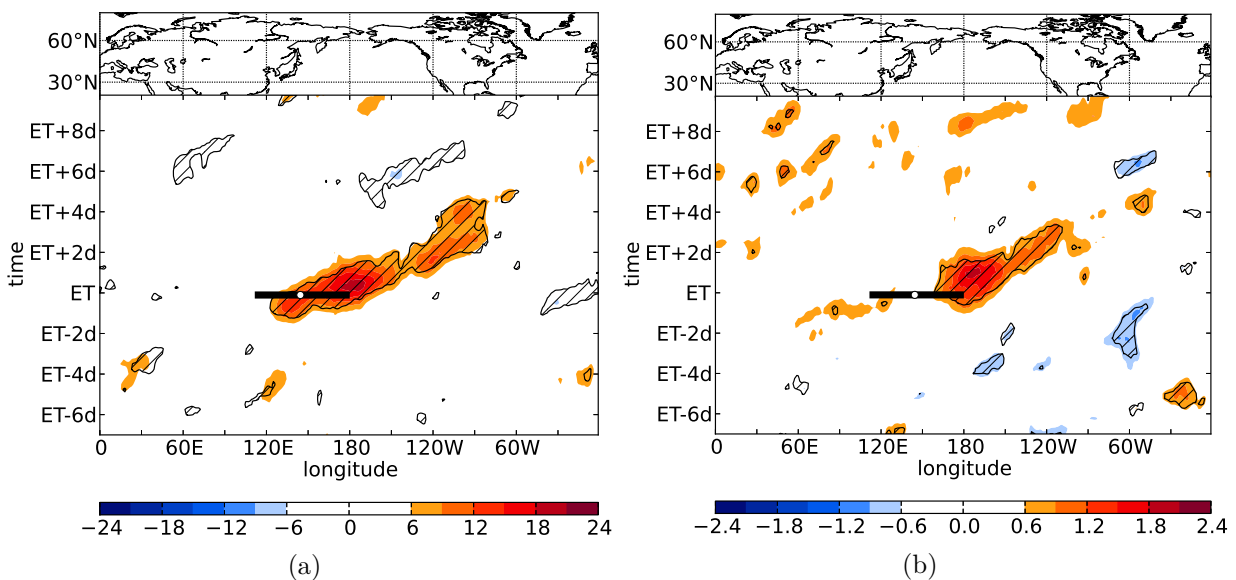


**Figure 4.3:** Anomaly of (a) RWP occurrence frequency (shading in %) and (b) RWP amplitude (shading in  $m s^{-1}$ ) relative to June to November climatology for western North Pacific TCs. Values that are statistically significant at the 95% confidence level are hatched. Black horizontal bar marks the range of longitudes of TCs at ET-time. White circle marks the mean longitude of all TCs at ET-time. Data are smoothed with a Gaussian filter.

occurs over the eastern North Pacific. This relative minimum is due to the fact that the climatological RWP occurrence frequency reaches maximum values in this region (Fig. 4.2a). The statistical significance and the anomaly of RWP occurrence frequency decrease rapidly about five days after the ET events. This shows that the change of the variability of RWP occurrence frequency downstream of western North Pacific ET events is limited to the North Pacific and western North America.

The ET relative composite exhibits a significantly negative RWP occurrence frequency anomaly of -6 to -3% over the eastern North Pacific between 4 to 7 days after the ET events. The findings in the ET relative composite reflect what has been observed in a case study of Typhoon Choi-Wan (Julia Keller 2014, personal communication). A first Rossby wave train developed immediately downstream of Choi-Wan. A second Rossby wave train developed three days after the decay of Choi-Wan. Without Choi-Wan, the first wave train exhibited a weaker amplification. However, the second Rossby wave train developed earlier and was stronger when Choi-Wan was removed. This suggests that the massive amplification of the meridional flow after ET events prevents the development of strong Rossby wave trains a few days later.

The RWP amplitude is amplified significantly from the central Pacific to western North America (Fig. 4.3b). This reveals that RWPs that are amplified by TCs exhibit a greater amplitude than RWPs that are associated with extratropical cyclones. The strongest anomaly of more than  $1.8 \text{ m s}^{-1}$  occurs between  $180^\circ$  and  $150^\circ\text{W}$  one day after the ET events. This amplification is most likely associated with the development of the downstream ridge-trough couplet. An amplification of the RWP amplitude does not occur before ET as we observe for the RWP occurrence frequency. This indicates that the TCs interact with midlatitude disturbances that are not extraordinarily strong but that are amplified strongly during ET events. The RWP amplitude anomaly decreases considerably three days after ET. We suggest that this decrease is associated with Rossby wave breaking and the dispersion of kinetic energy. While we observe a significantly enhanced RWP occurrence frequency over central North America the RWP amplitude is not significantly enhanced. Hence, Rossby waves are more likely to occur in this region after western North Pacific ET events, but their amplitude is not enhanced compared to the general variability.

#### 4.1.4 South Indian Ocean tropical cyclones

The RWP occurrence frequency is significantly amplified by 12 to 15% downstream of the South Indian Ocean ET events (Fig. 4.4a). However, the anomaly is not as strong as for the TCs in the western North Pacific (Fig. 4.3a). The RWP occurrence frequency starts to increase significantly one day prior to ET in the vicinity of the ET events. The statistically significant signal persists for three days and decreases downstream over Australia. A further increase of RWP occurrence frequency that is only partially statistically significant can be observed over the western South Pacific. The RWP occurrence frequency anomaly reaches 6 to 12% from two to four days after the ET events. The RWP amplitude enhancement is as strong as over the western North Pacific. From one to five days after the ET events we observe a considerable amplification of the RWP amplitude by more than  $1.8 \text{ m s}^{-1}$  between  $90^\circ$  to  $150^\circ\text{E}$  (Fig. 4.4b). A second region with an amplified Rossby wave envelope can be found between  $150^\circ\text{E}$  to  $150^\circ\text{W}$  from three to seven days after ET. The amplification of the Rossby wave envelope and an increase in occurrence frequency in the same region indicates the development of a further downstream trough over the western South Pacific after ET events. It is still amplified by more than  $1.8 \text{ m s}^{-1}$  compared to the climatological

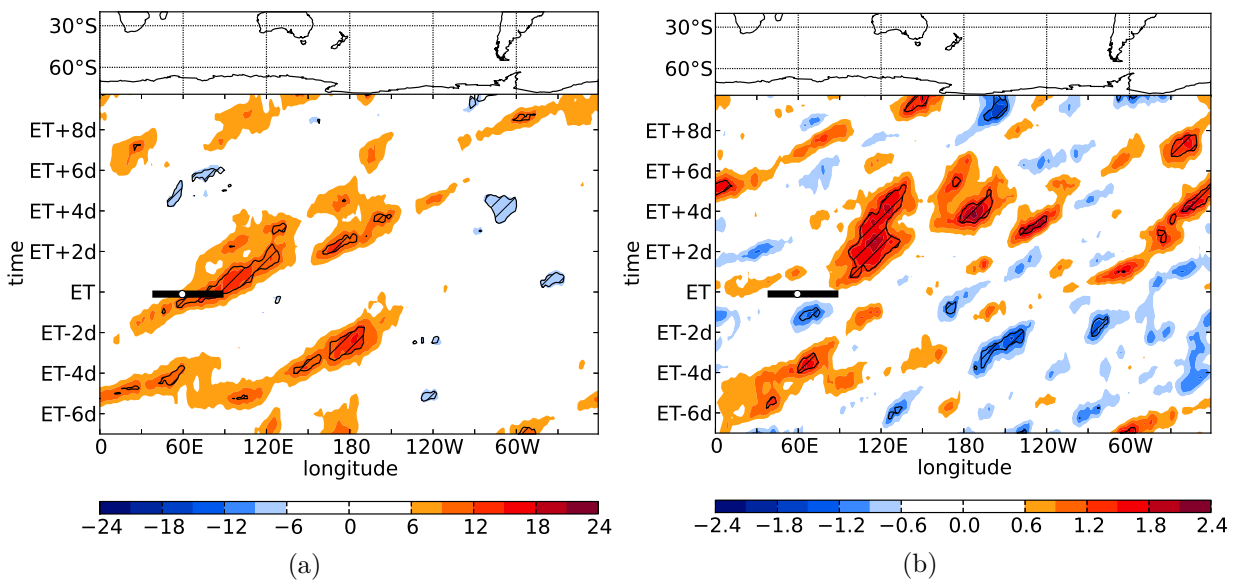


**Figure 4.4:** As in Fig. 4.3 for anomaly relative to December to April climatology for the western South Indian Ocean TCs.

mean. The decrease of the mean Rossby wave amplitude and occurrence frequency over eastern Australia is indicative of a Rossby wave breaking event or the development of a planetary scale ridge.

#### 4.1.5 North Atlantic tropical cyclones

Case studies have highlighted the impact of North Atlantic TCs on the midlatitude flow and shown that these midlatitude flow modifications can be associated with high impact weather or forecast uncertainties in downstream regions (e.g. Agustí-Panareda et al., 2004; Grams et al., 2011). However, we do not observe a statistically significant increase in RWP occurrence frequency and amplitude downstream of in total 129 ET events in this basin (Fig. 4.5a). These observations indicate that TCs over the North Atlantic are able to modify RWPs but that modifications do not lead to a departure from the general variability of RWPs. A possible explanation is that the climatological RWP occurrence frequency and amplitude are higher in this region than over the western North Pacific (Fig. 4.2a). Over the western North Pacific, the climatological RWP occurrence frequency is well below 33% over a large longitudinal range where ET events occur. Over the North Atlantic, the climatological RWP occurrence frequency exceeds 33% in those areas where ET events occur. Therefore, an enhancement of the Rossby wave activity as observed for the western North Pacific ET events does not occur. We investigated the sensitivity of the results to the variability of ET locations over the North Atlantic by compositing the Hovmöller diagrams on a central longitude. The composite Hovmöller did not reveal a significant impact of North Atlantic TCs on RWPs either (not shown).

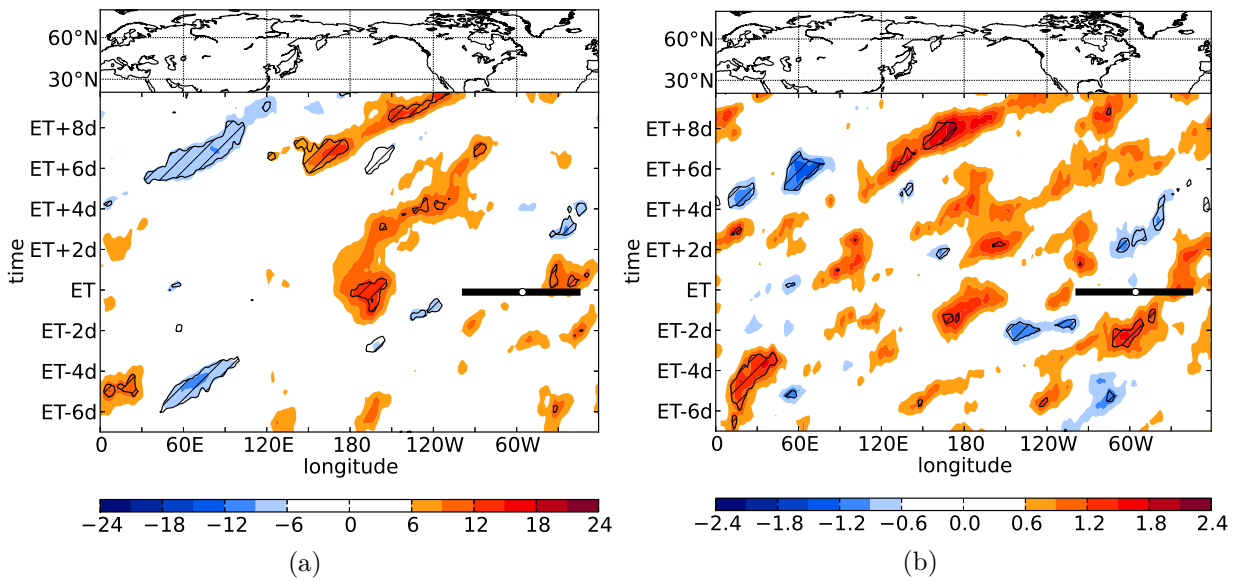


**Figure 4.5:** As in Fig. 4.3 for anomaly relative to June to November climatology for the North Atlantic TCs.

#### 4.1.6 Sensitivity of the results

The results of our analysis depend on the choice of the clipping parameter  $\tau^*$  (cf. equation 3.5). Glatt and Wirth (2013) concluded that the dependence on the clipping parameter is most critical when an increase of  $\tau^*$  splits a single objects into several fragments, and vice versa. Therefore, an increase of  $\tau^*$  would lead to a decrease in RWP occurrence frequency. Glatt and Wirth (2013) suggested that a good choice for  $\tau^*$  is between  $\tau^* = 3$  and  $\tau^* = 4$ . We computed the Hovmöller composites and their statistical significance for the western North Pacific ET events for  $2.5 \leq \tau^* \leq 3.2$ . The results of the Monte-Carlo approach are confirmed for both the RWP occurrence frequency and amplitude (Fig. 4.6). The area where the RWP occurrence frequency differs significantly from the general variability extends from the western North Pacific to central North America (Fig. 4.6a). The significance falls merely below the 95% percentile along  $150^\circ\text{W}$ . The area where RWP are stronger than those RWP which are associated with midlatitude cyclones increases with a lower clipping threshold (Fig. 4.6b). The significance exceeds the 95% percentile now from the western North Pacific to central North America.

The Zimin et al. (2003) filtering technique exhibits the tendency to fragment a single RWP into several parts (Glatt and Wirth, 2013). This undesirable effect results from the fact that RWPs feature substantial deviations from the almost plane wave paradigm (Wolf and Wirth, 2014). A constant frequency (i.e. a single wave number), a constant peak-to-peak amplitude and surfaces of constant phase that are parallel to the phase velocity vector characterize plane waves. Almost plane waves exhibit more than a single wave number. However, the distribution of the wave numbers is fairly narrow and maximizes at the carrier wave number. Observed RWP are not almost plane waves as their wave number

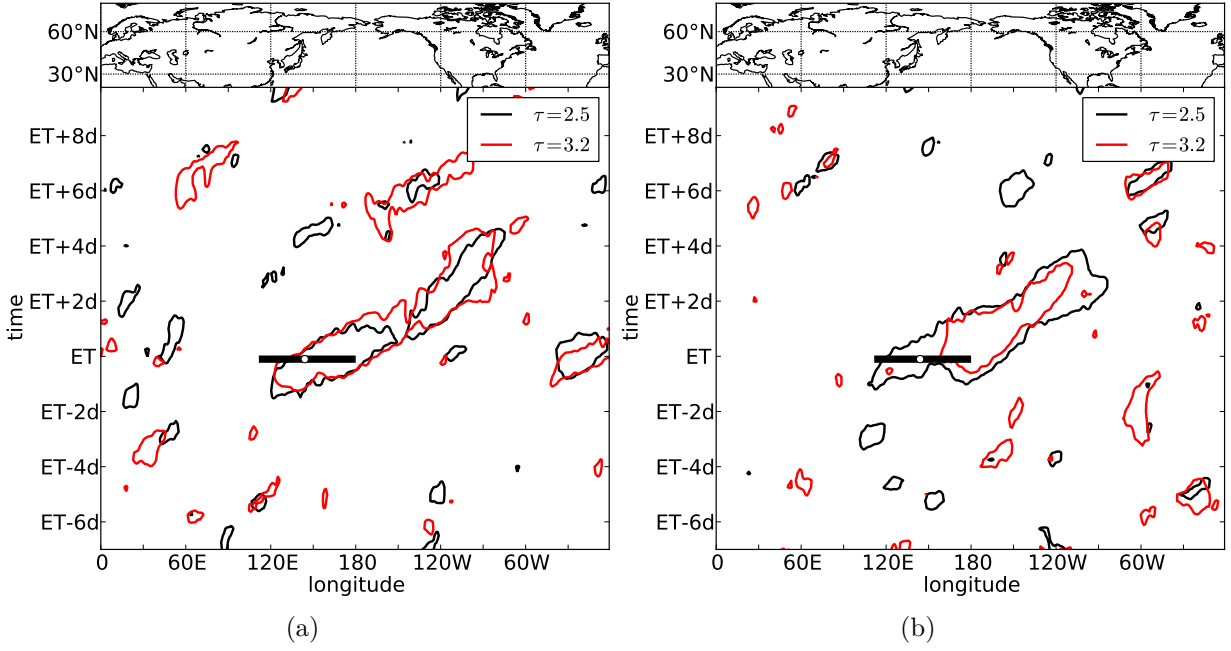


**Figure 4.6:** 95% percentiles for RWP occurrence frequency (a) and amplitude (b) downstream of western North Pacific ET events for two different clipping threshold values. Black horizontal bar marks the range of longitudes of TCs at ET-time. White circle marks the mean longitude of all TCs at ET-time.

spectrum peaks at several wave numbers. This is due to the fact that midlatitude troughs are narrower than ridges as can be inferred from semigeostrophic theory (Hoskins, 1975). The existence of several peaks in the wave number spectrum of observed Rossby waves causes significant spikes in the reconstructed envelope when applying the Hilbert transform. These spikes lead to an artificial strengthening (weakening) of troughs (ridges). Thus, clipping the envelope at a threshold value  $\tau$  (cf. equation 3.5) can split a RWP artificially. In addition, the signal of ridges might get lost in the RWP occurrence frequency. The spikes can be avoided by the application of a semi-geostrophic coordinate transformation to the meridional wind component on a regular latitude-longitude-grid (Wolf and Wirth, 2014). The semi-geostrophic coordinates are defined as

$$\lambda_{sg} = \lambda + \frac{v_g}{f a \cos\phi} \quad (4.2)$$

$$\phi_{sg} = \phi - \frac{u_g}{f a} \quad (4.3)$$

with the regular longitude  $\lambda$  and latitude  $\phi$ , the Coriolis parameter  $f$ , and the geostrophic wind components  $u_g$  and  $v_g$ . The re-transformation from the transformed grid back to the regular latitude-longitude-grid is done by a linear interpolation routine. After the re-transformation, RWP can be identified as illustrated in section 3.3.

We tested the sensitivity of our results to the semigeostrophic coordinate transformation by computing the RWP occurrence frequency and anomaly with this refined method

for the western North Pacific ET events for the same period. The results coincide well with previous findings. A statistically significant positive RWP occurrence frequency anomaly occurs downstream of the western North Pacific ET events (Fig. 4.7a). The maximum in the RWP occurrence frequency anomaly one day after ET along  $180^\circ$  weakened slightly whereas the anomaly increased between  $150^\circ$  and  $120^\circ$ W. We argued in subsection 4.1.3 that these relative extrema are most probably related to a ridge-trough couplet between  $180^\circ$  and  $120^\circ$ W. Since the refined method does not overemphasize (underemphasize) troughs (ridges) any longer, we obtain a somewhat more uniform RWP occurrence frequency anomaly than in Fig. 4.3a.

The RWP amplitude anomaly exhibits a statistically significant increase between  $150^\circ$ E and  $120^\circ$ W (Fig. 4.7b). This increase coincides well with the findings in Fig. 4.3b. However, the anomalous values in RWP amplitude are slightly weaker in the semigeostrophic framework.

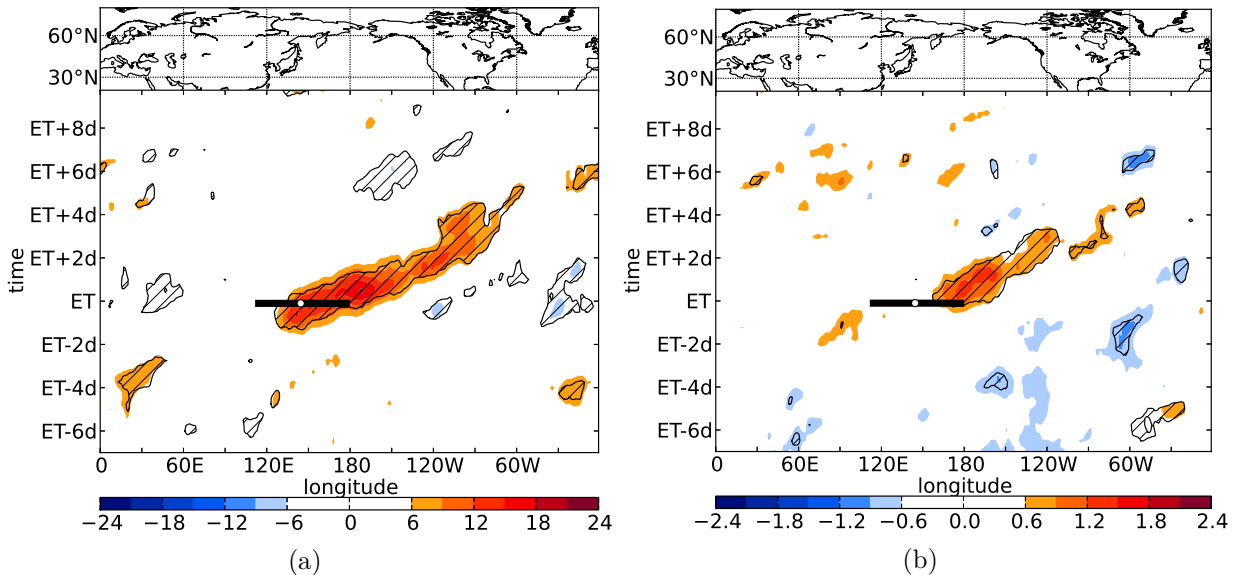


**Figure 4.7:** As in Fig. 4.3, but computed with the refined method described in subsection 4.1.6.

As noted in section 3.2 the locations and times of ET for South Indian Ocean TCs should be handled with care due to a rather subjective definition of ET during the period 1980–1989. We considered this by computing recurvature relative Hovmöller composites of RWP occurrence frequency and RWP amplitude anomaly for the western South Indian Ocean TCs. We defined the recurvature time as the time when a TC reached the minimum longitude along the best track. The RWP occurrence frequency anomaly in the recurvature relative composite (Fig. 4.8a) is similar to the anomaly for the ET relative composite (Fig. 4.4a). A RWP occurrence anomaly of more than 15% between two to eight days after recurvature indicates a downstream Rossby wave development. In particular, the RWP occurrence frequency anomaly over eastern Australia and the western South Pacific is stronger than in the ET relative composite. Thus, once a Rossby wave train has been

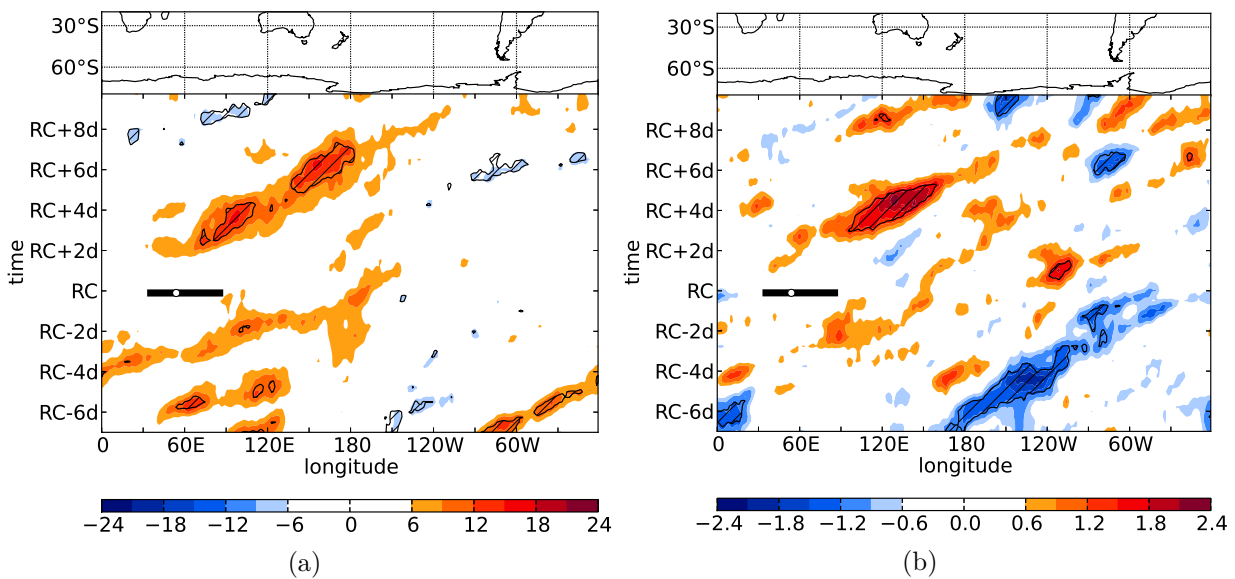


**Figure 4.8:** As in Fig. 4.4, but centered on the recurvature time of the western South Indian Ocean TCs.

amplified by the recurving TC it has the ability to propagate from the western South Indian Ocean to the western South Pacific. A statistically significant positive RWP amplitude anomaly is collocated with the positive RWP occurrence frequency anomaly (Fig. 4.8b). The RWP amplitude anomaly extends from the South Indian Ocean to Australia and is more coherent than in the ET relative composite (Fig. 4.4b). Thus, the results confirm that RWPs are more frequent downstream of recurving western South Indian Ocean TCs and that they are stronger than RWP associated with extratropical cyclones.

#### To conclude section 4.1:

The results presented in this section provide answers to some of the initially raised research questions. The RWP amplitude and occurrence frequency increase significantly downstream of western North Pacific and south Indian Ocean ET events. The Monte-Carlo approach shows that the RWP amplitude downstream of these ET events differs significantly from the general variability of midlatitude RWPs. Thus, we state that RWPs which are associated with ET events in the western North Pacific and the south Indian Ocean are stronger than those which are associated with midlatitude synoptic systems. This stands in contrast to the characteristics of midlatitude RWPs downstream of North Atlantic ET events which do not vary statistically significant from the general midlatitude variability. Sensitivity tests concerning the filtering technique, the clipping parameter and the reference time confirm the robustness of the results.

## 4.2 Composite analysis of cases with and without Rossby wave development

Section 4.1 shows that TCs undergoing ET modify the RWP amplitude and occurrence frequency in downstream regions. Reanalysis data enable us to investigate the main physical processes involved in the amplification of RWPs through TCs for numerous cases. Due to the large sample size of western North Pacific TCs we investigate in the following the amplification of Rossby waves through these TCs in a composite view. After the identification of cases with and without downstream Rossby wave development we document the Rossby wave amplification in a PV framework and in an eddy kinetic energy framework.

### 4.2.1 Identification of cases

The identification of RWPs as separate objects enables us to distinguish between two downstream development scenarios. We determined cases with and without downstream Rossby wave development for the western North Pacific ET events. By doing so, we are able to make a classification based on the downstream flow response that is independent of the structure of the TC. This type of classification complements the study by Archambault et al. (2013) who distinguished between two scenarios based on a TC-midlatitude flow interaction metric.

In order to separate between these two cases we generated a mask. This mask is defined by the 90% confidence level of the Monte-Carlo approach between 115°E to 140°W and from two days prior to three days after ET (Fig. 4.9). Afterward, we determined for each case the area in this mask that exhibits a Rossby wave amplitude greater than zero. The quintile of cases with the largest fractional area of the mask is defined in the following as Rossby wave case (RW case). The quintile of cases with the smallest fractional area of the mask is defined as no Rossby wave case (noRW case). Each quintile contains 56 ET events. We computed the RWP occurrence frequency anomaly for both quintiles.

A Hovmöller composite centered on ET-time for the RW case exhibits a RWP occurrence frequency anomaly of considerably more than 40% over the western and central North Pacific (Fig. 4.9a). The climatological RWP occurrence frequency exhibits values between 15 and 45% in the range of the mask (Fig. 4.2a). This indicates that the RW case composite contains a RWP in 55 to 85% of the cases. A Hovmöller composite for the noRW case exhibits large areas with a RWP occurrence frequency anomaly of -25% (Fig. 4.9b). With a climatological RWP occurrence frequency of 15 to 45% in the range of the mask the noRW case composite contains in 0 to 20% a RWP.

Hovmöller composites of the meridional wind centered on ET-time and on the mean longitude at ET-time illustrate nicely the downstream Rossby wave development. A

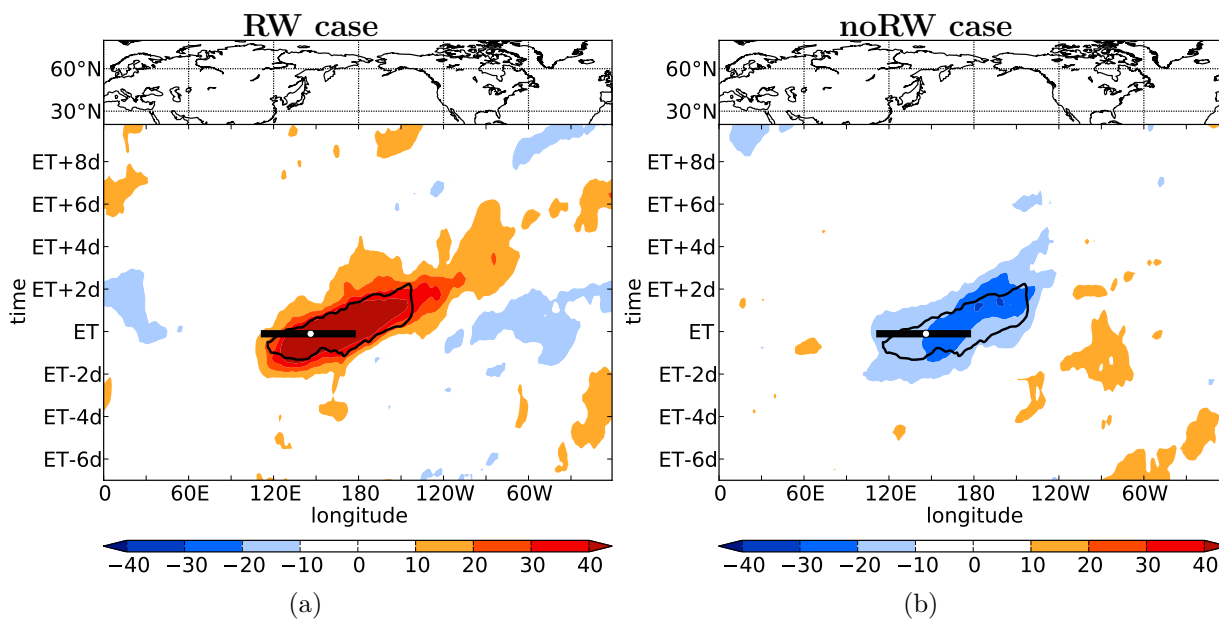


**Figure 4.9:** Anomaly of RWP occurrence frequency (shading in %) relative to June to November climatology for RW case (a) and noRW case (b). Data are smoothed with a Gaussian filter. The black contour indicates the mask that we used to determine the lower and upper quintile.

precursor Rossby wave emanates from the Asian continent in the RW case (Fig. 4.10a). A weak ridge exists over eastern Asia at  $90^{\circ}\text{E}$  about three days prior to the ET event. A trough develops downstream and its axis is located about  $15^{\circ}$  west of the approaching TC at ET-time. The TC itself is collocated with the eastern flank of this trough which is strongly amplified prior to ET-time. This amplification indicates the interaction between the transitioning TC and the midlatitude flow. A typical Rossby wave train pattern develops downstream of the ET events. The pattern decreases about three days after ET-time over North America. The estimated Rossby wave group velocity of about  $2600 \text{ km day}^{-1}$  is in the range that was observed in earlier studies (e.g. Simmons and Hoskins, 1979; Riemer et al., 2008).

In the noRW case this precursor wave train does not exist (Fig. 4.10b). A weak ridge starts to develop between  $120^{\circ}$  and  $150^{\circ}\text{E}$  about two days prior to ET. It reaches its peak intensity at ET-time which suggests that the ET system acts as a local source of eddy kinetic energy leading to an amplification of the meridional wind. However, the ridge vanishes by two days after ET. Interestingly, a second Rossby wave pattern starts to develop two days after the ET event. A rather weak Rossby wave train propagates downstream and reaches central North America about six days after ET-time. This second wave train development could be investigated in future case studies.

The observed pattern suggests that a precursor Rossby wave emanating from the Asian continent favors the conditions for a Rossby wave development over the North Pacific. However, the existence of a precursor Rossby wave does not necessarily result in a strong

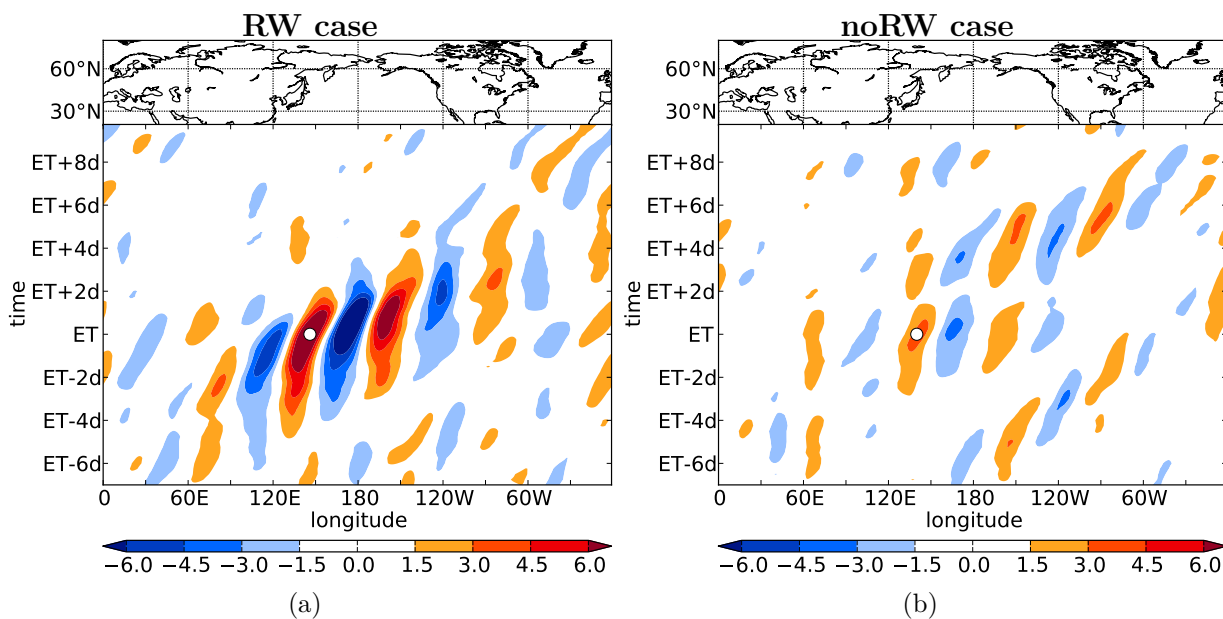


**Figure 4.10:** ET-relative composite Hovmöller diagram of the  $20^{\circ}$ – $80^{\circ}$ N-averaged 250 hPa meridional wind (shading in  $m s^{-1}$ ) for zonal wave number 5 to 15. RW case (a) and noRW case (b). White circle marks the longitude of the composite TC at ET-time.

downstream development. Previous studies showed that the further development of the ET system and the downstream flow amplification also strongly depends on the phasing between the transitioning TC and the midlatitude flow (Klein et al., 2002; Ritchie and Elsberry, 2007; Grams et al., 2013a). The systematic investigation of the phasing between the midlatitude flow and the TCs in the RW and noRW case could be a task for future studies.

The RW cases occur more frequently in August–September and less frequently in June, July, October and November relative to the climatological distribution of TCs that underwent ET (Fig. 4.11). The distribution of the noRW cases relative to the climatological distribution is exactly opposite. The noRW cases occur less frequently during August–September and more frequently in June, July, October and November. Generally speaking, the monthly distribution of the noRW cases is more homogeneous than the monthly distribution of the RW cases. Interestingly, despite a stronger climatological jet and hence a stronger instability the RW cases occur less frequent in November. From the observations of a number of recent cases, we suppose that ET events which occur in late fall lead to a remarkable jet and downstream ridge amplification. However, these ridges are usually associated with an anticyclonic wave breaking which transports kinetic energy back into the subtropics and not into downstream regions. The systematic investigation of ET events and downstream wave breaking provides an intriguing research opportunity.

TCs that are followed by a Rossby wave development tend to exhibit a lower central pressure than TCs which are not followed by a Rossby wave development. Two days prior to ET the RW case TCs exhibit a mean central pressure of 967 hPa and the

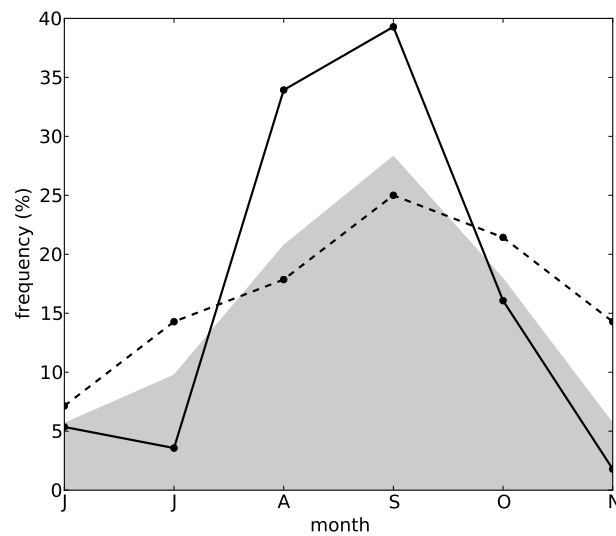


**Figure 4.11:** Monthly frequency distribution of 280 western North Pacific TCs that underwent ET (gray shading), and of 56 TCs that underwent ET in the RW case (black solid line) and of 56 TCs that underwent ET in the noRW case (black dashed line).

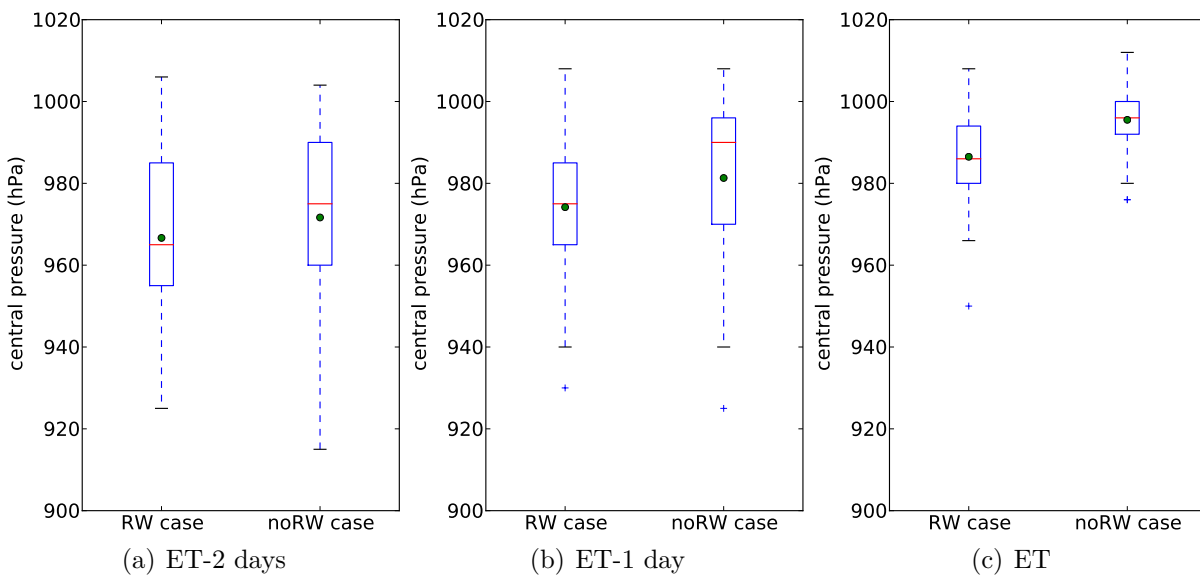


**Figure 4.12:** Best track central pressure (hPa) of RW case and noRW case TCs (a) two days prior to ET, (b) one day prior to ET and (c) at ET-time. The box-whisker plots show 5%, 25%, 50% (median), 75% and 95% percentiles. Blue crosses mark outliers, the green circle denotes the mean.

noRW case TCs a mean central pressure of 972 hPa (Fig. 4.12a). The differences become significant at the 99% confidence level based on a Student's  $t$  test one day prior to ET (Fig. 4.12b). At that time the RW case TCs exhibit a mean central pressure of 974 hPa whereas the noRW case TCs exhibit a mean central pressure of 981 hPa. The noRW case TCs weaken to a mean central pressure of 996 hPa at ET-time (Fig. 4.12c). At the same

time the RW case TCs exhibit a mean central pressure of 986 hPa. The difference between the RW case and noRW case is significant at the 99.9% confidence level based on a Student's  $t$  test. Possible mechanisms that contributed to a lower central pressure in the RW case than in the noRW case and a potential impact of the more intense TC on the midlatitude flow will be part of the discussion in the following to sections.

## 4.2.2 Rossby wave amplification from a potential vorticity perspective

As discussed in section 2.4.2, the initiation, amplification and downstream propagation of a Rossby wave can be explained by the advection of PV anomalies by the winds induced by the circulation anomalies themselves (Hoskins et al., 1985). In order to quantify mechanisms that contributed to the amplification of the Rossby wave in response to the ET events, we investigated the synoptic development in the noRW and RW case in a composite PV framework. The composites are computed from ERA-Interim reanalyses at  $1^\circ$  horizontal resolution. In order to account for the poleward convergence of the meridians we interpolated the data for each case onto a cartesian grid, centered the grid on the mean position of the 56 TCs in each scenario (according to the best track data) and interpolated the data back on a regular latitude/longitude grid. We considered the seasonal variation of the tropopause height by averaging the upper-level data between 330  $K$  to 350  $K$ .

### Rossby wave amplification two days prior to ET-time

In the noRW case, the TCs are located about  $15^\circ$  south of the midlatitude wave guide two days prior to ET (Fig. 4.13a). The meridional PV gradient reaches its maximum over the western North Pacific. There, the midlatitude flow pattern is zonally oriented and exhibits a jet streak of up to  $50 \text{ m s}^{-1}$  about  $25^\circ$  northeast of the TC. The flow configuration in the noRW case strongly resembles the flow configuration during the ET of Typhoon Jangmi (2008) where a downstream Rossby wave development did not occur (Grams et al., 2013a). Accordingly, Typhoon Jangmi (2008) is one of the noRW case TCs. In the RW case the TC approaches a midlatitude wave guide (Fig. 4.13b) which is not as zonal as in the noRW case. The PV indicates the existence of an upper-level trough over eastern Asia upstream of the TC which coincides with the Hovmöller composite of the meridional wind (Fig. 4.10a). A weak upper-level ridge exists directly downstream of the TC. The jet streak is slightly weaker than in the noRW case and exhibits maximum values of more than  $45 \text{ m s}^{-1}$  about  $20^\circ$  northeast of the cyclone.

We quantified the contributions of different circulation anomalies to the Rossby wave amplification by performing a Helmholtz partition of the flow. Therefore, we defined two non-divergent circulation anomalies based on TC relative composites of mean relative vorticity at 330  $K$  and 350  $K$  (Fig. 4.14). The circulation anomalies consist of the upper-

---

<sup>1</sup> 1 potential vorticity unit (PVU)  $\equiv 10^{-6} \frac{K \text{ m}^2}{kg \text{ s}}$

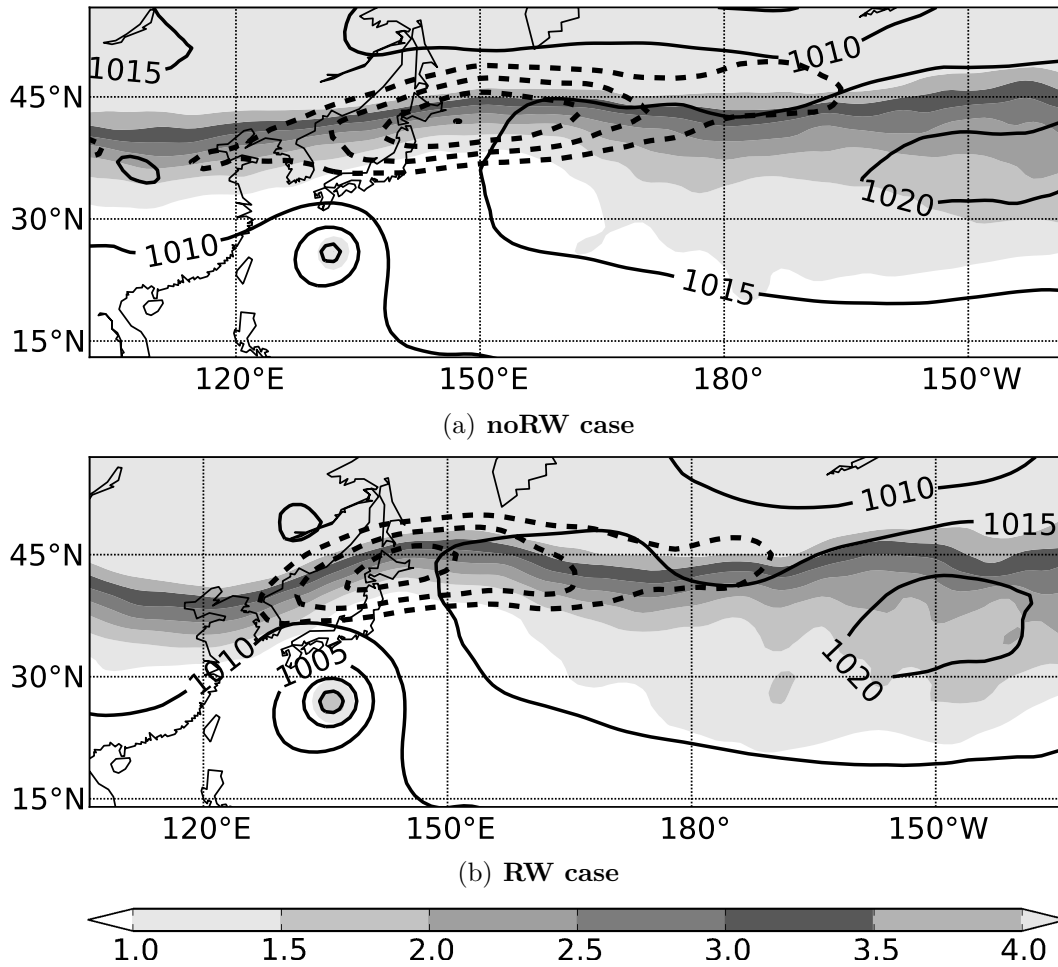


**Figure 4.13:** ET-relative composite analyses for the (a) noRW and (b) RW case two days prior to ET. 330–350-K PV (shading in  $PVU^1$ ), 330–350-K wind speed (dashed contours, interval  $5 m s^{-1}$  starting at  $35 m s^{-1}$ ) and mean sea level pressure (continuous contours in  $hPa$ ). For illustrative purposes the coastlines are shown relative to the mean TC position.

level TC circulation itself ( $\psi_{TCcore}$ ) and the upper-level anomalies associated with the Rossby wave ( $\psi_{RW}$ ). The non-divergent anomalies are characterized by positive (negative) relative vorticity values of greater (less) than  $10^{-5} s^{-1}$  ( $-10^{-5} s^{-1}$ ). Two days prior to ET, the composites of relative vorticity clearly depict the TC which is surrounded by negative relative vorticity. The TC and its associated cyclonic circulation is stronger in the RW case (Fig. 4.14a) than in the noRW case (Fig. 4.14b). The region of negative vorticity to the northeast of the TC is associated with the downstream ridge and the anticyclonic outflow anomaly of the TC. The anticyclonic outflow anomaly becomes in particular evident to the east of the TC where northerly winds indicate the transport of air masses toward the tropics. A separation between the anticyclonic TC outflow anomaly and the anticyclonic anomaly associated with the downstream ridge was not accomplished.

In particular, we are interested in the contribution of the circulation anomalies to the PV advection at a specific vertical level. In contrast to Riemer et al. (2008) and Riemer

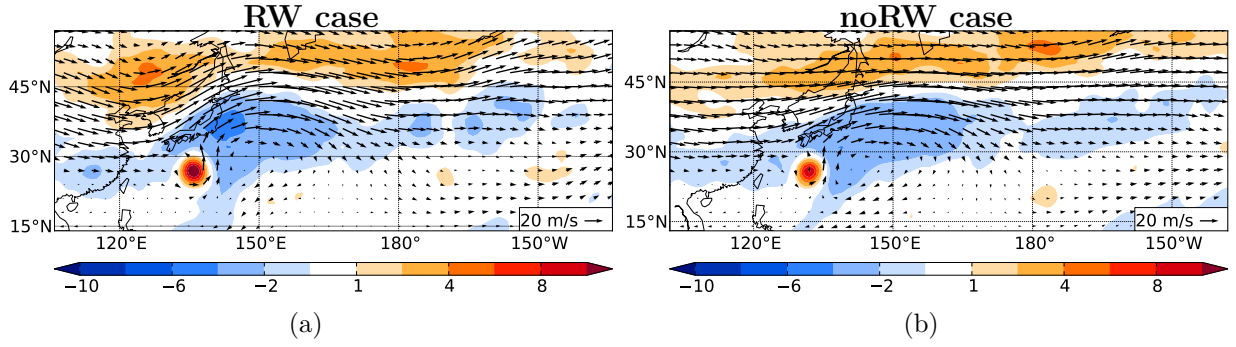


**Figure 4.14:** ET-relative composite analyses of (a) the RW case and (b) the noRW case two days prior to ET. 330–350-K relative vorticity (shaded in  $10^{-5} s^{-1}$ ) and 330–350-K winds (vectors in  $m s^{-1}$ ). For illustrative purposes the coastlines are shown relative to the mean TC position.

and Jones (2010), we computed the rotational wind components from the distribution of relative vorticity instead of computing the rotational wind components from the distribution of PV via piecewise PV inversion. As the relative vorticity gives the full rotational wind field at an isentropic level, the Helmholtz partition represents an effective tool to assess the contribution of cyclonic and anticyclonic anomalies to the PV advection. We decided to use isentropic levels as PV is conserved here for frictionless and adiabatic motions. We computed the rotational wind components of the non-divergent circulation anomalies by solving

$$\nabla^2 \psi_{TCcore} = \zeta_{TCcore}; \quad \psi_{TCcore} = 0 \text{ on lateral boundaries} \quad (4.4)$$

$$\nabla^2 \psi_{RW} = \zeta_{RW}; \quad \psi_{RW} = 0 \text{ on lateral boundaries} \quad (4.5)$$

via a successive over-relaxation method.  $\psi$  is the streamfunction and  $\zeta$  denotes the relative vorticity.

In addition, we determined the contribution through the upper-level divergent winds to the Rossby wave development. Technically we could not attribute the divergent flow to a specific anomaly such as the TC outflow, the divergence above the ascent along the baroclinic zone and the divergence which was forced from the midlatitude upper-level flow. Hence, we computed the divergent wind from the full divergence  $\delta$  at 330 K and 350 K by solving

$$\nabla^2 \chi = \delta; \quad \chi = 0 \text{ on lateral boundaries} \quad (4.6)$$

where  $\chi$  denotes the velocity potential. Computing the wind components from the streamfunction and the velocity potential via  $\mathbf{v}_\psi = \mathbf{k} \times \nabla \psi$  and  $\mathbf{v}_\chi = \nabla \chi$ , the PV advection can be written as

$$-\mathbf{v} \cdot \nabla PV = -(\mathbf{v}_{TCcore} + \mathbf{v}_{\psi_{RW}} + \mathbf{v}_\chi + \mathbf{v}_{BG}) \cdot \nabla PV \quad (4.7)$$

where  $\mathbf{v}_{BG}$  denotes the background wind which is computed as the difference between the total wind field and the wind induced by the circulation anomalies and divergence.

The cyclonic circulation associated with  $\psi_{TCcore}$  induces a dipole pattern of PV advection along the midlatitude wave guide two days prior to ET (Fig. 4.15a; Fig. 4.15e). Southward advection of high-PV air into the base of the upstream trough reveals a deepening of the trough. The simultaneous negative PV advection into the downstream ridge indicates a subsequent amplification. Both negative and positive PV advection through  $\psi_{TCcore}$  are weaker in the noRW case (Fig. 4.15e). Both the upper-level PV gradient and the distance between the TC center and the midlatitude waveguide are very similar in the RW and noRW case. Thus, we expect that a weaker amplification of the ridge-trough couplet through  $\psi_{TCcore}$  in the noRW case can be attributed to a weaker upper-level cyclonic TC circulation. The negative PV advection into the downstream ridge in the RW case reaches values of about  $6 \cdot 10^{-6} PVU s^{-1}$  in regions where the PV gradient does not exceed  $5 \cdot 10^{-6} PVU m^{-1}$ . Thus, we would expect a northward deflection of the isolines of PV by about 100 km over a 24 hour period. In fact, the 2 PVU isoline shifts northward by about 400 km in the crest of the ridge during the next 24 hours. Hence, the ridge amplification downstream of the TC can not be solely explained by the cyclonic TC circulation itself.

A significant contribution to the downstream ridge amplification comes from the PV advection through the divergent winds. The amplitude of the negative PV advection through the divergent winds is similar in both cases (Fig. 4.15b, Fig. 4.15f). Strongest upper-level divergence occurs primarily to the north and northeast of the TC. This indicates that ascent to the north of the TC, presumably along the primary midlatitude baroclinic zone, contributes to the divergent flow component. The negative PV advection by the divergent wind into the crest and into the western flank of the downstream ridge suggests a subsequent amplification and a deceleration of the eastward translation of the upstream trough. In addition, the negative PV advection on the western flank of the downstream ridge reveals a strengthening of the PV gradient and thus a jet intensification.

The TCs are embedded in an anticyclonic circulation in the RW case (Fig. 4.15c) as well as in the noRW case (Fig. 4.15g). The advection that results from  $\psi_{RW}$  is about one order of magnitude more intense than the advection through  $\psi_{TCcore}$  as the wind anomalies associated with  $\psi_{RW}$  are much stronger. A strong wind component perpendicular to the isolines of PV causes a slightly more intense PV advection in the RW case than in the noRW case. The dipole pattern in PV advection through  $\psi_{RW}$  is  $90^\circ$  out of phase with the axes of the upstream trough and downstream ridge. Negative (positive) PV advection to the west (east) of the downstream ridge allow the wave pattern to propagate westward relative to the basic flow (Hoskins et al., 1985). This way,  $\psi_{RW}$  reduces the eastward translation of the RWP and favors a phase locking between the TC and the upper-level wave pattern (Riemer et al., 2008). However, the negative PV advection through  $\psi_{RW}$  does not contribute to an amplification of the downstream ridge as the advection of PV is mostly directed into the western flank of the downstream ridge. The southward advection of high PV air through the anticyclonic anomaly associated with the downstream ridge extends far downstream. Thus, it potentially contributes to the initiation and amplification of the downstream trough. A dipole pattern of PV advection by  $\psi_{RW}$  centered on the TC indicates a westward movement of the TC relative to the basic flow which might further contribute to a phase locking between the upstream trough and the TC. This would coincide

with findings in idealized studies which suggested that midlatitude circulation anomalies induce a flow that attracts the TC (Scheck et al., 2011a; Scheck et al., 2011b).

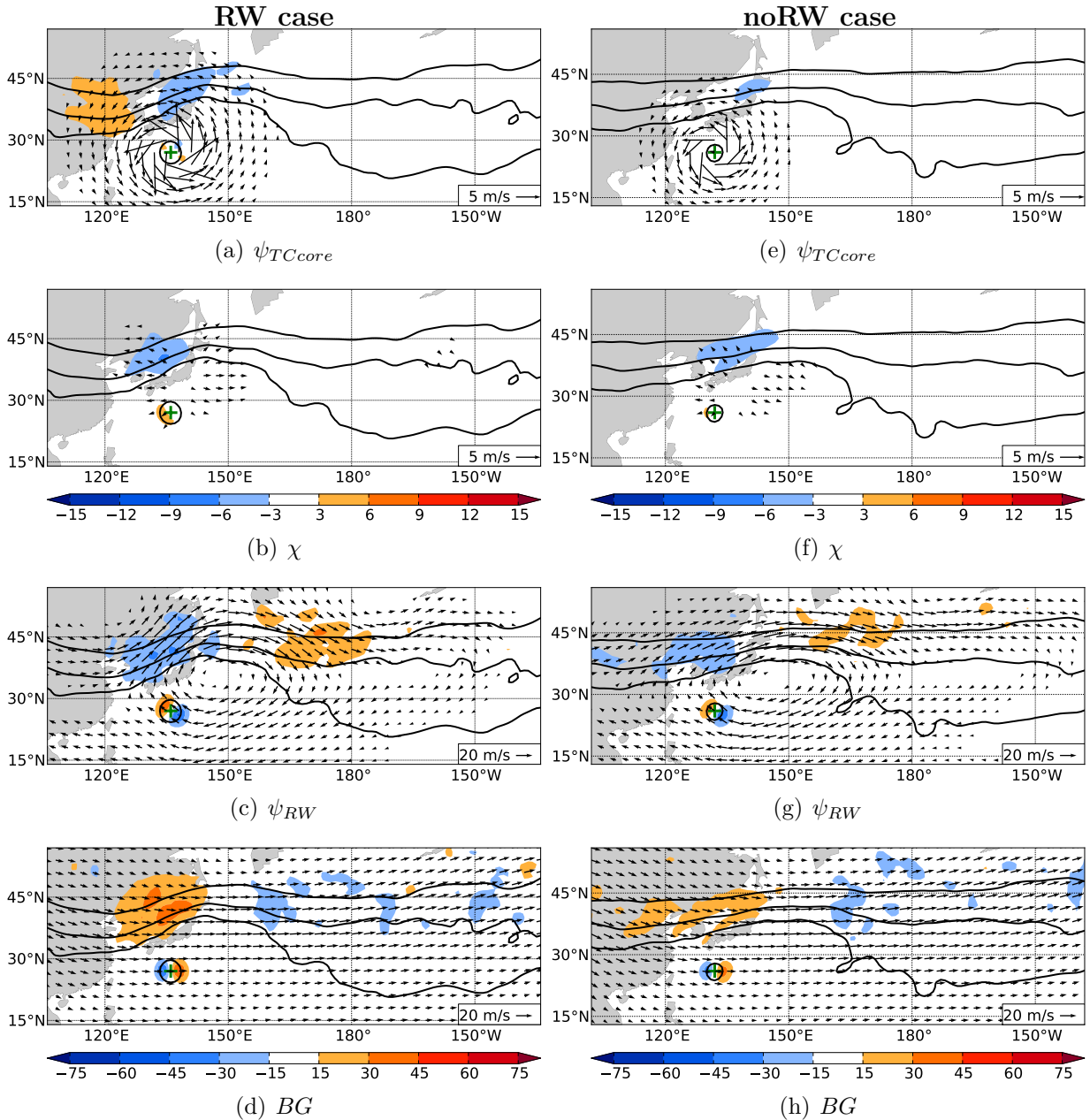


**Figure 4.15:** ET-relative composite analyses of the RW case (left column) and noRW case (right column) two days prior to ET. 330–350-K PV (contoured in black at 1, 2, 4  $PVU$ ), 330–350-K winds (vectors in  $m s^{-1}$ ) and 330–350-K PV advection (shaded in  $10^{-6} PVU s^{-1}$ ) induced by circulation anomalies as given in subcaptions. (b, f) colorbar also valid for (a, e); (d, h) colorbar also valid for (c, g). For illustrative purposes the coastlines are shown relative to the mean TC position (green cross).

The advection patterns that are related to the background flow  $\mathbf{v}_{BG}$  are typical of the downstream propagation of a Rossby wave (Fig. 4.15d, Fig. 4.15h). Positive (negative) PV advection on the western (eastern) flank of the downstream ridge suggest an eastward translation of the wave.

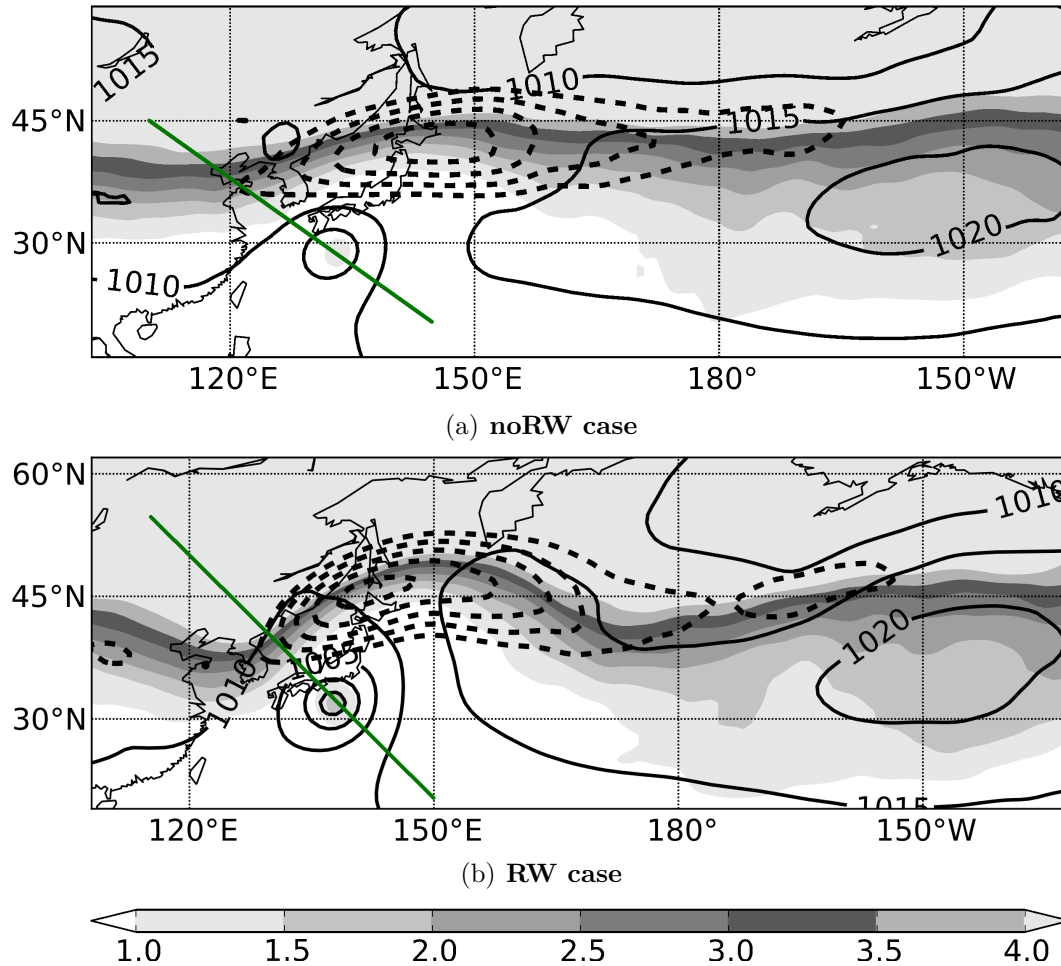


**Figure 4.16:** Same as in Fig. 4.13, but one day prior to ET.

The impact of the various circulation anomalies on the developing Rossby wave are similar to those identified in Riemer et al. (2008) for the initial interaction between a TC and a zonal midlatitude flow. The divergent winds and the winds associated with  $\psi_{TCcore}$  contribute strongest to the downstream ridge amplification. The flow associated with  $\psi_{RW}$  attracts the TC and decelerates the eastward propagation of the upstream trough which favors a phase locking between the two systems. In addition,  $\psi_{RW}$  contributes strongest to the amplification of the downstream trough. The negative PV advection by  $\psi_{TCcore}$  and  $\chi$  is weaker than in the RW case which indicates less ridge amplification over the next 24 hours in the noRW case. In both cases the PV advection by  $\psi_{TCcore}$  is weaker than in Riemer et al. (2008). A possible explanation is either an inadequate representation of the TCs in the reanalysis dataset (Schenkel and Hart, 2012) or that Riemer et al. (2008) used a more intense TC for their experiments.

### Rosby wave amplification one day prior to ET-time

The TC in the noRW case has weakened to a mean central pressure of about 1005 hPa one day prior to ET (Fig. 4.16a). This indicates that the TC has entered a region with stronger vertical wind shear, low-level baroclinicity and lower sea surface temperature. These environmental conditions are unfavorable for the maintenance of the TC structure. Furthermore, the weakening suggests that upper-level forcing for the reintensification as an extratropical cyclone is rather weak. The TC is still located  $10^\circ$  south of the midlatitude wave guide and  $20^\circ$  to the southwest of a jet streak which has intensified to values of more than  $50 \text{ m s}^{-1}$ . A vertical cross section along the green line in Fig. 4.16a indicates a remnant PV tower associated with the TC. The 1 PVU contour of the remnant PV tower extends up to 350 hPa (Fig. 4.17b). The potential temperature reveals that the TC still exhibits a warm core which shows that the system is still predominantly tropical.

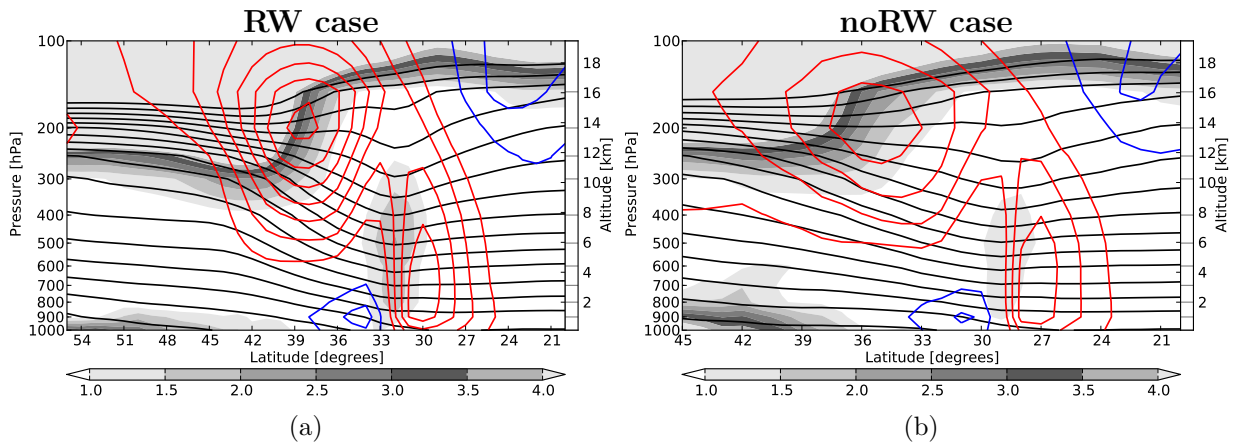


**Figure 4.17:** Cross sections of the RW case (left) and noRW case (right) one day prior to ET as indicated by thick green line in Fig. 4.16. PV (shading in  $PVU$ ), potential temperature (black lines, contoured every  $5K$ ) and horizontal wind perpendicular to cross section (colored lines, contoured every  $5 \text{ m s}^{-1}$  starting at  $\pm 5 \text{ m s}^{-1}$ ).

In the RW case the TC maintains its intensity and exhibits a surface pressure of less than 995 hPa one day prior to ET (Fig. 4.16b), i.e. the surface pressure is lower than in the noRW case composite. This coincides with the findings in Fig. 4.12 which reveals a lower best track central pressure for the RW case TCs than for the noRW case TCs. However, the central pressure derived from the best track data is considerably lower than that of the reanalysis data which can be attributed to an underestimation of the central pressure of TCs in this type of datasets (Schenkel and Hart, 2012). The PV tower associated with the TC is more intense than in the noRW case. The 1 PVU contour of the remnant PV tower extends up to 250 hPa (Fig. 4.17a). The warm core of the TC as indicated by the dip of the isolines of potential temperature even extends up to 150 hPa. The midlatitude wave pattern has strongly amplified and is dominated by a deep trough upstream of the TC and a strong ridge directly downstream (Fig. 4.16b). The southerly flow that is associated with the remarkable upstream trough extends down to about 600

hPa (Fig. 4.17a). The reduction of this southerly flow between 600 and 300 hPa to the west of the TC as well as the asymmetric TC circulation indicate that the wind fields associated with the trough and the TC impact each other. The upper-level southerlies are stronger in the RW case than in the noRW case which leads to a further northward displacement of the TC in the RW case.

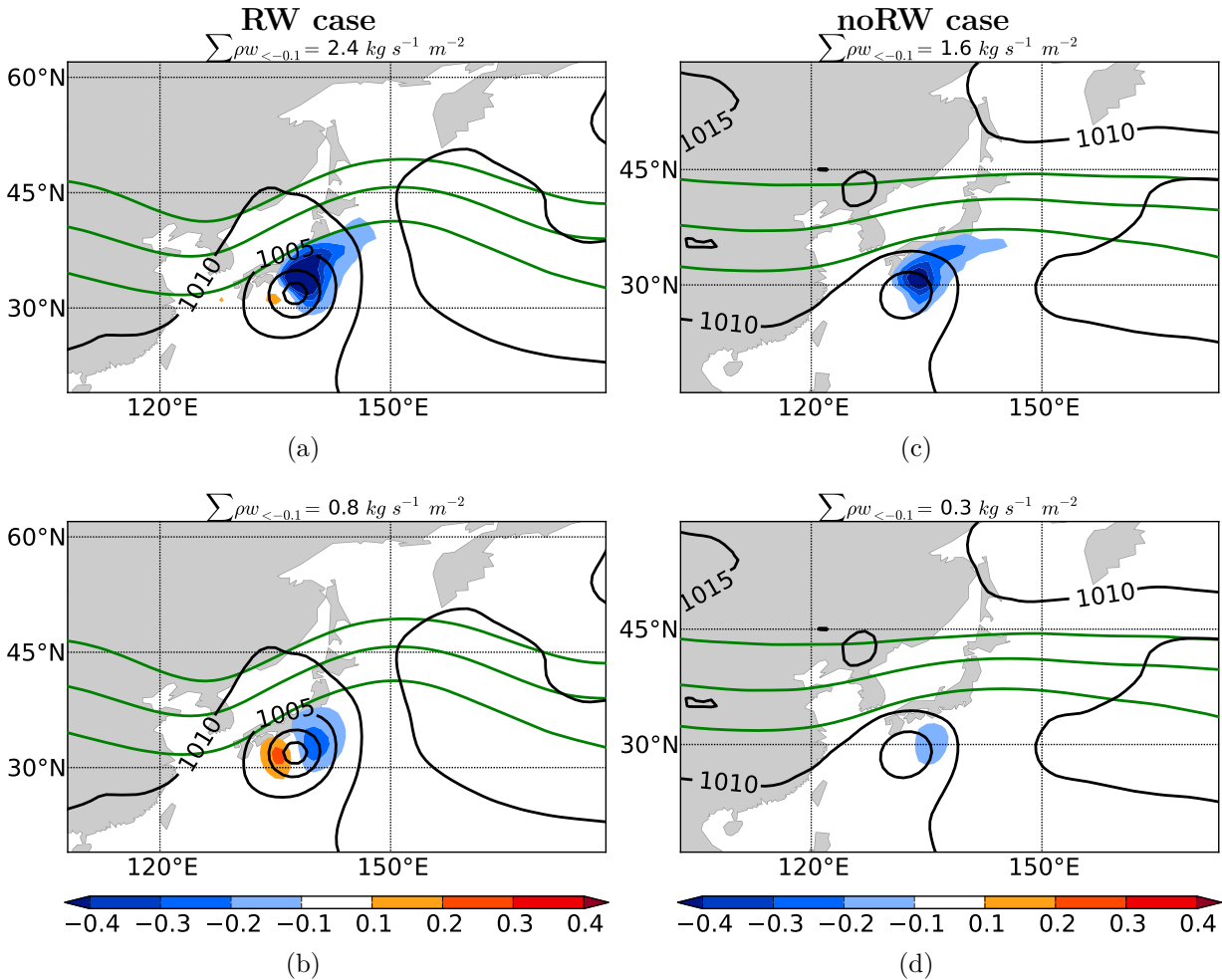


**Figure 4.18:** ET-relative composite analyses of the RW case (left column) and noRW case (right column) two days prior to ET. (a, c) 700 hPa vertical motion and (b, d) 700 hPa QG vertical motion (shaded  $Pa\ s^{-1}$ ), 250 hPa geopotential (green contours,  $1500\ m^2\ s^{-2}$  intervals) and mean sea level pressure (black contours in  $hPa$ ). For illustrative purposes the coastlines are shown relative to the mean TC position. The title of each plot gives the upward vertical mass flux.

The TC position ahead of a trough and in the entrance region of the midlatitude jet indicates a favorable position for an extratropical re-intensification through QG forcing of vertical motion. The QG forcing diagnostics (section 3.5) show QG forcing for ascent to the east of the cyclone center (Fig. 4.18b). This forcing can be attributed to warm air advection at low-levels through the TC circulation and to differential vorticity advection ahead of the upstream trough. The QG ascent in the RW case, is considerably more intense

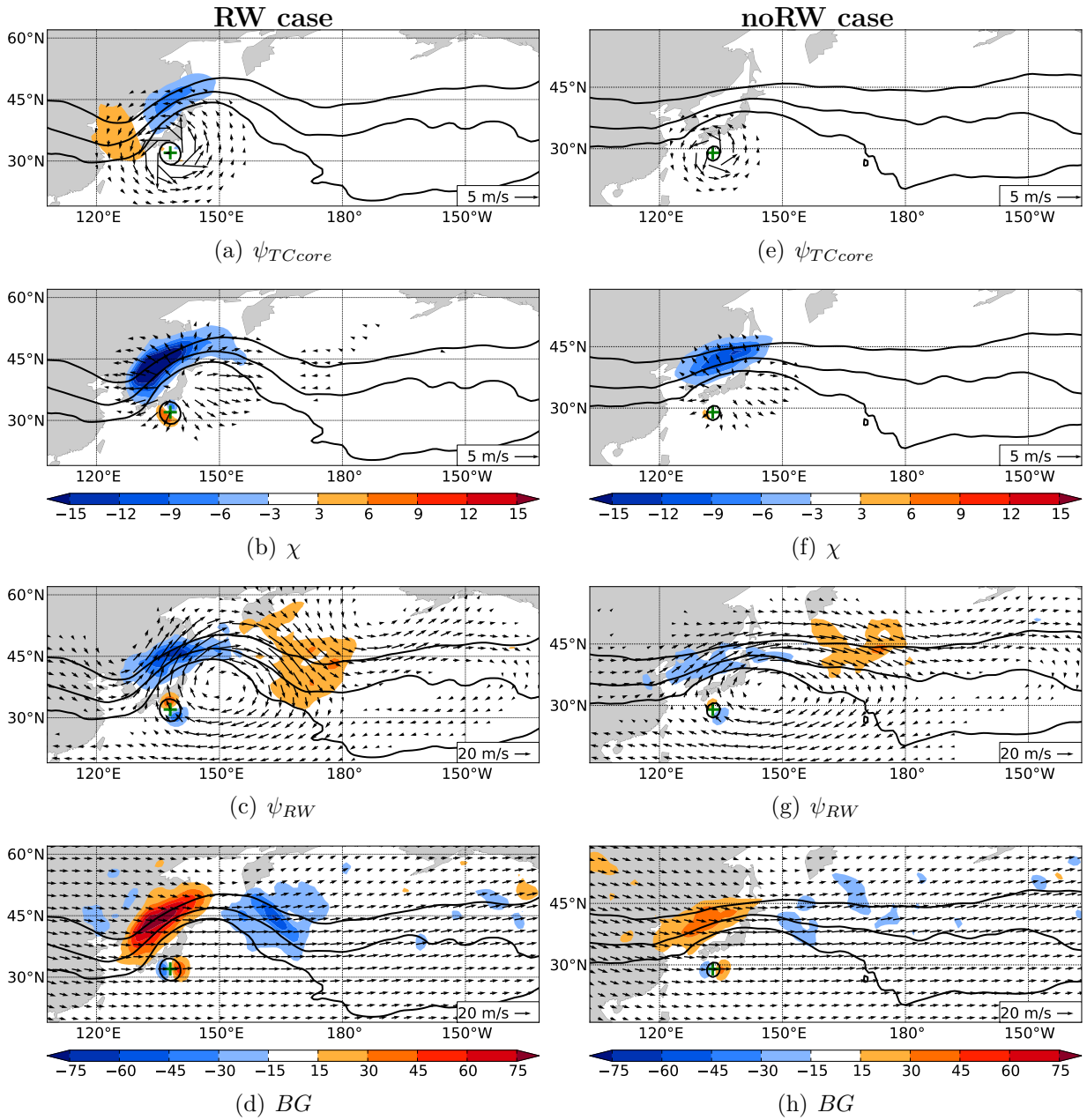


**Figure 4.19:** Same as in Fig. 4.15, but one day prior to ET.

than in the noRW case (Fig. 4.18d) which can be attributed to both a stronger low-level cyclonic TC circulation and a more pronounced upper-level trough.

A dipole pattern characterizes the PV advection through  $\psi_{TCcore}$  in the RW case 24 hours prior to ET (Fig. 4.19a). The magnitude of the advection intensified in the RW case due to a stronger midlatitude PV gradient and weakened in the noRW case due to a less intense cyclonic circulation (Fig. 4.19e). In the RW case, the negative PV advection by the divergent wind and that associated with  $\psi_{TCcore}$  peaks on the western flank of the downstream ridge. Thus, it amplifies the ridge remarkably to the west of its axis and

hinders the eastward movement of the upstream trough at the same time. Both the PV advection through  $\psi_{RW}$  (Fig. 4.19c) and that associated with  $\chi$  (Fig. 4.19b) intensified significantly and dominate the negative PV advection. Thus, negative PV advection through  $\chi$  and  $\psi_{RW}$  into the crest of the ridge contribute strongest to the remarkable ridge amplification in the RW case composite. In addition, the divergent winds contribute to an intensification of the jet streak on the western flank of the downstream ridge through upper-level frontogenesis. The sum of the negative PV advection through  $\psi_{RW}$  and  $\chi$  exhibits values of  $30 \cdot 10^{-6} \text{ PVU s}^{-1}$  in the crest of the ridge. Under the assumption that this is the average advection over a 24 hour period and estimating the PV gradient with  $7 \cdot 10^{-6} \text{ PVU m}^{-1}$  in that region, the 2 PVU contour would shift northward by approximately 370 km. This rather rough estimate is close to the observed  $4^\circ$  northward deflection of the 2 PVU contour over the next 24 hours. Thus, we conclude that diabatic effects that lead to a PV reduction at upper-levels are less important than the dynamical effects. The contributions to the ridge amplification through  $\chi$  and  $\psi_{RW}$  are much weaker in the noRW case (Fig. 4.19f, Fig. 4.19g).

Quasi-geostrophic forcing diagnostics enable us to assess the contribution of QG vertical motion to the total vertical motion and to the upper-level divergent wind field. The computation of the upward vertical mass flux at 700 hPa suggests that about one third of the total mass flux in the RW case (Fig. 4.18a) can be attributed to vertical motion through QG forcing (Fig. 4.18b). For continuity reasons, we expect that the contribution to upper-level divergence through QG ascent reaches a similar magnitude. The QG upward mass flux in the noRW case (Fig. 4.18d) is only one fifth of the total vertical mass flux (Fig. 4.18b). Hence, the vertical motion of the ET system in the noRW case is mostly convectively driven and QG vertical motion has only a minor contribution of the divergent outflow.

The positive PV advection through  $\psi_{RW}$  increased significantly east of the downstream ridge in the RW case due to a stronger northward wind component on the eastern flank of the upper-level anticyclone (Fig. 4.19c). This suggests that positive PV advection through  $\psi_{RW}$  has a major contribution to the deepening of the downstream trough. The deepening of the downstream trough characterizes the downstream development which may be associated with a cyclogenesis event over the central Pacific ahead of this downstream trough. The maximum of the positive PV advection is twice as strong as in the noRW case so that we expect a stronger trough intensification in the RW case. The advection pattern through  $BG$  reveals the downstream advection of the ridge-trough couplet in both cases (Fig. 4.19d, Fig. 4.19h).

### Rossby wave amplification at ET-time

The differences between the two cases become most evident at ET-time. In the noRW case the TC is located  $15^\circ$  southwest of a jetstreak that exceeds values of  $55 \text{ m s}^{-1}$  (Fig. 4.20a). Except for a weak downstream ridge, the midlatitude flow is nearly zonally oriented. An extratropical reintensification of the TC can not be observed as the core pressure of the

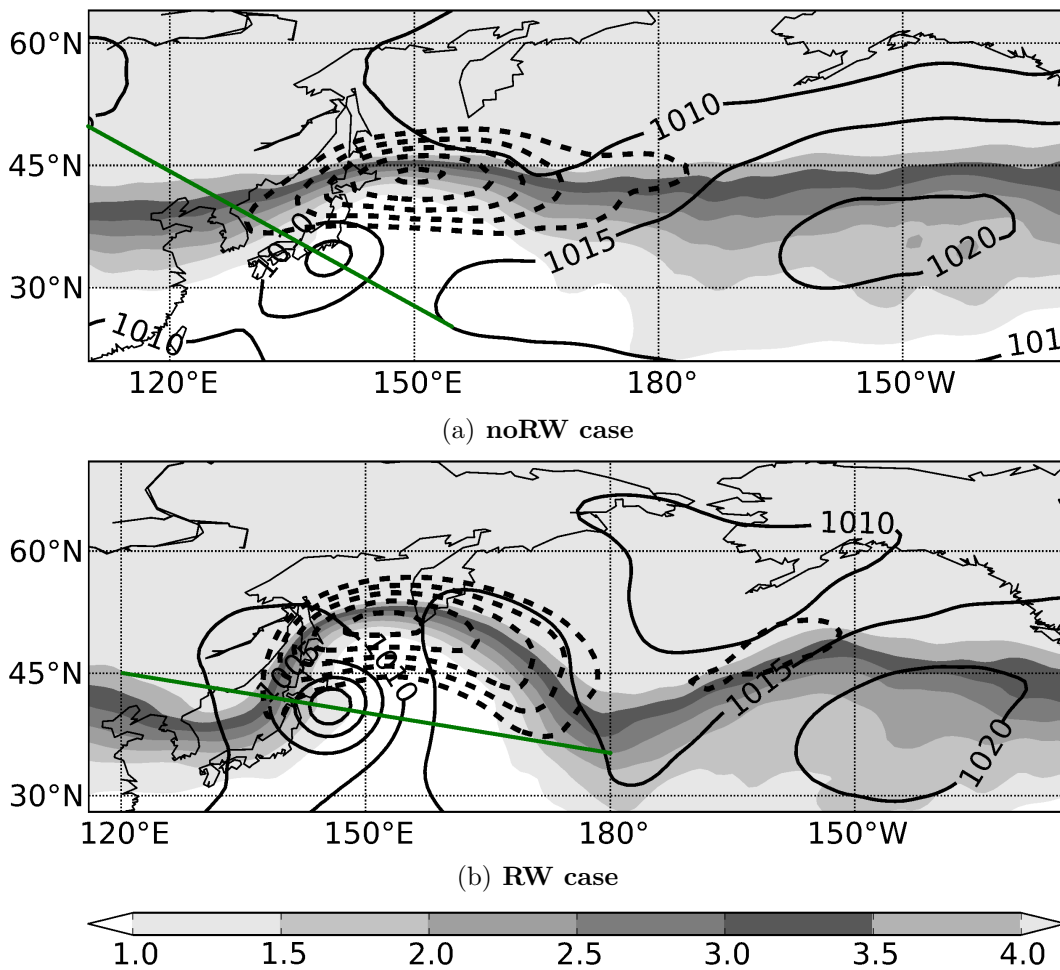


**Figure 4.20:** Same as in Fig. 4.13, but at ET-time.

system exhibits a constant value of about 1005 hPa. The PV tower of the transitioning TC has weakened further and hardly reaches the 500 hPa level (Fig. 4.21b). However, a warm core structure is still visible. Interestingly, the warm core seems to tilt eastward with height. This could be related to a strong westerly shear which separates the upper-level warm core from the low-level PV tower. In the RW case the TC keeps its intensity of about 995 hPa and increases slightly in size (Fig. 4.20b). At ET-time, the surface pressure is relatively close to the mean central pressure derived from the best track data (Fig. 4.12c) which suggests a better representation of the TC intensity in the analyses than at earlier times. The TC is located about  $10^\circ$  farther north than the TC in the noRW case. This indicates a phase locking between the ET system and the meridional midlatitude flow. A vertical cross section supports clearly this statement (Fig. 4.21a) since the 0.5 PVU isosurface of the TC related PV tower and the upstream trough have connected. The remnant TC still exhibits a warm core structure that is slightly out of phase with the PV distribution, but which does not tilt eastward with height. Both the northerly flow west of the TC and the southerly flow east of the TC indicate an interaction with the upper-level midlatitude flow. The resulting circulation indicates a westward tilt with height which is typical of a developing midlatitude baroclinic system. The lower core pressure than in the noRW case indicates an

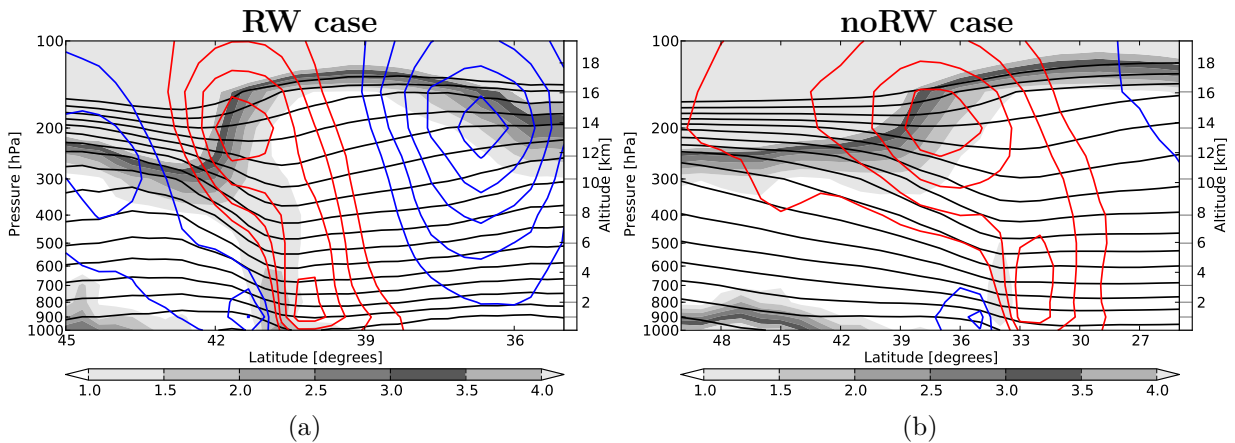


**Figure 4.21:** Same as in Fig. 4.17, but at ET-time along thick green line in Fig. 4.20.

extratropical reintensification of the system potentially through upper-level forcing. This circulation configuration strongly resembles the northwest pattern as identified by Harr and Elsberry (2000).

The fact that the wind speed in the jetstreak is similar in both cases is quite remarkable (Fig. 4.20). In both scenarios, the outflow of the ET system seems to strengthen the midlatitude PV gradient and the jet in the crest of the ridge. There, the maximum jet strength exceeds in both cases  $55 \text{ m s}^{-1}$ . However, the strengthening of the PV gradient and the jet amplification occur farther downstream in the noRW case. The results suggest that a remarkable jet amplification is not necessarily followed by a downstream Rossby wave development. These findings coincide with results from Grams et al. (2013a). A relocation of Typhoon Jangmi (2008) in full-physics simulations did not impact the magnitude of the jet streak but led to a completely different downstream development.

The midlatitude trough downstream of the primary ridge deepened further in the RW case. A jet streak formation on the eastern flank of this trough indicates the dispersion of energy into downstream regions. A further ridge amplification can be seen over the Gulf of Alaska as part of the Rossby wave dispersion.

In the RW case, the PV structure and the advection patterns indicate a wrap up of the upstream trough as  $\psi_{TCcore}$  advects low-PV air upstream and high-PV air downstream (Fig. 4.22a).  $\psi_{TCcore}$  equally contributes to both positive and negative PV advection on the eastern flank of the trough even though the magnitude of the PV advection is much weaker than during the previous 24 hours. In the noRW case, the upper-level  $\psi_{TCcore}$  does not contribute to the PV advection between 330–350 K (Fig. 4.22e) as its vertical extent is limited to the lowest 500 hPa of the troposphere (Fig. 4.21b). This indicates that the remnant TC core weakened significantly under the influence of strong vertical wind shear and in a region with weak upper-level forcing for vertical motion. QG forcing diagnostics exhibit weak QG upward motion to the east of the weak TC and thus support the previous statement (Fig. 4.23). The QG vertical motion reaches maximum values of

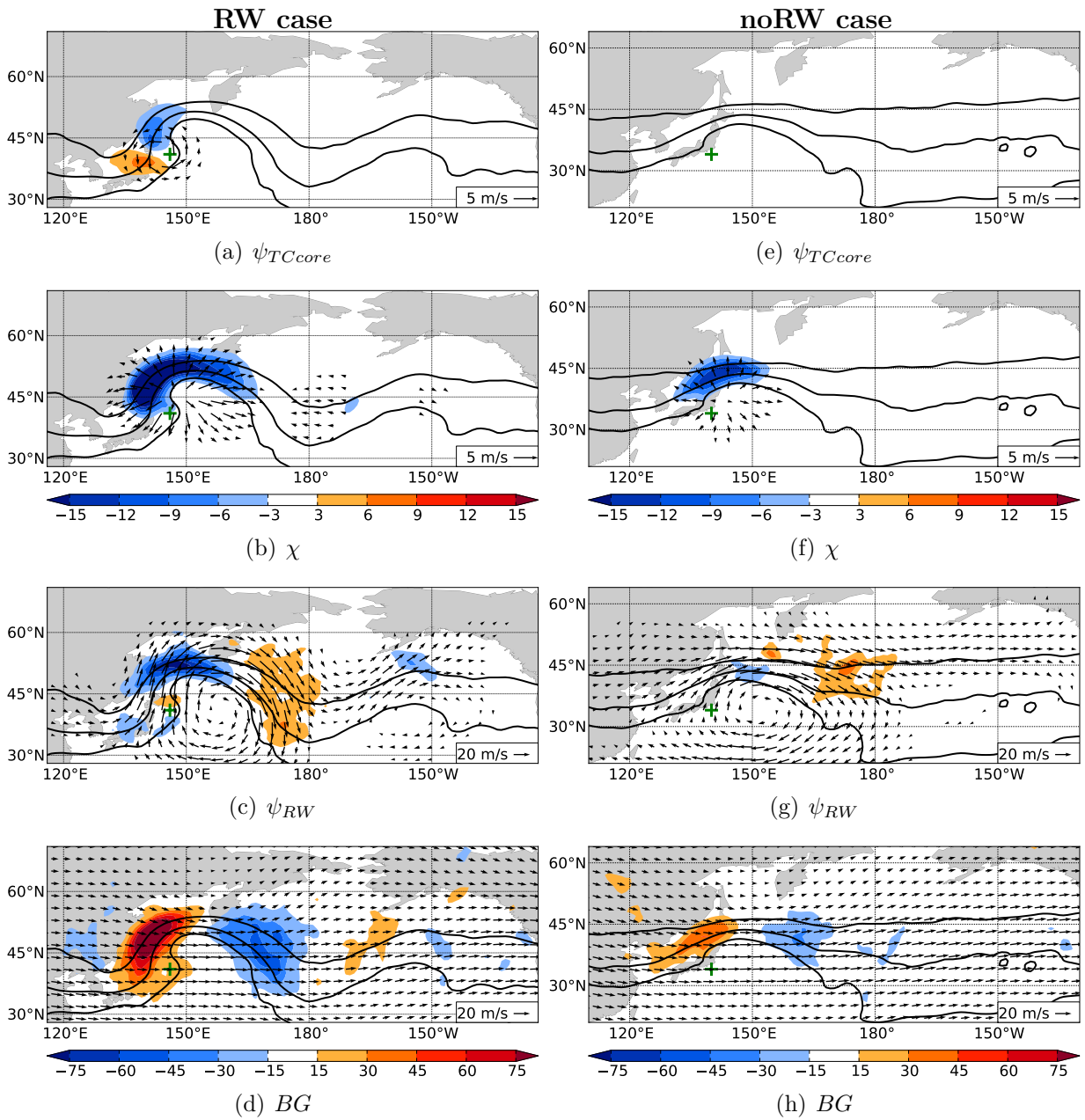


**Figure 4.22:** Same as in Fig. 4.15, but at ET-time.

about  $-0.2 \text{ Pa s}^{-1}$  whereas the total vertical motion (Fig. 4.23c) exceeds  $-0.4 \text{ Pa s}^{-1}$  in vast areas. Thus, the ascent of the transitioning TC in the noRW case is mostly convectively driven.

Negative PV advection through  $\chi$  (Fig. 4.22b) and  $\psi_{RW}$  (Fig. 4.22c) still contributes to the ridge amplification in the RW case. Archambault et al. (2013) concluded that the divergent outflow of the TC plays an important role in the amplification of a Rossby wave. The QG forcing diagnostics allow us to quantify whether the upper-level divergence is purely related to the convectively driven TC outflow or to vertical motion

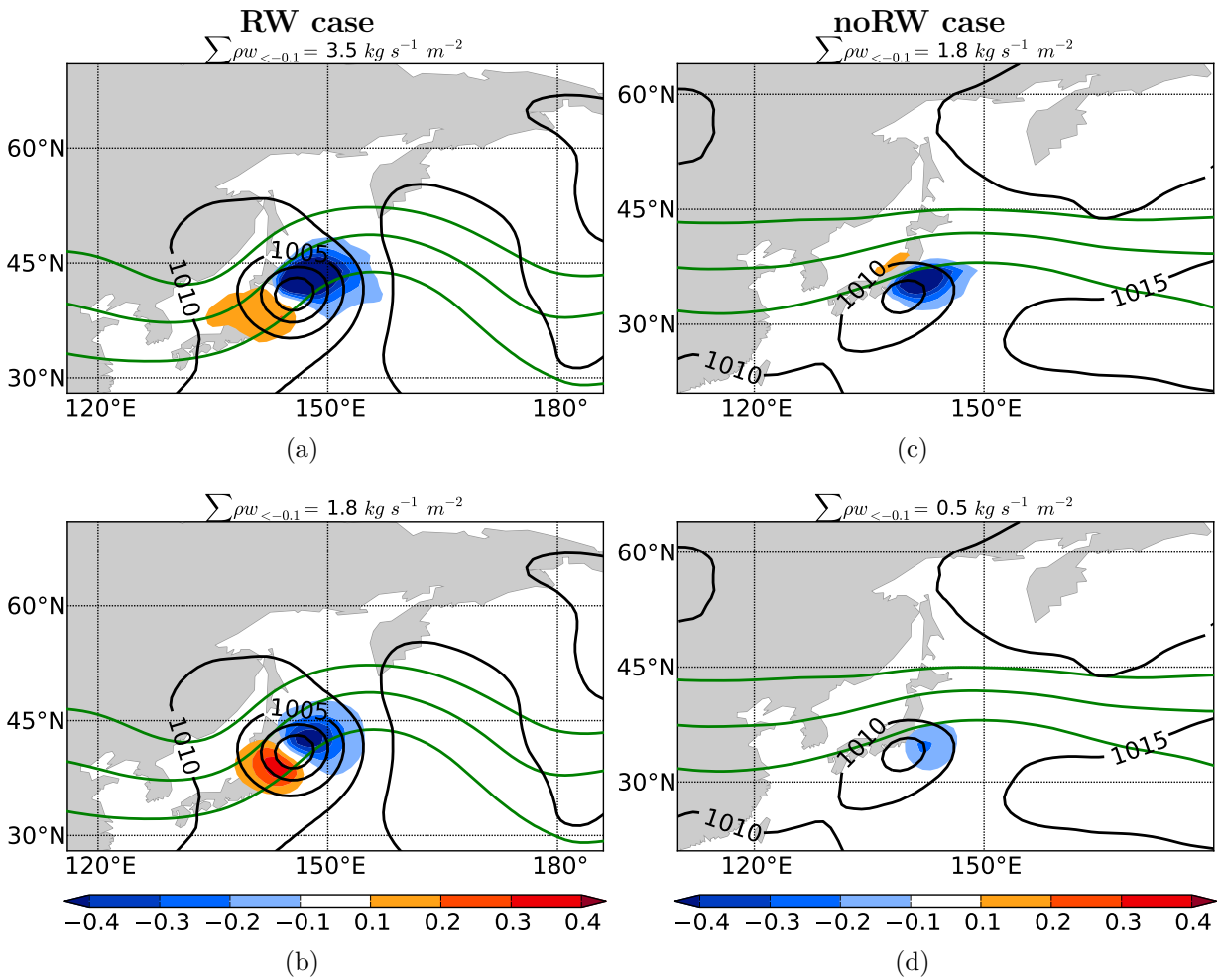


**Figure 4.23:** Same as in Fig. 4.18, but at ET-time.

that is forced through QG dynamics. In the RW case, QG ascent (Fig. 4.23b) is collocated with a region of the total upward motion to the east of the TC (Fig. 4.23a). The upward mass flux which was computed from the QG vertical motion and from the total vertical motion suggests that 50% of the upward mass flux can be attributed to QG dynamics. For continuity reasons we argue that QG vertical motion contributes by about 50% to the upper-level divergent flow. Thus, the divergent outflow of the TC plays an important role in the amplification of the downstream ridge, but equally important is upper-level divergence due to quasi-geostrophically forced vertical motion.

The downstream ridge and its associated anticyclonic circulation strengthened over the two day period in the RW case. The resulting northward wind component on its eastern flank advects high-PV air southward (Fig. 4.22c) and thus contributes to the deepening of the trough further downstream. The southward advection of high-PV air is less extended in the noRW case (Fig. 4.22g). This results from a weaker northerly flow in that region, but not from a weaker PV gradient. The advection patterns through *BG* indicate a downstream translation of the Rossby wave in both scenarios (Fig. 4.22d, Fig. 4.22h).

The composites of mean sea level pressure suggest that the TCs in the RW case and noRW case exhibit different tracks (cf. Fig. 4.13, Fig. 4.16, Fig. 4.20). A comparison of the best tracks in a recurvature relative framework confirms this impression. Most of the TCs in the noRW case make a quite sharp recurvature and move eastward (Fig. 4.24b). In the RW case, the TC tracks exhibit a stronger meridional component (Fig. 4.24a). This indicates that in the case of a Rossby wave development the TC is locked with the midlatitude meridional flow of an upstream trough. A similar track behavior has been described by Harr and Elsberry (2000) (their Fig. 2). In their northeast pattern the TCs moved eastward without an upstream trough due to a strong zonal flow, which is similar to the noRW case. The RW case is similar to the northwest pattern in which the TCs followed a rather meridional track. The TCs in the RW case cross the 2 PVU isoline (Fig. 4.24a). Assuming that the 2 PVU isoline marks the midlatitude jet region, Fig. 4.24a indicates that the transitioning TCs cross the midlatitude jet stream which is characteristic of the life-cycle of a midlatitude cyclone.

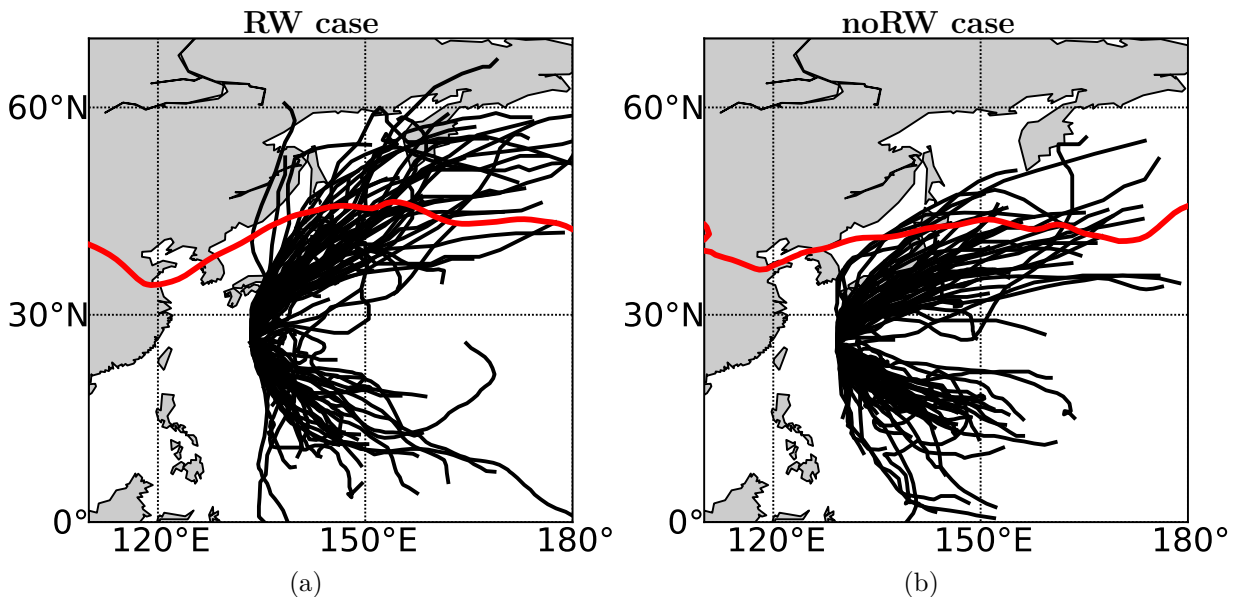


**Figure 4.24:** Best tracks of TCs in the RW case (a) and in the noRW case (b) in a recurvature-relative framework. 330–350-K PV (contoured in red at 2 PVU). For illustrative purposes the coastlines are shown relative to the mean TC position.

### 4.2.3 The role of warm conveyor belts in the amplification of Rossby waves during extratropical transition

Several structural characteristics develop during the ET of TCs that are characteristic of midlatitude cyclones. These features include fronts, dry intrusions and regions of isentropic, slantwise ascent which are comparable to WCBs in midlatitude cyclones (Section 2.4.2). Latent heat release due to condensational heating within these slantwise ascending air

masses produces a positive temperature anomaly in the mid-troposphere. The modification of the static stability leads to the development of a positive PV anomaly below the level of maximum heating and to the development of a negative PV anomaly above the level of maximum heating. The WCB-like ascent transports the diabatically generated low PV air into the upper troposphere. The resulting negative upper-level PV anomaly may distort and/or strengthen the midlatitude wave guide (Grams et al., 2011; Schemm et al., 2013). We estimate the importance of diabatic processes for the downstream ridge amplification in the following by investigating the structure of the WCB-like ascent. The WCB-like features were identified by computing trajectories from 6 hourly ERA-Interim reanalyses at  $1^\circ$  horizontal resolution. The trajectory data were kindly provided by Erica Madonna. We identified trajectories as TC related WCB-like features when they

- ascended at least 600 hPa within 48 or less hours (Madonna et al., 2014)
- had their origin in a box of  $10^\circ \times 10^\circ$  around a TC (according to best track data)
- exhibited a potential temperature between 330 to 350 K at the final time

In order to distinguish between particles that ascended within the inner-core of the TC and particles that ascended in the WCB-like structure we introduced an additional baroclinicity criterion. First, we identified the six hour time interval of the strongest pressure change (ascent) along the trajectory. Second, we computed the gradient of equivalent potential temperature at 850 hPa between the location of the air parcels prior to the strongest ascent and after the strongest ascent. To account for the temporal change in equivalent potential temperature we computed the gradient between these coordinates twice: at the beginning of the strongest ascent and at the end of the strongest ascent. Our baroclinicity criterion is fulfilled if the equivalent potential temperature gradient exceeds  $3 \text{ K } 100 \text{ km}^{-1}$  at one of these times. We investigated all trajectories which started in a 48 hour period prior to the time of interest (here at six hourly intervals from two days prior to ET to ET-time) and which fulfilled the criteria.

The number of trajectories that fulfill the baroclinicity criterion increases from two days prior to ET until ET-time (Fig. 4.25). Two days prior to ET, twice as many trajectories do not fulfill the baroclinicity criterion than fulfill it. Only small differences between the noRW and RW cases are evident at that time. The number of trajectories that do not fulfill the baroclinicity criterion increase approximately linearly in the RW case as well as in the noRW case until ET-time. The increase with time suggests that air masses ascend in a larger area during ET than two days prior to ET. Previous studies suggest that reanalyses show a better representation of ET systems than of TCs as ET systems expand in size and are thus better resolved (Röbke et al., 2004; Schenkel and Hart, 2012). Schenkel and Hart (2012) could show that the intensity of TCs at later stages of their life-cycle is much better resolved in reanalyses than the intensity during their intensification or peak intensity period. Thus, it is difficult to clarify whether the increasing number of trajectories is purely related to the structural changes of the TC during ET or to a better representation of the ET system than of the TC in the reanalyses.

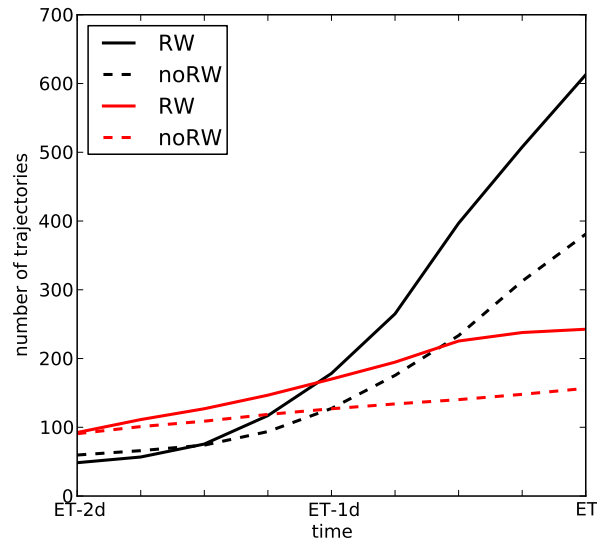


**Figure 4.25:** Mean number of trajectories per ET event that fulfill the baroclinicity criterion (black) and that do not fulfill the criterion (red) for the RW and noRW case.

With around 240 (150) trajectories per ET event in the RW (noRW) case that do not fulfill the baroclinicity criterion, the differences between both cases become evident at ET-time. The differences reveal that ascent occurs in the RW case over a larger region than in the noRW case. The number of trajectories that fulfill the baroclinicity criterion grows approximately exponentially between 36 to 18 hours prior to ET. The number of trajectories that fulfill the criterion equals the number of trajectories that do not fulfill the criterion for the first time around one day prior to ET. Finally, around 620 trajectories per event fulfill the baroclinicity criterion in the RW case at ET-time. 380 trajectories ascend baroclinically per event in the noRW case. The remarkable temporal increase of trajectories that fulfill the criterion indicates a change of the characteristics of ascent. Two days prior to ET most trajectories ascend in a rather barotropic environment. Ascent in a baroclinic environment starts to dominate from one day prior to ET. The higher number of baroclinically ascending trajectories reveals that WCB-like ascent contributes more strongly to upper-level divergence and hence to the wave amplification than ascent within the TC. The fact that more trajectories ascend in the RW case than in the noRW case coincides with the previous findings in this section which revealed a stronger upward mass flux and a stronger divergent outflow in the RW case than in the noRW case. The lower number of trajectories in the noRW case indicates less baroclinic conversion which has implications for the generation of kinetic energy as will be discussed in section 4.2.4.

We investigated the spatial distribution of the WCB-like trajectories by gridding the trajectory start and end points on a regular grid with  $1^\circ$  horizontal resolution. We considered only those trajectories that ascended at least 600 hPa, that fulfilled the baroclinicity criterion and which reached an isentropic level between 330 to 350 K. The start points are the initial coordinates of trajectories that fulfilled these criteria. Accordingly, the end points are those coordinates which were reached by all parcels that started 48 to 6

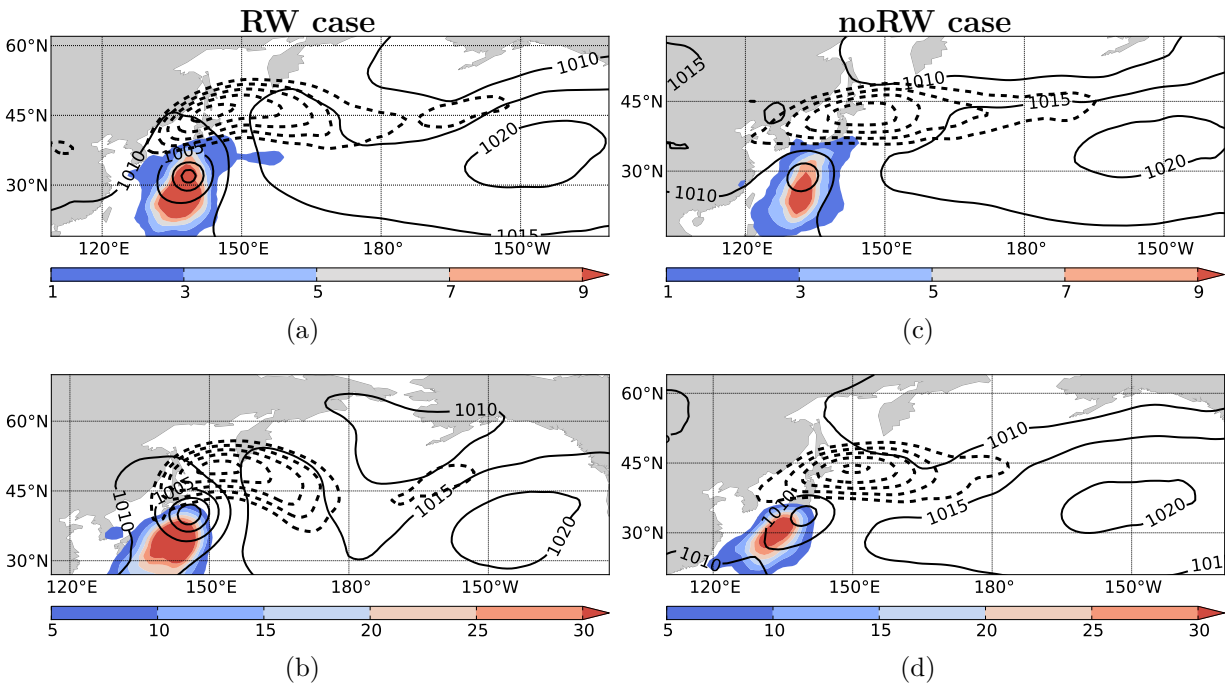


**Figure 4.26:** Number of trajectory start points per case and gridpoint in the RW case (a, b) and in the noRW case (c, d). (a, c) one day prior to ET; (b, d) at ET-time. Note different scaling of colorbar. Mean sea level pressure (solid black contours in  $hPa$ ) and 330–350-K wind speed (dashed contours, interval  $5 m s^{-1}$  starting at  $35 m s^{-1}$ ).

hours prior to the time of interest (e.g. one day prior to ET or at ET-time). Most of the trajectories that meet the criteria start to the south of the TC (Fig. 4.26a; Fig. 4.26c) and end at upper-levels to the north of the TC one day prior to ET (Fig. 4.27a; Fig. 4.27c). In the RW case as well as in the noRW case, the trajectories end most frequently immediately north of the TC and along the western flank of the downstream ridge. This coincides well with the structure of the divergent winds which indicate a strong upper-level divergence in this region. The higher density of trajectory end points in the RW case coincides with a stronger upward mass flux and stronger divergent winds than in the noRW case. Furthermore, the location of the trajectory end points suggests that diabatic processes along the trajectories could support a further amplification of the downstream ridge as they transport low PV air into the crest of the ridge. The collocation of the trajectory end points and the jet streak indicates that air parcels are transported into remote downstream regions after they ascended in the ET system. The split distribution on the eastern flank of the downstream ridge in the RW case indicates that air parcels are not only transported into the midlatitudes, but also back into the tropics. This transport of air parcels back into the tropics is indicative of a strong anticyclonic outflow anomaly.

At ET-time, the spatial distribution of trajectory start points (Fig. 4.26b; Fig. 4.26d) and end points (Fig. 4.27b; Fig. 4.27d) is similar. The air parcels that ascend WCB-like start to the southeast of the TC and end to the north of the TC, but also upstream of the TC. This indicates that the ascending air parcels turn in both directions,

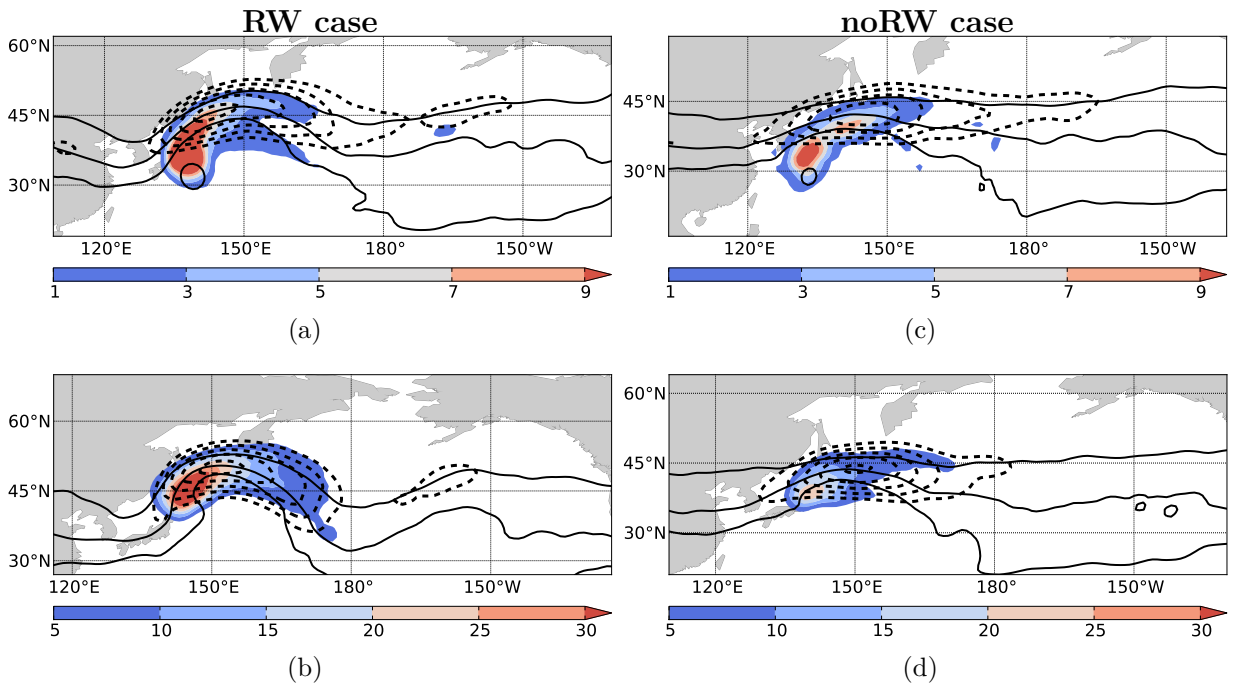


**Figure 4.27:** Number of trajectory end points per case and gridpoint in the RW case (a, b) and in the noRW case (c, d). (a, c) one day prior to ET; (b, d) at ET-time. Note different scaling of colorbar. 330–350-K PV (solid black contours at 1, 2, 4  $PVU$ ) and 330–350-K wind speed (dashed contours, interval  $5 m s^{-1}$  starting at  $35 m s^{-1}$ ).

cyclonically and anticyclonically, as suggested in the conceptual model of Klein et al. (2000). The air parcels that turn cyclonically may contribute to a reduction of PV upstream of the TC and in this way to the earlier mentioned wrap up of the upstream trough. The trajectories which turn anticyclonically are collocated with the jet streak and are thus transported into downstream regions. Differences between the noRW and RW case are limited mostly to the number of trajectories. This coincides with the weaker divergent winds in the noRW case.

Earlier in this section, we stated that diabatic effects are less important for the downstream ridge amplification than the dynamical effects. However, the analysis of the WCB-like ascending trajectories reveals that in the RW case considerably more diabatically generated low-PV air is transported into the downstream ridge than in the noRW case. Thus, the diabatic reduction of upper-level PV certainly has an impact on the ridge amplification. At the end of this section, we address the question whether different heating profiles along the trajectories in the RW case and in the noRW case impact the diabatic PV reduction and thus the upper-level ridge building. The potential temperature change along the trajectories allows us to estimate heating rates of the WCB-like ascent. We compare the equivalent potential temperature, heating rates and PV along the trajectories for the RW and noRW case.

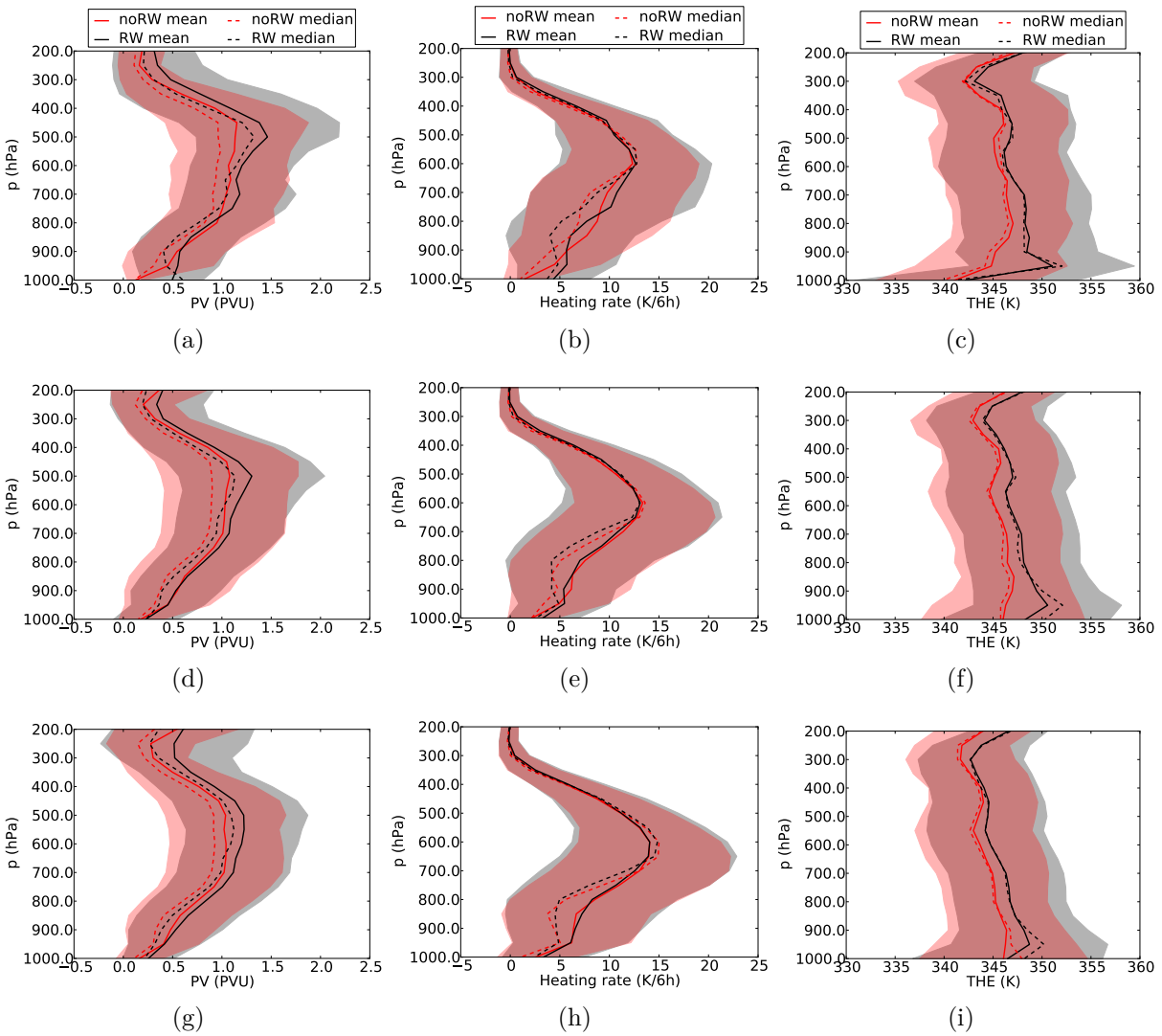


**Figure 4.28:** Vertical profiles of (a, d, g) PV ( $PVU$ ), (b, e, h) heating rate ( $K/6h$ ), (c, f, i) equivalent potential temperature ( $K$ ) along the trajectories that reached the 330 to 350  $K$  isentropic layer (a, b, c) two days prior to ET, (d, e, f) one day prior to ET, (g, h, i) at ET-time. Dashed lines represent the median, solid lines the mean for the RW case (black) and the noRW case (red). The shading marks the mean  $\pm$  one standard deviation for the RW case (gray) and the noRW case (red). Trajectories were interpolated on equally spaced pressure levels.

Vertical profiles of PV along the trajectories exhibit several characteristics that indicate ascent in a region of steady latent heating from two days prior to ET to ET-time. Trajectories that start at 1000 hPa exhibit initially in both cases mean PV values of 0 to 0.5  $PVU$  (Fig. 4.28 a, d, g). The heating profiles exhibit a very similar profile in the RW and in the noRW case. Thus, we state that different heating profiles along the trajectories in the RW case and in noRW case do not contribute significantly to a different outcome of the upper-level flow. At the level of maximum heating, the heating rates vary

between 5 to 20  $K/6h$  (Fig. 4.28 b, e, h) and intensify slightly until ET-time. The PV increases strongly below the level of maximum heating, i.e. between 900 to 600 hPa, and reaches mean values of about 1  $PVU$  in the midtroposphere. In a Eulerian sense, the diabatically produced PV is advected upward adiabatically so that high PV air extends through the whole mid-troposphere. According to the standard deviation, the PV exceeds 2  $PVU$  in 34% of the RW case trajectories at 500 hPa. It should be noted here, that the maximum PV values occur above the level of maximum heating. We assume that this can be attributed to the averaging process or to the implicit retrieval of the heating rate which was computed as the potential temperature change along a trajectory. The increase of equivalent potential temperature in the lowest 900 hPa indicates moisture uptake in the boundary layer (Fig. 4.28 c, f, i). The increase of equivalent potential temperature is considerably higher in the boundary layer in the RW case than in the noRW case from two days prior to ET to ET-time. Above the boundary layer the approximate conservation of equivalent potential temperature indicates slantwise ascent along moist isentropes.

Above the level of maximum heating, i.e. between 450 to 300 hPa the PV along the trajectories decreases rapidly to values which are close to the initial values in the lower troposphere. As this low PV air is transported vertically into the upper-troposphere it potentially contributes to the downstream ridge amplification. This becomes obvious by a comparison of Fig. 4.27 and Fig. 4.28. Fig. 4.28 a, d, g show that trajectories that reached the 330 to 350  $K$  isentropic layer exhibited upper-level PV values of 0 to 1  $PVU$ . The trajectory end points in Fig. 4.27 reveal that a remarkable number of trajectory endpoints are located to the north of the 1  $PVU$  isoline, i.e. in a region of higher ambient PV values. Thus, the trajectories contributed to a reduction of the upper-level PV and hence to an amplification of the downstream ridge.

#### 4.2.4 Rossby wave amplification from an eddy kinetic energy perspective

The previous subsections identified mechanisms which are relevant for the initial Rossby wave amplification from a PV perspective. In particular, the divergent flow associated with WCB-like ascending air masses in the vicinity of the ET system contributes to the wave amplification. From an energetics perspective, the slantwise WCB-like ascent of warm air masses is related to the baroclinic conversion from available potential energy into eddy kinetic energy ( $K_e$ ). This baroclinic generation of  $K_e$  contributes to an intensification of the energy centers on the flanks of troughs and ridges and thus amplifies the upper-level wave pattern (section 3.4). We investigated this amplification and the further downstream development by computing composites of  $K_e$  budgets according to equation 3.25 for the RW and noRW case from ERA-Interim reanalyses. This type of analysis allows us to identify regions which are relevant for the generation of  $K_e$  and hence for the midlatitude flow amplification. The vertically integrated form of the  $K_e$  tendency equation has the advantage that it condenses the three-dimensional flow evolution to two dimensions. The  $K_e$  budget analysis has been successfully applied to describe characteristics of downstream

development associated with TC - midlatitude flow interactions (Harr and Dea, 2009; Keller et al., 2014). These studies showed that TCs may act as an additional  $K_e$  source to the midlatitude flow where the  $K_e$  can progress into downstream regions. Whereas recent studies focused on a limited number of cases this is the first analysis of  $K_e$  budgets in a composite view.

### Rossby wave amplification two days prior to ET-time

Two days prior to ET the geopotential height at 250 hPa is quite zonal in the noRW case (Fig. 4.29b) whereas a wave pattern can be identified in the RW case (Fig. 4.29a). A  $K_e$  center over the western North Pacific is associated with the TC itself. A second  $K_e$  center can be found far downstream. The TCs exhibit higher  $K_e$  values in the RW case than in the noRW case which coincides with a lower mean sea level pressure of the TCs in the RW case (Fig. 4.13).  $K_e$  flux vectors emanate from the TC, indicating a total flux of  $K_e$  toward the midlatitudes. Enhanced baroclinic conversion to the north of the TCs indicates that an interaction between the TC and the primary midlatitude baroclinic zone is in progress since upward motion of warm moist air along the baroclinic zone leads to a conversion of available potential energy to  $K_e$ . The baroclinic conversion in the RW case (Fig. 4.29a) is a lot stronger than in the noRW case (Fig. 4.29b). This corresponds to a higher number of WCB-like ascending trajectories in the RW case than in the noRW case.

In both cases the baroclinically produced  $K_e$  is dispersed via a strong ageostrophic geopotential flux divergence (Fig. 4.29c, 4.29d). Negative values of the total generation of  $K_e$ , i.e. the sum of baroclinic conversion and ageostrophic geopotential flux divergence, indicate a dispersion of  $K_e$  toward the midlatitudes to the north of the TC. This dispersion is considerably stronger in the RW case (Fig. 4.29c). Ageostrophic geopotential flux convergence leads to an accumulation of  $K_e$  between the upstream trough and downstream ridge. This accumulation is stronger in the RW case (Fig. 4.29c) than in the noRW case (Fig. 4.29d) due to a stronger convergence of the ageostrophic winds between the TC outflow and the midlatitude flow. This stronger convergence of the ageostrophic winds can be attributed to a stronger divergent and TC related cyclonic upper-level flow in the RW case as identified in Fig. 4.15 (a, b). The ageostrophic geopotential flux convergence in this region contributes notably to the total generation of  $K_e$  (Fig. 4.29e, 4.29f). Finally, the  $K_e$  flux divergence in the same region indicates a transport of  $K_e$  into the downstream ridge (Fig. 4.29g). Ageostrophic geopotential flux convergence in the crest of the downstream ridge indicates the amplification of a  $K_e$  center on the eastern flank of the ridge.

### Rossby wave amplification one day prior to ET-time

The described accumulation of  $K_e$  results in the development of two additional centers of  $K_e$  in the RW case during the next 24 hours. A first midlatitude  $K_e$  center develops immediately north of the transitioning TC on the western flank of the downstream ridge

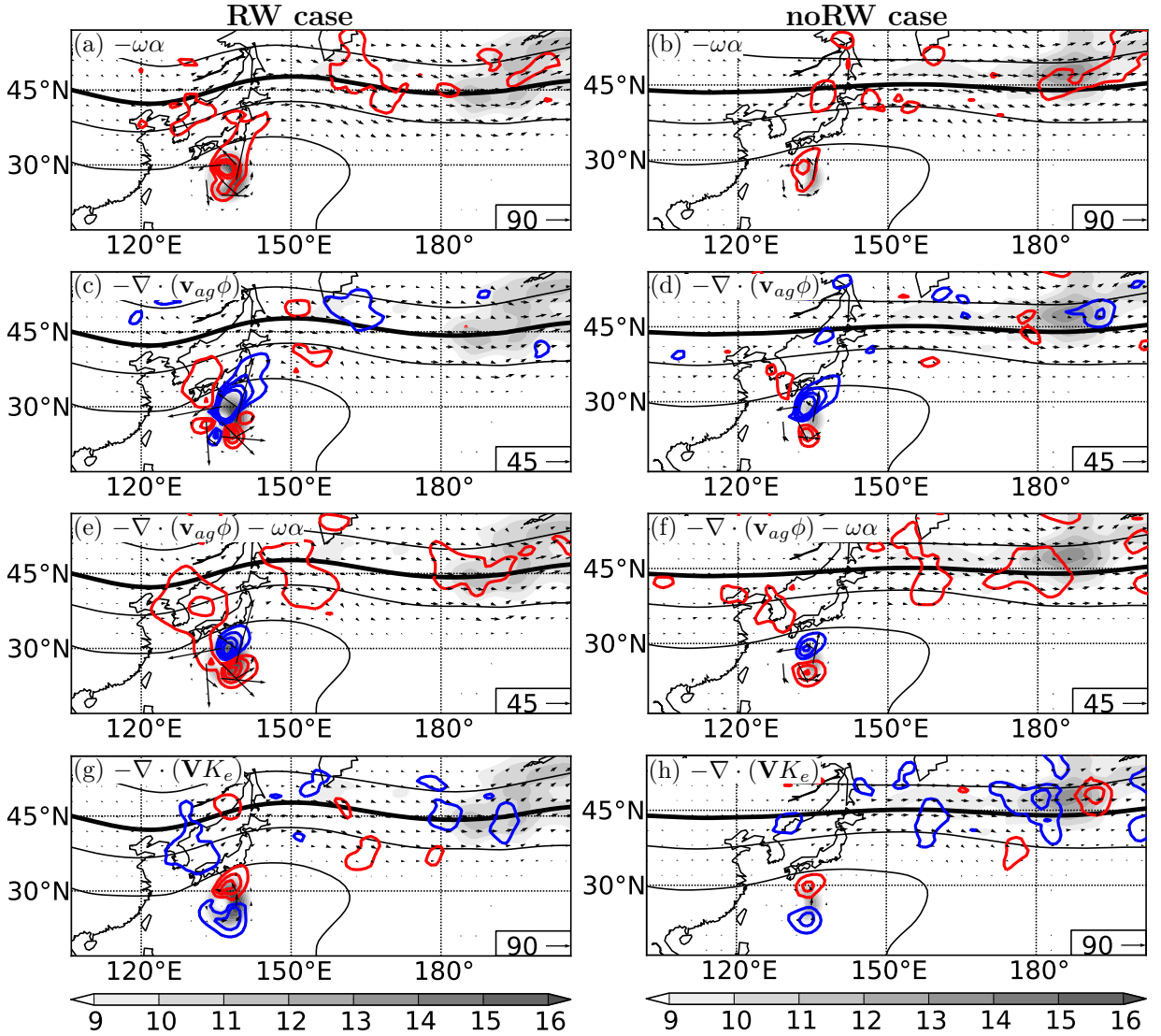


**Figure 4.29:** ET-relative composite analyses of  $K_e$  budget terms for the RW case (a, c, e, g) and the noRW case (b, d, f, h) two days prior to ET-time. Vertically averaged  $K_e$  (shaded,  $10^5 J m^{-2}$ ), vertically averaged budget terms (colored contours, contour interval  $8 W m^{-2}$ ) of baroclinic conversion (a, b), ageostrophic geopotential flux convergence (c, d), total generation of  $K_e$  (e, f) and  $K_e$  flux convergence (g, h). 200 hPa geopotential (black contours,  $2000 m^2 s^{-2}$  intervals, thick black line illustrates  $118000 m^2 s^{-2}$  isoline). (a, b) total  $K_e$  flux vectors (reference vector in lower right,  $10^6 W m^{-1}$ ), (c, d) ageostrophic  $K_e$  flux vectors (reference vector in lower right,  $10^6 W m^{-1}$ ), (e, f) ageostrophic  $K_e$  flux vectors (reference vector in lower right,  $10^6 W m^{-1}$ ) and (g, h)  $K_e$  flux vectors (reference vector in lower right,  $10^6 W m^{-1}$ ). For illustrative purposes the coastlines are shown relative to the mean TC position.

(Fig. 4.30a). A northward  $K_e$  flux suggests the transport of  $K_e$  from the TC into this first  $K_e$  center. The  $K_e$  is transported further downstream through the crest of the ridge toward its eastern flank where the second  $K_e$  center is situated. In the noRW case, a weak

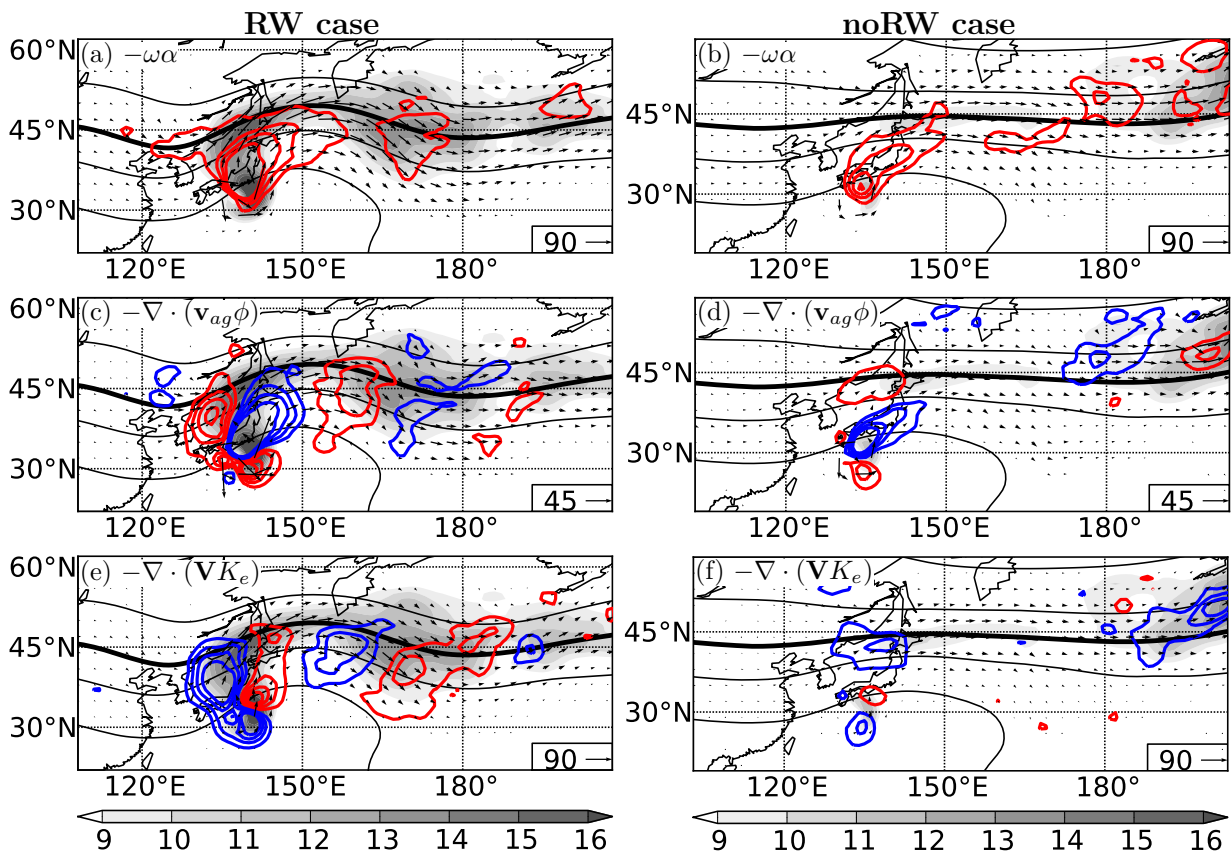


**Figure 4.30:** As in Fig. 4.29, but one day prior to ET. (a, b) total  $K_e$  flux vectors (reference vector in lower right,  $10^6 W m^{-1}$ ), (c, d) ageostrophic  $K_e$  flux vectors (reference vector in lower right,  $10^6 W m^{-1}$ ) and (e, f)  $K_e$  flux vectors (reference vector in lower right,  $10^6 W m^{-1}$ ).

midlatitude  $K_e$  center develops to the northeast of the TC (Fig. 4.30b) in the crest of the weak downstream ridge. This  $K_e$  center is collocated with the jet streak (Fig. 4.16a). A weaker total flux of  $K_e$  from the TC toward the midlatitudes suggests a weaker impact of the TC on the midlatitude flow than in the RW case. In the RW case the baroclinic conversion is stronger and extends over a much larger region (Fig. 4.30a). This indicates a lifting of warm air masses in the vicinity and to the northeast of the TC along the baroclinic zone. Midlatitude forcing for vertical motion through the upstream trough enhances the baroclinic conversion rates. The stronger baroclinic conversion coincides with a much higher number of WCB-like trajectories in the RW case as illustrated in section 4.2.3. In both scenarios, ageostrophic geopotential flux divergence compensates the baroclinic conversion term which indicates the dispersion of baroclinically produced  $K_e$  into the midlatitudes (Fig. 4.30c, 4.30d).

In the noRW case, ageostrophic geopotential flux convergence in the crest of the downstream ridge indicates the accumulation of  $K_e$  and thus an amplification of the jet streak (Fig. 4.30d). The ageostrophic wind vectors suggest that the convergence results from the merging of the TC outflow and the midlatitude jet. This coincides well with

findings in the PV framework which showed that the divergent flow of the ET system and the midlatitude cyclonic flow converged and led potentially to an intensification of the jet streak. Much stronger ageostrophic geopotential flux convergence can be found in the RW case (Fig. 4.30c). A convergence of the ageostrophic flow between the upstream trough and the TC outflow leads to an accumulation of  $K_e$ . This results primarily in an amplification of the meridional flow on the western flank of the downstream ridge. As noted earlier, this observations fits into the conclusions that were drawn from the PV framework. In section 4.2.2 we stated that convergence of the divergent outflow and the midlatitude flow contributed presumably to upper-level frontogenesis and hence to a jet streak intensification. A further amplification of the meridional flow component can be found downstream. Ageostrophic geopotential flux convergence leads to an accumulation of  $K_e$  in the developing downstream midlatitude trough. In both scenarios, the regions of the strongest geopotential flux convergence are also the regions of the strongest total generation of  $K_e$  (not shown). The massive flux of  $K_e$  indicates the transport of  $K_e$  through the downstream ridge and the accumulation of  $K_e$  in the base of the downstream trough (Fig. 4.30e).

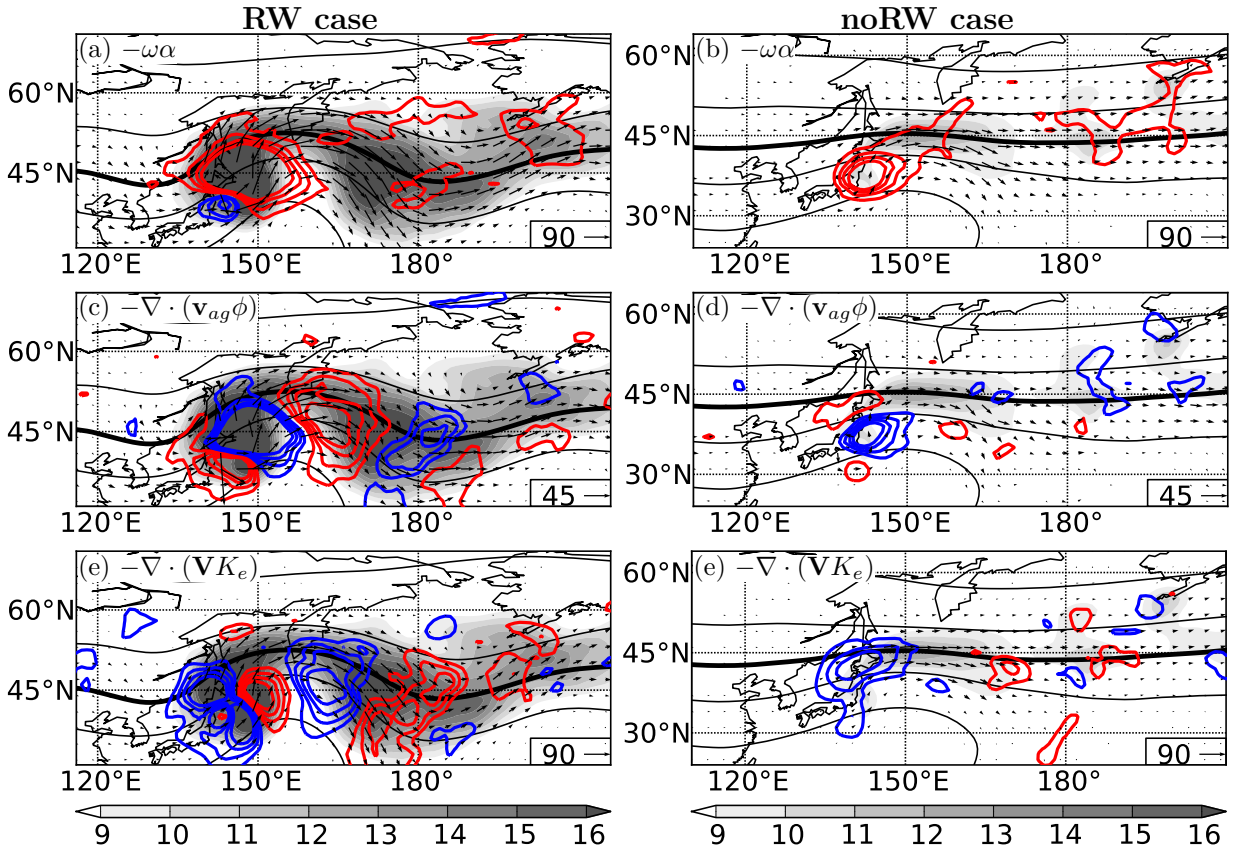


**Figure 4.31:** As in Fig. 4.29, but at ET-time. (a, b) total  $K_e$  flux vectors (reference vector in lower right,  $10^6 W m^{-1}$ ), (c, d) ageostrophic  $K_e$  flux vectors (reference vector in lower right,  $10^6 W m^{-1}$ ) and (e, f)  $K_e$  flux vectors (reference vector in lower right,  $10^6 W m^{-1}$ ).

### Rossby wave amplification at ET-time

Two dominant  $K_e$  centers exist at ET-time (Fig. 4.31a). The first  $K_e$  center is associated with the ET system and the western flank of the downstream ridge. The increase of  $K_e$  compared to the previous time indicates an reintensification of the ET system. At the eastern flank of the downstream ridge the second  $K_e$  center has developed. The energy flux is directed through the downstream ridge and trough into downstream regions. The fact that we do not observe a third maximum of  $K_e$  at the eastern flank of the downstream trough can be attributed to the smearing effect in the composite framework. In general we can state that the  $K_e$  increases continuously over the entire western North Pacific from two days prior to ET to ET-time. The energy flux vectors suggest that the ET system provides additional  $K_e$  to the midlatitude flow over the analyzed period. In the noRW case the increase of  $K_e$  over the western North Pacific is remarkably weaker (Fig. 4.31b).

Largest differences concerning the baroclinic conversion rates occur in the vicinity of the TC. In the noRW case, the highest rates of baroclinic conversion are almost collocated with the TC (Fig. 4.31b). In the RW case strong baroclinic conversion occurs northeast of the TC center along the baroclinic zone (Fig. 4.31a). The fact that the mean sea level pressure is lower and that the vertically averaged  $K_e$  is much higher in the RW case than in the noRW case coincides with more intense rates of baroclinic conversion.

Similarly to the previous time, the collocation of the strongest baroclinic conversion with the ageostrophic geopotential flux divergence (Fig. 4.31c) indicates the dispersion of  $K_e$  into the midlatitudes. The ageostrophic geopotential flux convergence between the upstream trough and the TC outflow has nearly vanished. Instead,  $K_e$  is transported through the downstream ridge to the western flank of the downstream trough through  $K_e$  flux con- and divergence (Fig. 4.31e). Strong ageostrophic geopotential flux convergence leads to an amplification of the  $K_e$  center on the western flank of the downstream trough (Fig. 4.31c). In the noRW case weak ageostrophic geopotential flux divergence is collocated with the baroclinic conversion (Fig. 4.31d). The divergence still indicates the dispersion of  $K_e$  which is accumulated to the north of the TC.

To verify our conclusions further and to test their general validity, we performed a correlation analysis between the  $K_e$  and the generation terms of  $K_e$ , i.e. baroclinic conversion and ageostrophic geopotential flux convergence. In a first step, we computed  $K_e$  budgets for all western North Pacific TCs that underwent ET in the period 1980 to 2010. This yields a sample size of 280 cases. Second, we computed the correlation coefficient between the  $K_e$  and the generation terms in the following way

$$r(\mathbf{x}_{ij}^{t-\Delta t}, \mathbf{K}_e^t) = \frac{\text{cov}(\mathbf{K}_e^t, \mathbf{x}_{ij}^{t-\Delta t})}{\sigma(\mathbf{x}_{ij}^{t-\Delta t})\sigma(\mathbf{K}_e^t)} \quad (4.8)$$

where  $\text{cov}$  is the covariance,  $\sigma$  is the standard deviation and  $\mathbf{x}_{ij}^{t-\Delta t}$  and  $\mathbf{K}_e^t$  have the dimension of the sample size.  $\mathbf{K}_e^t$  includes the mean  $K_e$  in a downstream box at time  $t$  for each ET event. We chose  $t$  to be the ET-time.  $\mathbf{x}_{ij}^{t-\Delta t}$  is either the baroclinic conversion or the ageostrophic geopotential flux convergence at grid point  $ij$  at an earlier time  $t - \Delta t$ .

A TC centered composite of vertically integrated  $K_e$  for all 280 cases at ET-time is similar to the RW case composite and indicates the existence of a wave like structure over the North Pacific (Fig. 4.32). Two pronounced  $K_e$  maxima that are associated with the ET system and the eastern flank of the downstream ridge exist over the North Pacific at ET-time. We computed the mean  $K_e$  for each of the 280 ET events in a box centered on the eastern flank of the ridge at ET-time (green rectangle in Fig. 4.32) and correlated this with the baroclinic conversion and ageostrophic geopotential flux convergence over the entire domain two days prior to ET, one day prior to ET and at ET-time.

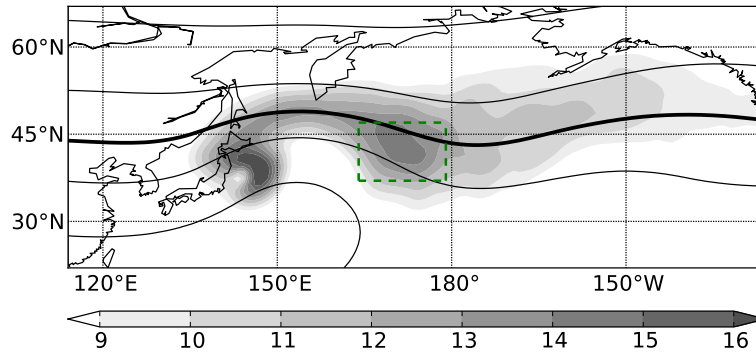


**Figure 4.32:** ET-relative composite of vertically integrated  $K_e$  (shaded,  $10^5 J m^{-2}$ ) and 200 hPa geopotential (black contours,  $2000 m^2 s^{-2}$  intervals, thick black line illustrates  $118000 m^2 s^{-2}$  isoline) for western North Pacific TCs that underwent ET between 1980–2010. Green dashed rectangle marks area where  $K_e^t$  was averaged for the correlation analysis. For illustrative purposes the coastlines are shown relative to the mean TC position.

Highest correlation scores between the generation terms of  $K_e$  two days prior to ET and the mean  $K_e$  in the downstream box at ET-time are located close to the TC (Fig. 4.33a; Fig. 4.33d). The correlation patterns confirm the statements which had been drawn from  $K_e$  budget composites in the RW case. A positive/negative correlation in a region of baroclinic conversion (Fig. 4.33d), and ageostrophic geopotential flux divergence (Fig. 4.33a) indicates that the generation of  $K_e$  energy through baroclinic processes which is dispersed via ageostrophic geopotential flux divergence is relevant for the downstream flow evolution at later times. A positive correlation upstream of the TC in a region of ageostrophic geopotential flux convergence reveals that the stronger the convergence between the TC outflow and the upstream midlatitude flow, the higher the downstream  $K_e$ . This points to the importance of the phasing between the TC outflow and the upstream trough as a weaker convergence would produce less  $K_e$ .

24 hours later the regions of positive and negative correlations expand in size and amplitude. The correlations still indicate that baroclinically produced  $K_e$  (Fig. 4.33e) which is accumulated between the TC outflow and the midlatitude flow impacts the midlatitude flow evolution (Fig. 4.33b). A positive correlation between ageostrophic geopotential flux convergence and the downstream  $K_e$  center has developed downstream of the transitioning TC along  $160^\circ E$ . The flux convergence and the positive correlation with the downstream energy center indicate the dispersion of  $K_e$  as part of the downstream

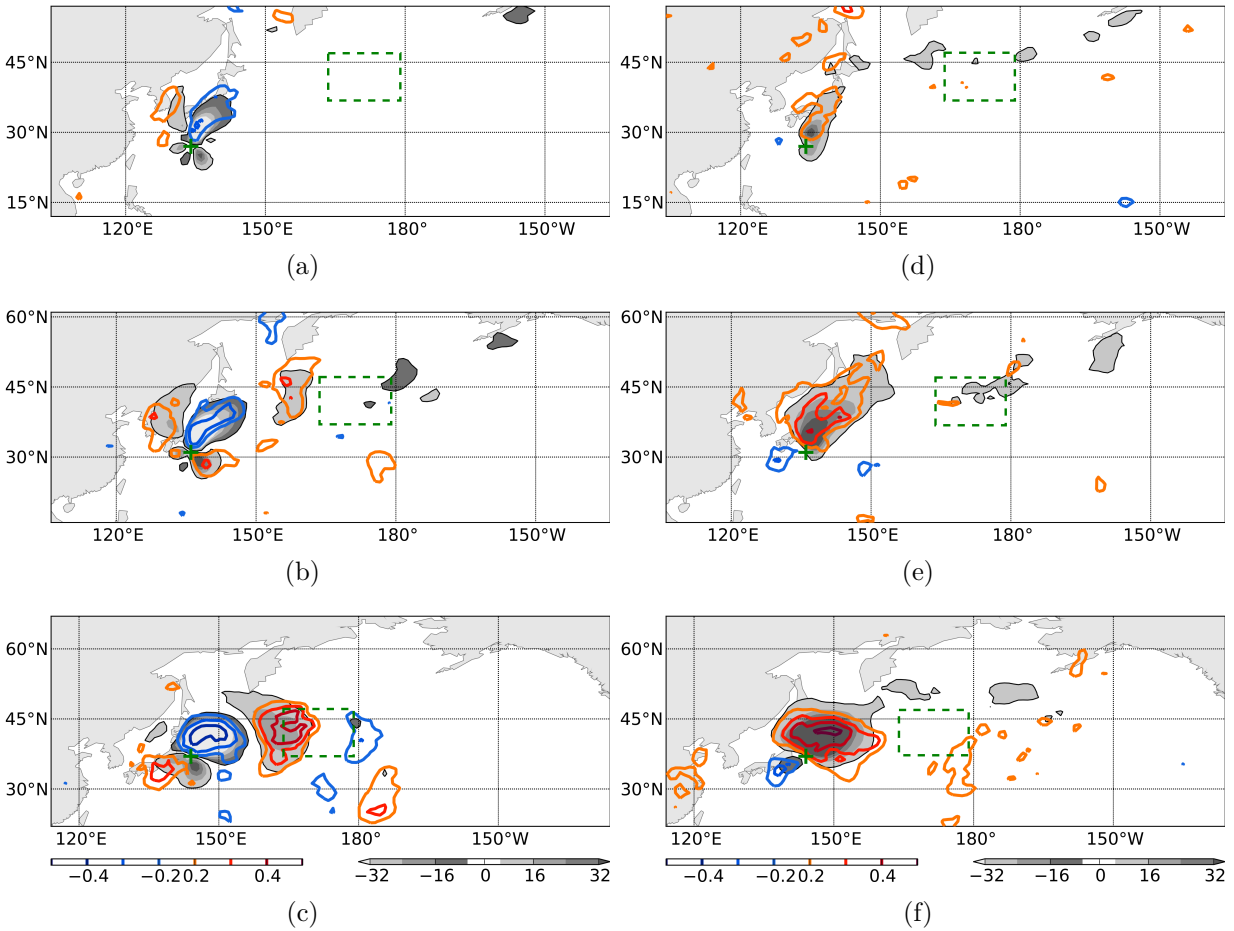


**Figure 4.33:** ET-relative composite of vertically integrated ageostrophic geopotential flux convergence (left column, shaded,  $W m^{-2}$ ) and baroclinic conversion (right column, shaded,  $W m^{-2}$ ) two days prior to ET (a, d), one day prior to ET (b, e) and at ET-time (c, f). Correlation of ageostrophic geopotential flux convergence with averaged eddy kinetic energy in green dashed rectangle at ET-time (left column, colored contours) and correlation of baroclinic conversion with eddy kinetic energy in green dashed rectangle at ET-time (right column, colored contours). For illustrative purposes the coastlines are shown relative to the mean TC position (green cross).

development. Interestingly, a positive correlation between ageostrophic geopotential flux convergence and the downstream energy center occurs in the southeastern quadrant of the TC. We suggest that the ageostrophic geopotential flux convergence is related to a convergence between the TC circulation and the circulation of the subtropical anticyclone. The ageostrophic geopotential flux convergence leads to an increase of  $K_e$  and hence to a stronger southerly flow component in this region. The increase of the southerly flow leads to an increased poleward transport of tropical air masses which could affect the baroclinic conversion to the northeast of the TC.

The correlations as well as the generation terms of  $K_e$  peak at ET-time. The positive correlation between the ageostrophic geopotential flux convergence upstream of the TC and the energy center downstream vanishes (Fig. 4.33c). Thus, the convergence between the outflow of the TC and the midlatitude flow upstream of the TC does not seem to impact the energy center at this stage of the downstream development. It is the dispersion of baroclinically produced  $K_e$  to the north of the ET system (Fig. 4.33f) that affects the downstream development most significantly.

The results of the correlation analysis for the 280 ET events in the period 1980–2010 coincide well with the conclusions that were drawn from the  $K_e$  budgets for the RW cases. At early stages of the ET, the confluence between the TC outflow and the midlatitude flow correlates with the downstream energy center two days later. To the author’s knowledge, the importance of this confluence has not been documented in previous studies. At later stages of the ET, the ageostrophic geopotential flux convergence upstream of the TC becomes less important. Baroclinically produced  $K_e$  is dispersed directly into the midlatitude flow to the north of the ET system. Ageostrophic geopotential flux convergence on the eastern flank of the downstream ridge allows the  $K_e$  to disperse downstream.

**To conclude section 4.2:**

An upper-level trough that emerges from the Asian continent upstream of a TC provides favorable conditions for a downstream development.

Negative PV advection through the cyclonic TC circulation and through an upper-level divergent flow play a major role in the amplification of the downstream ridge two days prior to ET. The upper-level divergent flow intensifies remarkably until ET-time. Quasi-geostrophic forcing diagnostics suggest that 50% of the upper-level divergent flow at ET-time can be attributed to QG vertical motion. At ET-time, PV advection through the upper-level divergent flow and an upper-level anticyclonic flow dominate the downstream ridge amplification.

The upper-level anticyclonic circulation associated with the downstream ridge favors a phase locking between the TC and the upstream trough as it allows the TC to move westward relative to the mean flow and hinders the eastward translation of the Rossby wave at the same time. Southward advection of high-PV air through the anticyclonic circulation associated with the downstream ridge contributes strongest to the deepening of the downstream trough.

The PV advection through the upper-level cyclonic TC circulation anomaly leads to a wrap up of the upstream trough. This process has been referred to as a cyclonic wave breaking of the upstream trough in previous studies.

The number of WCB-like ascending trajectories increases rapidly from two days prior to ET to ET-time. About 56% more trajectories ascent WCB-like in the RW case than in the noRW case at ET-time. The trajectories end in the downstream ridge and contribute to its amplification as the trajectories are associated with the transport of low PV air into a region with higher ambient PV values.

The heating rates along the trajectories do not differ between the RW case and the noRW case and thus do not explain the different upper-level flow evolutions.

The RW case composite is characterized by a remarkable increase of  $K_e$  over the entire North Pacific. The  $K_e$  centers are collocated with the flanks of the troughs and ridges, and with the ET system itself. In the noRW case, one single  $K_e$  center develops which is collocated with the downstream jet streak.

Ageostrophic geopotential flux convergence between the TC and the upstream trough is crucial for the initial development of a  $K_e$  center on the western flank of the downstream ridge. Once this  $K_e$  center has developed,  $K_e$  is dispersed into downstream regions where further  $K_e$  centers form as described in Orlandi and Sheldon (1995). The importance of the ageostrophic flux convergence between the TC and the upstream trough suggests that small differences concerning the phasing of the TC outflow and the upstream trough would lead to very different midlatitude flow modifications. In addition, the strength of the TC outflow is essential for the ageostrophic geopotential flux convergence and thus for the development of the  $K_e$  center on the western flank of the downstream ridge.

The ageostrophic geopotential flux convergence decreases between the TC outflow and the upstream trough at later stages of the interaction. Exceptionally strong and persistent baroclinic conversion which can be attributed at least partly to the WCB-like ascent in the vicinity of the ET system feeds continuously the downstream midlatitude flow with additional  $K_e$ .



# 5 The interaction between the Madden-Julian Oscillation and midlatitude Rossby waves

The MJO impacts planetary-scale Rossby wave dispersion as well as midlatitude synoptic-scale systems (e.g. Jin and Hoskins, 1995; Matthews and Kiladis, 1999b; Moore et al., 2010; section 2.4.1). Planetary-scale Rossby waves develop as a direct response to the MJO convection, whereas synoptic-scale baroclinic systems are triggered by an initial perturbation to the midlatitude waveguide. Hence, the further development and propagation of these baroclinic systems depends strongly on the structure of the midlatitude flow which is modified by the MJO related convection. In this chapter, we investigate the response of synoptic-scale midlatitude RWPs to the MJO related planetary-scale circulation anomalies in reanalysis data as well as in reforecast data. The correct representation of the response of synoptic-scale RWPs to the MJO is of particular interest as these RWPs play an essential role in the midlatitudes concerning the transport of heat, moisture and momentum. In addition, synoptic-scale RWPs that propagate back into the tropics may modify the tropical convective variability or even contribute to the initiation of a new MJO event. Finally, synoptic-scale RWPs may lead to severe weather events in midlatitudes so that the correct prediction of their response to the MJO is of economic and societal interest.

## 5.1 The interaction between the Madden-Julian Oscillation and Rossby waves packets in analyses

The climatological investigation of the midlatitude synoptic-scale Rossby wave response to the MJO is based on the method of Zimin et al. (2006). This method enables us to consider the propagation characteristics of synoptic-scale RWPs in response to a changing background flow. We used the same parameters as given in section 3.3 except for the clipping threshold  $\tau$ . We set  $\tau = 2.5$  in order to keep the signal of rather weak RWPs that propagate southward into the subtropics. As in the previous chapter, we investigate the mean RWP occurrence frequency  $F$  according to

$$F = \frac{1}{N_c} \sum_c M_{i,j}^c \quad . \quad (5.1)$$

$N_c$  denotes the number of cases and  $M_{i,j}^c$  is a mask for case  $c$  at the grid point  $i, j$  now in the spatial longitude-latitude domain.  $M_{i,j}^c$  is set to 1 if the clipped envelope is greater than zero. The computation of the RWP occurrence frequency in the longitude-latitude domain enables us to explore the propagation characteristics of the RWPs in response to the MJO.

In order to compare the response of midlatitude synoptic-scale RWPs to the MJO with a climatological value we computed first the climatological distribution of RWP occurrence frequency. Thereby, we focus on the months December, January and February (DJF). The spatial distribution of the climatological RWP occurrence frequency between December to February (Fig. 5.1) is similar to that observed between June to November (Fig. 4.2). However, the absolute values of RWP occurrence frequency differ. Synoptic-scale RWPs are most probable over the storm track regions, i.e. over the North Atlantic and over the eastern North Pacific. The climatological occurrence frequency exceeds 25% in these regions. The lowest RWP occurrence frequency is seen over the Asian continent and over the east Asian coast which coincides with findings in Fig. 4.2. Regions of RWP onset, as indicated by an increase of RWP occurrence frequency from west to east, are the western to central North Pacific and the western North Atlantic. Rossby wave packets decay either over North America or over Europe. The spatial distribution of RWPs over Europe and the Eurasian region indicates two propagation paths of RWPs. Rossby wave packets that reach Europe propagate either northeastward along the polar jet toward central Asia or southeastward along the subtropical jet toward India. The propagation along the subtropical jet coincides with findings of Hakim (2003) (see their Fig. 13).

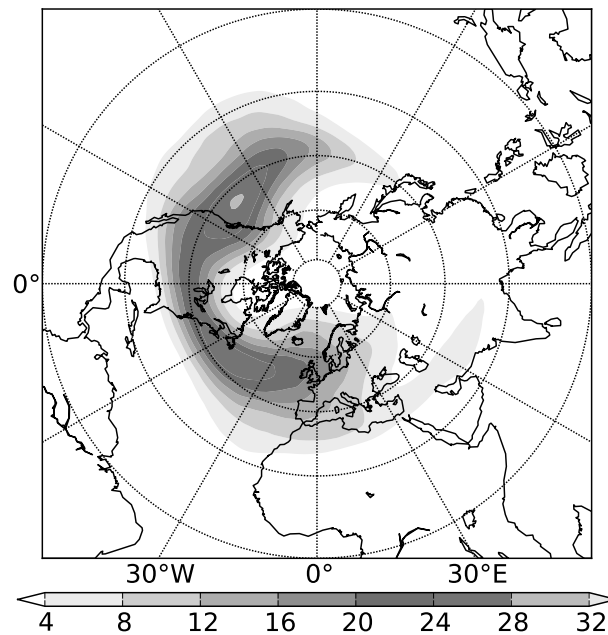


**Figure 5.1:** DJF climatology of RWP occurrence frequency (shading, %). Latitude circles are given in 20° increments from the equator.

We computed the RWP occurrence frequency for DJF 1980–2009 for the MJO phases 1 to 8 according to the RMM-Index (Wheeler and Hendon, 2004) when the MJO was in its active phase, i.e.  $\sqrt{RMM_1^2 + RMM_2^2} > 1$ . In addition, we investigated the RWP occurrence frequency for days of an inactive MJO, i.e.  $\sqrt{RMM_1^2 + RMM_2^2} < 1$ . The inactive phase of the MJO will be referred to as MJO phase 0. We computed the RWP occurrence frequency in a time range of  $\pm 2$  days around an MJO phase. The resulting averaging period of five days corresponds approximately to the duration of one phase in the MJO life-cycle. Anomalies of the RWP occurrence frequency are computed as the difference between the mean RWP occurrence frequency for each MJO phase and the DJF climatology of RWP occurrence frequency. The statistical significance of the RWP occurrence frequency anomalies was determined via a Monte-Carlo approach (for details see section 4.1.2). In contrast to section 4.1.2, we determined the upper and lower 1% percentiles of the Monte-Carlo composites and define those values of the MJO relative composite as statistically significant that either exceed or fall below these percentiles.

The RWP occurrence frequency anomalies reveal a clear variation with the MJO phases (Fig. 5.2). Smallest and least significant RWP occurrence frequency anomalies occur during the inactive phase of the MJO (Fig. 5.2a) which suggests that there is not a preferred midlatitude RWP response to inactive MJO convection. A negative RWP occurrence frequency anomaly of about 5% occurs from the eastern North Pacific to the eastern North Atlantic. This anomaly is statistically significant only in small parts of the Northern Hemisphere.

Much stronger RWP occurrence frequency anomalies appear during the first phase of the MJO (Fig. 5.2b). The occurrence frequency is anomalously low from the central North Pacific to central North America and over the North Atlantic. Thus, less RWPs propagate into North America between 30 to 50°N and into central Europe between 40 to 60°N. At the same time, a positive RWP occurrence frequency anomaly can be found over North America between 15 to 30°N and between 50 to 60°N. The resulting positive-negative-positive anomaly pattern indicates either a split of the waveguide which forces the RWPs to propagate further south or further north or a weaker waveguide which allows the RWPs to leak out of the jet. Finally, a northwest to southeast oriented positive anomaly over the Atlantic between 20° to 40°N indicates a southward penetration of RWPs into the subtropics.

A rather inconclusive picture during MJO phase 2 (Fig. 5.2c) changes into a clear picture during phase 3 (Fig. 5.2d) during which the RWP occurrence frequency anomalies are almost opposite to the anomalies during phase 1. Positive anomalies north of 40°N and negative anomalies between 20 to 40°N indicate a northward shift of the jet and less RWPs that propagate into the subtropics over the eastern North Pacific and over the North Atlantic. The different propagation characteristics in phase 1 and 3 can potentially be attributed to a change in the jet structure. During MJO phase 1, the midlatitude flow over the North Pacific north of 40°N was characterized by easterly anomalies (Fig. 2.10a). These easterly wind anomalies reduce the westerly zonal flow and increase the stationary wave number  $K_s$  (equation 2.5) which allows synoptic-scale Rossby waves to propagate

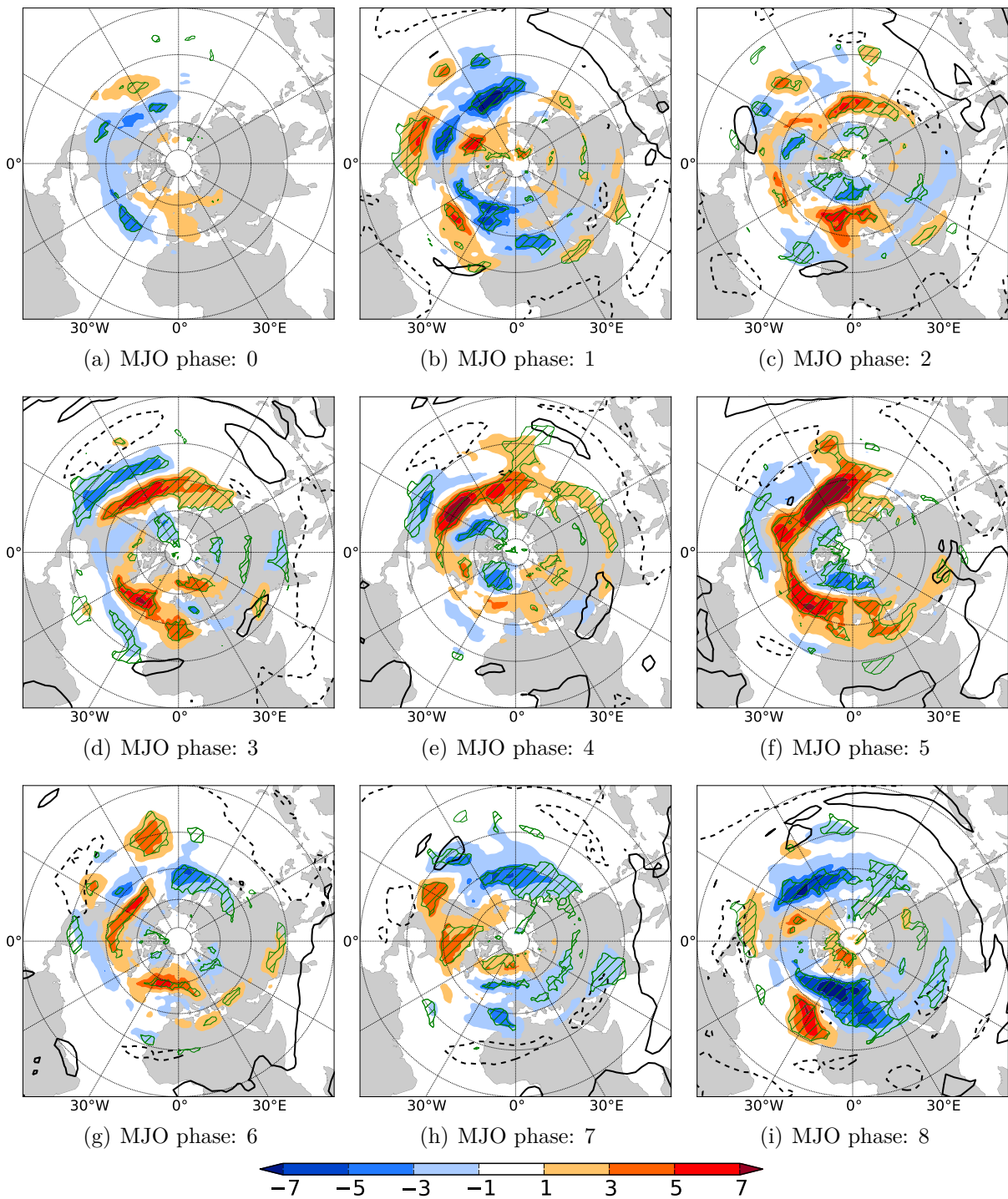


**Figure 5.2:** Anomaly of RWP occurrence frequency (shading, %) relative to December to February climatology for MJO phases 0 to 8. Values that are statistically significant at the 99% confidence level are hatched. MJO filtered OLR anomaly (black contours,  $W m^{-2}$ ) with negative values dashed. Data are smoothed with a Gaussian filter.

meridionally. Thus, the weaker, leakier jet potentially contributed to the RWP propagation into the subtropics. During MJO phase 3, a strong anticyclonic anomaly over the North Pacific results in an acceleration of the westerly winds north of  $45^{\circ}\text{N}$  (Fig. 2.10c). Hence, RWPs are trapped along the wave guide so that more RWPs propagate into North America and less RWPs propagate into subtropical regions.

The positive anomaly over the eastern North Pacific intensifies remarkably during MJO phases 4 (Fig. 5.2e) and 5 (Fig. 5.2f). In addition, a significantly positive RWP occurrence frequency develops over the North Atlantic. Negative anomalies that were identified during MJO phase 3 weaken. Thus, MJO phases 4 and 5 are characterized by a global increase of RWP occurrence frequency in midlatitudes. More RWP propagate into North America and into central Europe. The propagation characteristics are presumably linked to planetary-scale circulation patterns that developed in response to the MJO. During MJO phase 4, a prominent anticyclone is located over the North Pacific at  $45^{\circ}\text{N}$  and  $180^{\circ}$  (Fig. 2.10d). Downstream, a cyclonic anomaly over Alaska, an anticyclone over Canada and a cyclonic circulation over Greenland indicate the dispersion of a planetary-scale Rossby wave train. Both the anticyclonic anomaly over the North Pacific and the cyclonic anomaly over Greenland strengthen the westerly midlatitude flow at around  $45^{\circ}\text{N}$ . Negative RWP occurrence frequency anomalies to the north and south of the westerly wind anomalies indicate that RWPs are confined to the jet due to a smaller stationary wave number. Hence, RWPs cannot propagate northward and southward, respectively.

Cassou (2008) and Lin et al. (2009) found an increased probability for the positive North Atlantic Oscillation (NAO) regime during MJO phases 3 and 4. A positive NAO is characterized by a negative height anomaly over Iceland and a positive height anomaly over the subtropical North Atlantic which results in an anomalously strong westerly flow over the North Atlantic (Fig. 2.10d). We computed RWP occurrence frequency anomalies for a time range of  $\pm 2$  days around the positive and negative NAO phases during DJF 1980–2009. We defined a positive (negative) NAO regime when the daily NAO index exceeded (went below) plus (minus) one standard deviation for this period. The NAO index was obtained from the NOAA Climate Prediction Center<sup>1</sup>. The RWP occurrence frequency anomalies are characterized by a negative-positive-negative RWP occurrence frequency anomaly pattern over the North Atlantic during the positive phase of the NAO (Fig. 5.3a). Less RWPs occur over the subtropical Atlantic Ocean and north of  $60^{\circ}\text{N}$ . A positive and statistically significant anomaly occurs inbetween these negative anomalies over the North Atlantic and Europe. This coincides with the fact that the positive (negative) height anomaly over the subtropical North Atlantic (Iceland) enhances the westerly flow over the North Atlantic. Rossby wave packets are trapped on this strong westerly flow and propagate eastward instead of experiencing a north- or southward deflection. This coincides with findings of Lin et al. (2009) who found an increased northward momentum flux along the storm track during a positive NAO. To the south of the storm track, negative momentum flux anomalies were found in the subtropical Atlantic. Lin et al. (2009) attributed this to a reduced southward penetration of extratropical transient eddies. They could show that

---

<sup>1</sup><http://www.cpc.ncep.noaa.gov/products/precip/CWlink/pna/nao.shtml>

the modulation of the momentum flux by these transient eddies changed the zonal winds across the tropical Atlantic.

Interestingly, the spatial structure of MJO related negative and positive RWP occurrence frequency anomalies over the North Atlantic during MJO phase 5 resemble the spatial structure of RWP anomalies associated with the positive NAO. However, Cassou (2008) did not find a significant relation between the MJO phase 5 and the NAO, but between the earlier MJO phases 3 and 4. Therefore, we suggest that the RWP occurrence frequency anomalies during MJO phase 5 are rather a response to the positive NAO than a contributor to the positive NAO. This underlines the importance of correct predictions of the MJO related planetary-scale circulation anomalies.

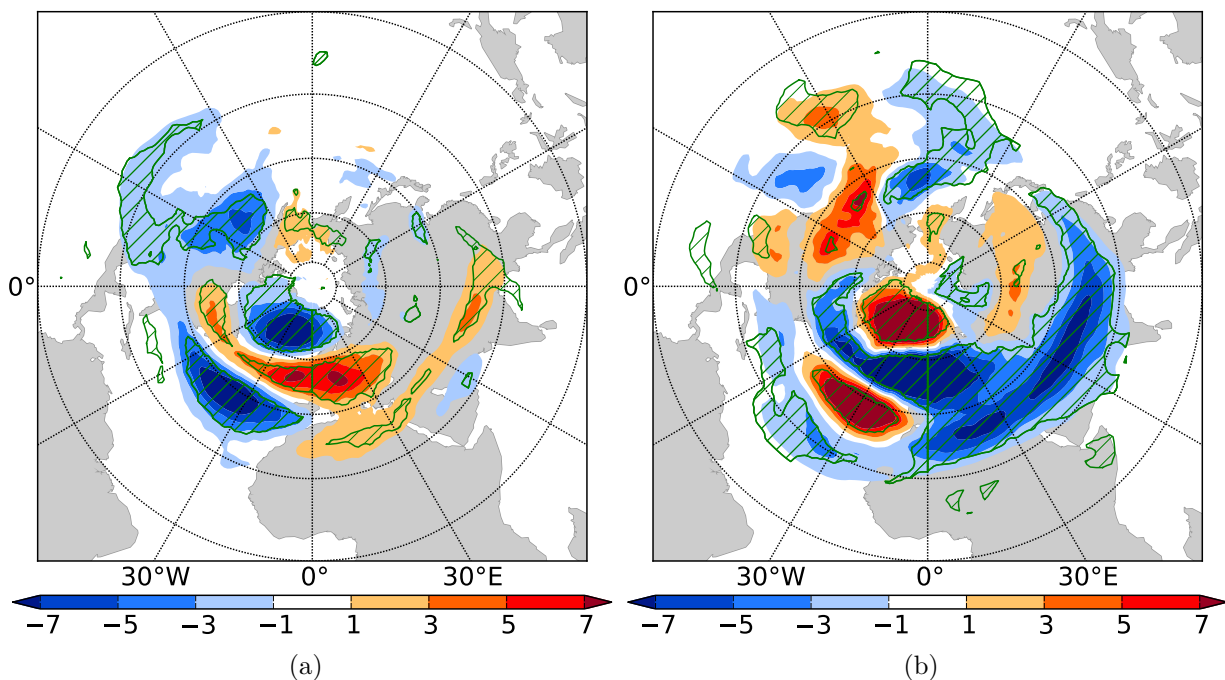


**Figure 5.3:** Anomaly of RWP occurrence frequency (shading, %) relative to December to February climatology for (a) positive and (b) negative NAO. Values that are statistically significant at the 99% confidence level are hatched. Data are smoothed with a Gaussian filter.

A negative OLR anomaly developed during MJO phases 2 to 5 over the tropical central Pacific between 180 to 120°W (black contours in Fig. 5.2c-f). Matthews and Kiladis (1999b) identified this convection as a high-frequency convective variability over the central Pacific intertropical convergence zone that forms an integral part of the slowly varying diabatic heating field of the MJO. They argued that during the phase of the MJO with enhanced convection over the Maritime Continent, and suppressed convection over the South Pacific convergence zone (phase 4 and 5), the Asian-Pacific jet and tropical easterlies over the warm pool are displaced westward. The retraction of the Asian-Pacific jet (cf. Fig. 2.10c-e) allows high-frequency transient waves to propagate equatorward into the deep tropics over the central Pacific near the date line. Matthews and Kiladis (1999b)

suggested that the high-frequency cyclonic transients provide upper-level forcing, reduce static stability and thus enhance the convective activity. Our results for MJO phase 5 coincide with findings of Matthews and Kiladis (1999b). A positive RWP occurrence frequency anomaly that extends south of  $20^{\circ}\text{N}$  over the central North Pacific indicates the propagation of synoptic-scale RWPs into the subtropics (Fig. 5.2f). The previously mentioned negative OLR anomaly is located southeast of the positive RWP occurrence frequency anomaly which suggests that it is forced from the midlatitude synoptic-scale variability. However, the negative OLR anomaly exhibits a comparable intensity over the tropical North Pacific already during MJO phases 3 and 4. Interestingly, our results suggest that less RWPs propagate into the subtropics over that region during MJO phase 3. This would imply that the convective anomaly over the central Pacific is not solely forced by extratropical transients propagating into the tropics.

In phase 6, the positive RWP occurrence frequency anomaly over the subtropical central North Pacific still indicates a southward propagation of RWPs. According to Matthews and Kiladis (1999b) this would maintain the convective anomaly in that region. Future research could help to better understand the processes linking the extratropics with the tropical convection and the tropical wind anomalies. The positive RWP occurrence frequency anomalies in midlatitudes weaken considerably until phase 6 and thus indicate less Rossby wave activity.

The decrease of RWP occurrence frequency continues over large areas of the globe during MJO phases 7 (Fig. 5.2h) and 8 (Fig. 5.2i). The continuous decrease in RWP occurrence frequency results in significant anomalies of less than -7% over the North Atlantic and the eastern North Pacific. Thus, less RWPs propagate into central North America and Europe at later stages of an MJO life-cycle. Cassou (2008) and Lin et al. (2009) reported an enhanced probability of the negative phase of the NAO during MJO phase 7 and 8. The negative NAO is characterized by a negative height anomaly over the subtropical Atlantic Ocean and a positive height anomaly over the polar North Atlantic. This configuration leads to a weaker westerly flow such that RWPs might leak out of the wave guide (see also wind anomaly in Fig. 2.10h). This becomes obvious in the anomalies of RWP occurrence frequency for the negative NAO regime (Fig. 5.3b). Positive anomalies occur over the subtropical and polar North Atlantic, negative anomalies occur over the central North Atlantic and Europe. Thus, the anomaly pattern is exactly opposite to that during the positive NAO regime. Rossby wave packet occurrence frequency anomaly patterns during MJO phase 8 and 1 are similar to the anomalies during a negative NAO regime. A weakly positive, but significant anomaly occurs over the polar North Atlantic during MJO phase 8. A highly significant and positive RWP occurrence frequency anomaly occurs over the eastern Atlantic between  $20$  to  $40^{\circ}\text{N}$  during phases 8 and 1. This positive anomaly reveals a propagation of RWPs into the subtropics in this region. A negative OLR anomaly is located to the southeast of this positive RWP occurrence frequency anomaly which indicates a forcing of tropical convection through southward propagating RWPs as identified over the East Pacific during MJO phase 5. The southward propagation of RWPs into the subtropics may also impact the upper-level tropical zonal winds. The transient

eddies which reach the tropics lead to a southward momentum flux that converges in the tropics.

Lin et al. (2009) suggested that the convergence of the momentum flux in the subtropical eastern Atlantic results in an increase of the tropical westerly winds which might then even be able to trigger a new MJO event. Similar to MJO phase 5, the most significant midlatitude RWP occurrence frequency anomalies occur one MJO phase after the establishment of the negative NAO regime in response to the MJO as identified by Cassou (2008). Therefore, we come to the conclusion that the propagation characteristics of RWPs change in response to the NAO regime. The propagation characteristics of RWPs during MJO phase 8 are potentially also associated with an increased blocking frequency over the European region (Hamill and Kiladis, 2014). These blocking events may lead to a split flow regime that forces RWPs to propagate either along the polar jet toward Scandinavia or along the subtropical jet toward Africa.

In the following, we will investigate  $K_e$  budget terms (section 3.4) around MJO phases 5 and 8 as these phases reveal major differences concerning the RWP occurrence frequency. In order to identify potential mechanisms that contributed to the generation of  $K_e$  and thus to the enhanced RWP occurrence frequency, we investigate the baroclinic conversion, convergence of  $K_e$  fluxes and barotropic conversion for a period of 3–7 days prior to MJO phase 5. We computed the  $K_e$  budgets for the DJF 1980–2009 period from ERA-Interim reanalysis data with a horizontal resolution of  $1^\circ$  and a vertical resolution of 100 hPa (see also section 4.2.4).

The regions which exhibited an increase in RWP occurrence frequency during MJO phase 5 (Fig. 5.2f) are characterized by a positive  $K_e$  anomaly (Fig. 5.4a). The MJO related  $K_e$  anomalies exceed the climatological mean  $K_e$  between  $40$  to  $60^\circ\text{N}$  and fall below the climatological mean  $K_e$  south of  $40^\circ\text{N}$  over the North Pacific. A comparison with the maxima of the climatological  $K_e$  distribution (black contours in Fig. 5.4a) indicates further a northward shift of the storm track region by about  $10^\circ$ . The anomalously high values of  $K_e$  over the North Pacific during MJO phase 5 have been documented in a previous study by Deng and Jiang (2011). Over the North Atlantic, the  $K_e$  decreases mainly north of  $60^\circ\text{N}$  and increases between  $40$  to  $60^\circ\text{N}$ . This coincides well with the anomalously high RWP occurrence frequency anomaly. The baroclinic conversion is characterized by a dipole pattern over the North Pacific (Fig. 5.4b) (see also Deng and Jiang, 2011). The positive baroclinic conversion anomaly over the western North Pacific indicates lifting of warm air masses which can be attributed to an increased cyclonic activity. The increased cyclonic activity may lead more frequently to deflections of the midlatitude waveguide that result in a downstream Rossby wave development. An increase of cyclone frequency during MJO phase 5 coincides with results of Moore et al. (2010) who documented an increased cyclone frequency over the western North Pacific when the MJO convection was located over the Maritime Continent. A negative anomaly of the  $K_e$  flux divergence in the region of enhanced baroclinic conversion indicates that the baroclinically produced energy is advected downstream (Fig. 5.4c). Positive anomalies of  $K_e$  flux convergence indicate an accumulation of  $K_e$  over both the eastern North Pacific and the central subtropical

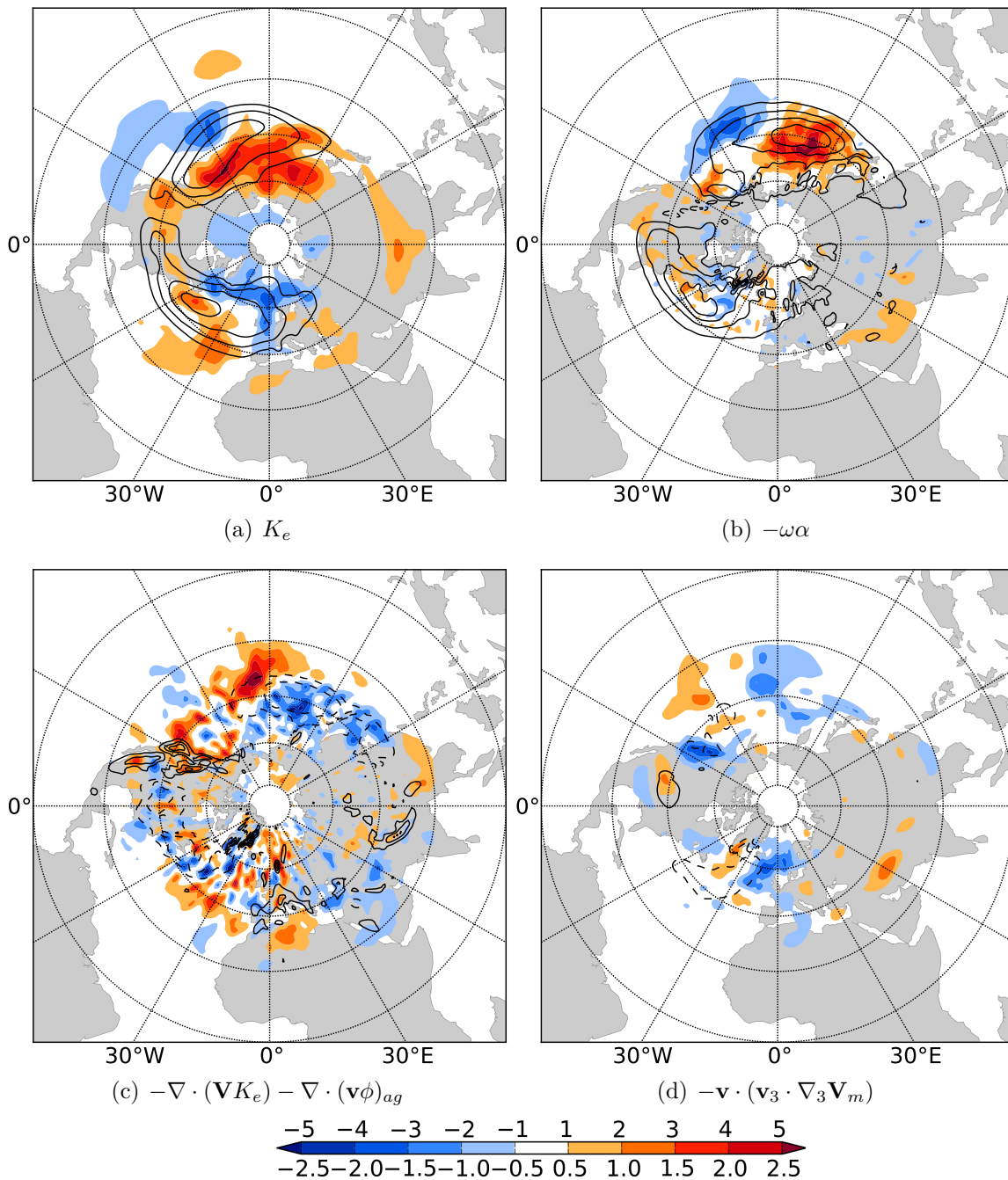


**Figure 5.4:** Anomalies of  $K_e$  budget terms relative to climatology for MJO phase 5. (a)  $K_e$  anomaly (shaded,  $10^5 J m^{-2}$  according to upper row in colorbar), (b) baroclinic conversion anomaly, (c)  $K_e$  flux divergence anomaly and (d) barotropic conversion anomaly (shaded,  $W m^{-2}$  according to lower row in colorbar). Black contours give climatologies of (a)  $K_e$  (10, 12, 14, 16  $J m^{-2}$ ), (b) baroclinic conversion, (c)  $K_e$  flux divergence and (d) barotropic conversion ( $\pm 4, 8, 12, 16, 20 W m^{-2}$ ). Negative values are dashed.

Pacific. Barotropic conversion of  $K_e$ , i.e. the exchange of energy between the synoptic eddies and the background flow seems to play a minor role over the Pacific (Fig. 5.4d). The anomalies indicate that synoptic eddies feed the background flow over the central Pacific and extract  $K_e$  over the east Pacific. Over the North Atlantic, the barotropic conversion gives a much clearer signal than the baroclinic conversion or the  $K_e$  flux convergence. Hence, the reduction of  $K_e$  and RWP occurrence frequency north of  $60^\circ\text{N}$  over the Atlantic might be attributed to a delivery of  $K_e$  by synoptic eddies to the background flow, e.g. through wave breaking events.

The  $K_e$  anomalies that occur during MJO phase 8 (Fig. 5.5a) are nearly opposite to the anomalies during MJO phase 5 (Fig. 5.4a). The anomalously low  $K_e$  over the North Pacific during phase 8 coincides with an anomalously low RWP occurrence frequency (Fig. 5.2i). Baroclinic conversion anomalies reveal a dipole structure over the North Pacific (Fig. 5.5b) that is exactly opposite to the dipole structure during phase 5 (Fig. 5.4b) (see also Deng and Jiang, 2011). Less baroclinic conversion over the western North Pacific indicates weaker cyclonic activity whereas a positive baroclinic conversion anomaly over the eastern North Pacific indicates an increase in cyclone frequency. These findings coincide well with results of Moore et al. (2010). They found a decrease (increase) of surface cyclone frequency over the western (eastern) North Pacific at later stages of an MJO life-cycle. They concluded that an anomalously strong westerly flow over the North Pacific (cf. Fig. 2.10g, h) constitutes a waveguide spanning the central Pacific. The jet exit region over the eastern North Pacific represents an optimal location for cyclonic wave breaking events which leads to an increased surface cyclone frequency. The anomaly patterns of  $K_e$  flux divergence indicate an increased  $K_e$  energy dispersion over the eastern North Pacific (Fig. 5.5c). This suggests that baroclinically produced  $K_e$  is transported into downstream regions.

The  $K_e$  anomalies over the eastern North Atlantic during MJO phase 8 (Fig. 5.5a) exhibit a positive-negative-positive pattern that is similar to the observed anomalies of RWP occurrence frequency.  $K_e$  is anomalously low over the North Atlantic between  $40$  to  $60^\circ\text{N}$  and exceptionally high over the polar North Atlantic and between  $20$  to  $40^\circ\text{N}$ . The northwest to southeast tilt of the positive  $K_e$  anomaly between  $20$  to  $40^\circ\text{N}$  indicates the propagation of positive  $K_e$  anomalies – potentially in the form of RWPs – into subtropical regions. A negative baroclinic conversion anomaly indicates a decrease in surface cyclone frequency (Fig. 5.5b). This corresponds to the negative NAO regime that develops preferentially at later stages of an MJO life-cycle (Cassou, 2008; Lin et al., 2009). The circulation anomalies associated with the negative NAO regime weaken the westerly flow over the North Atlantic and thus deteriorate the conditions for baroclinic life-cycles. The barotropic conversion of  $K_e$  seems to be less important over the North Atlantic during phase 8 (Fig. 5.5d) than during phase 5 (Fig. 5.4d).

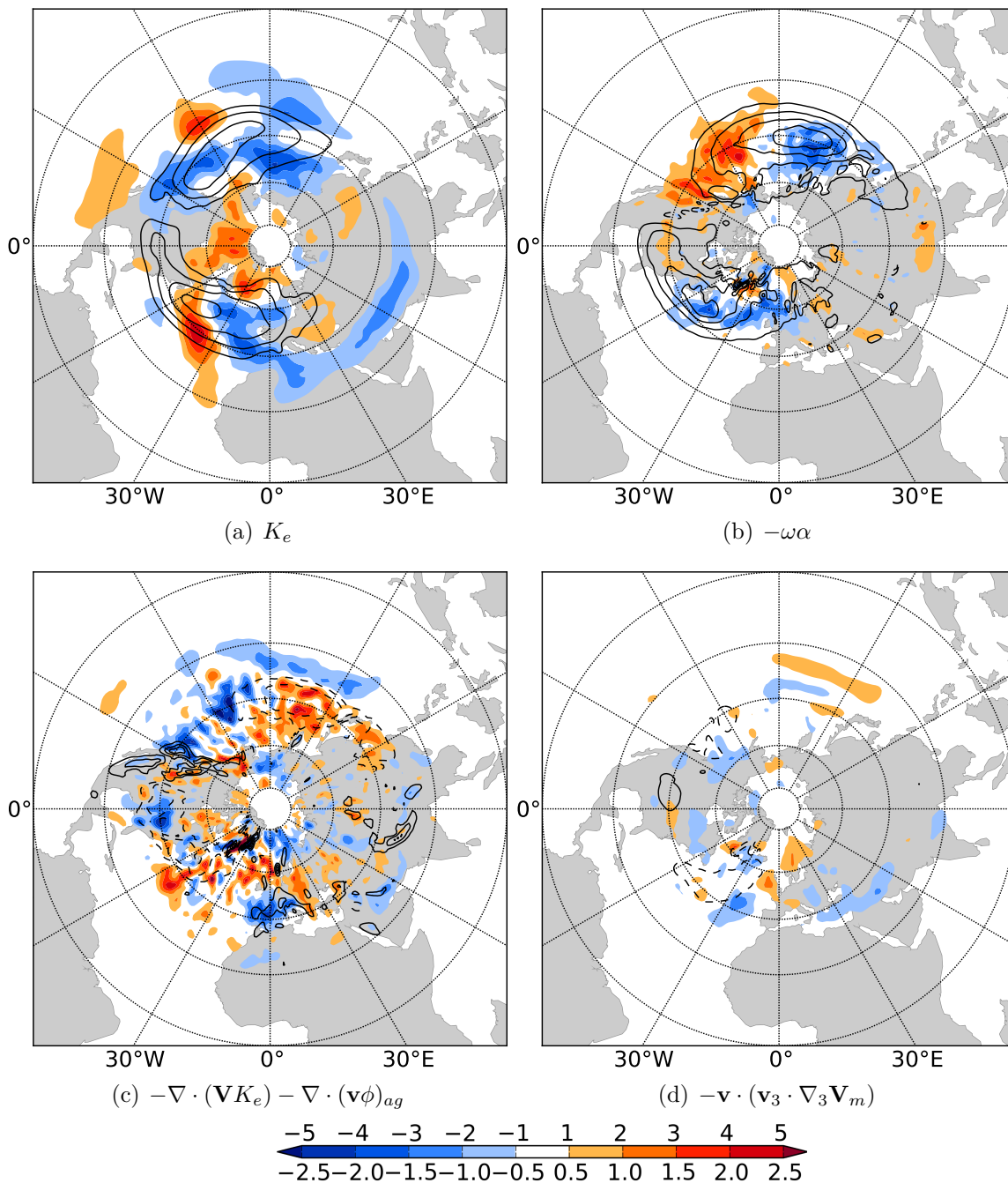


**Figure 5.5:** Same as in Fig. 5.4, but for MJO phase 8.

**To conclude section 5.1:**

We motivated this section with the research question “How does the synoptic-scale RWP occurrence frequency vary with the location of the MJO convectively active region?” Several previous studies have addressed this question. However, to the author’s knowledge this is the first time that the question has been investigated with an object-based approach.

The anomalies of RWP occurrence frequency reveal a clear variation with the location of the MJO convectively active region. The RWP occurrence frequency increases over the Northern Hemisphere when the MJO related convection is located over the Maritime Continent (MJO phases 4 and 5). Positive and highly significant RWP occurrence frequency anomalies are located over the eastern North Pacific and the North Atlantic. During MJO phases 1 and 8, the RWP occurrence frequency anomalies are lowest over the North Pacific and the North Atlantic.

The spatial distribution of RWP occurrence frequency anomalies over the North Atlantic corresponds to changes of the NAO in response to the MJO. When the MJO related convection is located over the Maritime Continent, there is an enhanced probability of a positive phase of the NAO (Cassou, 2008) which is associated with a stronger midlatitude zonal flow over the North Atlantic. RWPs are trapped on this anomalously strong westerly flow and do not experience a north- or southward deflection. When the MJO related convection is decaying near the dateline, there is an enhanced probability of a negative phase of the NAO which leads to a weaker North Atlantic zonal flow. RWPs leak out of this weaker westerly flow and propagate into the subtropics.

Due to similar modifications of the zonal flow over the eastern North Pacific, RWPs propagate more frequently into the subtropics when the MJO related convection is located over the Maritime Continent.

Anomalies in RWP occurrence frequency correspond with anomalies in eddy kinetic energy. Eddy kinetic energy budget terms suggest that the baroclinic conversion over the western North Pacific is essential for the generation of eddy kinetic energy anomalies and hence presumably for the distribution of RWP occurrence frequency anomalies.

## 5.2 The representation of the Madden-Julian Oscillation in ERA-Interim reforecasts

The correct medium-range prediction of the MJO still poses a challenge to global numerical weather prediction (NWP) models (e.g. Matsueda and Endo, 2011; Hamill and Kiladis, 2014). These studies highlighted the inability of NWP models to simulate the eastward propagation and the amplitude of the MJO signal. However, the correct representation of the MJO is essential for predicting tropical-extratropical teleconnection patterns. Thus, we briefly document the representation of the MJO in the ERA-Interim reforecast data. In agreement with previous studies (e.g. Matsueda and Endo, 2011) we will use three standard verification scores for the MJO that are based on the RMM-Index (section 2.1): the phase

error (PERR), the amplitude error (AERR) and the root mean square error (RMSE). The scores are defined as

$$RMSE(t, \tau) = \sqrt{(f_1(t, \tau) - a_1(t))^2 + (f_2(t, \tau) - a_2(t))^2} \quad (5.2)$$

$$PERR(t, \tau) = \tan^{-1} \left( \frac{a_1(t)f_2(t, \tau) - a_2(t)f_1(t, \tau)}{a_1(t)f_1(t, \tau) + a_2(t)f_2(t, \tau)} \right) \quad (5.3)$$

$$AERR(t, \tau) = \sqrt{f_1(t, \tau)^2 + f_2(t, \tau)^2} - \sqrt{a_1(t)^2 + a_2(t)^2} \quad (5.4)$$

where  $\mathbf{f}(t, \tau) = (f_1(t, \tau), f_2(t, \tau))$  is the forecast in the RMM-Index phase space initialized at  $\tau$  and valid at time  $t$ .  $\mathbf{a}(t) = (a_1(t), a_2(t))$  is the analysis in the RMM-Index phase space at time  $t$ . PERR gives the angle between the observation  $\mathbf{a}(t)$  and the forecast  $\mathbf{f}(t, \tau)$  using the properties of the cross product (numerator) and the dot product (denominator). PERR indicates the predicted phase speed (propagation) relative to that observed. Negative values of PERR indicate a slower eastward propagation than in the observation. AERR is the difference between the predicted and analyzed amplitudes in the RMM-Index phase space and the RMSE contains information about both the phase error and the amplitude error. A RMSE of zero indicates a perfect MJO forecast. An AERR of zero indicates a perfect forecast concerning the MJO amplitude in the RMM-Index phase space. We computed these scores for ERA-Interim reforecasts in the period December to February 1980–2009 that were initialized during MJO phases 0 to 8. Phase 0 indicates an inactive MJO which we define as  $\sqrt{RMM_1^2 + RMM_2^2} < 1$ . We used the RMM-Index from ERA-Interim reanalysis data as verification.

The results clearly reveal that the magnitude of the RMSE, PERR and AERR varies with the MJO phases in the reforecast dataset (Fig. 5.6). According to the RMSE, the model exhibits the best performance in forecasts that were initialized during phases 1 (Fig. 5.6b) and 8 (Fig. 5.6i). The RMSE of these MJO forecasts does not exceed 0.8 after a forecast time of 9 days. In particular, forecasts initialized during an inactive MJO phase and during phase 1 show a relatively small amplitude and phase error. For both initial phases 1 and 8 the PERR is positive which indicates that the MJO signal propagates eastward too quickly. A negative AERR reveals that the MJO signal weakens with forecast lead time. This is a common feature for all initial phases and stands in contrast to findings of Vitart and Molteni (2010) who reported that the MJO, simulated by a subsequent model version, tended to be too strong. Forecasts that were initialized during phases 4–6 exhibit the largest RMSE (Fig. 5.6e-g). The magnitude of AERR is comparable to previous phases. PERR is largely negative which indicates a too slow eastward propagation. Forecasts with the initial phase 4 reveal a PERR of  $30^\circ$  which corresponds almost to one MJO phase. This finding coincides with results of Vitart and Molteni (2010) who stated that the MJO in the ECMWF model has difficulties in crossing the Maritime Continent. About 50% of their forecast MJO events did not propagate from the west part of the Maritime Continent into the west Pacific. They found cases in which the MJO related convection was locked over the Maritime Continent for a time range of up to 46 days. Vitart and Molteni (2010) attributed this model behaviour to an erroneous representation of the interaction between the MJO convection and the Maritime Continent land masses.

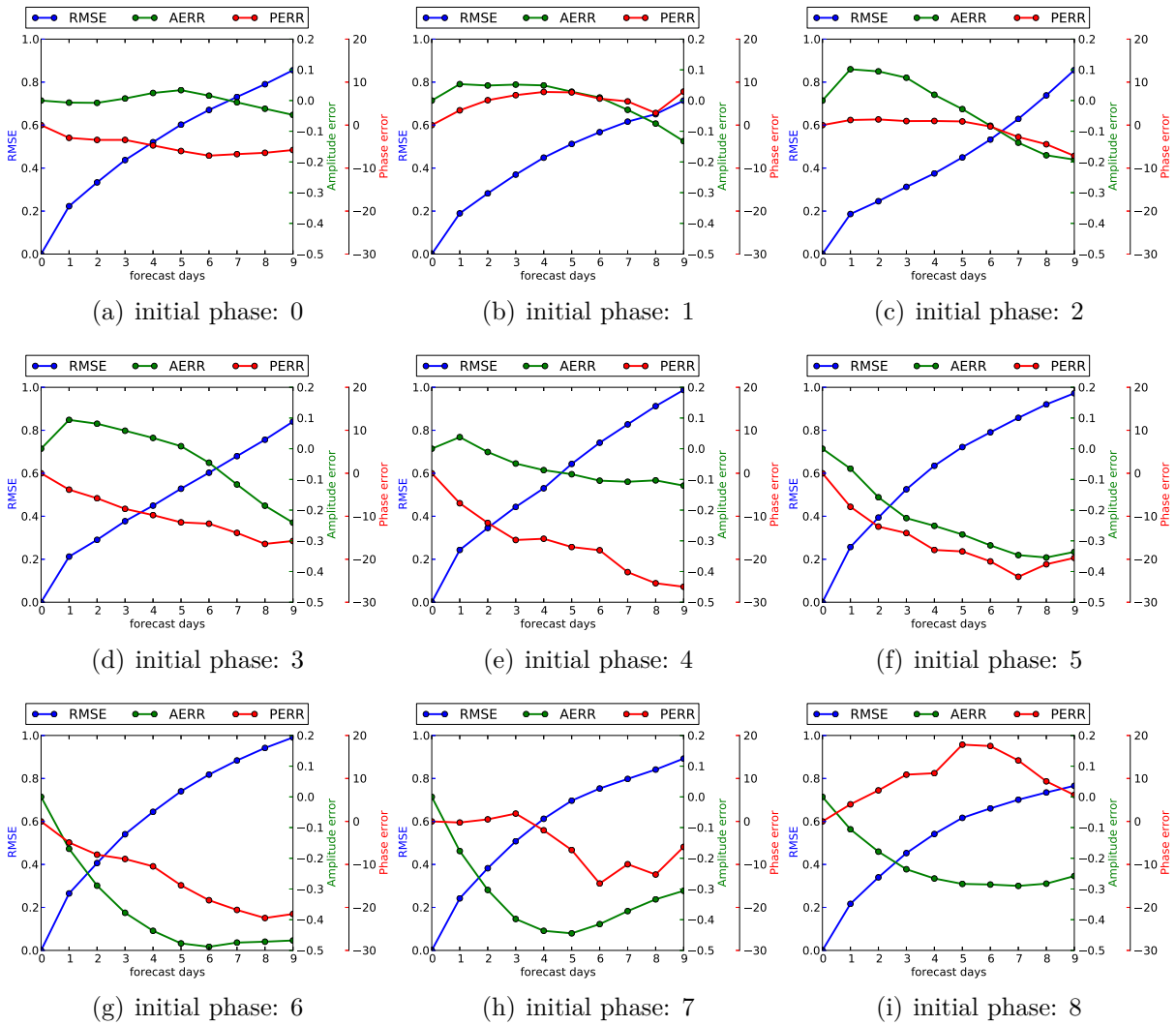


**Figure 5.6:** RMSE, PERR and AERR for the RMM-Index as a function of forecast days in the ERA-Interim reforecast dataset. The phases (0–8) at initialization time are given in the subcaptions. The forecasts and analyses are valid at phases 0–8. For example, the scores at forecast day 7 in Fig. 5.6a correspond to all cases where the MJO was in phase 0 at initialization time and in phases 0–8 at forecast day 7.

These difficulties become obvious in the MJO convection and its associated dynamical fields. The MJO convective center is located over the Maritime Continent during the initial phase 4 (Fig. 5.7). Upper-tropospheric easterlies to the west of the convection and upper-tropospheric westerlies to the east of the convection indicate divergence above the MJO convective center. The convective center as well as the upper-level zonal wind anomalies propagate eastward and weaken gradually. Nine days after initial phase 4 the convection has propagated eastward by about  $20^\circ$ . The forecasts do not show any eastward propagation of the MJO convection and its associated dynamical fields. They rather stay stationary over the Maritime Continent. In addition, the zonal wind anomalies weaken to

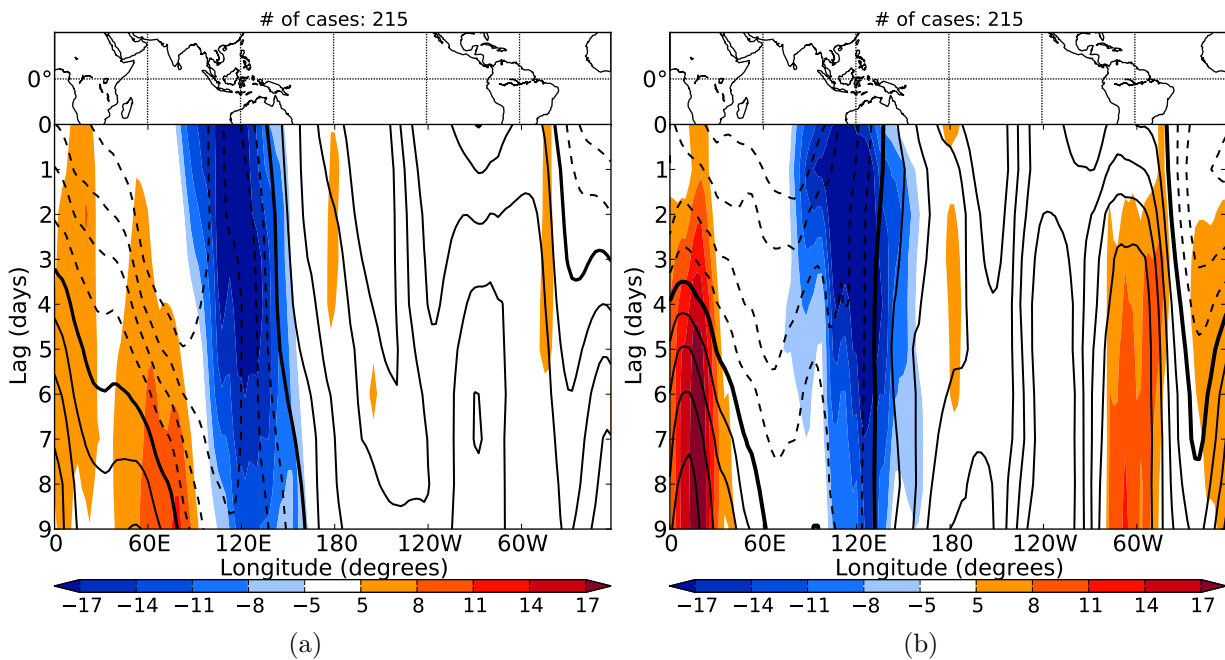


**Figure 5.7:** Hovmöller diagram of MJO filtered OLR (shading,  $W m^{-2}$ ) and 200 hPa zonal wind (black contours, contour interval  $\pm 1, 2, 3, 4 m s^{-1}$ ) averaged between  $15^{\circ}S$  to  $15^{\circ}N$ . (a) computed from analyses and (b) computed from forecasts with the initial phase 4.

quickly whereas the convective anomaly keeps its intensity. The suppression of the MJO convection and associated westerly wind anomalies are more pronounced in the forecast dataset after several days of forecast lead time.

The magnitude of PERR decrease for forecasts that were initialized during MJO phases 6 (Fig. 5.6g) and 7 (Fig. 5.6h). In particular, forecasts that were initialized during MJO phase 7 exhibit a relatively small phase error of about  $-10^{\circ}$ . However, AERR reaches highest values at this stage of the MJO life-cycle. The negative scores after about 5 days reveal that the MJO related signal weakens to quickly in the forecast dataset.

More recent modifications to the ECMWF IFS led to significant advances in the simulation of the atmospheric variability on intraseasonal time-scales (Bechtold et al., 2008; Hirons et al., 2013). Therefore, we assume that the MJO verification scores would achieve better results in a more recent operational model cycle of the ECMWF IFS. Nevertheless, the reforecast data present a dynamically consistent dataset that allows us to investigate the representation of the MJO and the linkage between the MJO and midlatitude RWP from a climatological perspective. This consistent analysis would not be possible with the operational forecast data since the model configuration changed considerably from model cycle to model cycle over the last 30 years.

**To conclude section 5.2:**

The results in this section document for the first time the performance of ERA-Interim reforecasts in representing the MJO. The findings coincide with results of previous studies by Matsueda and Endo (2011) and Hamill and Kiladis (2014) which reveal that the correct representation of the MJO convection and dynamics still poses a challenge to NWP models.

The MJO related convection has problems in crossing the Maritime Continent. This results in large phase errors for forecasts that were initialized during phases 4 and 5 of the MJO.

The MJO related signal weakens to quickly in the reforecast dataset during all phases. The errors are greatest when the forecasts were initialized during MJO phases 6 and 7.

The results of the verification score analysis is well reflected in the dynamical fields associated with the MJO related convection. The inadequate representation of the MJO dynamics may considerably impact midlatitude forecasts as the extratropical troposphere responds to the MJO convection. A too slow eastward propagation of the MJO convection modifies the propagation characteristics of the anticyclone northwest of it which leads then to a different structure of the midlatitude zonal flow.

### **5.3 The interaction between the Madden-Julian Oscillation and Rossby wave packets in a reforecast data set**

We showed in section 5.1 that the synoptic-scale RWP occurrence frequency anomalies in the ERA-Interim reanalysis data revealed a clear variation with the MJO phases. The results in section 5.2 revealed that the correct representation of the MJO convection and dynamics still poses a challenge to NWP models. Although consistent results have been identified in several previous studies, the following question has not been addressed yet: Do the reforecast data represent the MJO related anomalies of synoptic-scale RWP occurrence frequency? Therefore, we investigate the midlatitude synoptic-scale RWP response to the MJO convection in the ERA-Interim reforecast dataset (see section 3.1) in the last part of this thesis. We identified synoptic-scale RWPs with the method of Zimin et al. (2006) using the parameters as described in section 3.3. The 20-day background flow was computed from the ERA-Interim reanalysis data.

Ten-day forecasts, valid at the analyzed MJO phases 0 to 8, exhibit a variation of RWP occurrence frequency anomalies with the MJO phase. However, the results differ quite remarkably from the analyzed variation and suggest that the forecasts generally overestimate the midlatitude RWP occurrence frequency.

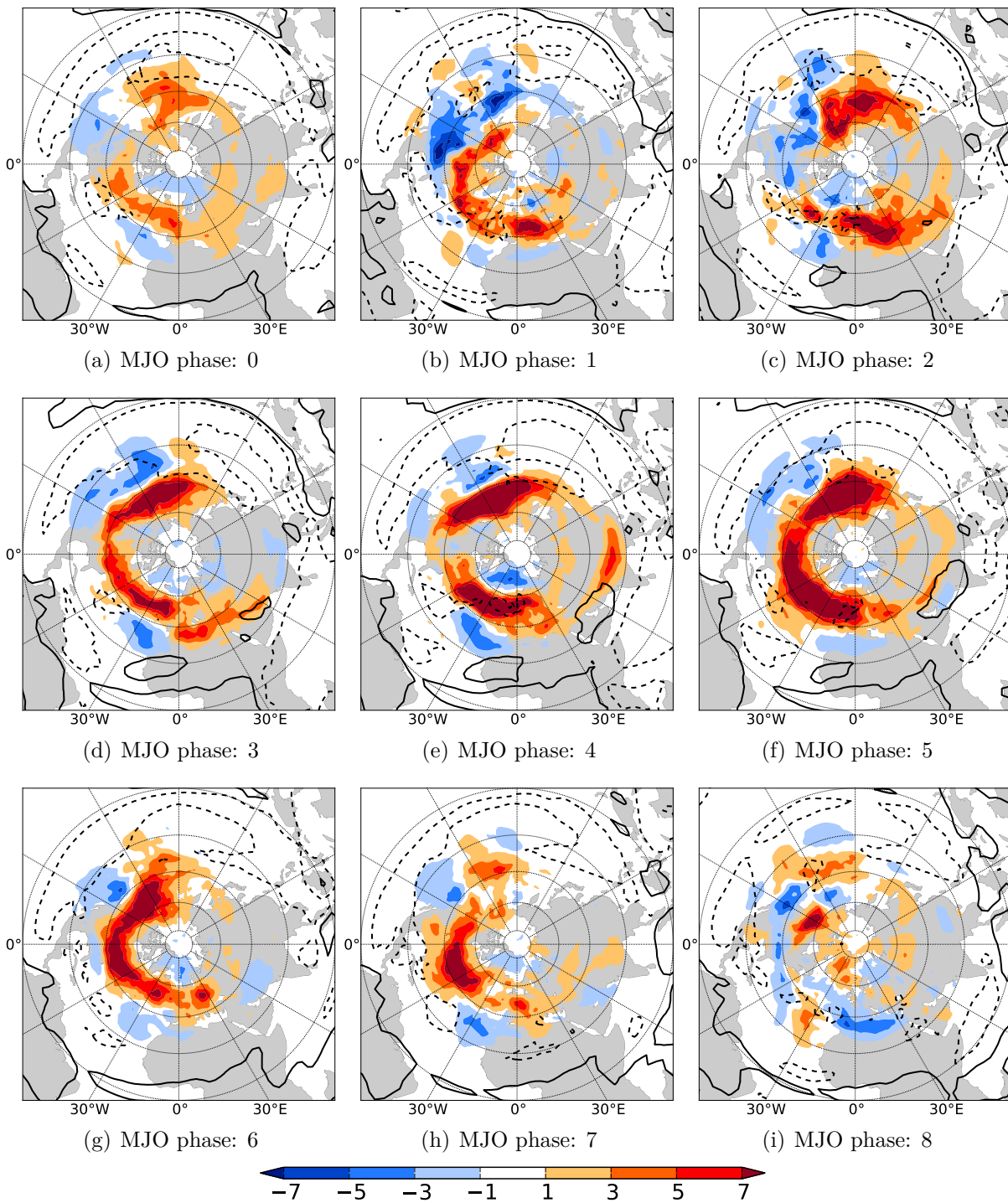


**Figure 5.8:** Anomaly of RWP occurrence frequency (shading, %) relative to December to February climatology for MJO phases 0 to 8 computed from ten-day ERA-Interim reforecasts. MJO filtered OLR anomaly (black contours,  $W m^{-2}$ ) with negative values dashed. Data are smoothed with a Gaussian filter. The analyzed anomalies of RWP occurrence frequency are shown in Fig. 5.2.

Inactive phases of the MJO are characterized by positive RWP occurrence frequency anomalies over the North Pacific and the North Atlantic (Fig. 5.8a). This stands in contrast to the analyzed RWP occurrence frequency anomalies that were negative over large portions of the Northern Hemisphere (Fig. 5.2a). The negative-positive-negative structure of the forecast RWP occurrence frequency anomalies over the North Atlantic suggests that more RWPs are trapped along a slightly stronger wave guide (Fig. 5.9d) than in the analyses (Fig. 5.9a).

The RWP occurrence frequency anomalies are much stronger during the active MJO phases 1 to 8. In the reforecast dataset, the RWP occurrence frequency is anomalously low over the eastern North Pacific and North America during MJO phase 1 (Fig. 5.8b). This coincides qualitatively with the analyzed RWP occurrence frequency anomalies (Fig. 5.2b). However, weaker positive RWP occurrence frequency anomalies south of the negative anomalies over central North America and the east Atlantic indicate that less RWPs propagate into the subtropics. Positive RWP occurrence frequency anomalies occur over the North Atlantic and Europe. These positive RWP occurrence frequency anomalies stand in contrast to the analyzed RWP distribution which revealed a decrease of RWP occurrence frequency over the North Atlantic and Europe (Fig. 5.2b). Thus, the forecast midlatitude flow is less zonal and more RWPs than observed propagate into the European region. The anomalously high RWP occurrence frequency over the European region in the forecast data set is potentially related to a too strong westerly flow over the eastern Atlantic due to a cyclonic anomaly over western Europe (not shown). The westerly wind anomaly leads to an eastward extension of the midlatitude waveguide which enables RWPs to propagate into Europe. The circulation patterns suggest that the forecasts produce a too strong positive NAO signal which projects back on the propagation characteristics of the RWPs. Hence, the inadequate representation of the planetary-scale Rossby wave response to the MJO presumably projects back on the forecast synoptic-scale RWP propagation.

Phase 2 of the MJO was characterized by rather weak RWP occurrence frequency anomalies in the analysis (Fig. 5.2c). Positive anomalies occurred mainly over the western North Pacific and over Europe. The forecasts reveal positive anomalies in the same region (Fig. 5.8c). However, these anomalies exceed the analyzed RWP occurrence frequency by more than 5%. In particular, the anomalously high RWP occurrence frequency over the western North Pacific might be related to too strong low-level cyclone activity which contribute to the amplification of upper-level wave disturbances.

The positive anomalies between 40 to 60°N over the North Pacific intensify until MJO phase 5 and reach much greater values than the anomalies in the analyses. Negative anomalies between 20 to 40°N over the North Pacific are comparable to the anomalies in the analysis. The resulting dipole structure over the North Pacific indicates a northward shift of the waveguide which coincides with the conclusions that were drawn from the analyses and are confirmed by the zonal wind anomalies in Fig. 5.9b and Fig. 5.9e.

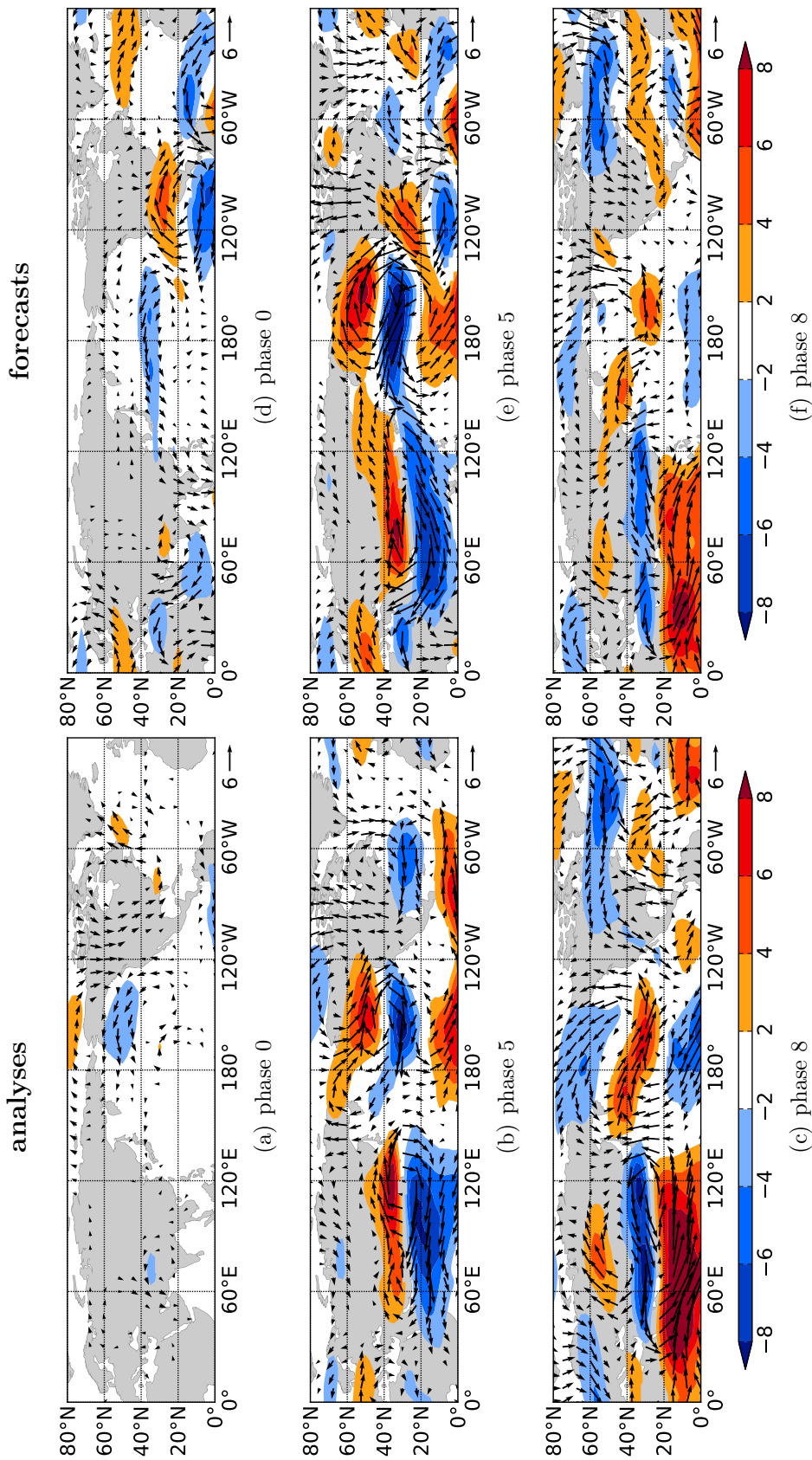


**Figure 5.9:** Zonal wind anomaly relative to DJF 1980–2009 climatology (shading,  $m s^{-1}$ ) from ERA-Interim reanalyses (left) and ten-day ERA-Interim reforecasts (right) for MJO phases as given in subsection. Horizontal wind anomaly relative to DJF 1980–2009 climatology (vectors,  $m s^{-1}$ ).

The analysis data indicated the propagation of RWPs into the subtropical eastern North Pacific during MJO phases 4 to 6 (Fig. 5.2e-g). The ten day forecasts seem to not represent the southward propagation at all (Fig. 5.8e-g). We attribute this to the fact that the forecast upper-level zonal wind is stronger between 40 to 60°N over the North Pacific and exhibits at the same time an exceptionally strong easterly wind anomaly between 20 to 40°N (Fig. 5.9e). The westerly wind anomaly leads to a decrease of the stationary wave number which indicates that RWPs are trapped along the wave guide. At the same time, the easterly wind anomaly provides an environment that is less favorable for an equatorward penetration of the RWPs. The too strong westerly and easterly winds can be attributed to the overestimation of the anticyclone over the North Pacific. Thus, the results illustrate the importance of the correct representation of planetary-scale connections between the MJO and midlatitudes for an accurate prediction of synoptic-scale RWPs. Matthews and Kiladis (1999b) suggested that this penetration of midlatitude synoptic-scale systems into the tropics modifies the convective variability. Therefore, an erroneous representation of the southward propagation of synoptic-scale RWPs might also effect the representation of the tropical convection which finally projects back on the MJO signal. It is suggested that the analyzed southward propagating RWPs are associated with the transport of westerly momentum into the tropics. A comparison of the zonal wind anomalies over the tropical Pacific supports this statement as the forecast zonal wind (Fig. 5.9e) is considerably weaker than the analyzed westerly wind (Fig. 5.9b).

The positive RWP occurrence frequency anomaly amplified remarkably from phase 3 to phase 5 over the North Atlantic in the forecast data set. It exceeds the analyzed RWP occurrence frequency anomaly during these phases. During MJO phase 4 a tripole structure has become established over the North Atlantic (Fig. 5.8e). The tripole structure indicates that RWPs are trapped along the wave guide and that less RWPs propagate into the subtropics and into polar regions. The tripole structure is typical of the distribution during the positive NAO phase (Fig. 5.3a). Thus, the results indicate that the forecasts represent the NAO like structure. The wind anomalies confirm this impression. The cyclonic circulation associated with the low pressure system over Iceland is even stronger in the forecast than in the analysis (not shown). Interestingly, the NAO related tripole structure occurs in the reforecast dataset during MJO phase 4 whereas it occurred in the reanalysis data during MJO phase 5. Future studies could investigate whether the positive phase of the NAO and the RWP response is developing too soon in the reforecast dataset.

As for the analyzed RWP occurrence frequency anomalies, the forecast RWP occurrence frequency decreases until MJO phase 8 (Fig. 5.8i). In contrast to the analyzed fields, the forecast distribution is rather inconclusive. The negative anomalies that were identified in the analyses over the eastern North Pacific and over the North Atlantic (Fig. 5.2i) are not well represented in the forecast dataset. The analyses showed a tripole structure in the RWP occurrence frequency anomalies over the North Atlantic which presumably developed in response to a negative NAO regime. The forecasts indicate a tripole structure as well. However, the tripole is much weaker which might suggest that the forecasts do not adequately represent the negative NAO regime at later stages of a MJO life-cycle. In particular, the analyzed positive RWP occurrence frequency anomaly which indicated

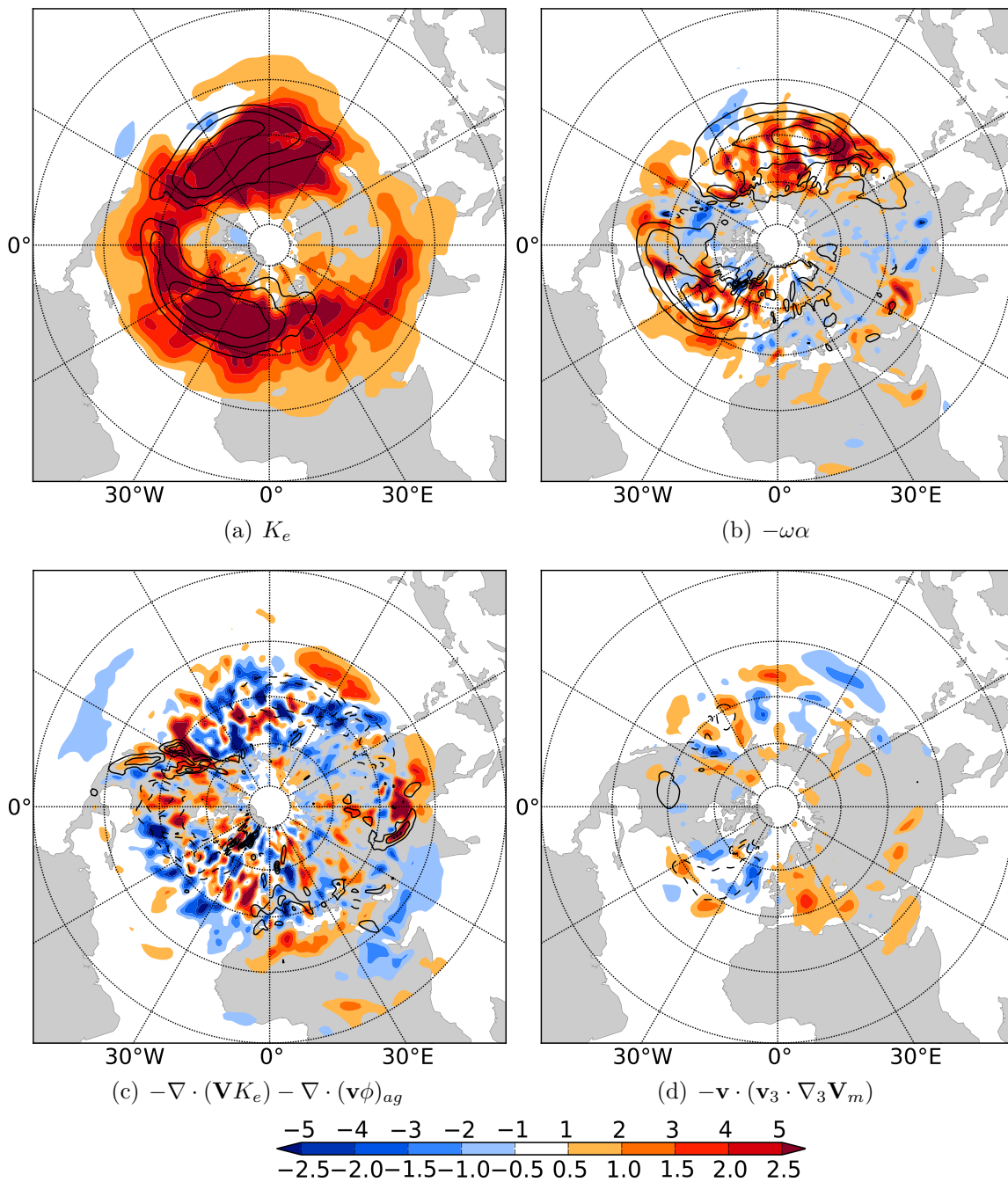


**Figure 5.10:** Anomalies of  $K_e$  budget terms relative to climatology for MJO phase 5 as represented in ten-day ERA-Interim reforecasts. (a)  $K_e$  anomaly (shaded,  $10^5 J m^{-2}$  according to upper row in colorbar), (b) baroclinic conversion anomaly, (c)  $K_e$  flux divergence anomaly and (d) barotropic conversion anomaly (shaded,  $W m^{-2}$  according to lower row in colorbar). Black contours give climatologies of (a)  $K_e$  (10, 12, 14, 16  $J m^{-2}$ ), (b) baroclinic conversion, (c)  $K_e$  flux divergence and (d) barotropic conversion ( $\pm 4, 8, 12, 16, 20 W m^{-2}$ ). Negative values are dashed.

the propagation of RWPs into the subtropics west of Africa is not well represented in the forecast dataset. In addition, the statistically significant negative anomaly over western Europe is not represented in the forecast data. The analyzed and forecast wind anomalies for phase 8 exhibit several similarities. An anticyclonic circulation over Greenland and a cyclonic circulation over the subtropical east Atlantic indicate that the forecasts represent the negative NAO phase (Fig. 5.9f). However, the easterly flow on the southern flank of the anticyclone is slightly weaker than in the analysis (Fig. 5.9c). Sensitivity experiments would help to investigate whether these small differences are sufficient to impact the propagation characteristics of RWPs significantly. These experiments are beyond the scope of this study. Lin et al. (2009) suggested that transient eddies which propagate into the tropics west of Africa have a considerable impact on the upper-level zonal winds in the tropics. They proposed that the southward propagation of RWPs transports westerly momentum into the tropics which results in an eastward extension of tropical westerly anomalies. During MJO phases 7 and 8, the analyzed westerly wind anomalies over Africa and in particular over the Indian Ocean are much stronger than forecast westerly wind anomalies. It may be an intriguing future project to investigate whether the underestimation of the westerly wind anomalies in the reforecasts can be attributed to an inaccurate representation of the synoptic-scale RWP propagation.

Finally,  $K_e$  budgets were computed from the ten-day forecasts of the ERA-Interim reforecast dataset. We used the same vertical and horizontal resolution as for the analysis data. The 20-day background wind field was computed from the ERA-Interim reanalysis data. As noted earlier, the reforecasts seem to generally overestimate the RWP occurrence frequency. We expect that the analysis of  $K_e$  budgets will give insights into why the forecasts overestimate the number of RWPs. The investigation will focus on MJO phases 5 and 8. Consistent with the overestimation of RWP occurrence frequency, the ten-day reforecasts generally overestimate the  $K_e$  (Fig. 5.10). Positive anomalies of  $K_e$  occur globally and peak in the storm track regions. Negative anomalies as observed in the analysis data do hardly occur. The systematic overestimation of  $K_e$  is potentially related to too strong baroclinic conversion. For MJO phase 5 and 8, positive anomalies of baroclinic conversion cover vast areas of the Northern Hemisphere (Fig. 5.10b; Fig. 5.11b). The dipole structure with positive (negative) anomalies over the western (eastern) North Pacific during MJO phase 5 are not well represented in the reforecasts. This indicates a too strong cyclonic activity over the eastern North Pacific in the ten-day forecasts independent of the MJO phases which stands in contrast to the conclusions drawn from the analyses. Future studies could investigate the reasons for the much higher baroclinic conversion rates and higher cyclone frequency in the reforecast dataset. The baroclinically produced  $K_e$  is dispersed into midlatitudes as indicated by large areas of divergent  $K_e$  fluxes (Fig. 5.10c). We propose that an increased cyclone frequency perturbs the midlatitude flow more frequently which is reflected in the overestimation of RWP occurrence frequency. We concluded in section 5.1 that the barotropic conversion seems to play a minor role for the generation/destruction of  $K_e$ . This statement holds also true for the  $K_e$  budgets computed from the reforecast data set (Fig. 5.10d).

The analyzed baroclinic conversion during MJO phase 8 exhibited a negative (positive) anomaly over the western (eastern North Pacific). These anomalies are not represented in the reforecast dataset (Fig. 5.11b). Instead, highly positive anomalies dominate over the western and eastern North Pacific. Thus, we expect that the decrease of cyclone frequency over the western North Pacific is not accurately forecast. We draw a similar conclusion for the North Atlantic. An analyzed negative baroclinic conversion revealed a decrease of cyclonic activity over the North Atlantic which is consistent with the negative phase of the NAO. The decrease of baroclinic conversion is not represented in the forecast dataset. Instead, a remarkably positive anomaly can be found along the North American east coast. This is consistent with a strong divergence of  $K_e$  fluxes. Interestingly, the barotropic conversion indicates an increase of  $K_e$  over the North Atlantic (Fig. 5.11d). Thus, the synoptic-scale eddies grow by extracting  $K_e$  from the background flow. The stronger baroclinic and barotropic conversion allows synoptic-scale systems to grow over the North Atlantic which might be reflected in a higher RWP occurrence frequency in the forecasts than in the analyses.

**To conclude section 5.3:**

The forecasts generally overestimate the RWP occurrence frequency as indicated by higher RWP occurrence frequency anomalies than in the analyses. In addition, the variation in RWP occurrence frequency anomalies in response to the MJO is not as prominent as in the analysis dataset. Similarly the eddy kinetic energy as well as its generation terms do not show a variation with the MJO phases as identified in section 5.1. We suggest that too strong baroclinic conversion rates independent of the MJO are associated with a higher frequency of midlatitude cyclones in the forecast dataset. These cyclones contribute to the amplification of pre-existing upper-level disturbances which projects onto the RWP occurrence frequency anomalies.

Finally, the propagation of synoptic-scale RWPs into the subtropics is not well represented in the reforecast dataset. The different propagation characteristics of synoptic-scale RWPs in analyses and forecasts can be attributed to a different representation of planetary-scale RWPs in analyses and forecasts that modify the background zonal wind. Future studies could address the reasons for this inaccurate representation and investigate the implications for the tropical dynamics.

This section answers in parts the question whether an inaccurate representation of the MJO projects back onto forecasts of midlatitude synoptic-scale Rossby waves. To the author's knowledge this question has not been investigated in previous research. The results are promising and require further studies to better understand the processes which cause the differences between forecasts and analyses. As Rossby waves contribute to the exchange of energy between the subtropics and polar regions, an overestimation of their occurrence frequency in forecasts might have implications for the dynamics and energy budgets in polar regions. As these regions are highly relevant in a changing climate it would be worthwhile to investigate the representation of RWPs, but also of the eddy kinetic energy budgets in state of the art climate models in a future study.

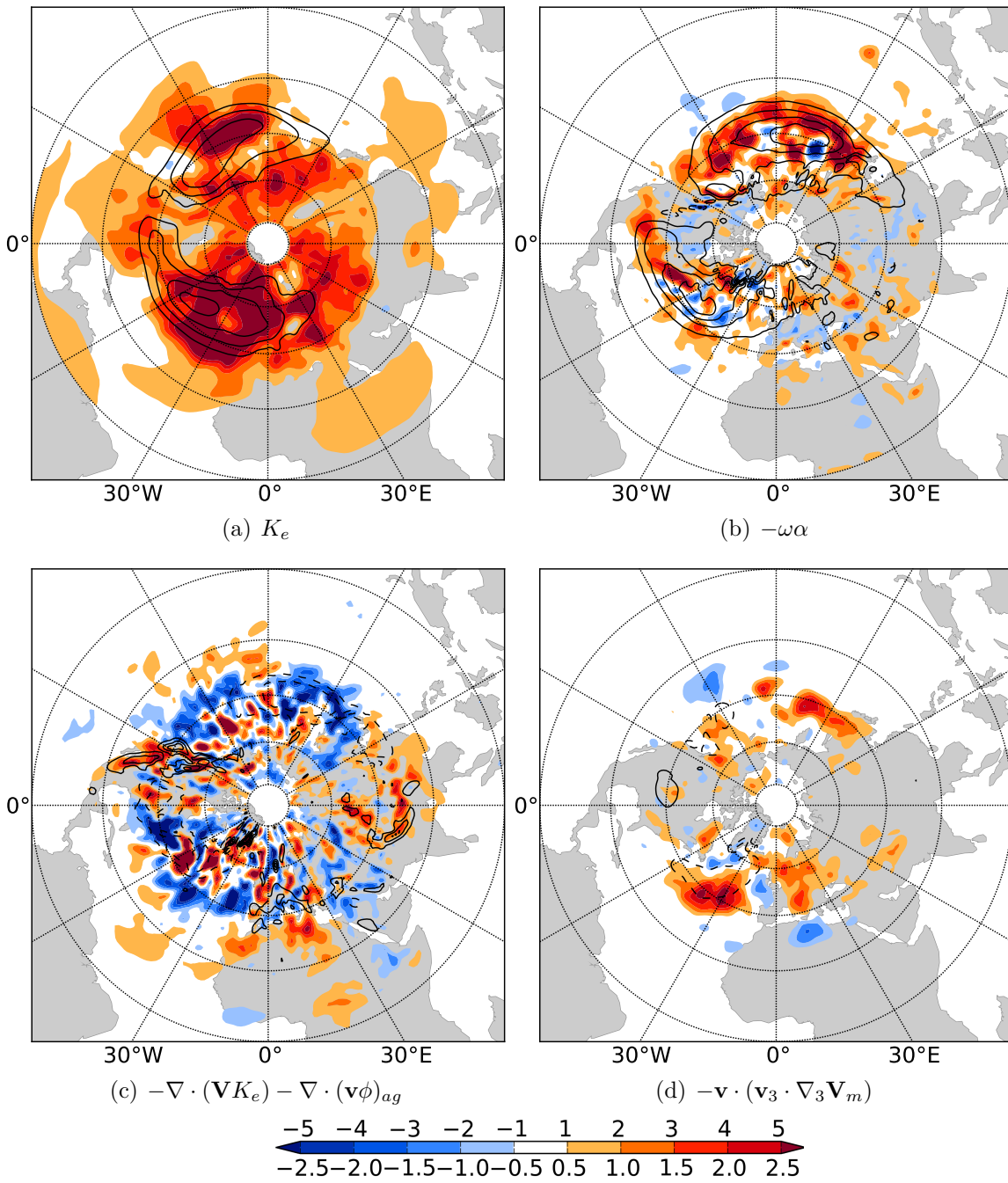


**Figure 5.11:** Same as in Fig. 5.10, but for MJO phase 8.

## 6 Conclusions and Outlook

This study focuses on the impact of two prominent tropical weather systems – tropical cyclones (TCs) and the Madden-Julian Oscillation (MJO) – on the dynamics and forecasts of midlatitude Rossby wave packets (RWPs) from a climatological perspective. To the author’s knowledge this is the first study which has investigated systematically the impact of TCs that underwent extratropical transition and the impact of the MJO on synoptic-scale RWPs.

An essential part of the investigation is the identification of RWPs in ERA-Interim reanalyses and reforecasts. Two methodologies which were initially proposed by Zimin et al. (2003) and Zimin et al. (2006) enabled us to identify synoptic-scale wave packets in the upper-tropospheric meridional wind. Different assumptions are made concerning the propagation characteristics of the midlatitude RWPs. The method of Zimin et al. (2003) is based on the assumption that RWPs propagate only zonally. This assumption holds true in situations when the background flow is zonally oriented. The method of Zimin et al. (2006) assumes that RWPs propagate with the background flow and thus exhibit a zonal and meridional propagation.

We explored the question whether TCs impact the occurrence frequency and amplitude of midlatitude synoptic-scale RWPs for three different ocean basins by applying the method of Zimin et al. (2003) in the first part of this thesis. We adhered to this technique since we considered only meridional averages. In addition, we could rely on results of Glatt and Wirth (2013) who tested systematically the sensitivity of the method to the choice of various parameters. Finally, the method is computationally less expensive.

The RWP amplitude and occurrence frequency increase statistically significant downstream of 280 western North Pacific ET events in the period June to November 1980–2010 (Fig. 4.3). The RWP occurrence frequency exceeds the climatological mean by up to 20% between the western North Pacific and central North America from one day prior to four days after the ET events. The coherent signal of positive RWP occurrence frequency indicates the downstream dispersion of a Rossby wave train. There is a statistically significant increase in RWP amplitude of up to  $2 \text{ m s}^{-1}$  over the North Pacific from ET-time to four days after ET. The observed amplification of the meridional flow is consistent with recent results of Archambault et al. (2013) who found an increase of the North Pacific meridional flow pattern downstream of ET events.

114 South Indian Ocean TCs underwent ET in the period December to April 1980–2010. South Indian Ocean TCs have a statistically significant impact on RWP occurrence

frequency and amplitude, too (Fig. 4.4). The RWP occurrence frequency exceeds the climatological mean by up to 15% over the South Indian Ocean and Australia from one day prior to ET to two days after ET. Over the same region, the RWP amplitude is enhanced significantly by up to  $2 \text{ m s}^{-1}$ . In order to address the question how ET related RWPs differ from the general variability of midlatitude RWPs, we performed a statistical analysis. A Monte-Carlo approach reveals for both basins, the western North Pacific and the South Indian Ocean, that RWPs which are associated with ET events are stronger than those which are associated with midlatitude synoptic systems.

The amplitude and occurrence frequency of RWPs downstream of 124 North Atlantic ET events in the period 1980–2010 do not differ statistically significant from the general variability (Fig. 4.5). We attribute this to the fact that most of the North Atlantic ET events occur in a region where the climatological RWP occurrence frequency and amplitude exhibit comparatively high values. Thus, North Atlantic TCs potentially interact with mature and high-amplitude midlatitude RWPs instead of amplifying rather weak initial midlatitude disturbances like western North Pacific TCs do.

We determined western North Pacific ET events with downstream Rossby wave development (RW case) and without downstream Rossby wave development (noRW case). This enabled us to identify synoptic conditions which favour the development of a Rossby wave downstream of TCs in a composite framework. The results suggests that a precursor Rossby wave that emerges from the Asian continent provides favorable conditions for a downstream development (Fig. 4.10). The precursor Rossby wave is strongly amplified during the interaction with the TC which coincides with findings of Riemer and Jones (2010). They concluded that an ET system can impact the downstream flow most significantly at the leading edge of a developing baroclinic wave. Finally, the Rossby wave disperses over the North Pacific toward central North America.

We investigated the Rossby wave amplification and its downstream dispersion further via TC relative composite maps. These show the existence of a deep trough upstream of the TCs in the RW case (Fig. 4.13b; Fig. 4.16b; Fig. 4.20b). The TCs phase lock with the meridional flow on the eastern flank of this trough and propagate northward (Fig. 4.24). The midlatitude jet amplifies during the interaction with the TC by about  $10 \text{ m s}^{-1}$  and a strong ridge develops downstream of the ET event. In the noRW case, the flow upstream of the ET event is characterized by a zonal flow to the north of the TC (Fig. 4.13a; Fig. 4.16a; Fig. 4.20a). The ridge amplification downstream of the ET event is rather weak which implies weaker diabatic forcing during the interaction of the TC with the baroclinic zone and a weaker upper-level outflow. The midlatitude jet amplification is similar to the RW case which illustrates that a strong jet amplification during ET is not necessarily associated with a downstream development. This finding coincides with results by Grams et al. (2013a).

We examined the question which physical processes are essential during the excitation of a Rossby wave in a PV and  $K_e$  composite framework. Both types of analysis give a coherent picture. In the RW case, the upper-level circulation of the TC and

the divergent outflow above the ET system contribute to the initial amplification of the downstream ridge and to a sharpening of the PV gradient on the western flank of the downstream ridge (Fig. 4.15a; Fig. 4.15b). A strengthening of the PV gradient corresponds to an intensification of the jetstreak and hence to an increase of  $K_e$ . From a  $K_e$  perspective, strong ageostrophic geopotential flux convergence contributes to the jet streak intensification and to the development of a primary midlatitude  $K_e$  center on the western flank of the downstream ridge (Fig. 4.29c; Fig. 4.30c). The accumulation of  $K_e$  results presumably from the convergence of the midlatitude flow associated with the upstream trough and the divergent outflow above the ET system toward lower heights. This indicates that the interaction of the TC with the upstream midlatitude trough is essential for the initial amplification of the primary  $K_e$  center. Once this midlatitude  $K_e$  center has developed,  $K_e$  is dispersed through ageostrophic geopotential fluxes into downstream regions where it contributes to the formation of further  $K_e$  centers. These findings coincide with results from Harr and Elsberry (2000), Harr and Dea (2009), Keller et al. (2014) and the conceptual model by Orlanski and Sheldon (1995). In the noRW case, the initial advection patterns in the PV framework are fairly similar to the RW case though slightly weaker. In particular, the upper-level cyclonic anomaly associated with the TC circulation contributes less effectively to the amplification of the ridge-trough couplet. The divergent outflow leads to a jet streak intensification, but not to an amplification of the downstream ridge. This is confirmed by results in the  $K_e$  framework. Convergence of ageostrophic fluxes leads to an acceleration of the midlatitude jet, but not to the amplification of the midlatitude meridional flow (Fig. 4.30d).

In the RW case, the divergent outflow above the ET system intensifies remarkably until ET-time (Fig. 4.22b). The divergent outflow is much stronger in the RW case than in the noRW case. Quasi-geostrophic forcing diagnostics suggest that about 50% of the upward mass flux and thus about 50% of the divergent outflow can be attributed to QG vertical motion (Fig. 4.23). Thus, both the convectively driven outflow of the TC and divergence through QG vertical motion contribute equally important to the divergent outflow during ET. The stronger divergent outflow in the RW case is associated with an enhanced negative PV advection which suggests a stronger ridge amplification. The advection of low-PV air through the anticyclonic flow associated with the downstream ridge itself contributes to the ridge amplification at later stages of the ET. In addition to that, we expect a stronger ridge amplification in the RW case through WCB-like transport of low-PV air. About 50% more WCB-like trajectories in the RW case than in the noRW case transport diabatically generated low PV air into the upper-troposphere (Fig. 4.25) and contribute thus to a stronger ridge amplification. From a  $K_e$  perspective, the greater number of slantwise ascending WCB-like trajectories in the RW case corresponds to a much stronger baroclinic conversion in the RW case than in the noRW case (Fig. 4.31a; Fig. 4.31b). Baroclinically produced  $K_e$  is still dispersed through the divergence of the ageostrophic geopotential fluxes into the midlatitude flow so that the TCs feed the downstream  $K_e$  center with additional  $K_e$  (Fig. 4.31c). The accumulation of  $K_e$  via ageostrophic geopotential flux convergence occurs primarily on the eastern flank of the downstream ridge. This reveals the amplification of a trough as part of the downstream development. The PV perspective reveals that it is the

anticyclonic anomaly associated with the downstream ridge that leads to the deepening of the downstream trough.

An important mechanism that becomes evident in the PV framework and that has been addressed in several previous studies is the phase locking between the TC and the upstream trough (e.g. Ritchie and Elsberry, 2007; Scheck et al., 2011b; Grams et al., 2013a; Riemer and Jones, 2013). The upper-level anticyclone allows the TC to move westward relative to the mean flow so that it phases favorably with the upstream trough. The phase-locking between the trough and the TC results in a stronger meridional displacement of the TC than in the noRW case (Fig. 4.24).

Rossby waves have been identified as precursors of high impact weather events (Martius et al., 2008; Wirth and Eichhorn, 2014; Screen and Simmonds, 2014). Thus, we hypothesize that regions downstream of western North Pacific and South Indian Ocean ET events may be affected more frequently by high impact weather events during seasons with an increased frequency of ET events. The Rossby wave dispersion downstream of ET events is presumably accompanied by low-level cyclogenesis ahead of the developing downstream troughs. A future study could investigate the impact of ET events on the occurrence frequency of surface cyclones and compare the intensity of these cyclones to the intensity of extratropical cyclones that develop independently of ET events. Rossby waves that travel along the waveguide may break under certain conditions. Anticyclonically breaking Rossby waves may lead to long-lasting blocking events whereas cyclonically breaking Rossby waves may cause intense precipitation that lead to flooding events. Therefore, it would be worthwhile to also investigate systematically the impact of TCs that undergo ET on the occurrence frequency, but also on the types of Rossby wave breaking events in downstream regions. The systematic exploration of a possible linkage between the ET of TCs and severe weather events downstream would be another valuable research opportunity. Finally, our results reveal a modification of synoptic-scale RWPs through TCs. However, we hypothesize that there is also a modification of planetary-scale Rossby waves which impact the weather on longer time-scales. The verification of this hypothesis through observational data and/or idealized numerical experiments would be a challenging research opportunity.

As initial perturbations and forecast uncertainties associated with the ET events tend to spread into downstream regions with a midlatitude Rossby wave train (Harr et al., 2008; Reynolds et al., 2009; Anwender et al., 2010) the forecasts of the severe weather events downstream of the ET events may pose considerable challenges to forecasters. The presented composite analyses suggest that the region between the TC outflow and midlatitude upstream trough is essential to the initial Rossby wave amplification. Sensitivity experiments would help to verify this statement and to develop observing strategies concerning forecasts of the downstream flow evolution. The development of a metric based on several parameters such as the strength of the divergent outflow, the distance between an upstream trough and the TC etc. could help to classify TCs prior to ET concerning their potential downstream impact.

The MJO related convection is associated with the poleward dispersion of planetary-scale Rossby waves. Previous work has shown that the circulation anomalies related to these planetary-scale Rossby waves modify the midlatitude background flow. Thus, the MJO impacts indirectly the distribution and the propagation characteristics of synoptic-scale RWPs. For the first time, this study investigates a potential impact of the MJO convection on the occurrence frequency of synoptic-scale RWPs with an object-based approach for the period December to February 1980–2009.

First, we examined the question whether and how the synoptic-scale RWP occurrence frequency varies with the location of the MJO convectively active region. The RWP occurrence frequency anomalies show a prominent variation with the active MJO phases 1–8 (according to Wheeler and Hendon, 2004). Strongest positive anomalies of RWP occurrence frequency occur in midlatitudes when the MJO convection is located over the Indian Ocean and the Maritime Continent, i.e. during MJO phases 3–5 (Fig. 5.2d-f). Centers of maximum RWP occurrence frequency are the North Pacific and North Atlantic during these phases. The spatial distribution of the anomalies suggests that the propagation characteristics of RWPs respond to the structure of planetary-scale Rossby waves that developed in response to the MJO. During MJO phase 5 a planetary-scale Rossby wave emerges from the central North Pacific and disperses into the North Atlantic (Fig. 2.10e). It is characterized by anticyclonic anomalies over the North Pacific and eastern North America, as well as by cyclonic anomalies over western North America and over Greenland. Easterly wind anomalies on the southern flank of the anticyclonic anomaly over the North Pacific lead to a weaker waveguide so that RWPs may leak out of the westerly flow and propagate into the (sub)tropics. This results in a positive RWP occurrence frequency over the subtropical North Pacific along the dateline. A region of enhanced convection developed to the southeast of the positive RWP occurrence frequency. Kiladis and Weickmann (1992) and Kiladis and Weickmann (1997) have shown that tropical convection in the central and eastern Pacific is induced by equatorward propagating waves. The equatorward propagating waves reduce static stability, provide upper-level forcing, and thus favor the conditions for convective activity. As the enhanced convective activity is represented in the MJO filtered OLR anomalies, Matthews and Kiladis (1999b) concluded that the convective anomaly which is forced from midlatitudes projects back onto intraseasonal timescales.

The RWP propagation characteristics over the North Atlantic during MJO phase 5 are determined by the cyclonic anomaly over Greenland which projects back onto the North Atlantic Oscillation index (Cassou, 2008; Lin et al., 2009). Westerly wind anomalies on the southern flank of this low pressure system lead to an anomalously strong jet over the North Atlantic. Rossby wave packets propagate eastward along the waveguide and do not exhibit a north- or southward deflection. The spatial distribution of the RWP occurrence frequency anomalies during MJO phase 5 is comparable to the RWP occurrence frequency during positive phases of the NAO which occur preferentially during MJO phase 4. Due to a lag of one MJO phase between the NAO establishment in response to the MJO and the NAO like RWP propagation characteristics, we conclude that the RWP propagation characteristics develop in response to a modified NAO.

Eddy kinetic energy composites coincide well with the RWP occurrence frequency anomalies. Positive (negative)  $K_e$  anomalies (Fig. 5.4a) are approximately collocated with positive (negative) RWP occurrence frequency anomalies (Fig. 5.2f) during MJO phase 5. A positive anomaly of baroclinic conversion over the western North Pacific during this phase of the MJO indicates an enhanced generation of  $K_e$  through cyclonic activity (Fig. 5.4b). The baroclinically generated  $K_e$  is advected into midlatitudes as indicated by a strong divergence of  $K_e$  fluxes (Fig. 5.4c). This  $K_e$  is accumulated in the midlatitude flow and therefore associated with an amplification of upper-level wave disturbances.

The anomalies of RWP occurrence frequency reverse during MJO phase 8. Significantly negative anomalies occur over the North Pacific and over the North Atlantic (Fig. 5.2i). In particular, the negative anomaly over the North Atlantic seems to be strongly coupled to the planetary-scale flow configuration. Planetary-scale Rossby wave dispersion in response to suppressed MJO convection leads to a strong anticyclone over Greenland and hence preferentially to a negative NAO (Cassou, 2008; Lin et al., 2009). Midlatitude easterlies on the southern flank of the anticyclone lead to a weaker jet over the North Atlantic (Fig. 2.10h). The weaker jet allows RWPs to leak out of the jet and to propagate southward. The southward propagation is depicted by a significantly positive RWP occurrence frequency over the subtropical North Atlantic. Similar to the situation over the eastern Pacific during MJO phase 5, the penetration of RWPs into the subtropical North Atlantic may enhance convective activity through a reduction of static stability and upper-level forcing. Lin et al. (2009) suggested that the southward propagation of extratropical eddies into the subtropics over the east Atlantic may even initiate a new MJO life-cycle. Therefore, a correct representation of the southward propagation of RWPs into the subtropics in forecasts is invaluable.

Although it has been shown in previous work that the MJO has a prominent impact on the midlatitude synoptic-scale Rossby wave variability and that forecasts do not adequately represent the MJO, not a single study has investigated the question whether reforecast data represent the MJO related synoptic-scale Rossby wave variability. A calculation of RWP occurrence frequency from ten day reforecasts for the period December to February 1980–2009 and for MJO phases 1 to 8 shows that the MJO related variation of RWP occurrence frequency is less prominent in the reforecast data than in the analyses. In addition, the forecasts generally overestimate the RWP occurrence frequency anomalies in midlatitudes. The overestimation of RWP occurrence frequency coincides with a systematic overestimation of  $K_e$ . The  $K_e$  budget terms suggests that the forecasts generate too much  $K_e$  through baroclinic conversion independent of the MJO which may also impact the amplification of RWPs. The different propagation characteristics of synoptic-scale RWPs can be attributed to a different representation of planetary-scale RWPs in analyses and forecasts that modify the background zonal wind. In particular, forecasts do not adequately represent the southward propagation of RWPs over the central North Pacific during MJO phase 5 and over the eastern North Atlantic during MJO phase 8. As the southward propagation of RWPs is associated with the transport of westerly momentum into the subtropics (Matthews and Kiladis, 1999b; Lin et al., 2009), the inadequate representation of

the southward propagation may explain the differences in the tropical zonal wind anomalies in forecasts and analyses.

The results reveal that the forecasts have difficulties to accurately represent the planetary-scale Rossby wave response to the MJO convection which then modifies the propagation characteristics of synoptic-scale RWPs. We hypothesize that the representation of the climatological mean midlatitude flow in NWP models – adjacent to the representation of the MJO convection – is crucial for an accurate forecast of planetary-scale Rossby wave dispersion away from the MJO convection. Therefore, it would be worthwhile to conduct idealized experiments which test the sensitivity of the planetary-scale Rossby wave response to the representation of the midlatitude flow in NWP models. Similar to Jin and Hoskins (1995) these experiments could be initialized with an idealized heating in the tropics and the mean December to February midlatitude flow as represented in the reanalyses and in ten-day reforecasts, respectively.

The results clearly show that the midlatitude synoptic-scale RWP response varies with the MJO phases. As forecasts errors tend to propagate downstream with these RWPs (Harr et al., 2008; Reynolds et al., 2009; Anwender et al., 2010) future studies could investigate whether there are MJO phases during which forecasts errors in the MJO convective region impact midlatitude forecasts more efficient than during other MJO phases. Ensemble experiments as well as ensemble reforecast data offer promising research opportunities.



# Acknowledgment

Countless people have contributed in very different ways to achieve the point where I am now very close to: the end of my time as a PhD student. Unfortunately! The support that I received by all of you made the last three years highly enjoyable. The time went by much too quickly. Thank you all very much! At this point, I would like to thank personally

my supervisor, Prof Sarah Jones who accompanied my scientific career from a student research assistant to a PhD student, and will hopefully do so during the next years. Sarah, I am grateful for introducing me to the interesting tropical meteorology, for an incredibly fascinating research topic and for giving me the opportunity to attend international conferences which gave me the chance to meet renowned scientists and to start international collaborations.

Prof Peter Braesicke for the kind acceptance to do the proof reading and for constructive feedback on an earlier version of this thesis.

Prof Lance Bosart for inviting me to the Department of Atmospheric and Environmental Sciences (DAES) at the University at Albany, for helpful and inspiring discussions that raised several research questions and for the holistic view of atmospheric dynamics. Lance, thank you for being an amazing motivator! I am grateful to all colleagues and friends in Albany for letting me being part of a great institute and having a very enjoyable and fruitful research stay. I am looking forward to the next visit!

Dr Heather Archambault, Dr Maxi Böttcher, Lawrence Gloeckler, Dr Christian Grams, Prof Pat Harr, Prof Daniel Keyser, Prof Olivia Martius, Benjamin Moore, Dr Michael Riemer, Dr Benjamin Schenkel, Prof Heini Wernli for instructive and imaginative discussions that contributed to the success of this thesis.

Dr Erica Madonna for providing the trajectory data and giving advice for their analysis.

my working group, namely Dr Julia Keller, Hilke Lentink, Marlon Maranan, Aurelia Müller, Lisa-Ann Quandt and Dr Leonhard Scheck for invaluable discussions and very enjoyable conference stays. Thank you for being great colleagues and friends!

Dr Christian Grams for very illuminating and motivating discussions, and acquainting me with scientists at several conferences. I am grateful to my PANDOWAE fellow PhD students Paraskevi Giannakaki, Franziska Gierth, Hilke Lentink, Lisa-Ann

Quandt, Luisa Röhner, Gabriel Wolf for inspiring discussions and joyful moments during the PANDOWAE Young Scientist Meetings. All the best for the finish of your PhD!

the colleagues on the 13th floor for creating a familiar working environment. I am grateful to Friederike Schönbein and to Doris Stenschke for their permanent willingness of advising me how to solve time-consuming administrative tasks efficiently. I thank Bernhard Mühr for daily weather discussions that raised several research questions.

the Karlsruhe House of Young Scientists (KHYS) whose travel funding enabled me to meet Prof Lance Bosart and to finally spend a three month research stay in Albany. I am also thankful to the German Research Foundation (DFG) who funded the research unit PANDOWAE (FOR896). I gratefully acknowledge ECMWF for access to the ERA-Interim products through the special project “Impact of blocking and tropical-extratropical interactions on predictability in the Atlantic-European Sector”.

my parents Karl Heinz Quinting and Klaudia Quinting, and my brothers Jannis Quinting and Manuel Quinting for their overwhelming support at all times.

# List of abbreviations

AERR	amplitude error
ECMWF	European Centre for Medium-Range Weather Forecasts
EOF	Empirical Orthogonal Function
ET	extratropical transition
ITCZ	intertropical convergence zone
$K_e$	eddy kinetic energy
$K_s$	stationary wave number
lhs	left hand side
MJO	Madden-Julian Oscillation
NOAA	National Oceanic and Atmospheric Administration
NWP	numerical weather prediction
OLR	outgoing longwave radiation
PERR	phase error
PV	potential vorticity
PVU	potential vorticity unit
QG	quasi-geostrophic
rhs	right hand side
RMM-Index	real-time multivariate MJO Index
RMSE	root mean square error
RSMC	Regional Specialized Meteorological Center

RWP Rossby wave packet

TC tropical cyclone

WCB warm conveyor belt

# Bibliography

- Agustí-Panareda, A., S. L. Gray, G. C. Craig, and C. Thorncroft, 2005: The extratropical transition of tropical cyclone Lili (1996) and its crucial contribution to a moderate extratropical development. *Mon. Wea. Rev.*, **133** (6), 1562–1573.
- Agustí-Panareda, A., C. Thorncroft, G. Craig, and S. Gray, 2004: The extratropical transition of hurricane Irene (1999): A potential-vorticity perspective. *Quart. J. Roy. Meteor. Soc.*, **130** (598), 1047–1074.
- Aldrian, E., 2008: Dominant factors of Jakarta's three largest floods. *J. Hidrosfir. Indones.*, **3** (3).
- Anwender, D., S. C. Jones, M. Leutbecher, and P. A. Harr, 2010: Sensitivity experiments for ensemble forecasts of the extratropical transition of typhoon Tokage (2004). *Quart. J. Roy. Meteor. Soc.*, **136** (646), 183–200.
- Archambault, H. M., L. F. Bosart, and D. Keyser, 2007: Recurving typhoons as precursors to an early season arctic outbreak over the continental U.S. *Ninth Northeast Regional Operational Workshop*, Albany, NY, National Weather Service/Amer. Meteor. Soc., 1–55, [Available online at <http://cstar.cestm.albany.edu/nrow/nrow9/Archambault/archambault.ppt>].
- Archambault, H. M., L. F. Bosart, D. Keyser, and J. M. Cordeira, 2013: A Climatological Analysis of the Extratropical Flow Response to Recurving Western North Pacific Tropical Cyclones. *Mon. Wea. Rev.*, **141**, 2325–2346.
- Atallah, E. H. and L. F. Bosart, 2003: The extratropical transition and precipitation distribution of Hurricane Floyd (1999). *Mon. Wea. Rev.*, **131** (6).
- Barlow, M., M. Wheeler, B. Lyon, and H. Cullen, 2005: Modulation of daily precipitation over southwest Asia by the Madden-Julian oscillation. *Mon. Wea. Rev.*, **133** (12), 3579–3594.
- Bechtold, P., M. Köhler, T. Jung, F. Doblas-Reyes, M. Leutbecher, M. J. Rodwell, F. Vitart, and G. Balsamo, 2008: Advances in simulating atmospheric variability with the ECMWF model: From synoptic to decadal time-scales. *Quarterly Journal of the Royal Meteorological Society*, **134** (634), 1337–1351.
- Becker, E. J., E. H. Berbery, and R. W. Higgins, 2011: Modulation of cold-season US daily precipitation by the Madden-Julian Oscillation. *J. Climate*, **24** (19), 5157–5166.

- Berrisford, P., D. Dee, K. Fielding, M. Fuentes, P. Kallberg, S. Kobayashi, S. Uppala, et al., 2009: The ERA-Interim Archive. *ERA report series*, **(1)**, 1–16.
- Blackmon, M. L., Y. Lee, and J. M. Wallace, 1984: Horizontal structure of 500 mb height fluctuations with long, intermediate and short time scales. *J. Atmos. Sci.*, **41 (6)**, 961–980.
- Bond, N. A. and G. A. Vecchi, 2003: The Influence of the Madden-Julian Oscillation on Precipitation in Oregon and Washington. *Wea. Forecasting*, **18 (4)**, 600–613.
- Bosart, L. F. and D. B. Dean, 1991: The Agnes rainstorm of June 1972: Surface feature evolution culminating in inland storm redevelopment. *Wea. Forecasting*, **6 (4)**, 515–537.
- Brand, S. and C. Guard, 1979: An observational study of extratropical storms that evolved from tropical cyclones in the western North Pacific. *J. Meteor. Soc. Japan*, **57 (3)**, 479–483.
- Browning, K., P. Panagi, and G. Vaughan, 1998: Analysis of an ex-tropical cyclone after its reintensification as a warm-core extratropical cyclone. *Quart. J. Roy. Meteor. Soc.*, **124 (551)**, 2329–2356.
- Böttcher, M. and H. Wernli, 2011: Life cycle study of a diabatic rossby wave as a precursor to rapid cyclogenesis in the north atlantic-dynamics and forecast performance. *Mon. Wea. Rev.*, **139 (6)**, 1861–1878.
- Carlson, T. N., 1980: Airflow through midlatitude cyclones and the comma cloud pattern. *Mon. Wea. Rev.*, **108 (10)**, 1498–1509.
- Cassou, C., 2008: Intraseasonal interaction between the Madden-Julian oscillation and the North Atlantic oscillation. *Nature*, **455 (7212)**, 523–527.
- Chang, E. K., 1993: Downstream development of baroclinic waves as inferred from regression analysis. *J. Atmos. Sci.*, **50 (13)**, 2038–2053.
- Chang, E. K., 1999: Characteristics of wave packets in the upper troposphere. Part II: Seasonal and hemispheric variations. *J. Atmos. Sci.*, **56 (11)**, 1729–1747.
- Chang, E. K., 2000: Wave packets and life cycles of troughs in the upper troposphere: Examples from the Southern Hemisphere summer season of 1984/85. *Mon. Wea. Rev.*, **128 (1)**.
- Chang, E. K. and D. B. Yu, 1999: Characteristics of wave packets in the upper troposphere. Part I: Northern Hemisphere winter. *J. Atmos. Sci.*, **56 (11)**, 1708–1728.
- Charney, J. G., 1947: The dynamics of long waves in a baroclinic westerly current. *J. Meteor.*, **4 (5)**, 136–162.
- Clough, S., C. Davitt, and A. Thorpe, 1996: Attribution concepts applied to the omega equation. *Quart. J. Roy. Meteor. Soc.*, **122 (536)**, 1943–1962.
- Cordeira, J. M. and L. F. Bosart, 2010: The Antecedent Large-Scale Conditions of the “Perfect Storms” of Late October and Early November 1991. *Mon. Wea. Rev.*, **138 (7)**.

- Davis, C. A. and K. A. Emanuel, 1991: Potential vorticity diagnostics of cyclogenesis. *Mon. Wea. Rev.*, **119** (8), 1929–1953.
- Dee, D., S. Uppala, A. Simmons, P. Berrisford, P. Poli, S. Kobayashi, U. Andrae, M. Balmaseda, G. Balsamo, P. Bauer, et al., 2011: The ERA-Interim reanalysis: Configuration and performance of the data assimilation system. *Quart. J. Roy. Meteor. Soc.*, **137** (656), 553–597.
- Deng, Y. and T. Jiang, 2011: Intraseasonal modulation of the North Pacific storm track by tropical convection in boreal winter. *J. Climate*, **24** (4), 1122–1137.
- Dole, R., M. Hoerling, A. Kumar, J. Eischeid, J. Perlwitz, X.-W. Quan, G. Kiladis, R. Webb, D. Murray, M. Chen, et al., 2014: The Making of An Extreme Event: Putting the Pieces Together. *Bull. Amer. Meteor. Soc.*, **95** (3), 427–440.
- Eady, E., 1949: Long waves and cyclone waves. *Tellus*, **1** (3), 33–52.
- Emanuel, K., 2003: Tropical cyclones. *Annu. Rev. Earth Planet. Sci.*, **31** (1), 75–104.
- Emanuel, K. A., 1986: An air-sea interaction theory for tropical cyclones. Part I: Steady-state maintenance. *J. Atmos. Sci.*, **43** (6), 585–605.
- Evans, J. L. and R. E. Hart, 2003: Objective indicators of the life cycle evolution of extratropical transition for Atlantic tropical cyclones. *Mon. Wea. Rev.*, **131** (5), 909–925.
- Gill, A., 1980: Some simple solutions for heat-induced tropical circulation. *Quart. J. Roy. Meteor. Soc.*, **106** (449), 447–462.
- Glatt, I., A. Dörnbrack, S. Jones, J. Keller, O. Martius, A. Müller, D. H. Peters, and V. Wirth, 2011: Utility of Hovmöller diagrams to diagnose Rossby wave trains. *Tellus*, **63** (5), 991–1006.
- Glatt, I. and V. Wirth, 2013: Identifying Rossby wave trains and quantifying their properties. *Quart. J. Roy. Meteor. Soc.*
- Grams, C. M., S. C. Jones, and C. A. Davis, 2013a: The impact of Typhoon Jangmi (2008) on the midlatitude flow. Part II: Downstream evolution. *Quart. J. Roy. Meteor. Soc.*, **139** (677), 2165–2180.
- Grams, C. M., S. C. Jones, C. A. Davis, P. A. Harr, and M. Weissmann, 2013b: The impact of Typhoon Jangmi (2008) on the midlatitude flow. Part I: Upper-level ridgebuilding and modification of the jet. *Quart. J. Roy. Meteor. Soc.*, **139** (677), 2148–2164.
- Grams, C. M., H. Wernli, M. Böttcher, J. Čampa, U. Corsmeier, S. C. Jones, J. H. Keller, C.-J. Lenz, and L. Wiegand, 2011: The key role of diabatic processes in modifying the upper-tropospheric wave guide: a North Atlantic case-study. *Quart. J. Roy. Meteor. Soc.*, **137** (661), 2174–2193.
- Griffin, K. S. and L. F. Bosart, 2014: The Extratropical Transition of Tropical Cyclone Edisoana (1990). *Mon. Wea. Rev.*, (2014).

- Hadley, G., 1735: Concerning the Cause of the General Trade-Winds. *Philosophical Transactions*, **39 (436-444)**, 58–62.
- Hakim, G. J., 2003: Developing wave packets in the North Pacific storm track. *Mon. Wea. Rev.*, **131 (11)**.
- Hakim, G. J., C. Snyder, and D. J. Muraki, 2002: A new surface model for cyclone-anticyclone asymmetry. *J. Atmos. Sci.*, **59 (16)**, 2405–2420.
- Hall, J. D., A. J. Matthews, and D. J. Karoly, 2001: The Modulation of Tropical Cyclone Activity in the Australian Region by the Madden–Julian Oscillation. *Mon. Wea. Rev.*, **129 (12)**.
- Hamill, T. M. and G. N. Kiladis, 2014: Skill of the MJO and Northern Hemisphere blocking in GEFS medium-range reforecasts. *Mon. Wea. Rev.*, **142 (2)**, 868–885.
- Harr, P. A., D. Anwender, and S. C. Jones, 2008: Predictability associated with the downstream impacts of the extratropical transition of tropical cyclones: Methodology and a case study of Typhoon Nabi (2005). *Mon. Wea. Rev.*, **136 (9)**.
- Harr, P. A. and J. M. Dea, 2009: Downstream development associated with the extratropical transition of tropical cyclones over the western North Pacific. *Mon. Wea. Rev.*, **137 (4)**.
- Harr, P. A. and R. L. Elsberry, 2000: Extratropical transition of tropical cyclones over the western North Pacific. Part I: Evolution of structural characteristics during the transition process. *Mon. Wea. Rev.*, **128 (8)**.
- Harr, P. A., R. L. Elsberry, and T. F. Hogan, 2000: Extratropical transition of tropical cyclones over the western North Pacific. Part II: The impact of midlatitude circulation characteristics. *Mon. Wea. Rev.*, **128 (8)**.
- Hart, R. E., 2003: A cyclone phase space derived from thermal wind and thermal asymmetry. *Mon. Wea. Rev.*, **131 (4)**, 585–616.
- Hendon, H. H. and M. L. Salby, 1994: The life cycle of the Madden-Julian oscillation. *J. Atmos. Sci.*, **51 (15)**, 2225–2237.
- Hirons, L., P. Inness, F. Vitart, and P. Bechtold, 2013: Understanding advances in the simulation of intraseasonal variability in the ECMWF model. Part I: The representation of the MJO. *Quarterly Journal of the Royal Meteorological Society*, **139 (675)**, 1417–1426.
- Ho, C.-H., J.-H. Kim, J.-H. Jeong, H.-S. Kim, and D. Chen, 2006: Variation of tropical cyclone activity in the South Indian Ocean: El Niño–Southern Oscillation and Madden-Julian Oscillation effects. *J. Geophys. Res.*, **111 (D22)**.
- Hoskins, B., 1990: Theory of extratropical cyclones. *Extratropical Cyclones: The Erik Palmén Memorial Volume*, 64–80.
- Hoskins, B., I. Draghici, and H. Davies, 1978: A new look at the  $\omega$ -equation. *Quart. J. Roy. Meteor. Soc.*, **104 (439)**, 31–38.

- Hoskins, B. J., 1975: The geostrophic momentum approximation and the semi-geostrophic equations. *J. Atmos. Sci.*, **32** (2), 233–242.
- Hoskins, B. J. and T. Ambrizzi, 1993: Rossby wave propagation on a realistic longitudinally varying flow. *J. Atmos. Sci.*, **50** (12), 1661–1671.
- Hoskins, B. J., M. McIntyre, and A. W. Robertson, 1985: On the use and significance of isentropic potential vorticity maps. *Quart. J. Roy. Meteor. Soc.*, **111** (470), 877–946.
- Hovmöller, E., 1949: The Trough-and-Ridge diagram. *Tellus*, **1** (2), 62–66.
- Hsu, H.-H., B. J. Hoskins, and F.-F. Jin, 1990: The 1985/86 intraseasonal oscillation and the role of the extratropics. *J. Atmos. Sci.*, **47** (7), 823–839.
- Jeong, J.-H., C.-H. Ho, B.-M. Kim, and W.-T. Kwon, 2005: Influence of the Madden-Julian Oscillation on wintertime surface air temperature and cold surges in east Asia. *J. Geophys. Res.*, **110** (D11).
- Jin, F. and B. J. Hoskins, 1995: The direct response to tropical heating in a baroclinic atmosphere. *J. Atmos. Sci.*, **52** (3), 307–319.
- Jones, C., 2000: Occurrence of extreme precipitation events in California and relationships with the Madden-Julian oscillation. *J. Climate*, **13** (20), 3576–3587.
- Jones, S. C., 2002: *The dynamics of tropical cyclones in vertical shear and of their extratropical transition*. Habilitationsschrift, Universität München, Germany.
- Jones, S. C., P. A. Harr, J. Abraham, L. F. Bosart, P. J. Bowyer, J. L. Evans, D. E. Hanley, B. N. Hanstrum, R. E. Hart, F. Lalaurette, et al., 2003: The extratropical transition of tropical cyclones: Forecast challenges, current understanding, and future directions. *Wea. Forecasting*, **18** (6).
- Keller, J. H., S. C. Jones, and P. A. Harr, 2014: An eddy kinetic energy view of physical and dynamical processes in distinct forecast scenarios for the extratropical transition of two tropical cyclones. *Mon. Wea. Rev.*, (2014).
- Kiladis, G. N. and K. M. Weickmann, 1992: Extratropical forcing of tropical Pacific convection during northern winter. *Mon. Wea. Rev.*, **120** (9), 1924–1939.
- Kiladis, G. N. and K. M. Weickmann, 1997: Horizontal structure and seasonality of large-scale circulations associated with submonthly tropical convection. *Mon. Wea. Rev.*, **125** (9), 1997–2013.
- Kitabatake, N., 2002: Extratropical transformation of Typhoon Vicki (9807): Structural change and the role of upper-tropospheric disturbances. *J. Meteor. Soc. Japan*, **80** (2), 229–247.
- Klein, P. M., P. A. Harr, and R. L. Elsberry, 2000: Extratropical transition of western North Pacific tropical cyclones: An overview and conceptual model of the transformation stage. *Wea. Forecasting*, **15** (4).

- Klein, P. M., P. A. Harr, and R. L. Elsberry, 2002: Extratropical transition of western North Pacific tropical cyclones: Midlatitude and tropical cyclone contributions to reintensification. *Mon. Wea. Rev.*, **130** (9), 2240–2259.
- Knabb, R. D., J. R. Rhome, and D. P. Brown, 2005: *Tropical cyclone report: Hurricane Katrina, 23-30 august 2005*. National Hurricane Center.
- Knapp, K. R., M. C. Kruk, D. H. Levinson, H. J. Diamond, and C. J. Neumann, 2010: The international best track archive for climate stewardship (IBTrACS) unifying tropical cyclone data. *Bull. Amer. Meteor. Soc.*, **91** (3), 363–376.
- Knutson, T. R. and K. M. Weickmann, 1987: 30-60 day atmospheric oscillations: Composite life cycles of convection and circulation anomalies. *Mon. Wea. Rev.*, **115** (7), 1407–1436.
- Kornegay, F. C. and D. G. Vincent, 1976: Kinetic energy budget analysis during interaction of Tropical Storm Candy (1968) with an extratropical frontal system. *Mon. Wea. Rev.*, **104** (7), 849–859.
- Lackmann, G., 2011: *Midlatitude Synoptic Meteorology: Dynamics, Analysis, and Forecasting*. Tech. rep., Am. Meteor. Soc., ISBN 978-1-878220-10-3, 345 pp.
- Lee, S. and I. M. Held, 1993: Baroclinic wave packets in models and observations. *J. Atmos. Sci.*, **50** (10), 1413–1428.
- Liebmann, B., H. H. Hendon, and J. D. Glick, 1994: The relationship between tropical cyclones of the western Pacific and Indian Oceans and the Madden-Julian oscillation. *J. Meteor. Soc. Japan*, **72** (3), 401–412.
- Lin, H., G. Brunet, and J. Derome, 2008: Forecast skill of the Madden-Julian Oscillation in two Canadian atmospheric models. *Mon. Wea. Rev.*, **136** (11), 4130–4149.
- Lin, H., G. Brunet, and J. Derome, 2009: An observed connection between the North Atlantic Oscillation and the Madden-Julian oscillation. *J. Climate*, **22** (2), 364–380.
- Madden, R. A. and P. R. Julian, 1971: Detection of a 40–50 day oscillation in the zonal wind in the tropical Pacific. *J. Atmos. Sci.*, **28** (5), 702–708.
- Madden, R. A. and P. R. Julian, 1972: Description of global-scale circulation cells in the tropics with a 40–50 day period. *J. Atmos. Sci.*, **29** (6), 1109–1123.
- Madonna, E., H. Wernli, H. Joos, and O. Martius, 2014: Warm conveyor belts in the ERA-Interim dataset (1979–2010). Part I: Climatology and potential vorticity evolution. *J. Climate*, **27** (1), 3–26.
- Maloney, E. D. and D. L. Hartmann, 2001: The Madden-Julian oscillation, barotropic dynamics, and North Pacific tropical cyclone formation. Part I: Observations. *J. Atmos. Sci.*, **58** (17), 2545–2558.
- Martius, O., C. Schierz, and H. Davies, 2008: Far-upstream precursors of heavy precipitation events on the Alpine south-side. *Quart. J. Roy. Meteor. Soc.*, **134** (631), 417–428.

- Martius, O., C. Schwierz, and H. Davies, 2010: Tropopause-Level Waveguides. *J. Atmos. Sci.*, **67** (3).
- Martius, O., C. Schwierz, and H. C. Davies, 2006: A refined Hovmöller diagram. *Tellus*, **58** (2), 221–226.
- Matano, H. and M. Sekioka, 1971: Some aspects of extratropical transformation of a tropical cyclone. *J. Meteor. Soc. Japan*, **49**, 736–743.
- Matsueda, M. and H. Endo, 2011: Verification of medium-range MJO forecasts with TIGGE. *Geophys. Res. Lett.*, **38** (11).
- Matsuno, T., 1966: Quasi-geostrophic motions in the equatorial area. *J. Meteor. Soc. Japan*, **44** (1), 25–43.
- Matthews, A. J., 2000: Propagation mechanisms for the Madden-Julian Oscillation. *Quart. J. Roy. Meteor. Soc.*, **126** (569), 2637–2651.
- Matthews, A. J., B. J. Hoskins, and M. Masutani, 2004: The global response to tropical heating in the Madden-Julian oscillation during the northern winter. *Quart. J. Roy. Meteor. Soc.*, **130** (601), 1991–2011.
- Matthews, A. J. and G. N. Kiladis, 1999a: Interactions between ENSO, Transient Circulation, and Tropical Convection over the Pacific. *J. Climate*, **12** (10), 3062–3086.
- Matthews, A. J. and G. N. Kiladis, 1999b: The tropical-extratropical interaction between high-frequency transients and the Madden-Julian oscillation. *Mon. Wea. Rev.*, **127**, 661–677.
- McTaggart-Cowan, R., J. Gyakum, and M. Yau, 2001: Sensitivity testing of extratropical transitions using potential vorticity inversions to modify initial conditions: Hurricane Earl case study. *Mon. Wea. Rev.*, **129** (7), 1617–1636.
- Mendelsohn, R., K. Emanuel, S. Chonabayashi, and L. Bakkensen, 2012: The impact of climate change on global tropical cyclone damage. *Nature Climate Change*, **2** (3), 205–209.
- Milliff, R. F. and R. A. Madden, 1996: The existence and vertical structure of fast, eastward-moving disturbances in the equatorial troposphere. *J. Atmos. Sci.*, **53** (4), 586–597.
- Mo, K. C., 2000: The association between intraseasonal oscillations and tropical storms in the Atlantic basin. *Mon. Wea. Rev.*, **128** (12), 4097–4107.
- Moore, R. W., O. Martius, and T. Spengler, 2010: The Modulation of the Subtropical and Extratropical Atmosphere in the Pacific Basin in Response to the Madden-Julian Oscillation. *Mon. Wea. Rev.*, **138** (7).
- Murakami, H., 2014: Tropical cyclones in reanalysis data sets. *Geophys. Res. Lett.*, **41** (6), 2133–2141.

- Orlanski, I. and J. Katzfey, 1991: The life cycle of a cyclone wave in the Southern Hemisphere. Part I: Eddy energy budget. *J. Atmos. Sci.*, **48** (17), 1972–1998.
- Orlanski, I. and J. P. Sheldon, 1995: Stages in the energetics of baroclinic systems. *Tellus*, **47** (5), 605–628.
- Palmén, E., 1958: Vertical circulation and release of kinetic energy during the development of Hurricane Hazel into an extratropical storm. *Tellus*, **10** (1), 1–23.
- Park, T.-W., C.-H. Ho, S. Yang, and J.-H. Jeong, 2010: Influences of Arctic Oscillation and Madden-Julian Oscillation on cold surges and heavy snowfalls over Korea: A case study for the winter of 2009–2010. *J. Geophys. Res.*, **115** (D23).
- Parker, T. J., G. J. Berry, and M. J. Reeder, 2013: The influence of tropical cyclones on heat waves in Southeastern Australia. *Geophys. Res. Lett.*, **40** (23), 6264–6270.
- Petterssen, S. and S. J. Smebye, 1971: On the development of extratropical cyclones. *Quart. J. Roy. Meteor. Soc.*, **97** (414), 457–482.
- Quinting, J. F. and S. C. Jones, 2014: On the impact of tropical cyclones on Rossby wave packets: a climatological perspective. *Mon. Wea. Rev.*, **submitted**.
- Reynolds, C. A., M. S. Peng, and J.-H. Chen, 2009: Recurving Tropical Cyclones: Singular Vector Sensitivity and Downstream Impacts. *Mon. Wea. Rev.*, **137**, 1320–1337.
- Riehl, H., 1950: A Model of Hurricane Formation. *J. Appl. Phys.*, **21** (9), 917–925, doi:10.1063/1.1699784.
- Riemer, M., 2007: Außertropische Umwandlung tropischer Wirbelstürme: Einfluss auf das Strömungsmuster in den mittleren Breiten. Ph.D. thesis, Universität Karlsruhe, Germany.
- Riemer, M. and S. C. Jones, 2010: The downstream impact of tropical cyclones on a developing baroclinic wave in idealized scenarios of extratropical transition. *Quart. J. Roy. Meteor. Soc.*, **136** (648), 617–637.
- Riemer, M. and S. C. Jones, 2013: Interaction of a tropical cyclone with a high-amplitude, midlatitude wave pattern: Waviness analysis, trough deformation and track bifurcation. *Quart. J. Roy. Meteor. Soc.*
- Riemer, M., S. C. Jones, and C. A. Davis, 2008: The impact of extratropical transition on the downstream flow: An idealized modelling study with a straight jet. *Quart. J. Roy. Meteor. Soc.*, **134** (630), 69–91.
- Ritchie, E. A. and R. L. Elsberry, 2007: Simulations of the extratropical transition of tropical cyclones: Phasing between the upper-level trough and tropical cyclones. *Mon. Wea. Rev.*, **135** (3), 862–876.
- Rossby, C.-G., 1940: Planetary flow patterns in the atmosphere. *Quart. J. Roy. Meteor. Soc.*, **66**, 68–87.
- Rossby, C.-G., 1945: On the propagation of frequencies and energy in certain types of oceanic and atmospheric waves. *J. Meteor.*, **2** (4), 187–204.

- Rossby, C.-G. et al., 1939: Relation between variations in the intensity of the zonal circulation of the atmosphere and the displacements of the semi-permanent centers of action. *J. Mar. Res.*, **2** (1), 38–55.
- Rui, H. and B. Wang, 1990: Development characteristics and dynamic structure of tropical intraseasonal convection anomalies. *J. Atmos. Sci.*, **47** (3), 357–379.
- Röbcke, M., S. C. Jones, and D. Majewski, 2004: The extratropical transition of Hurricane Erin (2001): a potential vorticity perspective. *Meteorologische Zeitschrift*, **13** (6), 511–525.
- Scheck, L., S. C. Jones, and M. Juckes, 2011a: The resonant interaction of a tropical cyclone and a tropopause front in a barotropic model. Part I: Zonally oriented front. *J. Atmos. Sci.*, **68** (3), 405–419.
- Scheck, L., S. C. Jones, and M. Juckes, 2011b: The resonant interaction of a tropical cyclone and a tropopause front in a barotropic model. Part II: Frontal waves. *J. Atmos. Sci.*, **68** (3), 420–429.
- Schemm, S., H. Wernli, and L. Papritz, 2013: Warm Conveyor Belts in Idealized Moist Baroclinic Wave Simulations. *J. Atmos. Sci.*, **70** (2), 627–652.
- Schenkel, B. A. and R. E. Hart, 2012: An examination of tropical cyclone position, intensity, and intensity life cycle within atmospheric reanalysis datasets. *J. Climate*, **25** (10), 3453–3475.
- Scherrer, S. C., M. Croci-Maspoli, C. Schwierz, and C. Appenzeller, 2006: Two-dimensional indices of atmospheric blocking and their statistical relationship with winter climate patterns in the Euro-Atlantic region. *Int. J. Climatol.*, **26** (2), 233–249.
- Schreck III, C. J. and J. Molinari, 2009: A case study of an outbreak of twin tropical cyclones. *Monthly Weather Review*, **137** (3), 863–875.
- Screen, J. A. and I. Simmonds, 2014: Amplified mid-latitude planetary waves favour particular regional weather extremes. *Nature Climate Change*.
- Shapiro, M. A. and A. J. Thorpe, 2004: THORPEX international science plan. *WMO/TD*, **1246**.
- Simmons, A. J. and B. J. Hoskins, 1979: The downstream and upstream development of unstable baroclinic waves. *J. Atmos. Sci.*, **36** (7), 1239–1254.
- Slingo, J., 2013: Why was the start to spring 2013 so cold? *Met Office briefing note, April*.
- Souders, M. B., B. A. Colle, and E. K. Chang, 2014: The Climatology and Characteristics of Rossby Wave Packets Using a Feature-Based Tracking Technique. *Mon. Wea. Rev.*, (2014).
- Torn, R. D., 2010: Diagnosis of the downstream ridging associated with extratropical transition using short-term ensemble forecasts. *J. Atmos. Sci.*, **67** (3), 817–833.

- Uppala, S. M., P. Kållberg, A. Simmons, U. Andrae, V. Bechtold, M. Fiorino, J. Gibson, J. Haseler, A. Hernandez, G. Kelly, et al., 2005: The ERA-40 re-analysis. *Quart. J. Roy. Meteor. Soc.*, **131** (612), 2961–3012.
- Vecchi, G. A. and N. A. Bond, 2004: The Madden-Julian Oscillation (MJO) and northern high latitude wintertime surface air temperatures. *Geophys. Res. Lett.*, **31** (4).
- Vitart, F. and F. Molteni, 2010: Simulation of the Madden-Julian Oscillation and its teleconnections in the ECMWF forecast system. *Quart. J. Roy. Meteor. Soc.*, **136** (649), 842–855.
- Weickmann, K. M., 1983: Intraseasonal circulation and outgoing longwave radiation modes during Northern Hemisphere winter. *Mon. Wea. Rev.*, **111** (9), 1838–1858.
- Weickmann, K. M., G. R. Lussky, and J. E. Kutzbach, 1985: Intraseasonal (30–60 day) fluctuations of outgoing longwave radiation and 250 mb streamfunction during northern winter. *Mon. Wea. Rev.*, **113** (6), 941–961.
- Wheeler, M. C. and H. H. Hendon, 2004: An all-season real-time multivariate MJO index: Development of an index for monitoring and prediction. *Mon. Wea. Rev.*, **132** (8), 1917–1932.
- Wirth, V. and J. Eichhorn, 2014: Long-lived Rossby wave trains as precursors to strong winter cyclones over Europe. *Quart. J. Roy. Meteor. Soc.*, **140** (680), 729–737.
- Wolf, G. and V. Wirth, 2014: Implications of the semigeostrophic nature of rossby waves for rossby wave packet detection. *Mon. Wea. Rev.*, (2014).
- Yoo, C., S. Lee, and S. B. Feldstein, 2012: Mechanisms of arctic surface air temperature change in response to the Madden-Julian Oscillation. *J. Climate*, **25** (17), 5777–5790.
- Zhang, C., 2005: Madden-Julian Oscillation. *Rev. Geophys.*, **43** (2).
- Zhang, C., 2013: Madden-Julian Oscillation: Bridging Weather and Climate. *Bull. Amer. Meteor. Soc.*, **94** (12).
- Zhu, C., T. Nakazawa, J. Li, and L. Chen, 2003: The 30–60 day intraseasonal oscillation over the western North Pacific Ocean and its impacts on summer flooding in China during 1998. *Geophys. Res. Lett.*, **30** (18).
- Zimin, A. V., I. Szunyogh, B. R. Hunt, and E. Ott, 2006: Extracting Envelopes of Nonzonally Propagating Rossby Wave Packets. *Mon. Wea. Rev.*, **134** (4).
- Zimin, A. V., I. Szunyogh, D. Patil, B. R. Hunt, and E. Ott, 2003: Extracting envelopes of Rossby wave packets. *Mon. Wea. Rev.*, **131** (5).